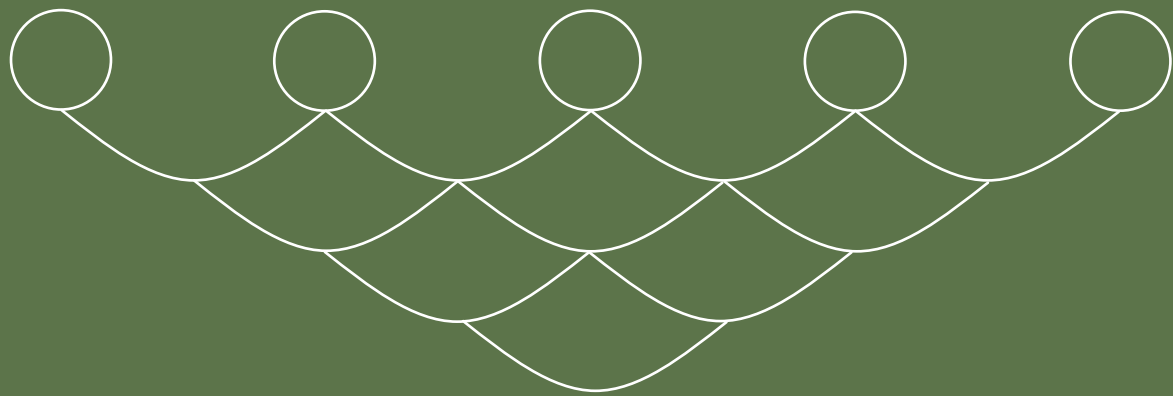


Adaptive design of the Wide Green Dike with multivariate uncertainty



Chris Veldman

Master Thesis

Adaptive design of the Wide Green Dike with multivariate uncertainty

Author:

C. R. Veldman

Studentnumber:

4702301

In fulfilment to obtain the degree of

Master of Science

at the Delft University of Technology

Faculty of Civil Engineering & Geosciences

Department of Hydraulic Engineering

Tracks: Coastal Engineering, Flood Risk & Hydraulic Structures

To be defended publicly on August 30, 2023.

Thesis Committee:

Dr. ir. O. Morales-Nápoles

Prof. dr. ir. M. R. A. van Gent

Dr. ir. P. Mares-Nasarre

Ir. T. Vrinds

Organisation:

TU Delft (chair)

Deltares, TU Delft

TU Delft

Sweco Nederland

An electronic version of this thesis is available at: <https://repository.tudelft.nl/>.

Cover image is obtained from Waterboard Hunze and Aa's (2023)



Preface

Dear reader,

This master's thesis fulfils my final requirement in order to obtain the degree of Master of Science in Hydraulic Engineering at Delft University of Technology. It marks the end of my time as a student at Delft. A time which has proven to be filled with great experiences both socially and academically. This thesis is a testament to those experiences. It combines the themes I am most passionate about in hydraulic engineering; probabilistic design, design methodology and finally some common sense.

I would like to use this preface to show my gratitude to several people. First and foremost, my thesis committee: Patricia, thank you for your great guidance and insights throughout the course of this thesis, your willingness to meet on a frequent basis, your firm hand to try and limit the scope of this thesis (which was not always easy), and of course the enjoyable discussions and conversations. Oswaldo, thank you for your interest in my thesis and my next steps, your help and input where needed, and most certainly your eternal enthusiasm. Thijs, thank you for your guidance and welcoming at Sweco, for introducing me to new topics and organisations, your willingness to dive into a very different topic, and not to forget, your endurance to stay till the end, where finally the adaptive design strategies were addressed. Marcel, thank you for your technical knowledge where needed, our enjoyable conversations, and your valuable insights in all our meetings. I want to thank all four of you for your constructive criticism, insightful comments, and most importantly your enthusiasm throughout my thesis.

In addition, I would like to thank Sweco for the opportunity to execute this thesis. Their support, new insights, hospitality, and the conversations we had during coffee moments and group meetings, resulted in an enjoyable time and most certainly improved this work.

Finally, I would like to extend my heartfelt gratitude to my loving family and dear friends, whose support, encouragement and laughter helped me throughout the years.

*Chris Veldman
Delft, August 2023*

Abstract

The uncertainty paired with the effects of climate change impacts the design aspects of hydraulic structures. To comprehend the uncertainty of the evolving conditions, methods and models that differ from the traditional ones could provide a better understanding of the uncertainty and potential risks associated with a design. This thesis aims to provide a framework for combining such methods. The thesis considers the Wide Green Dike project, which combines water safety and sustainability. The project, located in the Ems-Dollard estuary, involves the reinforcement of a primary water defence using locally ripened clay by removing sediment from the estuary. This helps to solve the silt problem in the Ems-Dollard. The objective is stated by ‘*develop a multivariate probabilistic tool to provide insight into incorporating adaptive design strategies, and to gain extra information that contributes to assessing the feasibility of the Wide Green Dike concept given the uncertainty of sea level rise*’.

Hydraulic structures like the Wide Green Dike are designed to withstand extreme natural events. Such events are characterized by the joint behaviour of random variables. Five variables are considered for which modelling the joint behaviour could be of interest; nearshore water level, offshore significant wave height and peak period, and nearshore wind speed and direction. The extremes of the design variables are sampled by a Peaks-Over-Threshold method. The water level is considered to be the dominant variable to which the method is applied, with a threshold of NAP +2.8 meters and a declustering time of 45 hours. The extreme conditions for the remaining variables correspond to the coinciding times of the dominant variable. The selected multivariate dataset contains 142 extreme events. A stationary and non-stationary extreme value analysis is performed for the extreme water level. The analyses showed that the water level is well-modelled using both approaches. The best model was found to be a non-stationary Generalized Pareto distribution with the wave height as the covariate.

The joint behaviour of the extremes is modelled using a vine copula. A vine copula is a structure of bivariate copulae, which are functions that examines the association of $N = 2$ variables. Connecting the copulae creates a multivariate $N > 2$ model. It was investigated whether a non-stationary extreme value analysis could be combined with copula modelling with the wave height as covariate. Introducing the non-stationary marginal distribution into copula modelling resulted that the transformation from the copula by the marginal distribution is no longer increasingly monotonic. This concluded that the built dependence structure was not preserved. Hence, to model using a vine copula, the water level is modelled by a stationary Generalized Pareto distribution. The best-performing vine copula was found a C-vine with the water level as the central node. The vine copula was found using a Brute Force approach by examining all possibilities using Morales-Nápoles et al. (2023). The vine copulae were assessed based on the AIC and the predicted exceedance probabilities.

A hybrid approach proposed by Camus et al. (2011a) is used to propagate the offshore wave characteristics to nearshore conditions. The method combines the numerical wave model SWAN with a surrogate model. The surrogate model captures the input-output behaviour of SWAN using radial basis functions. This approach significantly reduced the computational effort of the offshore-nearshore transformations. The surrogate model was extrapolated to include the SSP5-8.5 sea level rise scenario for the Dutch coast projected by KNMI (2021).

The Wide Green Dike is probabilistically assessed for its clay-erosion failure mechanism using a Monte Carlo simulation. The model to determine the erosion volume and profile results from Sweco (2021c). The vine-based design, with a design life of up to 2150, is selected by minimizing the cross-sectional area of the design while meeting the required failure probability. This design is compared to a deterministic design. The deterministic design resulted in significant increases; an increase of the crest height by 2 meters and the clay layer thickness of 52 centimetres. The mild outer slope of the Wide Green Dike of 1:7 resulted that the cross-sectional area of the deterministic design being +146% larger than the vine-based design. Moreover, the deterministic design intruded 19 meters further into the adjacent Natura 2000 area.

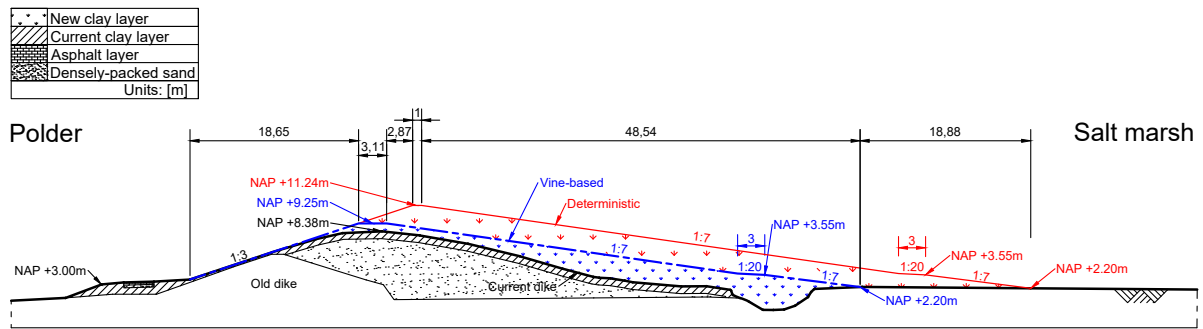


Figure 1: The vine-based and deterministic designs of the WGD for the year 2150.

To cope with the uncertainty of sea level rise, it is explored to incorporate an adaptive design strategy into the project. An adaptive design handles the uncertainty in long-term decisions by emphasizing adaptivity in its design (Haasnoot et al., 2013). Four different adaptive design strategies were created and assessed against the baseline strategy. The baseline strategy implies creating the final design with a sight-year of 2150 in one go. The strategies are assessed based on the amount of required clay, the up-scaling capacity of the clay refinery in the ED2050 program, the possible benefits associated with each strategy and the impact on the adjacent Natura 2000 area.

It was found that incorporating an adaptive design strategy into the WGD project can promote its business case and help mitigate the risk of over-designing in a Natura 2000 area. Adaptive strategies can help lower the initial clay capacity required for the construction of the WGD. Hence, the risk of not meeting the ambitious up-scaling capacity goals could be reduced. If the goals are met, the excess clay can be used for other purposes, resulting in an export product. Including adaptive strategies can also be beneficial for the business case of the WGD. The possible benefits can be reinvested elsewhere and compound over time. Moreover, the risk of over-designing can be mitigated by using adaptive strategies. The uncertainty in SLR could result in the risk of over-designing when a milder SLR scenario becomes a reality. The preferred strategy concerns constructing a design with a sight-year of 2090 in 2050 and adding two possible adaptations with sight-years of 2120 and 2150 during its design life.

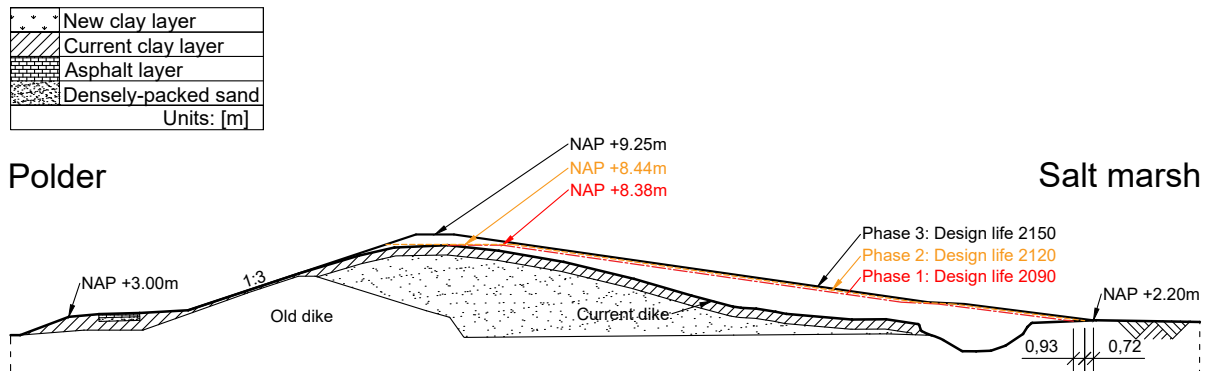


Figure 2: The cross-section and construction phases of the selected adaptive design strategy.

Contents

Preface	i
Abstract	iii
1 Introduction	1
1.1 Context of the Problem	1
1.2 Objective & Research Questions	2
1.3 Methodology & Structure	3
1.4 Thesis Scope	5
2 Case Study: The Wide Green Dike	6
2.1 Introduction to the Wide Green Dike project	6
2.2 Up-scaling of the Clay Refinery from the Ems-Dollard 2050 Program	7
2.3 The Clay-Erosion failure mechanism of the Wide Green Dike	8
2.4 Data Collection & Selection	10
2.4.1 Water level Data Selection	10
2.4.2 Wave Data Selection	13
2.4.3 Wind Data Selection	13
2.4.4 Bathymetry	14
2.5 Accounting for an Uncertain Sea Level Rise	14
3 Extreme Value Analysis	16
3.1 Extreme Value Sampling Techniques	16
3.1.1 The Block Maxima method	16
3.1.2 The Peaks-Over-Threshold Method	17
3.2 Peaks-Over-Threshold Method with water level as the dominant variable	18
3.3 Stationary Extreme Value Analysis	21
3.3.1 Selection of Extreme Value Distributions	22
3.3.2 Application of the Stationary Extreme Value Analysis	23
3.4 Non-stationary Extreme Value Analysis	26
3.4.1 Introduction of a Non-stationary Extreme Value Analysis	26
3.4.2 Application of multiple Non-stationary models	28
3.5 Conclusion of the Extreme Value Analysis	30
4 Copula & Vine modelling	31
4.1 Theory on multivariate modelling	31
4.1.1 Measures of Association	31
4.1.2 Bivariate Copulae	32
4.1.3 Vine Copulae	34
4.2 Selection of the Marginals of the Concomitant variables	37
4.3 Application of Bivariate Copulae Modelling	39
4.4 Application of Non-stationary marginals in Copula modelling	43
4.4.1 Proposed Algorithm	44
4.4.2 Findings from the application	44
4.4.3 Conclusion and Remarks	47
4.5 Vine Copula modelling	48
4.5.1 Selecting Vine Copulae by a Brute Force procedure	48
4.5.2 Performance of the Maximum Spanning Tree Algorithm	50
4.5.3 Vine Copula Validation	51
4.6 Conclusions of the Multivariate Modelling	52

5	Base Design of the Wide Green Dike	53
5.1	Offshore-Nearshore Transformation	53
5.1.1	Selection of representative Storm Conditions	53
5.1.2	Transformation in SWAN	55
5.1.3	Surrogate model using Radial Basis Functions	56
5.1.4	Storm Progression in the Wadden Sea area	57
5.1.5	Simulating the Nearshore Wave conditions including Sea Level Rise	58
5.2	Vine-based Design of the Wide Green Dike	59
5.3	Comparison with a Deterministic Design	63
6	Adaptive Design Strategies	65
6.1	Introduction to Adaptive Design Strategies	65
6.2	Creating the Adaptive Design Strategies	66
6.3	Assessment of the Adaptive Strategies	68
6.3.1	The Required Clay and associated Costs per Adaptive Strategy	69
6.3.2	Benefits per Strategy including the Uncertainty of Sea Level Rise	70
6.3.3	The Preferred Adaptive Strategy	74
7	Discussion	75
7.1	Available Data in the Ems-Dollard estuary	75
7.2	Multivariate Modelling of Extremes by Vine Copulae	75
7.3	The effect of Climate Change on Extremes	76
7.4	Offshore-Nearshore Transformation by SWAN and a Surrogate model	77
7.5	The Design and Clay-Erosion failure mechanism	77
7.6	Adaptive Design Strategies and the Clay Ripening process	78
8	Conclusion & Recommendations	79
8.1	Conclusion	79
8.2	Recommendations for future work	81
8.2.1	Case Study: The Wide Green Dike	81
8.2.2	Results of the Multivariate Design	82
8.2.3	Future Applications of a Multivariate Approach	83
	References	88
A	Information on the Datasets used	89
B	Results Extreme Value Analysis	91
C	Modelling the Concomitants	100
D	Selection of Bivariate Copulae	105
E	Additional Results for Non-stationary marginals in Copula modelling	119
F	Vine Copulae Analysis	121
G	SWAN Input File	125
H	The Deterministic Design of the Wide Green Dike	126
I	Additional results of the Vine-Based Design	129
J	SSP5-8.5 Sea Level Rise scenario	133
K	Selected Adaptive Design Strategy	134

Nomenclature

Abbreviations

Abbreviation	Definition
AIC	Akaike Information Criterion
BIC	Bayesian Information Criterion
BM	Block Maxima
CM	Cramér-Von Mises test
DI	Dispersion Index
DTM	Digital Terrain Model
ECMWF	European Centre for Medium-Range Weather Forecasts
EI	Extremal Index
EMODnet	European Marine Observation and Data Network
ERA5	ECMWF Re-Analysis 5 th Generation
EVA	Extreme Value Analysis
GEV	Generalized Extreme Value distribution
GPD	Generalized Pareto Distribution
IPCC	Intergovernmental Panel on Climate Change
KNMI	Royal Netherlands Meteorological Institute
LL	Lower-Left
LM	L-moments estimator
LOOCV	Leave-One-Out Cross Validation
LR	Lower-Right
MDA	Maximum Dissimilarity Algorithm
MLE	Maximum Likelihood Estimator
MST	Maximum Spanning Tree algorithm
NAP	Amsterdam Ordnance Datum
NEVA	Non-stationary Extreme Value Analysis
POT	Peaks-Over-Threshold method
Q-Q	Quantile-Quantile plot
RBF	Radial Basis Function
RL	Return Level
RQ	Research Question
SLR	Sea Level Rise
SSP	Shared Socioeconomic Pathways
SWAN	Simulating WAVes Nearshore
UL	Upper-Left
UR	Upper-Right
WBI	Dutch Legal Assessment Toolkit
WGD	Wide Green Dike

Symbols

Symbol	Definition	Unit
A_d	Design cross-sectional area [m^2]	
b_{cr}	Crest width	[m]
$b_{cr,d}$	Design crest width	[m]
$b_{cr,min}$	Minimum crest width	[m]
c	Shape parameter of Gaussian	[$-$]
c_e	Erosion coefficient for clay erosion	[$-$]
d_0	Starting erosion depth for clay erosion	[m]
d_e	Perpendicular erosion depth for clay erosion	[m]
$d_{e,d}$	Design clay layer thickness	[m]
d_t	Erosion depth below water level for clay erosion	[m]
f_β	Influence factor for β	[$-$]
F_X	Marginal distribution of X	
g	Gravitational constant (= 9.81)	[m/s^2]
h	Water level	[NAP + m]
h_{SLR}	Maximum water level including SLR	[NAP + m]
h_{18}	18-hour storm average water level	[NAP + m]
h_{cr}	Crest height	[NAP + m]
$h_{cr,d}$	Design crest height	[NAP + m]
$h_{cr,min}$	Minimum crest height	[NAP + m]
H_{m0}	Average significant wave height	[m]
H_s	Significant wave height	[m]
H_{s-p}	Propagated significant wave height	[m]
L_e	Erosion length for clay erosion	[m]
n	Number of samples	[$-$]
N	Number of variables	[$-$]
	Number of years for return period	[$-$]
	Set of nodes	
N_{obs}	Number of observed data points	[$-$]
N_{par}	Number of model parameters	[$-$]
N_s	Number of extremes per year	[$-$]
p	p -value	
P_f	Failure probability	[$1/y$]
$P_{f,req}$	Required failure probability	[$1/y$]
r_S	Spearman's correlation coefficient	[$-$]
r_{18}	Reduction factor to 18-hour average storm conditions	[$-$]
R	Rank	[$-$]
R^2	Coefficient of determination	[$-$]
s_{op}	Wave steepness	[$-$]
t	Time	[h]
T	Return period	[y]
	Set of trees	
T_{block}	Block period of BM method	[h]
T_p	Peak wave period	[s]
T_{p-p}	Propagated peak wave period	[s]
u	Threshold of POT method for the water level	[NAP + m]
V_e	Erosion volume for clay erosion	[m^3/m]
V_{tot}	Total design volume	[m^3]
w_s	Wind speed	[m/s]
w_d	Wind direction	[$^\circ$]

Greek	Definition	Unit
α	Outer embankment slope (= 1 : 7)	[rad]
α_{cliff}	Erosion profile slope of the cliff for clay erosion	[rad]
α_{in}	Inner embankment slope (= 1 : 3)	[rad]
$\alpha_{terrace}$	Erosion profile slope of the terrace for clay erosion	[rad]
β	Angle of wave attack	[°]
δ	Declustering time of POT method for the water level	[h]
ϵ	Standard error	[-]
θ	Wave direction	[°]
	Copula parameter	[-]
θ_p	Propagated wave direction	[°]
λ	Rate parameter	[-]
μ	Location parameter	[NAP +m]
μ_0	Stationary part of location parameter	[NAP +m]
μ_1	Non-stationary part of location parameter	[NAP +m]
ξ	Shape parameter	[-]
ξ_0	Stationary part of shape parameter	[-]
ξ_1	Non-stationary part of shape parameter	[-]
ρ_P	Pearson's correlation coefficient	[-]
σ	Scale parameter	[-]
σ_0	Stationary part of scale parameter	[-]
σ_1	Non-stationary part of scale parameter	[-]
τ_K	Kendall's correlation coefficient	[-]
Φ	Gaussian function	

Mathematical operators	Definition	Unit
cov	Covariance	
\mathcal{C}	Copula	
\mathcal{C}_n	Empirical copula	
$\overline{\mathcal{C}}$	Survival copula	
E	Expected value	
I	Domain [0,1]	
P	Probability	
\mathcal{L}	Log-likelihood function	
$\hat{\mathcal{L}}$	Maximum log-likelihood value	
\mathcal{V}	Vine	

List of Figures

1.1	Demonstration project of the Wide Green Dike. Retrieved an modified from ‘Proef-project Brede Groene Dijk’ (https://www.hunzeenaas.nl/projecten/brede-groene-dijk/brede-groene-dijk/) by Waterboard Hunze and Aa’s (2022)	1
1.2	Thesis structure and chapter layout of Chapters 2 up to 6.	3
1.3	Illustration of the failure cases for a Monte Carlo simulation.	4
2.1	The Dutch Wadden Sea area, with the Ems-Dollard estuary enlarged. Retrieved from OpenStreetMap (https://www.imergis.nl/) by van Aalst (2021).	6
2.2	The land reclamation in time of the Ems-Dollard estuary. Retrieved from Kirchhoff (1992).	7
2.3	Sketch of the erosion profile with variables. Retrieved and modified from ‘Prediction of the erosion velocity of a slope of clay due to wave attack’ by Deltares (2020), p.3.	8
2.4	Erosion profile from the Delta Flume tests after 16 hours (bold green line) and calculated from Mourik’s model (red line) (black line is the dike profile, the blue line is the water level). Retrieved from ‘Vergelijking erosieprofiel Deltagoot en berekend’ by Sweco (2021d), p.5.	9
2.5	Measurement locations in the Ems-Dollard. The water level measurement in the Dollard estuary: Dollard West, Groote Gat, Nieuwe Statenzijl, Reide and Schanskersdiep.	11
2.6	Water level comparison between Nieuwe Statenzijl and the other four locations Dollard West, Schanskersdiep, Groote Gat and Reide for the years 1994 up to 2001.	12
2.7	Station plots of the water level with Nieuwe Statenzijl on the x-axis and the other four locations Dollard West, Schanskersdiep, Groote Gat and Reide on the y-axis.	12
2.8	Wind rose signifying the directional frequency and the maximum hourly wind velocities. The wind data is sourced from KNMI (2022).	14
2.9	The observed and sea level projections for the Dutch coast up to the year 2100 (left) and 2300 (right). The images are retrieved and modified from KNMI (2021), pp. 29-30.	15
3.1	An example of a Block Maxima method. The peaks of T_1 , T_3 , T_4 , T_5 and T_6 are selected as extreme values. The peak of T_2 is not selected since it occurs within the same block as T_1	16
3.2	An example of a Peaks-Over-Threshold method. The peaks of times T_1 and T_2 are selected extremes, where the peak of T_3 is not suitable. This is due to an inter-cluster time that is smaller than the declustering time, $C_2 < \delta$. The threshold u is shown by the red horizontal line.	17
3.3	Mean Residual Life plot of the water level as the dominant variable.	18
3.4	Parameter stability plots with the water level as the dominant variable.	19
3.5	Extremal Index plot for the water level as the dominant variable.	20
3.6	Dispersion Index plot for the water level with $\delta = 45$ hours.	21
3.7	Number of extremes per year for the water level with $\delta = 45$ hours.	21
3.8	Return level plot of the extreme water level for multiple distributions	23
3.9	Q-Q plots for multiple distributions of the extreme water level.	24
3.10	Exceedance probability $\mathbb{P}(h > x)$ plot (logarithmic scale) of the extreme water level h	24
3.11	Displaying a non-stationary trend and parameters showing the change in tail probabilities	26
3.12	Return period for a stationary versus non-stationary random variable. Image retrieved and modified from Salas and Obeysekera (2014), pp. 554–568.	28
3.13	The 10-, 100- and 1000-year effective return levels for the non-stationary GPD $_{H_s}$ models.	29
4.1	Examples of positive and negative correlation of two random variables X and Y in $[0, 1]^2$	32
4.2	A regular vine (left) and non-regular vine (right) on $n = 4$ variables. The blue edge in the non-regular vine shows a connection between two nodes which do not share a common node. Every edge on the left vine represents a (conditional) bivariate copula. Retrieved from Timmermans (2021).	35
4.3	A D-vine (left) and a C-vine (right) on $n = 4$ variables. Retrieved from Timmermans (2021).	35
4.4	Selection of the concomitant variable Y at the coinciding times of the dominant variable X	37
4.5	Exceedance probability $\mathbb{P}(H_s > x)$ of different models for wave height H_s	38

4.6	Wind rose of the selected extreme events.	39
4.7	Semi-correlation of the Survival Clayton model for water level h and wave height H_s	41
4.8	CDF of the Survival Clayton and empirical copula for water level h and wave height H_s	42
4.9	Samples of Survival Clayton in $[0, 1]^2$ for water level h and wave height H_s	42
4.10	Samples of Survival Clayton in variable space for water level h and wave height H_s	43
4.11	The results of transforming the copula samples of the water level and wave height into variable space using a non-stationary (left) and stationary (right) marginal for the water level.	45
4.12	Original extreme values and Survival Copula samples in unity space. Three extremes are selected resulting in points 1, 2 and 3. The orange planes show the trouble areas for point 1.	45
4.13	Exceedance probabilities of the original and transformed points 1, 2 and 3.	46
4.14	Transformation of variable space back into copula space. Showing the original samples for the Survival Clayton copula and the transformation by the non-stationary model.	47
4.15	The best-performing vine copula based on AIC from Procedure 3. The vine is a C-vine with the water level as the central node.	50
4.16	CDF of the performance of the MST algorithm versus Brute Force fitting for Procedure 3.	51
4.17	The predicted against empirical exceedance probabilities of the observations $\mathbb{P}(h > x \cap H_s > x \cap T_p > x \cap w_s > x \cap w_d > x)$ for the two best-fitting vine copulas from Procedure 3.	52
5.1	Selected cases for each variable using the MDA.	55
5.2	The significant wave height and directions for one of the selected cases transformed by SWAN.	56
5.3	Locations of Delfzijl, the WGD trajectory and water level measurements at Nieuwe Statenzijl.	58
5.4	The assumed water level progression (green line) for a storm with a 45-hour duration. Image retrieved and modified from ‘Ontwerprapport Brede Groene Dijk’ by Sweco (2021b), p.21.	58
5.5	Sketch of the plot from Algorithm 5.3. The green area shows the calculated cross-sectional area A_d . The black line shows the current dike geometry.	61
5.6	The vine-based and deterministic designs of the WGD for the year 2150.	63
6.1	Sketch of the change in dike profile due to an adaption by increasing $d_{e,d}$ or $h_{cr,d}$	66
6.2	The considered Probability Density Functions over time for the SSP5-8.5 scenario.	67
6.3	The required m^3 of clay over time for four different strategies and baseline.	69
6.4	Samples of the SLR scenarios, connecting the SLR samples in each year based on their ranks.	71
6.5	Benefits in million euros created by investing the benefits in clay costs against 4% interest per year. The costs of clay ($\text{€}30/m^3$) increase by 2% per year, accounting for inflation. The shaded areas enclose the 1 st and 99 th percentiles and the lines show the 50 th percentile of the strategies.	73
8.1	The vine-based and deterministic designs of the WGD for the year 2150.	80
8.2	The cross-section and construction phases of the selected adaptive design strategy.	81
A.1	Data points of the water level, wave height and wave period.	90
B.1	Selected extreme water levels on top of the hourly water level data points.	91
B.2	Extreme water levels for a threshold u of 2.8 and 3.3 meters NAP and the yearly maxima	92
B.3	The concomitant variables with water level as the dominant variable. A threshold of $u = 2.8$ meters NAP, showing a slightly decreasing trend over time.	93
B.4	The concomitant variables with water level as the dominant variable. A threshold of $u = 3.3$ meters NAP, showing a clear positive trend over time.	94
B.5	Selected extreme water levels with u of 2.8 and 3.3 meters NAP against the concomitant wave height.	95
B.6	Return level plot of the extreme water level for GPD using the MLE.	96
B.7	Return Level plot of GPD with the LM method.	96
B.8	Return Level plot of GEV with the MLE.	96
B.9	Return Level plot of Gumbel with the MLE	97
B.10	Return Level plot of Exponential with the MLE	97
B.11	Histogram of the extreme water level and the fitted GPD.	97
B.12	CDF plot of all models for the extreme water levels.	98
B.13	CDF plot of GPD with the MLE for the extreme water level.	98

B.14	Histogram of the extreme water level and the non-stationary GPD $_{H_s, \sigma}$ model.	99
C.1	Exceedance probability $\mathbb{P}(T_p > x)$ of different models for wave period T_p	101
C.2	Exceedance probability $\mathbb{P}(w_s > x)$ of different models for wind speed w_s	102
C.3	Exceedance probability $\mathbb{P}(w_d > x)$ of different models for rotated wind direction w_d	102
C.4	CDF plots of the concomitant variables and the selected models.	103
C.5	Histograms of the concomitant variables and the selected models.	104
D.1	Semi-correlation of the Gumbel model for water level h and wave period T_p	109
D.2	Semi-correlation of the Frank model for water level h and wind speed w_s	109
D.3	Semi-correlation of the Survival Gumbel model for wave height H_s and wave period T_p	109
D.4	Semi-correlation of the Gaussian model for wave height H_s and wind speed w_s	110
D.5	Semi-correlation of the Survival Gumbel model for wave height H_s and wind direction w_d	110
D.6	Semi-correlation of the Gaussian model for wave period T_p and wind direction w_d	110
D.7	Semi-correlation of the Joe rotated by 90° for wind direction w_d and wind speed w_s	111
D.8	CDF of the Gumbel and empirical copula for water level h and wave period T_p	111
D.9	CDF of the Frank and empirical copula for water level h and wind speed w_s	111
D.10	CDF of the Survival Gumbel and empirical copula for wave height H_s and wave period T_p	112
D.11	CDF of the Gaussian and empirical copula for wave height H_s and wind speed w_s	112
D.12	CDF of Survival Gumbel and empirical copula for wave height H_s and wind direction w_d	112
D.13	CDF of the Gaussian and empirical copula for wave period T_p and wind direction w_d	113
D.14	CDF of Joe rotated by 90° and empirical copula for wind direction w_d and wind speed w_s	113
D.15	Samples of Gumbel in $[0, 1]^2$ for water level h and wave period T_p	113
D.16	Samples of Frank in $[0, 1]^2$ for water level h and wind speed w_s	114
D.17	Samples of Survival Gumbel in $[0, 1]^2$ for wave height H_s and wave period T_p	114
D.18	Samples of Gaussian in $[0, 1]^2$ for wave height H_s and wind speed w_s	114
D.19	Samples of Survival Gumbel in $[0, 1]^2$ for wave height H_s and wind direction w_d	115
D.20	Samples of Gaussian in $[0, 1]^2$ for wave period T_p and wind direction w_d	115
D.21	Samples of Joe rotated by 90° in $[0, 1]^2$ for water level h and wave period T_p	115
D.22	Samples of Gumbel in variable space for water level h and wave period T_p	116
D.23	Samples of Frank in variable space for water level h and wind speed w_s	116
D.24	Samples of Survival Gumbel in variable space for wave height H_s and wave period T_p	116
D.25	Samples of Gaussian in variable space for wave height H_s and wind speed w_s	117
D.26	Samples of Survival Gumbel in variable space for wave height H_s and wind direction w_d	117
D.27	Samples of Gaussian in variable space for wave period T_p and wind direction w_d	117
D.28	Samples of Joe rotated by 90° in variable space for wind direction w_d and wind speed w_s	118
E.1	The relation between the wave height and the scale parameter $\sigma(H_s)$	119
E.2	The transformed samples to water levels against the scale parameter $\sigma(H_s)$	119
E.3	The water level plotted against its ranks. The ranks of the original samples change due to the introduction of the non-stationary model.	120
F.1	Best vine copulas of Procedure 1 and 2.	121
F.2	Vine copulas of Procedure 1, 2 and 3 selected by the MST algorithm. Note, the vine copulas selected for Procedures 1 and 2 are tree-equivalent.	122
F.3	CDF of the performance of the MST algorithm versus Brute Force fitting for Procedures 1 and 2.	123
F.4	Plot of the performance of the MST algorithm and all possible matrices for Procedure 3.	123
F.5	2 nd best-fitting vine copula from Procedure 3.	124
H.1	The deterministic design of the WGD.	128
I.1	The modelled erosion coefficient c_e for $n = 1, 000, 000$ samples.	130
I.2	The 18-hour average water level and wave height combinations for which the probabilistic design failed.	130
I.3	The combinations of wind direction w_d and 18-hour average water level h_{18} and reduced wave height H_s that led to the failure of the probabilistic design.	131
I.4	The probabilistic design of the WGD for the year 2150. A water line is drawn to emphasize the seaward side of the dike.	132
J.1	The considered Probability Density Functions for different years for the SSP5-8.5 scenario.	133
K.1	The cross-section and construction phases of the selected strategy, Strategy 2.	135

List of Tables

2.1	Acquired datasets and sources.	10
2.2	Statistical summary of the differences between the coinciding water level for the different locations with Nieuwe Statenzijl. A negative value represents that the coinciding water level at the location is lower than at Nieuwe Statenzijl.	13
2.3	Statistical summary of the wave data from ERA5 by ECMWF (2022).	13
2.4	Projected SLR scenarios for the Dutch coast by KNMI (2021). The SLR is projected against the period 1995-2014, with a 90% confidence interval. Soil subsidence is included in the SLR projections.	15
3.1	Parameter estimates and goodness-of-fit criteria of extreme water level for different models.	25
3.2	Non-stationary GPD model parameters and standard errors for covariates (CV) t and H_s	29
3.3	Goodness-of-fit criteria of the non-stationary GPD models for covariates t and H_s	29
3.4	Comparison between the selected stationary and non-stationary GPD models.	30
4.1	Number of possible labelled trees and regular vines on 3, 4, 5, 6, 7, and 8 nodes. This table is retrieved and adapted from Morales-Nápoles et al. (2010).	36
4.2	Estimated parameters of the selected concomitant models using MLE.	39
4.3	Spearman's r_S correlation for every variable pair.	40
4.4	AIC, CM scores and semi-correlations for the pair water level h and wave height H_s	41
4.5	The selected bivariate copulas and copula parameter θ for every variable pair.	43
4.6	The original and transformed wave height H_s and water level h values for points 1, 2 and 3.	47
4.7	The minimum and maximum AIC values for the three procedures of the Brute Force method and the p_i percentile and AIC of the Maximum Spanning Tree algorithm.	49
5.1	The WGD dike normal at P_1 , P_2 and P_3	60
5.2	The return period T in years for the 18-hour average water level h_{18} for different SLR scenarios for the year 2150.	63
5.3	Comparison of the deterministic and vine-based design.	63
6.1	The required design parameters: crest height $h_{cr,d}$, clay layer thickness $d_{e,d}$ and cross-sectional area A_d , over time for the WGD.	68
6.2	Overview of the design combinations for each adaptive strategy.	68
6.3	Required clay in m^3 for the construction and adaptation phases.	70
6.4	The total clay costs in million € for each phase for the strategies (based on the 2021 price level and not accounted for inflation).	70
6.5	The total benefits in 2150 in million € for the 1 st , 50 th and 99 th percentiles for each strategy, based on a fixed 4% interest rate and 2% inflation rate per year.	73
A.1	Information on the original datasets used in this project	89
A.2	Information of the original wave, water level and wind variable data used in this project	89
B.1	Return levels of extreme water level for different stationary models.	99
C.1	Goodness-of-fit criteria of wave height H_s and wave period T_p for several models. The best scores are displayed in bold green.	100
C.2	Goodness-of-fit criteria of wind speed w_s and wind direction w_d for several models. The best scores are displayed in bold green.	100
D.1	AIC, CM scores and semi-correlations for the pair water level h and wave period T_p	105
D.2	AIC, CM scores and semi-correlations for the pair water level h and wind speed w_s	105
D.3	AIC, CM scores and semi-correlations for the pair water level h and wind direction w_d	106
D.4	AIC, CM scores and semi-correlations for the pair wave height H_s and wave period T_p	106
D.5	AIC, CM scores and semi-correlations for the pair wave height H_s and wind speed w_s	107
D.6	AIC, CM scores and semi-correlations for the pair wave height H_s and wind direction w_d	107
D.7	AIC, CM scores and semi-correlations for the pair wave period T_p and wind speed w_s	107
D.8	AIC, CM scores and semi-correlations for the pair wave period T_p and wind direction w_d	108
D.9	AIC, CM scores and semi-correlations for the pair wind speed w_s and wind direction w_d	108
E.1	Parameter, semi-correlations and AIC of the original copula and transformed variable space and copulas samples from the non-stationary model $H_{u,\sigma_{H_s}}$	120
F.1	The (conditional) copulas and parameters θ for the vines of Procedures 1, 2 and 3.	121

F.2	The (conditional) copulas of the selected vines using MST for Procedures 1, 2 and 3. . . .	122
F.3	The (conditional) copulas of the 2 nd best-fitting vine copula of Procedure 3.	124
H.1	Design values of the deterministic design.	126
H.2	Propagated wave characteristics at points P_1 , P_2 and P_3 of the deterministic design. . . .	127
H.3	Erosion profile at point P_3 of the deterministic design.	127
I.1	Statistical summary of the input for the offshore-nearshore transformation.	129
I.2	Statistical summary of the input for the offshore-nearshore transformation.	129
I.3	Statistical summary of the 18-hour average water level h_{18} , offshore wave height $H_{s,o}$ and period $T_{p,o}$ and wind speed w_s and direction w_d for which the probabilistic design failed. .	131
I.4	Statistical summary of the reduced nearshore wave height H_s and period T_p for which the probabilistic design failed.	131
J.1	Log-Normal distribution parameters of the SLR for different years.	133

1 | Introduction

1.1 Context of the Problem

Hydraulic structures are essential for water management by creating protection against flooding, fresh-water supply, and marine and inland navigation. The design of such structures is bound to meet current and future social, economic and environmental needs (Epicum et al., 2020). With evolving challenges such as climate change, a design approach centred around sustainability and multidisciplinary perspectives could be favoured.

The Dutch National Water Program 2022-2027 defines a new policy that aims to adapt the Dutch water domain to clean, safe and sufficient water that is climate adaptive and future-proof (Rijksoverheid, 2022). In addition, it stimulates integral solutions between the water and common ground sectors. Creative design in hydraulic engineering that integrates different aspects, such as water safety with climate adaptation, sustainable freshwater supply, water quality, and various other functions, will be necessary to adapt the water domain to the impact of climate change. The Wide Green Dike (in Dutch: Brede Groene Dijk) project in the Ems-Dollard area is an example of such a creative design in hydraulic engineering. The project combines water safety and sustainability by creating a green dike, without any rock revetment, from local ripened clay acquired from the Ems-Dollard estuary. Implementing such creative designs could encounter new uncertainties. Methods and models required to deal with these uncertainties could also be different from the traditional ones used.

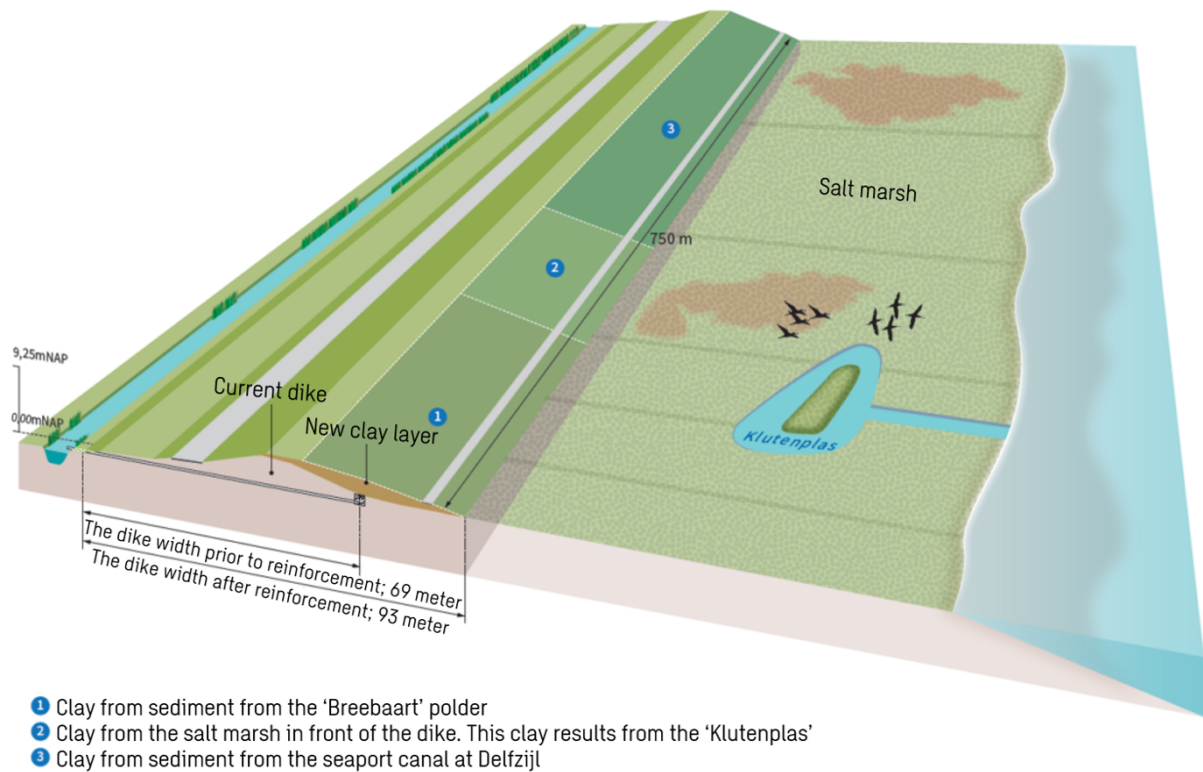


Figure 1.1: Demonstration project of the Wide Green Dike. Retrieved and modified from 'Proefproject Brede Groene Dijk' (<https://www.hunzeenaas.nl/projecten/brede-groene-dijk/brede-groene-dijk/>) by Waterboard Hunze and Aa's (2022)

In traditional design, a deterministic design approach is often preferred for its simplicity. It relies on well-known inputs, established design guidelines and deterministic models to determine the design parameters and dimensions of hydraulic structures. A deterministic approach does not explicitly consider variability or the uncertainty paired with the design conditions. Nowadays, the switch to (univariate)

semi-probabilistic and probabilistic approaches is increasing. A semi-probabilistic approach incorporates some degree of probabilistic techniques by including statistical distributions or safety factors when selecting design parameters while maintaining a predominantly deterministic framework. A probabilistic approach explicitly considers uncertainty and variability throughout the design process. The uncertainties associated with design parameters are quantified using statistical techniques and distributions. A probabilistic approach is used to assess the failure probability or performance of a hydraulic structure at a detailed level. It provides a more comprehensive understanding of the uncertainties and potential risks associated with a design.

Climate change results in a change in hydraulic conditions over time, such as sea level rise. The Intergovernmental Panel on Climate Change (IPCC, 2022) projected different climate scenarios, corresponding to different emission scenarios. These scenarios showed that over a time span of 50+ years, climate change can result in a significant sea level rise. If this is not taken into account in the design, the design variables could be well misrepresented. In hydraulic structure design, a design life of 50+ years is very typical, hence climate change should be accounted for. It is clear that climate change creates uncertain future boundary conditions. In the current context of climate change, a deterministic approach should be questioned and a probabilistic approach should be favoured.

Hydraulic structures are designed to withstand loading conditions related to extreme environmental scenarios. To comprehend the uncertainty of changing environmental conditions in hydraulic structure design, the introduction of new methods and models should be aspired. A method to model this change is a non-stationary extreme value analysis (Gumbel, 1958). The non-stationarity of variables, such as sea level rise, can be captured using statistical models to make a prediction for representative future values of the variable. Moreover, natural hazards are characterized by the shared dependence of several random variables (Salvadori et al., 2007). Multivariate probabilistic design clears the way for exploring dependencies between design variables. A multivariate approach models the joint occurrence of a combined condition, revealing new insights e.g., the correlation between wave height, wind speed and water level.

Next to incorporating new models that estimate the uncertainty and changing conditions related to climate change, there could be a leap forward could in design methodology. Adaptive design strategies can provide a way to mitigate over-designing hydraulic structures. To cope with the uncertainty of sea level rise, this methodology aims at handling the uncertainty in long-term decisions by emphasizing adaptivity in a design. An adaptive design can adapt to new boundary conditions when new future information is collected (Haasnoot et al., 2013).

1.2 Objective & Research Questions

This thesis provides a possible framework for combining non-stationary extreme value analysis, multivariate modelling and adaptive design strategies and explores the insights gained by incorporating such pioneering approaches for a real hydraulic structure project. The objective of the thesis is stated by ‘develop a multivariate probabilistic tool to provide insight into incorporating adaptive design strategies, and to gain extra information that contributes to assessing the feasibility of the Wide Green Dike concept given the uncertainty of sea level rise’. This objective is rephrased into a main research question.

How can a multivariate probabilistic tool provide insight into incorporating adaptive design strategies and how could it provide additional insights regarding the feasibility of the Wide Green Dike concept given the uncertainty of sea level rise?

To reach the objective of this thesis three research questions (RQ) are posed:

RQ 1: *Can a Non-stationary Extreme Value Analysis be applied in a multivariate design approach using Vine-Copulae?*

RQ 2: *What are the design differences between a multivariate probabilistic design and a deterministic design for the Wide Green Dike project?*

RQ 3: *How can incorporating an adaptive design strategy to the Wide Green Dike concept promote its feasibility given the uncertainty of sea level rise?*

1.3 Methodology & Structure

To achieve the thesis objective, this thesis is structured as visualized in Figure 1.2. The thesis starts with the collection and selection of data. The case study, the Wide Green Dike (WGD), results in the design variables of interest. Data of the variables and project information is gathered in Chapter 2. The design of the WGD is based on extreme conditions. To define and model such extremes, Chapter 3 performs an extreme value analysis on the selected data. The dependence structure of the extremes is modelled in Chapter 4. This results in a multivariate model that models the extreme conditions for the WGD while respecting the joint behaviour of the design variables during such extremes. To get design values for the design, an offshore-nearshore transformation is performed and sea level rise is included. The results are used to create a multivariate probabilistic base design in Chapter 5. This design is compared to a deterministic design. In Chapter 6, multiple adaptive design strategies are explored for the WGD project. The strategies are assessed based on several criteria ranging from the business case to the environmental aspects. The assumptions made and the limitations and challenges found over the course of this thesis are discussed in Chapter 7. Chapter 8 concludes the key findings of the thesis and provides multiple recommendations for the case study, multivariate modelling and future works regarding multivariate modelling for hydraulic structure design.

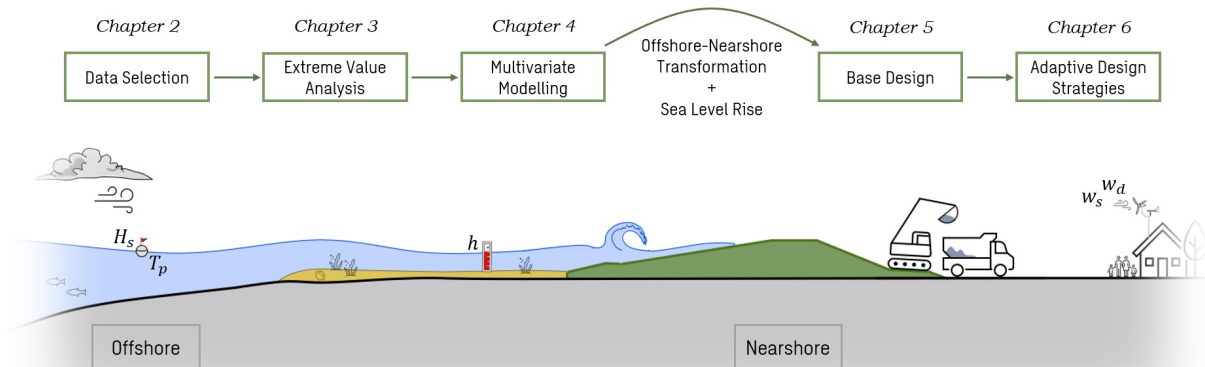


Figure 1.2: Thesis structure and chapter layout of Chapters 2 up to 6.

Chapter 2 introduces the WGD project. This thesis considers one of the dominant failure mechanisms of the WGD, the clay-erosion failure mechanism (Sweco, 2021b). To assess the failure mechanism, data is acquired for five design variables: the nearshore water level h , offshore significant wave height H_s and peak period T_p and nearshore wind speed w_s and direction w_d . According to Sweco (2021a), the governing wave impacts for the design result from distantly generated wind-generated waves. Therefore, it is assumed that the offshore wave direction θ equals the wind direction during extreme conditions. This assumption is grounded on Bowers et al. (2000) and Hildebrandt et al. (2019).

Coastal structures are designed for extreme events. To sample the extreme events from the collected data, an extreme value analysis is performed. The extremes are defined using a Peaks-Over-Threshold (POT, Salvadori et al., 2007) method; a sampling technique that involves selecting extremes based on an appropriate threshold and declustering time. To perform the multivariate analysis, the extremes are selected based on a dominant variable (Zachary et al., 1998), which in this project is the water level. The other variables correspond to the coinciding time of the dominant variable. The selected extreme water levels are then modelled using a stationary and non-stationary extreme value analysis. In the stationary

extreme value analysis, the marginal distribution of the water level remains constant in time. For the non-stationary extreme value analysis, the marginal distribution is non-stationary. This implies that the distribution is dependent on a covariate, e.g. time (Shumway and Stoffer, 2011). A non-stationary distribution could be useful in modelling phenomena with non-stationary characteristics, such as sea level rise.

The dependence structure of the selected extremes is modelled by a vine copula in Chapter 4. A vine copula is a tree-like structure consisting of (marginal and conditional) bivariate copulae (Salvadori et al., 2007). Bivariate copulae are functions that describe the joint distribution of $N = 2$ variables. In a vine copula, the bivariate copulae are connected to create a multivariate ($N > 2$) model. Vine copulae have proven to be a flexible tool that can model a wide range of complex dependencies, such as multivariate modelling of flood characteristics (e.g. Tosunoglu et al., 2020; Zhang et al., 2020). Chapter 4 also examines the possibility to combine non-stationary extreme value analysis with copula modelling.

Sampling the multivariate model provides the design values for the variables. In Chapter 5, an offshore-nearshore transformation is performed to propagate the sampled offshore wave characteristics to nearshore conditions. This is done using a hybrid approach proposed by Camus et al. (2011a). This approach combines a numerical wave model, SWAN, with a data-driven model (or surrogate model). This approach is applied to significantly reduce the computational effort for the offshore-nearshore transformation. For the offshore-nearshore transformation, sea level rise for the Dutch coast is included as projected by the ‘Klimaatsignaal 21’ report by KNMI (2021), based on the SSP5-8.5 emission scenario by IPCC (2022).

The design values resulting from the propagation are used to perform a probabilistic assessment of the clay-erosion failure mechanism. The principles in the design of the WGD are similar to the WGD’s demonstration project designed by Sweco (Sweco, 2021b). The vine-based design is designed with a design life of 2050 – 2150. The clay erosion is assessed using a Monte Carlo simulation to determine the failure probability of the design. Figure 1.3 illustrates the failure cases for a Monte Carlo simulation. The multivariate probabilistic assessment of the clay erosion results in an optimized design for the WGD. This design is compared to a deterministic design.

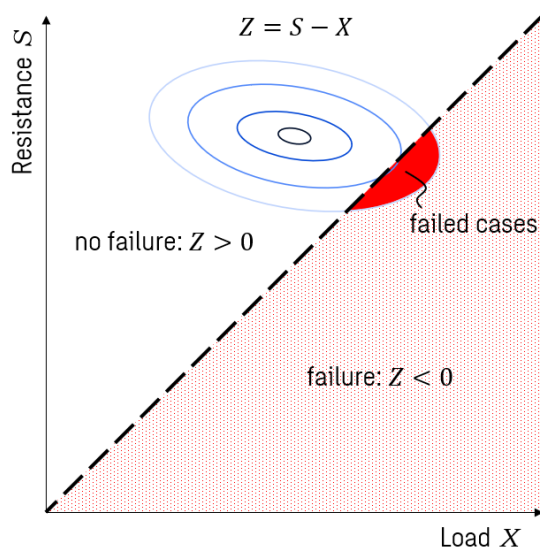


Figure 1.3: Illustration of the failure cases for a Monte Carlo simulation.

In Chapter 6, possible adaptive design strategies are explored. The design strategies are developed on the basis of Adaption Pathways and Adaptive Policymaking (Haasnoot et al., 2011; Kwakkel et al., 2010). These are two approaches that help decision-making for long-term decisions under uncertainty, such as sea level rise. The strategies are based on multiple designs created by the procedure from Chapter 5. The different strategies are assessed according to criteria including the business case, the up-scaling of the clay refinery in the Ems-Dollard area, the environmental impact on the adjacent Natura 2000 area and feasibility. The exploration results in a preferred long-term strategic plan for the WGD.

1.4 Thesis Scope

The scope of the thesis includes:

- The design life of the design is 2050 – 2150.
- This thesis focuses on the clay-erosion failure mechanism of the WGD. This failure mechanism is modelled by the adjusted model of Mourik (Sweco, 2021c).
- Required failure probability of the failure mechanism and other principles are reproduced from the WGD demonstration project (Sweco, 2021b).
- The limitations of the equations used to derive the failure probabilities for the failure mechanisms are respected and described.
- To account for sea level rise, the SSP5-8.5 emission scenario from the Sixth Assessment Report by IPCC (2022) is considered. The sea level rise for the Dutch coast results from the ‘Klimaat signaal 21’ report by KNMI (2021). In addition, it is assumed that the sea level rise at the coast translates one-to-one to the sea level rise in the Ems-Dollard estuary.
- In the offshore-nearshore transformation, the wind characteristics measured near the dike are assumed to be constant for the entire modelled domain.
- The measured nearshore water level is assumed constant along the entire dike’s trajectory.
- It is assumed that during extreme conditions, the offshore wave direction and wind direction are equal (Bowers et al., 2000; Hildebrandt et al., 2019; Sweco, 2021a).
- It is assumed that the surrogate model for the offshore-nearshore transformation can be extrapolated to extreme water levels that include sea level rise.
- In assessing the business case for the adaptive design strategies, a fixed interest rate at 4% and a fixed inflation rate at 2% is assumed (European Commission, nd).
- For the up-scaling of the clay refinery at Ems-Dollard, the results of the pilot studies discussed at the webinar ‘Kleirijpen voor dijkversterking’ by Deltares (2023) are used.

The following items are excluded from the thesis scope:

- The outer slope of the WGD is set at 1:7. Research by Waterboard Hunze and Aa’s (2022) selected this slope as it was found optimal for the WGD project given the crest height and clay layer thickness of the demonstration project.
- Development of the bathymetry of the Ems-Dollard estuary over time is not taken into consideration. The salt marshes in the Dollard will remain at a level of approximately NAP +2 meters. This is a crude assumption as Marijnissen et al. (2020) showed that the accretion of the foreshore could even outpace SLR for milder SLR scenarios and thus could play an important role in flood risk safety.
- The design of the WGD does not include additional crest height or clay layer thickness due to e.g. soil subsidence or construction margins.

2 | Case Study: The Wide Green Dike

This chapter introduces the Wide Green Dike project and describes the data selection. Sections 2.1 and 2.2 introduce the case study and the associated clay refinery program. The failure mechanism of interest is described in Section 2.3. The acquired datasets for the design variables, water level, wave and wind characteristics, are found in Section 2.4. In Section 2.5, the accounted sea level rise scenario is stated.

2.1 Introduction to the Wide Green Dike project

The case study applied in this thesis is the Wide Green Dike (WGD) project, located in the Ems-Dollard area. The WGD project forms part of the eastern primary water defences of the Netherlands, serviced by the Waterboard Hunze and Aa's. Its 12.5 kilometres long trajectory runs from the Kerkhovenspolder to the border with Germany, as shown in Figure 2.1. The Dutch primary water defences are periodically assessed according to the Dutch Legal Assessment Toolkit from 2017 (in Dutch: Wettelijke Beoordelingsinstrumentarium 2017, WBI-2017). This assessment, performed by Sweco, showed that the current dike does not comply with the safety standards on several dike aspects. Therefore, the dike design is revised, creating the WGD project (Sweco, 2021b).



Figure 2.1: The Dutch Wadden Sea area, with the Ems-Dollard estuary enlarged. Retrieved from OpenStreetMap (<https://www.imergis.nl/>) by van Aalst (2021).

A traditional dike reinforcement would replace the grass cover of the levee with asphalt or stone revetment. Ambitions of the Waterboard Hunze and Aa's resulted in the design of a natural embankment, where the dike is reinforced by local materials. This created the possibility to fit the embankment into the local environment of the Natura 2000 area. The project utilizes the clay refinery originating from the Ems-Dollard 2050 Program (Dijk, 2022). An excess of silt in the Ems-Dollard estuary results in a decrease in the local ecology. The variety and number of fish, birds and plants are heavily decreasing, due to the turbid water and loss of habitats. The use of locally ripened clay removes some of the silt from the estuary, thus helping to solve the silt problem in the Ems-Dollard estuary. The scope of the WGD project covers the technical potential of using locally ripened clay from new clay sources in dike design and the possibilities of integration of the WGD into the Natura 2000 area. The WGD project received the 'Zonnetje' award; a yearly award for innovative and inspirational projects of the Dutch Delta program (Nationaal, 2022).

To acquire knowledge, a demonstration project of 800 meters is constructed to act as a research field that is closely monitored. This design is a grass-covered clay dike with a mild outer slope of 1:7. The seaward side of the embankment meets with the Natura 2000 area. The foreshore is a 1-kilometre-long salt marsh. The landward part of the dike meets with polders from the eastern part of Groningen. The project is constructed seawards on top of the current dike. The WGD is designed by Sweco using a mix of probabilistic and semi-probabilistic approaches to the failure mechanisms. The mechanisms are assessed using empirical relations resulting from manuals and case-specific tests performed by Deltares. The hydraulic boundary conditions for the design are generated with Hydra-NL, a software program for the safety assessment of dikes (Duits, 2020). The WGD’s design takes into account some degree of climate change by considering the largest prediction of sea level rise (SLR) of the Royal Netherlands Meteorological Institute (KNMI) from 2006; climate scenario *W+* (KNMI, 2006).

A clear understanding of the erosion characteristics of the clay and the model used to estimate the clay erosion failure mechanism is of significant importance for the WGD. Insight into the erosion characteristics of the clay is gained through lab results and expert judgement. The model used to determine the erosion profile that develops during a storm, depends on the correlation between the different hydraulic conditions, e.g. water level and wave height. This thesis employs the opportunity provided by Sweco to investigate the uncertainty in these two key aspects of the WGD using a multivariate probabilistic approach.

2.2 Up-scaling of the Clay Refinery from the Ems-Dollard 2050 Program

During the webinar ‘Kleirijpen voor dijkversterking’ by Deltares (2023) several preliminary studies were presented. The studies involved the clay ripening process, vegetation on clay ripening, implementation of the process and the clay refinery business case and up-scaling. The goal of the clay refinery is to help reduce the silt concentration in the estuary. The WGD project serves as a haven for the clay originating from the collected silt. Consequently, helping create a positive business case for the clay refinery. The silt problem results from several causes. Over the years, large parts of the Ems-Dollard estuary were reclaimed. The land reclamation shown in Figure 2.2, resulted in a large loss of area for the silt to settle. In addition, dredging works deepened and widened the waterways to the local harbours. This resulted in a larger import of sediment due to the strong tidal current, while less sediment could settle (Dijk, 2022).

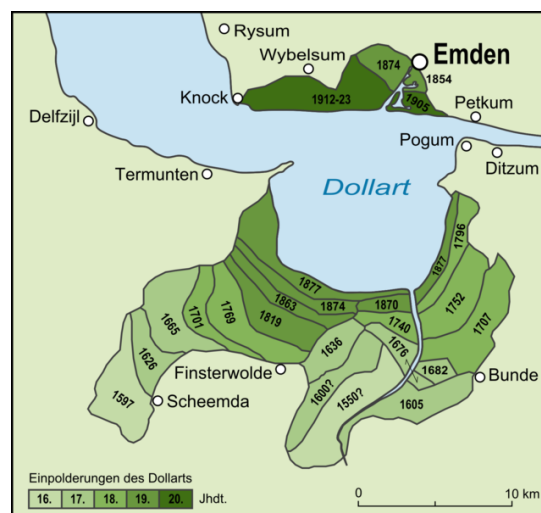


Figure 2.2: The land reclamation in time of the Ems-Dollard estuary. Retrieved from Kirchhoff (1992).

The technical and environmental aspects of the ripening process were studied during a pilot study to check the feasibility of maturing clay for dike adaptations (Deltares, 2023). The results showed that the environmental requirements were met and that the clay is sufficiently erosion-proof. Several locations were selected for the clay refineries. Two locations on land, near the Ems Harbour and Delfzijl, and one location in the Natura 2000 area. The latter is a pilot study itself, called the ‘Klutenplas’. The

Klutenplas is a small lake that traps sediment but also acts as a safe breeding ground for the avocet bird using a small island. However, the up-scaling of the refinery is not feasible for locations within the Natura 2000 area.

The studies provided great insight into the clay repining process. During the winter period, the depots are filled such that the clay is matured and can be used in the summer. The ratio of silt (without contamination) to densely packed clay, ready for use, is around 3.2 : 1. The capacity is thus limited to the amount of clay that is matured each cycle. The maturing rate is heavily impacted by weather conditions, resulting in a broad confidence interval for the production rate. The studies also looked at the costs associated with the process. The location of the clay refinery proved to be of great influence on the costs of clay. Land use costs for the clay refinery and transportation costs were around 50% of the total costs. The final costs were estimated at €25 – 35/ m^3 of clay (SCBA). This proved to be a positive business case when comparing the costs of acquiring clay elsewhere.

2.3 The Clay-Erosion failure mechanism of the Wide Green Dike

The failure mechanism for clay erosion is the dominant failure mechanism for the WGD. Clay erosion is assessed using the model of Mourik (Deltares, 2020). This model determines the total erosion volume and erosion profile. Figure 2.3 shows the erosion profile. The black line shows the erosion profile, in which: V_e is the erosion volume, d_e is the perpendicular erosion depth, d_0 is the starting erosion depth, $\alpha_{terrace}$ is the slope of the terrace, α_{cliff} is the slope of the cliff, L_e is the erosion length and d_t is the erosion depth below the water level (Deltares, 2012).

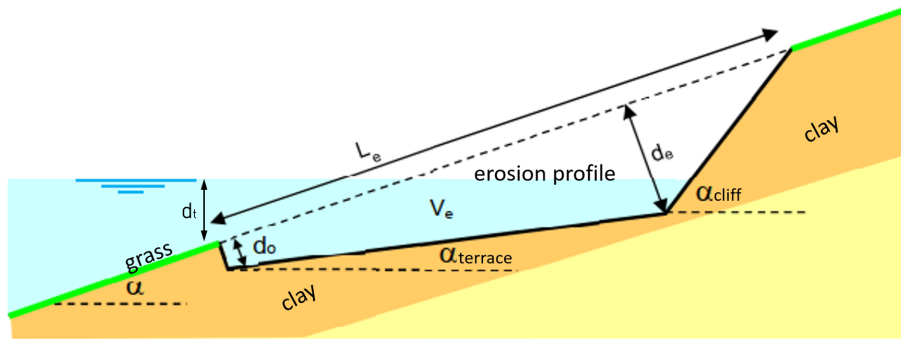
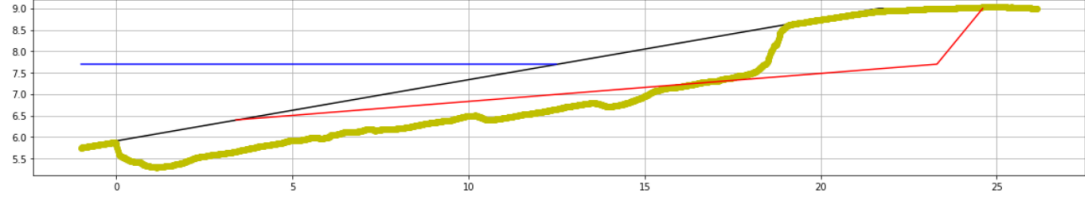


Figure 2.3: Sketch of the erosion profile with variables. Retrieved and modified from ‘Prediction of the erosion velocity of a slope of clay due to wave attack’ by Deltares (2020), p.3.

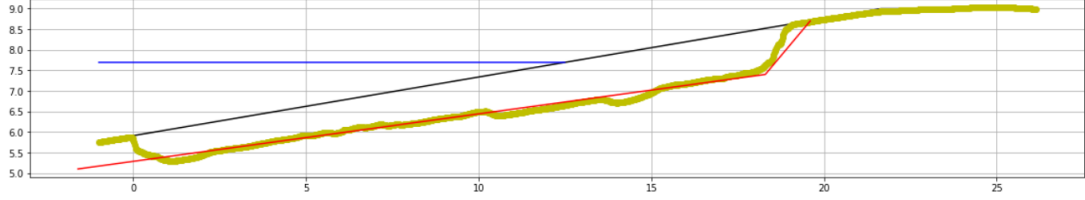
To verify the results of the model of Mourik several Delta Flume tests were performed by Deltares. The tests and the model resulted in similar total erosion volume for the same wave heights and water levels. However, Mourik’s model slightly overestimated d_e , underestimated the lower part of the erosion profile and overestimated the upper part of the erosion profile. Using knowledge gathered from the Delta Flume tests, the model is slightly adapted to comply with the WGD’s design criteria. This adaption resulted in matching results between what was calculated by the model and what was observed in the Delta Flume (Sweco, 2021c). The research done by Deltares resulted in the following adjustments, a visual is represented in Figure 2.4.

1. The outer slope of the dike α equals 1:7
2. The slope of the terrace $\alpha_{terrace}$ equals 1:10
3. The slope of the cliff α_{cliff} equals 2:1
4. An erosion depth d_0 of 0.5 meters on the seaside of the erosion profile is introduced
5. The entire erosion profile from Mourik’s model is lowered by half a meter (shift of y-axis by -0.5 meters)
6. The entire erosion profile from Mourik’s model is translated by three meters to the left (shift of x-axis by -3.0 meters)

Note: A positive coordinate system is assumed to have a positive x -axis to the right and a positive y -axis upwards as shown in Figure 2.4.



(a) Mourik's model before the adjustments



(b) Mourik's model after the adjustments

Figure 2.4: Erosion profile from the Delta Flume tests after 16 hours (bold green line) and calculated from Mourik's model (red line) (black line is the dike profile, the blue line is the water level). Retrieved from 'Vergelijking erosieprofiel Deltagoot en berekend' by Sweco (2021d), p.5.

Equation 2.1 shows the WGD-specific formula that is used to determine the total erosion volume V_e (Sweco, 2021c). The application of this formula is for wave heights H_{m0} larger than 0.4 meters. Erosion is neglected for wave heights below or equal to 0.4 meters. In addition, the application is restricted to a wave steepness within $0.01 \leq s_{op} \leq 0.05$ (Deltares, 2020).

$$V_e = 16.7 \cdot H_{m0}^2 (1 - e^{-0.55 \cdot c_e (\tan \alpha)^2 \cdot \min(3.6; 0.0061 \cdot s_{op}^{-1.5} \cdot (1 - \frac{0.4}{H_{m0}})^2 \cdot t)}) \quad (2.1)$$

Where:

V_e	Erosion volume per m dike	$[m^3/m]$
H_{m0}	Average significant wave height	$[m]$
c_e	Erosion coefficient	$[-]$
α	Outer dike slope	$[rad]$
s_{op}	Wave steepness based on significant wave height and peak wave period = $H_s / (g \cdot T_p^2 / 2\pi)$	$[-]$
t	Time	$[h]$

Using V_e , the erosion profile can be determined. The erosion depth d_e is defined by Equation 2.2.

$$d_e = \sqrt{\frac{2 \cdot V_e \cdot \tan(\alpha - \alpha_{terrace}) + d_0^2}{1 + \frac{\tan(\alpha - \alpha_{terrace})}{\tan(\alpha_{cliff} - \alpha)}}} \quad (2.2)$$

The erosion length L_e is stated in Equation 2.3.

$$L_e = \frac{d_e - d_0}{\tan(\alpha - \alpha_{terrace0})} + \frac{d_e}{\tan(\alpha_{cliff} - \alpha)} \quad (2.3)$$

The location of the erosion profile is related to the water level during the storm. In Equation 2.4, the erosion depth below the water level d_t can be determined.

$$\frac{d_t}{H_{m0}} = \min\left(0.4 \cdot \frac{V_e^{0.25}}{H_{m0}^{1.5}} + 0.7; 2\right) \quad (2.4)$$

In the WGD design, the failure mechanism can lead to two types of failure. Failure occurs if the calculated erosion depth d_e is larger than the thickness of the clay layer. If the clay layer thickness is insufficient, the erosion profile reaches the sand core of the dike. This is considered type I failure. Type II failure is due to the erosion of the outer slope reaching the crest of the dike. From calculations and

the Delta Flume tests, this type of failure is considered the dominant failure mechanism. The erosion volume is governed by the wave height. However, the water level determines the location of the erosion profile. A large water level results in an erosion profile closer to the crest. Consequently, erosion of the crest is reached earlier than for a lower water level. For a lower water level, the erosion volume at the outer slope can be significantly larger before the crest is reached. In addition, due to the mild outer slope of $\alpha = 1 : 7$ and the WGD being constructed from the current dike seawards, the clay layer of the WGD is thicker at lower levels of the outer slope. Hence, also the erosion depth for lower water levels can be larger. This results that the water level is the dominant design variable for the failure mechanism.

The erosion volume is determined for an average wave height during a storm period. In Sweco (2021c), the clay erosion is checked for three storm duration scenarios, namely for 14, 16 and 18-hour storm surge averages for a storm with a 45-hour storm duration. The 18-hour average resulted in the governing scenario. In this work, the required failure probability is assumed to be the same as in Sweco’s design for the WGD. The required failure probability of this failure mechanism is $P_{f,req} = 1/37,500$ per year. Furthermore, a project principle requires that the minimum required clay layer thickness is 0.8 meters. The current dike has a minimum clay layer thickness of 0.8 meters. As the WGD is constructed on top of the current dike, failure of type I occurs if the erosion depth reaches the current dike. Failure type II results when the erosion profile reaches the design crest height, with a minimum crest width of 1 meter (project principle).

2.4 Data Collection & Selection

To perform the multivariate analysis five variables are considered: the near-dike water level, the near-dike wind speed and direction, deepwater wave height and deepwater wave period. In this thesis, the near-dike water level is assumed constant along the dike’s trajectory. The near-dike wind speed and direction are also assumed constant in the Dollard for performing the offshore-nearshore transformation of the wave height and period. In order to perform the multivariate analysis, coinciding data for all variables is needed. Also, the bathymetry of the estuary is needed to perform the offshore-nearshore transformation of the variables in Section 5.1. The data acquired for the data analysis and the sources are listed in Table 2.1. Due to a lack of wave data from Rijkswaterstaat (2022), wave data from ERA5 is used. ERA5 is the fifth generation ECMWF Re-Analysis for the global climate and weather, created by the European Centre for Medium-Range Weather Forecasts (ECMWF). It combines model data with observations from across the world into a globally complete dataset. ERA5 provides hourly estimates for a large number of atmospheric, ocean-wave and land-surface quantities, such as water level. More explicit information on the datasets is given in Appendix A. Note, the locations of the data severely differ from Sweco’s design. Therefore, the two designs cannot be compared one-to-one. This thesis is a model study, therefore it compares the vine-based design to a deterministic design with the same data locations.

Table 2.1: Acquired datasets and sources.

Kind of data	Source	Location	Period [y]
Bathymetry	EMODnet (2016)	Ems-Dollard estuary	2012-2015
Deepwater wave data	Rijkswaterstaat (2022)	Randzelgat	2008-2022
Deepwater wave data	ECMWF (2022)	53°28'12.0"N 6°53'24.0"E	1990-2022
Water level data	Rijkswaterstaat (2022)	5 locations in the Dollard	1990-2022
Wind data	KNMI (2022)	Nieuw-Beerta	1990-2022

2.4.1 Water level Data Selection

Water level data is acquired for five locations in the Dollard estuary; Dollard West, Groote Gat, Nieuwe Statenzijl, Reide and Schankersdiep. The largest of these datasets, Nieuwe Statenzijl, spans from 1-12-1990 to 20-11-2022. Data from the other four locations are more sparse. These measurements stray from the years 1994 up to 2001. These four locations are used to verify the data from Nieuwe Statenzijl. The datasets contain water level measurements taken every 10 minutes.

Figure 2.5 shows the bathymetry, measurement locations and dike trajectory. It shows that the locations Dollard West, Nieuwe Statenzijl and Schankersdiep are closest to the dike. Dollard West and Schankersdiep are at the ends of the channel branches, where the salt marsh starts. The salt marsh has an average level of 2 meters above NAP, the Dutch measuring unit for water levels (Amsterdam Ordnance Datum, in Dutch: Normaal Amsterdams Peil). Nieuwe Statenzijl is located at the mouth of the Westerwoldse Aa canal where it meets the estuary. The measurement location Groote Gat is located in one of the two main channel branches in the Dollard and is placed in deeper water depths compared to the previous three locations. Reide is located before the main channel the Ems bifurcates. It is located near the tip of a land section, at the inlet of the Dollard.

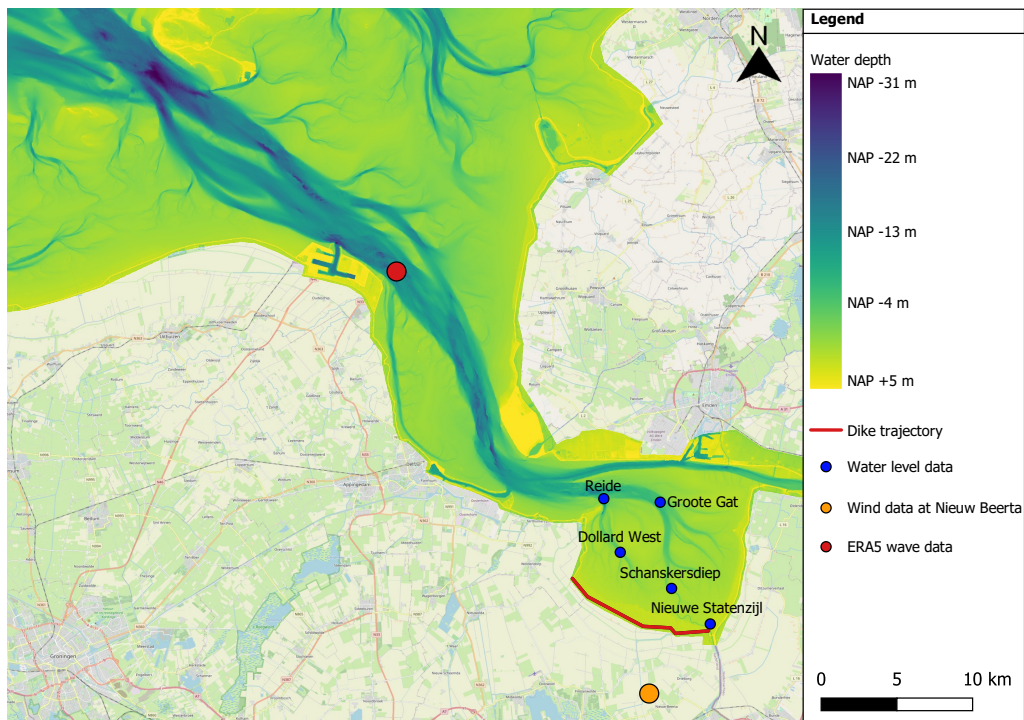


Figure 2.5: Measurement locations in the Ems-Dollard. The water level measurement in the Dollard estuary: Dollard West, Groote Gat, Nieuwe Statenzijl, Reide and Schankersdiep.

In Figure 2.6, the data of the locations Dollard West, Schankersdiep, Groote Gat and Reide is overlaid on top of the measurements from Nieuwe Statenzijl. The figure shows that the corresponding data overlaps quite well. A few significant differences are found for the locations Groote Gat and Schankersdiep, in the years 1999 and 1997 respectively. Figure 2.7 shows the station plots, where the four locations are plotted against Nieuwe Statenzijl. If the measurements of both locations are equal, the data points should follow the red line under an angle of 45 degrees, the one-one line. The station plots show a good match for extreme water levels, starting at approximately NAP +2.0 meters. More deviation takes place for lower water levels however, all plots appear to approximate the red line. The plots do show measurement errors, the linear horizontal or vertical lines of data points can identify those. In the station plots of Groote Gat and Schankersdiep, these are found for water levels at approximately NAP -1.0 and NAP -1.9 meters for Groote Gat and NAP +1.0 and NAP +2.5 meters for Schankersdiep. These two plots also show a vertical line at approximately NAP +1.3 meters for the Nieuwe Statenzijl station. Dollard West and Schankersdiep appear to have the best correspondence with the data from Nieuwe Statenzijl. This was as expected from their relative locations in the Dollard. The station plot of Groote Gat shows a decent fit, however, this location has a number of outliers with significant positive water levels. This is caused by the much larger water depth of Groote Gat compared to Nieuwe Statenzijl. Therefore, significant water levels will not be reduced by effects from the bottom and the salt marsh. Reide shows the most deviation from the red line. This could be expected because this location is furthest away from Nieuwe Statenzijl and is located in the Ems River, while the other locations are in the Dollard estuary.

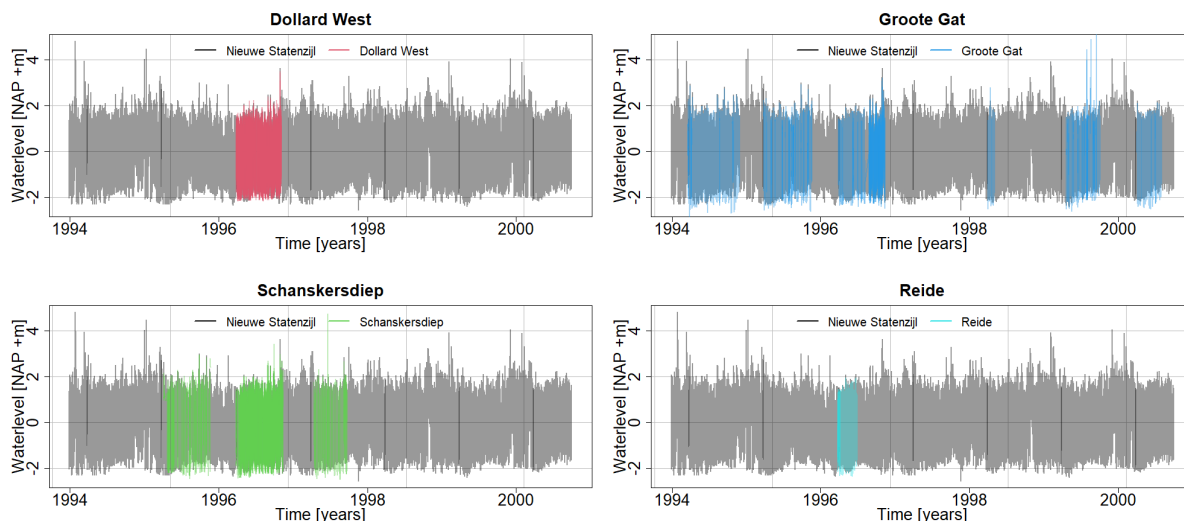


Figure 2.6: Water level comparison between Nieuwe Statenzijl and the other four locations Dollard West, Schankersdiep, Groote Gat and Reide for the years 1994 up to 2001.

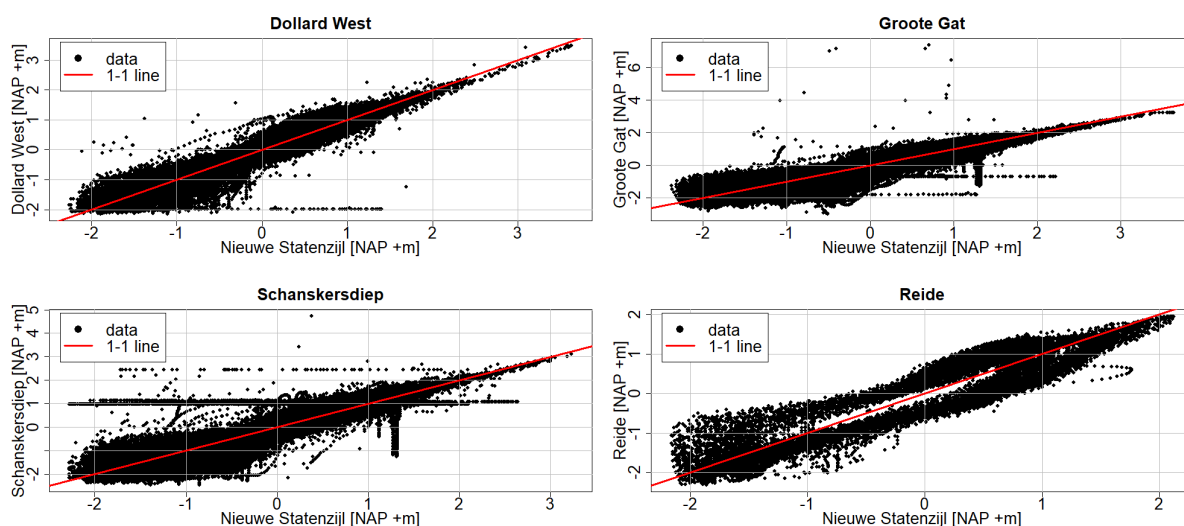


Figure 2.7: Station plots of the water level with Nieuwe Statenzijl on the x-axis and the other four locations Dollard West, Schankersdiep, Groote Gat and Reide on the y-axis.

Table 2.2 shows the differences between the coinciding water levels for the four locations with Nieuwe Statenzijl. The table shows that the deviation of the listed statistical values is limited. The largest deviations are found for the differences in minimum and maximum values. Due to outliers for the locations, Groote Gat and Schankersdiep large variations for the maximum values are found, 3.76 and 1.50 meters respectively. However, differences for the median, mean, 1st and 3rd quartiles are limited, with at most 0.18 meters for Groote Gat. The absolute average deviation is also determined. This value can provide a general idea of which station corresponds best to Nieuwe Statenzijl. It shows that Dollard West and Schankersdiep have a slightly lower average deviation than Groote Gat and Reide, with an absolute average deviation of between 0.24 and 0.28 meters. This was expected due to their relative locations. However, this value does include outliers and measurement errors and can hence be skewed.

Table 2.2: Statistical summary of the differences between the coinciding water level for the different locations with Nieuwe Statenzijl. A negative value represents that the coinciding water level at the location is lower than at Nieuwe Statenzijl.

Location	Unit	Absolute mean deviation	Min. value	1 st Quartile	Median	Mean	3 rd Quartile	Max. value
Dollard West	<i>m</i>	0.242	0.11	-0.10	0.03	-0.004	0.11	-0.13
Groote Gat	<i>m</i>	0.297	-0.63	-0.18	0.06	-0.094	0.02	3.76
Reide	<i>m</i>	0.354	-0.16	0.03	-0.04	-0.016	0.07	-0.16
Schankersdiep	<i>m</i>	0.280	-0.19	-0.13	0.07	-0.019	0.09	1.50

Combining the information gathered from Figures 2.5, 2.6, 2.7 and Table 2.2 the water level data from Nieuwe Statenzijl is adopted as an appropriate dataset to characterise the water level in the Dollard estuary in front of the dike trajectory. The correspondence with the other measurement locations is assumed as sufficient. The areas Dollard West and Schankersdiep are next to Nieuwe Statenzijl of most interest for this project. The absolute average deviation to these locations is in the order of 0.25 meters, including measurement errors. Figure 2.7 shows that removing the measurement errors could reduce this average deviation. In addition, the station plots show that the average deviation reduces significantly for more significant water levels, which is important for this project since the dike is designed to withstand storm surge conditions. In combination with a lack of datasets that match Nieuwe Statenzijl with a large timespan of 30+ years, the deviation to other stations is assumed to be sufficient. The data at Nieuwe Statenzijl is characterized by a mean value of $\mu = \text{NAP} + 0.43$ meters and a standard deviation of $\sigma = \text{NAP} + 0.99$ meters.

2.4.2 Wave Data Selection

The wave data used is sourced from ERA5 (ECMWF, 2022) and located at the inlet of the Ems River near the Ems harbour. The exact location is $53^{\circ}28'12.0''\text{N}$ $6^{\circ}53'24.0''\text{E}$, shown in Figure 2.5. The wave data used is already propagated from the North Sea to the Wadden Sea. Therefore, some wave characteristics could be affected due to the influence of the Wadden Islands and the Wadden Sea bathymetry. The dataset spans from 01-01-1990 up to 31-12-2021 and has an hourly measurement frequency. The ERA5 wave data has a significantly larger time span than the wave data sourced from Rijkswaterstaat (2022) which only spans from 20-08-2008 up to 01-02-2021. In this work, the wave and wind direction are assumed equal for extreme conditions. According to Bowers et al. (2000); Hildebrandt et al. (2019), such an assumption is grounded under extreme conditions. In addition, local knowledge from the Ems-Dollard area indicates a similar conclusion that due to the dike's location, wind-generated waves are governing the design (Sweco, 2021a). This assumption is taken to reduce the number of design variables from six to five. This significantly reduces the computational effort for the multivariate analysis in Chapter 4. A statistical summary of the wave data sourced from ERA5 is presented in Table 2.3. The time series of the wave height and period data is presented in Appendix A in Figures A.1a and A.1b, respectively.

Table 2.3: Statistical summary of the wave data from ERA5 by ECMWF (2022).

Variable	Unit	Min. value	1 st Quartile	Median	Mean	3 rd Quartile	Max. value	Standard deviation
Wave height	<i>m</i>	0.03	0.55	0.85	0.99	1.28	5.04	0.61
Wave period	<i>s</i>	1.77	4.05	4.72	4.88	5.56	11.03	1.15

2.4.3 Wind Data Selection

The wind data is sourced from KNMI (2022). The data is measured at NAP +10 meters by a weather station located near Nieuw-Beerta, as shown in Figure 2.5. The measurement station is approximately 4.5 kilometres away from the dike's trajectory. The dataset contains hourly measurements of the wind direction and several wind speed variables. The data spans from 01-01-1990 until 09-10-2022. In this work, the considered wind speed variable is the maximum hourly mean wind velocity. This selection is

made as the selected wind speed variable best represents the wind conditions during a storm compared to the other available wind speed variables. Figure 2.8 shows the wind rose of the selected data.

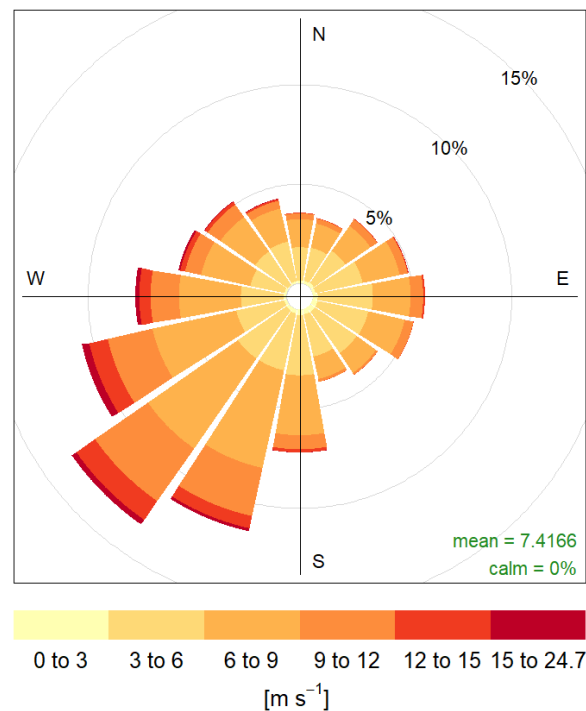


Figure 2.8: Wind rose signifying the directional frequency and the maximum hourly wind velocities. The wind data is sourced from KNMI (2022).

2.4.4 Bathymetry

The bathymetry data is obtained from the Federal Maritime and Hydrographic Agency at the ‘EMODnet Bathymetry portal’ (EMODnet, 2016). The data is a high-resolution Digital Terrain Model (DTM) based single beam, multi beam and Lidar covering the Ems-Dollard and Ems approach. The data is acquired in the years 2012-2015 and originates from multiple data providers, e.g. hydrographic offices, authorities, research institutes and the industry (EMODnet, 2016). The DTM is available with a spatial resolution of 1, 7, 15 and 25 meters. In this work, the DTM with a spatial resolution of 25 meters is selected, as this is sufficient for its application in the offshore-nearshore transformation.

2.5 Accounting for an Uncertain Sea Level Rise

The global sea level rose about 20 centimetres between 1901 and 2018. The rate at which the global sea level increases accelerates. Between 2006 and 2018 the rate of global SLR was 3.7 *mm* per year. The rate at which SLR will occur strongly depends on the amount of emissions that the world will pollute. The latest SLR observations and projections are stated in the Sixth Assessment Report (AR6) by the IPCC (2022). The different SLR scenarios are linked to emission scenarios. Exceeding 1 meter of global SLR with a significant reduction in worldwide emissions (SSP1-2.6) is projected between 2150 and 2350. If there is no reduction in emissions (SSP5-8.5), the 1-meter threshold is projected to be reached between 2090 and 2140 (both projections are for a 67% confidence interval).

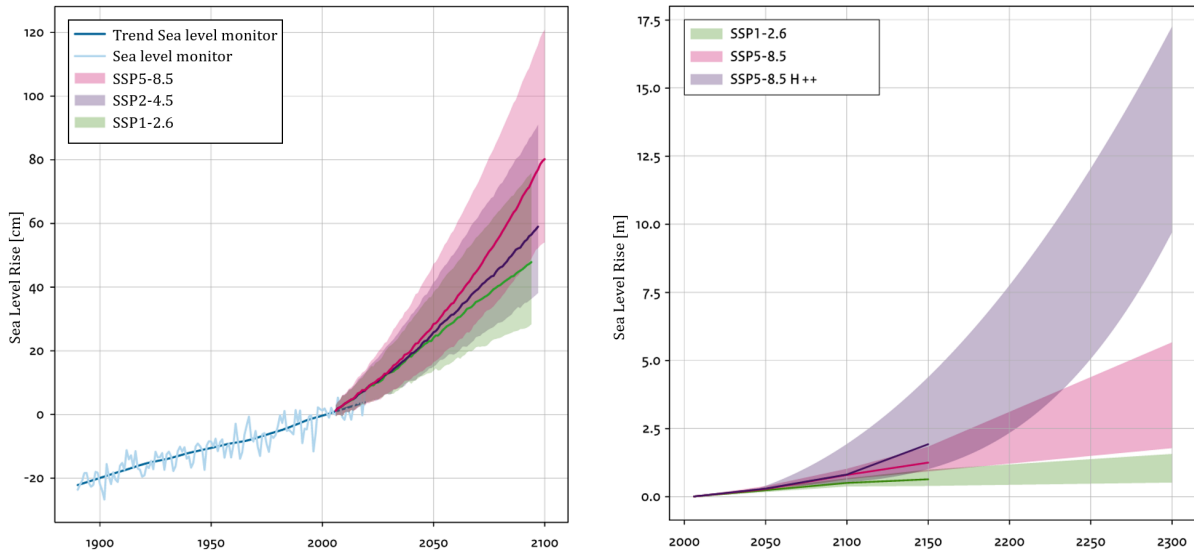
For smaller areas, such as the North Sea basin, a larger time period is needed to observe the acceleration of the trend. Such changes are distorted due to local effects, e.g. fluctuations in wind, sea currents and seawater temperature. The ‘Klimaatsignaal 21’ by KNMI (2021) conducted analyses of the SLR for the Dutch coast. This report includes numerous factors, such as an expansion of the oceans due to global warming, self-gravitation, changes in salinity and the mass loss of glaciers and ice sheets in Antarctica and Greenland. The projections by KNMI (2021) show that the SLR for the Dutch coast lags slightly

behind the global average. The SLR scenarios take into account a soil subsidence of 0.5 mm per year. In Table 2.4, the SLR projections for three emission scenarios are found for the years 2050 and 2100.

Table 2.4: Projected SLR scenarios for the Dutch coast by KNMI (2021). The SLR is projected against the period 1995-2014, with a 90% confidence interval. Soil subsidence is included in the SLR projections.

Year	2050	2050	2050	2100	2100	2100
Emission-scenario	SSP1-2.6	SSP2-4.5	SSP5-8.5	SSP1-2.6	SSP2-4.5	SSP5-8.5
SLR in [cm]	14 – 38	15 – 41	16 – 47	30 – 81	39 – 94	54 – 121
SLR in [mm/year]	2.8 – 8.7	5.2 – 10.6	5.8 – 12.1	2.9 – 9.1	4.4 – 10.5	7.2 – 16.9

In Figure 2.9, the SLR projections for the Dutch coast are shown up to 2100 and 2300 for several emission scenarios. The figure shows that the sea level will continue to rise beyond 2100 in all scenarios, even if the emissions are significantly reduced and the global commitments in the Paris Agreement are respected (Official Journal of the European Union, 2016). The reason is the long reaction time of the (deep) oceans. The global warming and mass loss of ice sheets that already have taken place have started the SLR processes. Due to the slow response of the processes, SLR cannot be stopped overnight.



(a) Sea level on the Dutch coast as observed and according to the new, indicative sea level projections. The lines drawn in green, purple, and red indicate the median of those projections, and the coloured area is the 90% confidence interval. The zero point of the median lines are in the year 2005; the bandwidth in 2005 corresponds to the natural variability.

(b) Sea level scenarios for the Dutch coast to 2300 for the SSP1-2.6 and SSP5-8.5 scenarios and SSP5-8.5 with the inclusion of uncertain ice sheet processes such as the collapse of ice cliffs at the edge of Antarctica (SSP5-8.5 H++). The median contours of those three scenarios can only be calculated up to 2150. The indicated range in colour corresponds to a 67% confidence interval.

Figure 2.9: The observed and sea level projections for the Dutch coast up to the year 2100 (left) and 2300 (right). The images are retrieved and modified from KNMI (2021), pp. 29-30.

In this work, the SSP5-8.5 SLR scenario of the Dutch coast by KNMI (2021) is accounted for, for the period between 2050 and 2150. It is assumed that the SLR for the Dutch coast is one-to-one related to the SLR in the Ems-Dollard estuary. The potential growth of the salt marsh at the foreshore of the WGD is not accounted for. Therefore, a rise in sea level results in the same rise in water depth on top of the salt marsh. The distributions approximating the SSP5-8.5 scenario are found in Appendix J.

3 | Extreme Value Analysis

This chapter aims to find the best model to approximate the extremes of the design variables of the WGD project, using extreme value theory. The results from this chapter are used in the multivariate modelling performed in Chapter 4. Section 3.1 provides an overview of the extreme value sampling techniques that are used in the analysis. In Section 3.2 the extreme values of the design variables are selected. These results are modelled in Sections 3.3 and 3.4, using a stationary and non-stationary approach, respectively. Section 3.5 provides a conclusion of the chapter and provides which model will be used as input of Chapter 4.

3.1 Extreme Value Sampling Techniques

Civil engineering structures are designed to withstand extreme loading conditions. Extreme value analysis (EVA) consists of statistically modelling the distribution functions of extreme events (Gumbel, 1958). Extreme events are either small or large values that deviate from the average observed events. The selection of what an ‘extreme event’ is, is part of performing an EVA and depends on its application (Coles et al., 2001). Subsections 3.1.1 and 3.1.2 describe two sampling techniques that can be used to select extreme values.

3.1.1 The Block Maxima method

The selection of extremes can be performed using a Block Maxima (BM) method. Using the BM method the time series of the variable is divided into non-overlapping periods of equal size (blocks). Samples are taken from the maximum value in each block (Gumbel, 1958). The length of the blocks depends on the characteristics of the variable and application. This method can for example provide daily, monthly or annual maxima. The BM method does have some drawbacks. The method only samples the most extreme value in a block, so some information could get lost. In addition, some values that are not considered extremes could be included. An example of a BM method is shown in Figure 3.1. The figure shows that the peaks of T_1 , T_3 , T_4 , T_5 and T_6 are selected as extreme values, shown by the orange dots. The peak of T_2 is not selected since it occurs within the same block as T_1 , despite it having a larger value than the peaks of T_3 and T_6 , shown by the red circle. The period of the blocks is T_{block} .

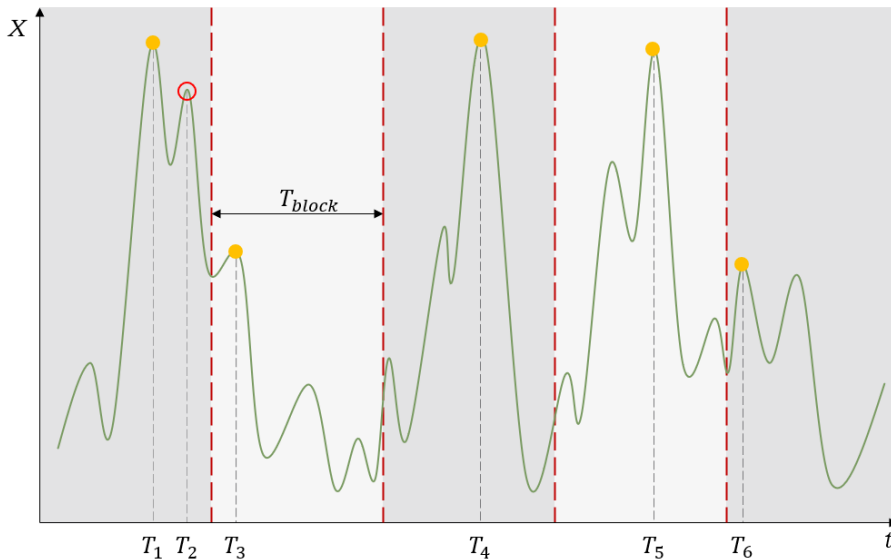


Figure 3.1: An example of a Block Maxima method. The peaks of T_1 , T_3 , T_4 , T_5 and T_6 are selected as extreme values. The peak of T_2 is not selected since it occurs within the same block as T_1 .

3.1.2 The Peaks-Over-Threshold Method

The POT method is a sampling technique to define extremes. Any value that exceeds a set threshold qualifies as an extreme (Salvadori et al., 2007). The POT method requires two parameters. The first parameter is the value of the threshold u and the second parameter is the declustering time δ . According to Salvadori et al. (2007), these two parameters must be chosen such that the filtered extremes are independent and identically distributed (i.i.d.) and therefore approximate a Poisson process. This implies that each random variable has the same probability distribution whilst being independent of the others. In addition, the excesses of the defined threshold should approximate a Generalized Pareto Distribution (GPD, Picklands, 1975). The GPD is described in Subsection 3.3.1.

To do so, the threshold value u should be chosen such that u is neither too low and includes non-extremes, nor too high and eliminates too much data. The declustering time δ is defined as the distance between two peaks and makes sure that the selected extremes are independent. During a single storm, multiple extreme waves can occur resulting in clusters of extremes. Therefore, δ is usually chosen such that it is about the average storm duration. An inter-cluster time that is lower suggests that the corresponding extremes might be related to each other. In this case, a POT only considers the maximum extreme value. It is unlikely for extremes with an inter-cluster time larger than δ that result within each wave storm, therefore they are independent.

An example of a POT method on a dataset is shown in Figure 3.2. It shows three peaks that exceed the threshold u , the red horizontal line. From those, two are selected as extreme values T_1 and T_2 , shown by the orange dots, and one is rejected T_3 , shown by the red circle. The extreme value of T_3 is rejected due to an inter-cluster time C_2 that is smaller than the required declustering time δ .

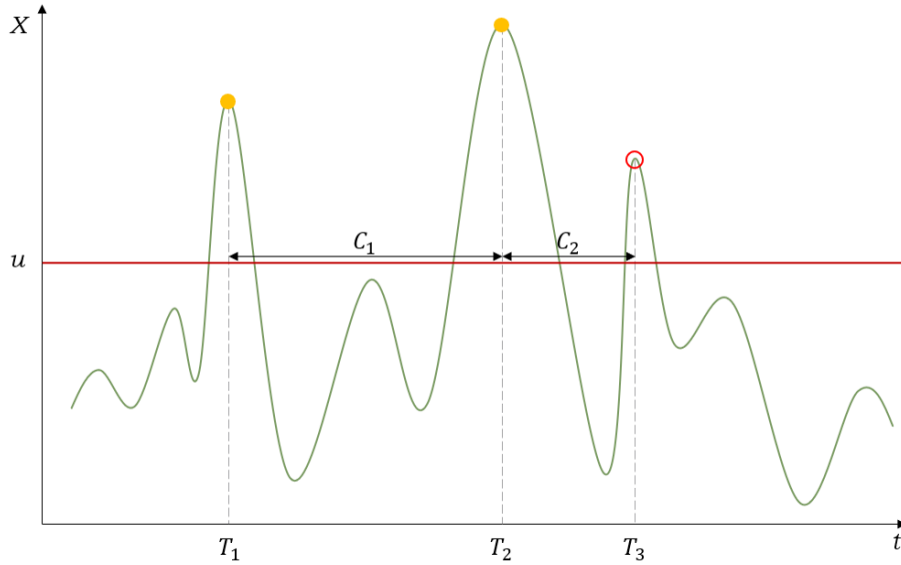


Figure 3.2: An example of a Peaks-Over-Threshold method. The peaks of times T_1 and T_2 are selected extremes, where the peak of T_3 is not suitable. This is due to an inter-cluster time that is smaller than the declustering time, $C_2 < \delta$. The threshold u is shown by the red horizontal line.

The selection of extremes by a POT is done for univariate variables. To perform a multivariate analysis a method is proposed by Zachary et al. (1998). The POT method is applied to only the dominant design variable. The other variables are referred to as the *concomitant* variables, these are the values that correspond to the coinciding time of the dominant variable (Zachary et al., 1998). The dominant variable is chosen based on the maximum loading condition on the structure, so it is linked to the relevant failure mechanism. In this project, the clay-erosion failure mechanism is considered. Resulting of calculations by Sweco (2021c) and Delta Flume test results by Deltares (2020), the water level is dominant for this failure mechanism.

3.2 Peaks-Over-Threshold Method with water level as the dominant variable

The 10-minute frequency of water level measurements was transformed into hourly measurements by selecting the maximum observation within each hour. This results in the same measurement frequency as the wave data. In order to select proper values for the threshold parameter u and the declustering time δ , multiple methods are used. The analysis is performed in the ‘*POT*’ package by Ribatet (2011) in the programming language *R*. First, appropriate threshold values are found by a graphical method suggested by Davison and Smith (1990), a Mean Residual Life (MRL) plot. The MRL plot shows the mean excesses over a range of thresholds. To select a proper threshold u , the excesses over u should approximate a GPD. The threshold stability property of a GPD requires that the threshold u should be on the domain where the mean excesses are a linear function of the thresholds. Suppose the GPD is a valid model for the excesses over some threshold u_0 for a series X_1, \dots, X_n . The threshold stability property means that if the GPD is a valid model for the excesses over u_0 , then it is valid for all excesses over all thresholds for $u > u_0$. Equation 3.1 shows this linear relationship between the mean excesses and the threshold u . Figure 3.3 shows the MRL plot of the water levels. The plot shows two (approximate) linear sections, one for lower water levels and one for large water levels. The domain of interest is for large water levels, this results in a domain of [1.5, 3.5] for an appropriate threshold. To put this in perspective, 99th percentile of the water level dataset equals NAP +2.26 meters and thus is in the domain of interest.

$$\mathbb{E}(X - u | X > u) = \frac{\sigma_u}{1 - \xi} = \frac{\sigma_{u_0} + \xi \cdot u}{1 - \xi} \quad (3.1)$$

Where:

u_0	Threshold for which a GPD is valid
u	Some threshold where $u > u_0$
ξ	Shape parameter of the GPD
σ_{u_0}	Scale parameter of the GPD with u_0
σ_u	Scale parameter of the GPD with u

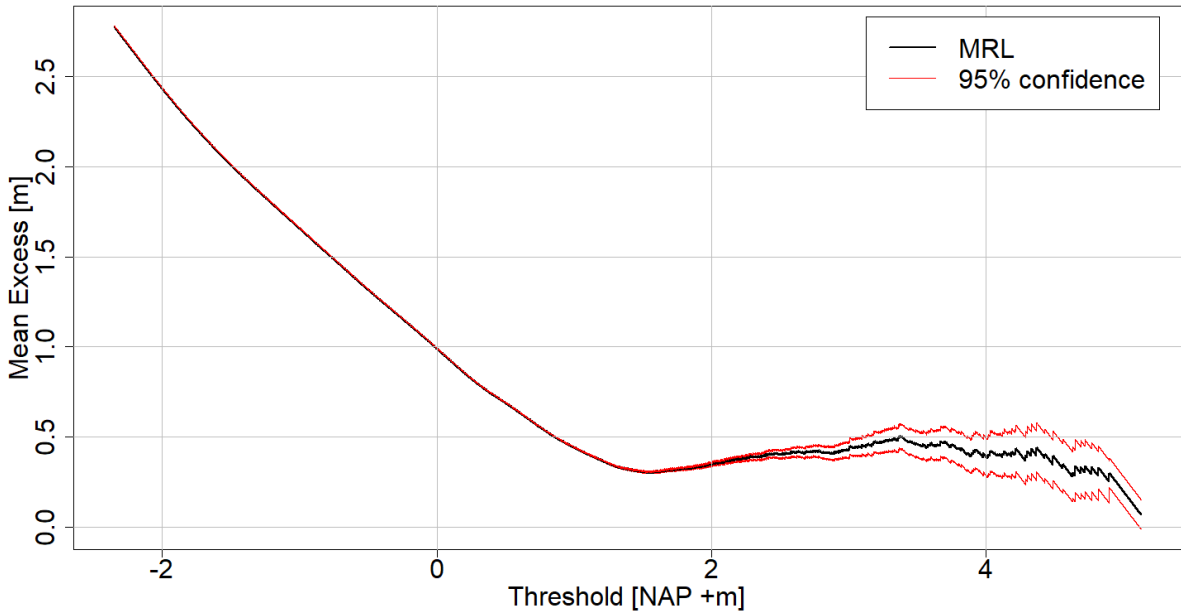
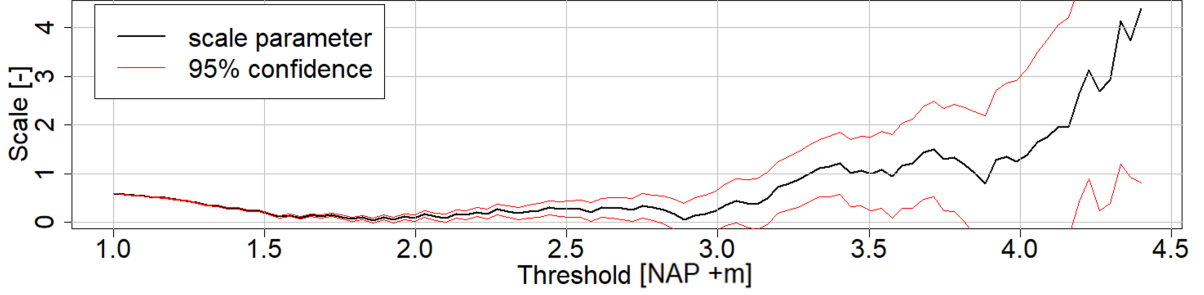


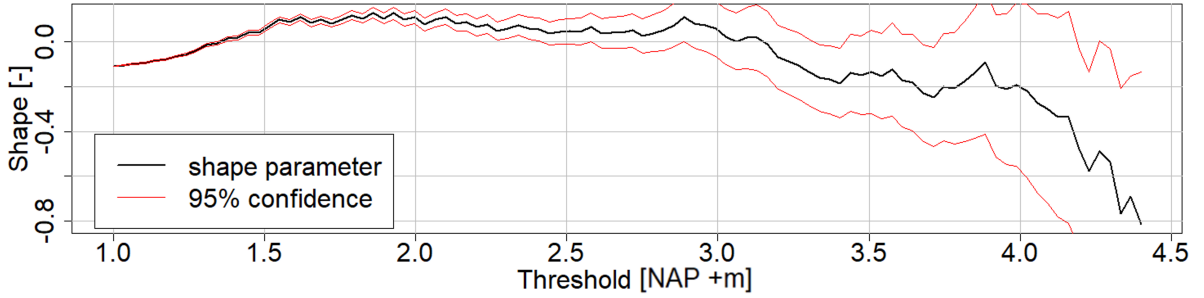
Figure 3.3: Mean Residual Life plot of the water level as the dominant variable.

Another graphical method that is widely used to determine an appropriate threshold is the parameter stability plot. The parameter stability plot shows the distribution parameter over a range of thresholds. An appropriate threshold should be chosen such that the parameters of the GPD remain constant. This

ensures that the selected threshold is not largely influencing the distribution itself. Figure 3.4 shows the parameter stability plots for the scale and shape parameter of the GPD, resulting in a domain of interest of approximately [1.5, 3.0].



(a) Parameter stability plot of the scale parameter



(b) Parameter stability plot of the shape parameter

Figure 3.4: Parameter stability plots with the water level as the dominant variable.

To make sure that the selected extremes are i.i.d. and follow a Poisson process, also the Extremal Index (EI) can be used. The EI is an indicator of how much clustering of the extremes occurs and is a function of the threshold and declustering time. A set of extremes is independent for an EI=1 and some dependency occurs for EI<1. In this case, the extremes are selected using a POT with a declustering time δ . The intervals estimator of the EI described in Ferro and Segers (2003) is used, as shown in Equation 3.2.

$$\tilde{\theta}_n(u) = \begin{cases} 1 \wedge \hat{\theta}_n(u) & \text{if } \max \{T_i : 1 \leq i \leq N-1 \leq 2\} \\ 1 \wedge \hat{\theta}_n^*(u) & \text{if } \max \{T_i : 1 \leq i \leq N-1 > 2\} \end{cases} \quad (3.2)$$

with

$$\hat{\theta}_n(u) = \frac{2 \left(\sum_{i=1}^{N-1} T_i \right)^2}{(N-1) \sum_{i=1}^{N-1} T_i^2}$$

and

$$\hat{\theta}_n^*(u) = \frac{2 \left\{ \sum_{i=1}^{N-1} (T_i - 1) \right\}^2}{(N-1) \sum_{i=1}^{N-1} (T_i - 1)(T_i - 2)}$$

Where:

u	Threshold of the GPD	[NAP +m]
N	Number of observation exceeding u	[-]
T_i	Observed inter-exceedance times for $i = 1, \dots, N-1$	[h]
$\hat{\theta}_n(u)$	Intervals estimator for the Extremal Index by Ferro and Segers (2003)	[-]

Figure 3.5 shows the EI for a range of thresholds. The plot shows that the excesses for all thresholds are independent of the declustering time. This result could be a wrong representation of reality. Due to the location of the gathered data, the clustering of the extremes could be damped. The presence of the Wadden islands in front of the estuary and the estuary itself could obstruct the observation of clustering by dampening the storms. To make sure that the selected extremes are independent a declustering time of $\delta = 45$ hours is selected. Dutch law prescribes a storm duration of 45 hours in the Wadden sea area. According to Deltares (2015) a base duration of a storm surge at Delfzijl (at the inlet of the Ems) is 43 hours. Thus, a declustering time of 45 hours is deemed sufficient.

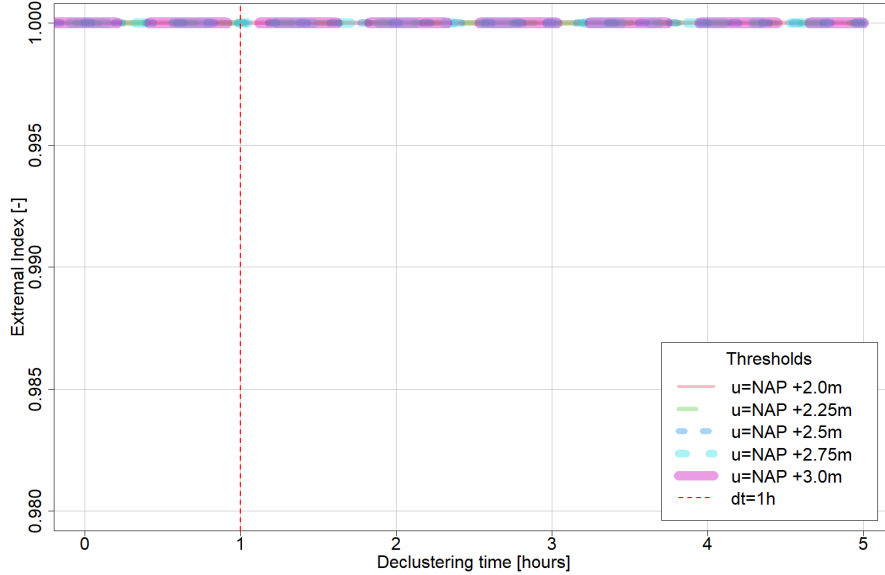


Figure 3.5: Extremal Index plot for the water level as the dominant variable.

According to extreme value theory, the excesses over the threshold of a POT method should be i.i.d. and thus approximate a Poisson process. Equation 3.3 shows a random variable X that is Poisson distributed with parameter λ . By definition, the Poisson process has the property that the intensity parameter λ equals both the expected (mean) number of events within a given time or space and also the variance.

$$P\{X = k\} = \exp(-\lambda) \cdot \frac{\lambda^k}{k!}, \text{ with } k \in \mathbb{N}, \text{ and } \mathbb{E}[X] = \text{Var}[X] = \lambda \quad (3.3)$$

The Dispersion Index (DI) introduced by Cunnane (1979) uses this property to validate whether the yearly number of excesses over the threshold of the POT method indeed approximate a Poisson process. The DI is defined as the variance σ^2 of the Poisson process over the yearly mean number of events μ , as stated in Equation 3.4. Therefore, the assumption that the sample of extremes can be modelled by a Poisson process is valid if the DI is significantly close to 1. The threshold u should be chosen such that the sampled extremes are in accordance with the DI (Bommier, 2014). The threshold is rejected if the corresponding DI is outside of the confidence interval of the DI plot.

$$DI = \frac{\sigma^2}{\mu}, \text{ for } \mu \neq 0 \quad (3.4)$$

Figure 3.6 shows the DI plot for the water levels with declustering time $\delta = 45$ hours for a range of thresholds. The grey area in the plot shows the 95% confidence interval. The plot shows that all thresholds in [1.8, 3.5] lie within the confidence interval, thus providing a DI close to 1 and are appropriate thresholds. The confidence interval is calculated by testing against a chi-squared (χ^2) distribution with a $M - 1$ degree freedom. Where M is the total number of years in the sample. The confidence interval is given below, between the 2.5 and 97.5 quantiles for the χ^2_{M-1} distribution.

$$\left[\frac{\chi^2_{2.5, M-1}}{M-1}, \frac{\chi^2_{97.5, M-1}}{M-1} \right]$$

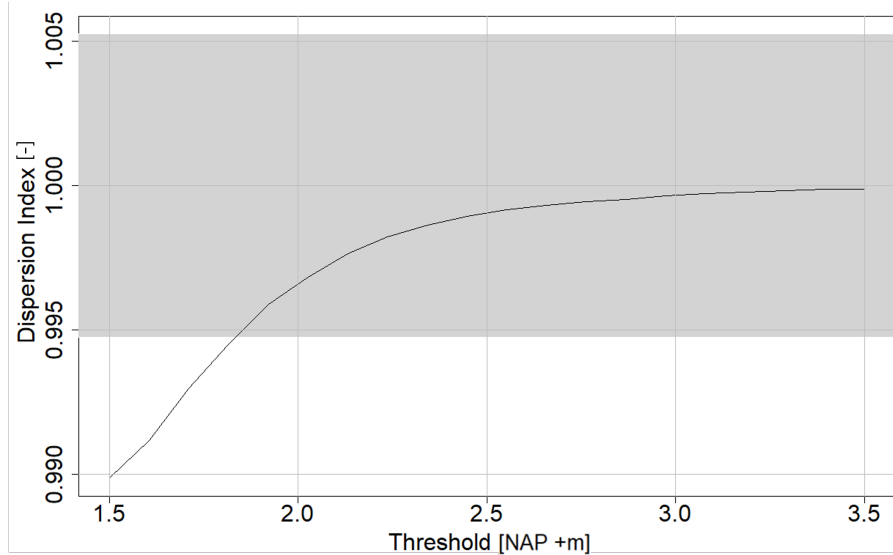


Figure 3.6: Dispersion Index plot for the water level with $\delta = 45$ hours.

Figure 3.7 shows the number of extremes per year for a range of thresholds for the water levels with a declustering time of $\delta = 45$ hours. This shows that the number of extremes significantly reduces for larger thresholds. A threshold of $u = \text{NAP} + 2.8$ meters is taken, resulting in 4.5 extremes per year, with 145 extremes in total. This results in a minimum inter-exceedance time of 48 hours between the extremes.

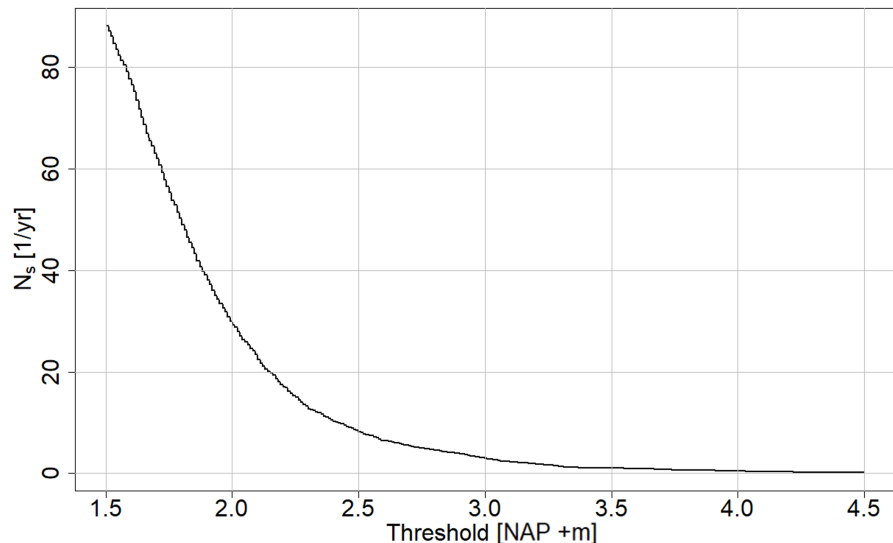


Figure 3.7: Number of extremes per year for the water level with $\delta = 45$ hours.

3.3 Stationary Extreme Value Analysis

The distributions of the extreme values of a random variable are determined by the tails of their underlying distribution. The aim of EVA is to select the best model that fits the sampled extremes. However, since limited data is available on extreme values, applications of the EVA differ and some assumptions are made in the selection process, there is not one best model. Section 3.3.1 describes the models that can be used to model the sampled extremes. In Section 3.3.2 different (stationary) models were applied to the selected extremes to determine the best model for this project. This analysis is performed using the ‘*extRemes*’ package by Gilleland (2022) in *R*.

3.3.1 Selection of Extreme Value Distributions

Samples from the BM method are modelled using the Generalized Extreme Value (GEV) distribution, shown in equation 3.5 (Salvadori et al., 2007). The GEV distribution is a parametrization of three types of distributions into one formula. Type I is known as the Gumbel distribution, type II is the Fréchet distribution and type III is the reversed Weibull distribution. The different distributions depend on the shape parameter ξ , which dominates the behaviour of the tail of the distribution. The Gumbel distribution is obtained for $\xi = 0$, the Fréchet is obtained for $\xi > 0$ and Weibull is obtained for $\xi < 0$.

$$G(x) = \exp \left\{ - \left(1 + \xi \cdot \frac{x - \mu}{\sigma} \right)^{-1/\xi} \right\} \quad (3.5)$$

for $\left(1 + \xi \cdot \frac{x - \mu}{\sigma} \right) > 0$; $-\infty < \mu < \infty$; $-\infty < \xi < \infty$; $\sigma > 0$

Where:

μ	Location parameter
ξ	Shape parameter
σ	Scale parameter

The extremal behaviour that is investigated by a POT method, can be expressed by conditional probabilities. The conditional distribution of the exceedances is described by the Generalized Pareto Distribution (GPD, Picklands, 1975). Equation 3.6 shows the GPD for an extreme event X with threshold u , where $Y = X - u$. The GPD parameters are uniquely determined from the GEV parameters. The shape parameter ξ of the GPD is equal to the shape parameter of the corresponding GEV distribution. The scale parameter σ_u of the GPD is a function of the GEV parameters, where $\sigma_u = \sigma + \xi(u - \mu)$. The shape parameter ξ of the GPD largely determines the behaviour of the tail. It shows that for $\xi = 0$, the GPD reduces to an exponential distribution. If $\xi < 0$, the GPD has an upper bound at $u - \frac{\sigma_u}{\xi}$. If $\xi > 0$, the GPD has no upper limit.

$$H_u(y) = \mathbb{P}(X - u < y | X > u) = \begin{cases} 1 - \left(1 + \frac{\xi \cdot y}{\sigma_u} \right)^{-1/\xi} & \text{if } \xi \neq 0 \\ 1 - \exp \left(-\frac{y}{\sigma_u} \right) & \text{if } \xi = 0 \end{cases} \quad (3.6)$$

for $y \geq 0$ if $\xi \geq 0$ and $0 \leq y \leq -\frac{\sigma_u}{\xi}$ if $\xi < 0$, where $y = x - u$

Nevertheless, many studies have applied a GEV distribution, such as the Weibull distribution, on POT samples when it provided a better fit for the data. If one considers other distribution types than the GPD on exceedances from a POT method, this should be done on some justification (Deltares, 2011). Using goodness-of-fit models, the 'best' distribution can be found. From the selected distribution one can extrapolate extreme values for the desired return period T to derive the return levels for a design. To go from Equation 3.6 to the exceedance probability per storm event Q , the number of extremes per year N_s should be accounted for in the exceedance probability, resulting in Equation 3.7.

$$Q = \frac{1}{T \cdot N_s} \quad (3.7)$$

To determine the N -year return level x_N of the GPD, which is exceeded once every N years, Equation 3.6 is rewritten to Equation 3.8. Here $\zeta_u = \mathbb{P}(X > u)$, meaning that ζ_u is the probability of occurrence of X exceeding an threshold u .

$$\mathbb{P}(X > x) = \zeta_u \left[1 + \xi \frac{x - u}{\sigma_u} \right]^{-1/\xi} \quad (3.8)$$

The assumption that the exceedances over the threshold u are Poisson distributed with parameter λ , results that ζ_u can be estimated by λ , the mean of the number of exceedances per year, over n_y , the number of observations per year. The rate of the Poisson distribution λ is estimated using n_u , the number of exceedances over the selected threshold u , divided by M , the number of years of the dataset.

Solving Equation 3.8 for $1/m$, where $m = N \cdot n_y$, results in the N -year return level x_N in Equation 3.9, with the estimated $\hat{\zeta}_u$ and $\hat{\lambda}$.

$$x_N = \begin{cases} u + \frac{\sigma_u}{\xi} \cdot [(\lambda \cdot N)^\xi - 1] & \text{if } \xi \neq 0 \\ u + \sigma_u \log(\lambda \cdot N) & \text{if } \xi = 0 \end{cases} \quad (3.9)$$

with

$$\hat{\zeta}_u = \frac{\hat{\lambda}}{n_y} \text{ and } \hat{\lambda} = \frac{n_u}{M}$$

3.3.2 Application of the Stationary Extreme Value Analysis

In Section 3.2, the extremes were selected by a POT method, such that the extremes are i.i.d. and approximate a Poisson process. According to Picklands (1975), the extremes selected by a POT are approximated by the GPD. The parameters of the GPD are estimated using both a Maximum Likelihood Estimator (MLE) and using an L-Moments (LM) estimator, to check for significant differences. The MLE is based on maximizing the log-likelihood that a set of values could be created by the model. The LM theory is based on linear combinations of probability-weighted moments to estimate the distribution parameters (Hosking, 1986). According to Anderson et al. (2001), the MLE is the one method that combines theoretical efficiency and extends straightforwardly to models that include non-stationarity and covariate dependency. Since these kinds of models are investigated in Section 3.4, using the MLE to estimate the model parameters is preferred. To check the goodness-of-fit of the GPD, three other distributions are fitted to the selected 145 extremes, the GEV, the Gumbel and the Exponential distributions. These three distributions are estimated using the MLE method. Note, that the Gumbel and Exponential distributions are obtained from the GEV and GPD for a shape parameter $\xi = 0$, respectively. The equations describing the GEV and GPD are found in Subsection 3.3.1.

The results are compared by creating the return level plots, the quantile-quantile (Q-Q) plots and the exceedance probability plots. The return level plots show the predicted variable value (return level) for different return periods. Figure 3.8 depicts the return level plot for the fitted distributions. For the application of the EVA, the interest lies in return levels corresponding to large return periods. The return level plot shows that the GPD and Exponential distribution best approximate the extremes. The GEV distribution overestimates the tail of the extremes, while the Gumbel distribution underestimates the tail. The difference between the GPD and the Exponential distribution is small. However, the Exponential distribution tends to slightly underestimate the tail compared to the GPD. Estimating the GPD parameters using the MLE or LM method provide similar results. In Appendix B, the individual return level plots are found, including the 95% confidence interval of the models.

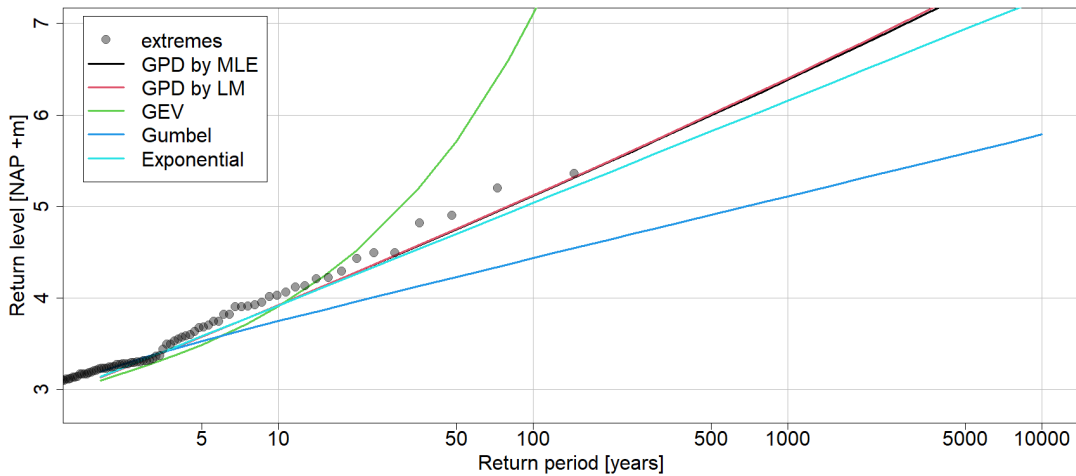


Figure 3.8: Return level plot of the extreme water level for multiple distributions

The Q-Q plot is a graphical method to check the goodness-of-fit by plotting the empirical and model quantiles against each other. The data points should approximate the one-one line if the model accurately predicts the empirical data. Figure 3.9 shows the Q-Q plots for the distributions. Comparing the results provides the same representation as the results from the return level plots. The GPD shows the smallest deviation from the one-one line compared to the other models, resulting in the best fit.

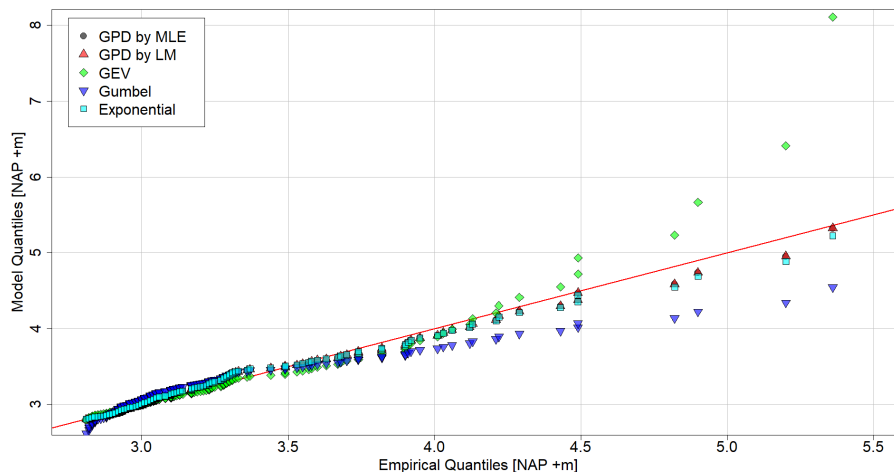


Figure 3.9: Q-Q plots for multiple distributions of the extreme water level.

The same conclusion is found when looking at the exceedance probabilities of the distributions. The GPD provides the best fit of the extremes. The Exponential distribution also provides a reasonable fit, while the Gumbel and GEV distributions perform poorly. In Appendix B the CDF of the models are found.

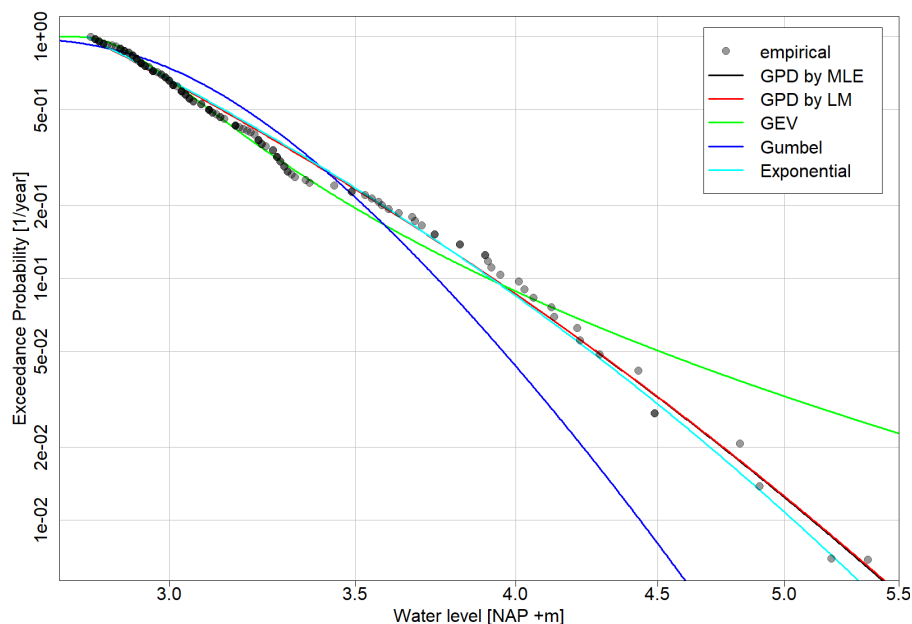


Figure 3.10: Exceedance probability $\mathbb{P}(h > x)$ plot (logarithmic scale) of the extreme water level h .

In addition, several statistics are used to determine how the models perform relative to each other. The Akaike Information Criterion (AIC, Akaike, 1974) and Bayesian Information Criterion (BIC, Schwarz, 1978) are estimators of the relative goodness-of-fit of a statistical model given the set of data. Both criteria are based on the maximum value of the log-likelihood function of the models $\hat{\mathcal{L}}$. The likelihood function $\mathcal{L}(\theta|\mathbf{x})$ provides the probability that a i.i.d. dataset $\mathbf{x} = x_1, \dots, x_n$ can be created by a model

with parameter(s) θ , as shown in Equation 3.10. The log-likelihood function, found by $\ln \mathcal{L}(\theta|\mathbf{x})$, can be solved to find the maximum log-likelihood value $\hat{\mathcal{L}}$. The AIC and BIC introduce a penalty for the number of model parameters and attempt to counter overfitting. Overfitting occurs when too many parameters are used to decrease the error of the model. Overfitting is prone to include noise from the data in the model and results in a model that is unable to make predictions for situations that deviate from the original data. Equation 3.11 and 3.12 show the AIC and BIC for the MLE models. For both criteria, it applies that the fit is better for a low score.

$$\mathcal{L}(\theta|\mathbf{x}) = f(x_1, \dots, x_n|\theta) = \prod_{i=1}^n f(x_i|\theta) \quad (3.10)$$

$$AIC = -2 \ln(\hat{\mathcal{L}}) + 2N_{par} \quad (3.11)$$

$$BIC = -2 \ln(\hat{\mathcal{L}}) + 2 \ln(N_{obs} \cdot N_{par}) \quad (3.12)$$

Where:

N_{obs}	Number of observed data points	[-]
N_{par}	Number of model parameters	[-]
θ	Parameter of the distribution $f(x)$	[-]
$\mathcal{L}(\theta \mathbf{x})$	Likelihood that \mathbf{x} comes from $f(x_1, \dots, x_n \theta)$	[-]
$\hat{\mathcal{L}}$	Maximum log-likelihood estimator	[-]

In order to evaluate the performance of the models, also the coefficient of determination R^2 is used. The R^2 is a goodness-of-fit measure based on the proportion of variance explained by the model (Di Bucchianico, 2008). The value of R^2 lies between $0 \leq R^2 \leq 1$, where the higher R^2 , the better the fit. However, R^2 can be negative for very poor fits. Equation 3.13 shows the R^2 , where N_o is the number of observations, o_i and e_i are the i^{th} observation and estimation, and \bar{o} is the average of the observations.

$$R^2 = 1 - \frac{\frac{1}{N_o} \sum_{i=1}^{N_o} (o_i - e_i)^2}{\frac{1}{N_o} \sum_{i=1}^{N_o} (o_i - \bar{o})^2} \quad (3.13)$$

The results of the estimated parameters and the criteria are found in Table 3.1. Note that the GPD and the Exponential distribution do not have a location parameter μ and also that the Gumbel and Exponential distributions do not have a shape parameter ξ . The criteria are only applied to the models that are estimated by the MLE. This is done in order to keep a fair comparison, such that all criteria are based on the maximum log-likelihood. For the criteria: AIC, BIC and the negative log-likelihood $-\mathcal{L}$, hold that a lower score corresponds to a better fit. For R^2 , the higher the better. The results show that the GPD using the MLE and LM methods, to estimate the parameters, provides very similar results. The goodness-of-fit criteria show that the GPD and the Exponential distribution have the best fit. Comparing these results with the visual inspection, the Exponential distribution provides a slightly better fit for extremes with lower return periods. Since there are more samples with lower return periods than there are with large return periods, the criteria scores seem to favour the Exponential distribution. However, the fit of the GPD and Exponential models is very close.

Table 3.1: Parameter estimates and goodness-of-fit criteria of extreme water level for different models.

Model	GPD _{MLE}	GPD _{LM}	GEV	Gumbel	Exponential
Parameter:					
Scale σ	0.4733	0.4722	0.2044	0.2930	0.4859
Shape ξ	0.0261	0.0282	0.5342	-	-
Location μ	-	-	3.0179	3.0870	-
Criterion:					
$-\mathcal{L}$	40.31	-	41.92	65.43	40.36
AIC	84.63	-	89.85	134.87	82.71
BIC	90.58	-	98.78	140.82	85.69
R^2	0.95	0.95	0.53	0.79	0.94

For the application of the EVA, the interest lies in return levels corresponding to large return periods. Therefore, the GPD is preferred as the model that best approximates extreme water levels. The results from the visual comparison, in addition to the goodness-of-fit criteria, suggest that the GPD model best approximates the sampled extreme water levels. Table B.1, in Appendix B, provides the return levels for different return periods for all models, including the 95% confidence interval of the models.

3.4 Non-stationary Extreme Value Analysis

A non-stationary extreme value analysis (NEVA) is the use of statistical models in EVA when the statistical characteristics are not stationary over a covariate, e.g. time (Shumway and Stoffer, 2011). Such non-stationary behaviour is often linked with climate change. Where extreme weather conditions of the present become more common or rare in the future. Sea level rise is an example of the non-stationary behaviour of the variable water level. To check the significance of this non-stationary behaviour for the sampled extremes, several NEVA models are investigated using the ‘*extRemes*’ package by Gilleland (2022) in *R*. Subsection 3.4.1 elaborates on the definition of a NEVA and the differences compared to stationary models. Several NEVA models are applied on the sampled extremes in Subsection 3.4.2.

3.4.1 Introduction of a Non-stationary Extreme Value Analysis

In observations that follow a clear trend, such as pictured in Figure 3.11, a stationary assumption is no longer valid. For a stationary assumption the distribution parameters (μ , ξ and σ for a GEV) are constant, a non-stationary assumption has parameters that depend on a covariate, such as time t . Such a variable should be modelled by a NEVA, where the model parameters depend on a covariate. In a GEV model, the non-stationarity of a variable could be accounted for in three cases, a changing mean μ , shape ξ or scale σ parameter of its distribution, as illustrated by the figure.

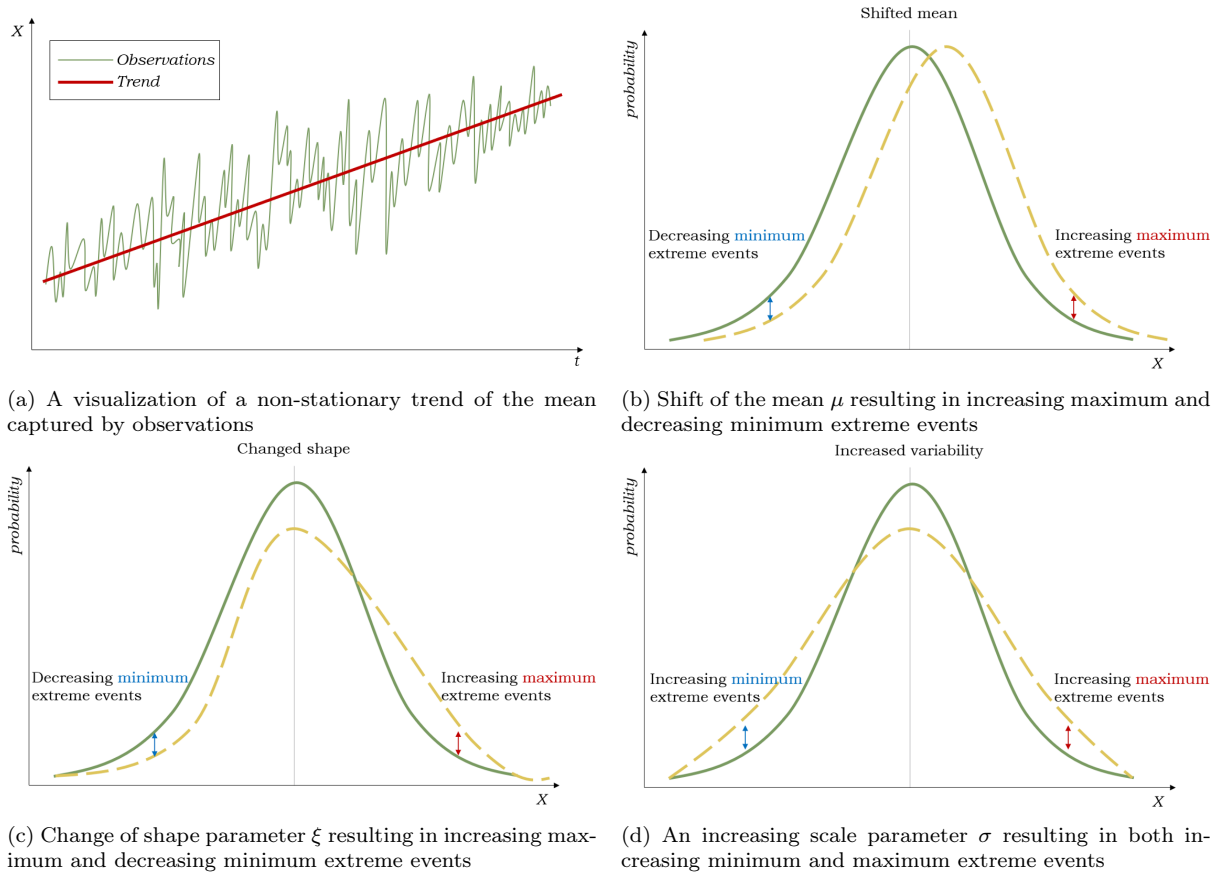


Figure 3.11: Displaying a non-stationary trend and parameters showing the change in tail probabilities

The stationary GEV distribution from Equation 3.5 changes to one that depends on t , such as given in Equation 3.14. This equation shows that the model parameters depend on the covariate t . This dependence is to be estimated by assuming the function that describes this change of the parameter, resulting in the need for additional parameters. Such a trend of a parameter could be assumed linear, resulting in one more parameter in the distribution equation. This linear assumption is shown in Equations 3.15, 3.16 and 3.17, for the location $\mu(t)$, shape $\xi(t)$ and scale $\sigma(t)$ parameter.

$$G_t(x, t) = \exp \left\{ - \left(1 + \xi(t) \cdot \frac{x - \mu(t)}{\sigma(t)} \right)^{-1/\xi(t)} \right\} \quad (3.14)$$

$$\text{for } \left(1 + \xi(t) \cdot \frac{x - \mu(t)}{\sigma(t)} \right) > 0 ; -\infty < \mu(t) < \infty ; -\infty < \xi(t) < \infty ; \sigma(t) > 0$$

with

$$\mu(t) = \mu_1 \cdot t + \mu_0 \quad (3.15)$$

$$\xi(t) = \xi_1 \cdot t + \xi_0 \quad (3.16)$$

$$\sigma(t) = \sigma_1 \cdot t + \sigma_0, \text{ for } \sigma(t) > 0 \quad (3.17)$$

Where:

t	The covariate, such as time
$\mu(t)$	Non-stationary location parameter for t
$\xi(t)$	Non-stationary shape parameter for t
$\sigma(t)$	Non-stationary scale parameter for t

Assuming a linear trend in one of the model parameters results in the expansion of the analysis by one additional parameter (μ_1 , ξ_1 and σ_1). Performing a NEVA using a linear trend in one of the model parameters should provide a clear insight into whether a trend of that parameter is present. If the introduced μ_1 , ξ_1 or σ_1 parameter is significant compared to μ_0 , ξ_0 or σ_0 , a trend is present for that parameter. Equation 3.18 shows the non-stationary GPD that depends on the covariate t . The GPD has two model parameters, the shape $\xi(t)$ and scale $\sigma(t)$ parameter, that depend on the covariate t . In addition, the threshold $u(t)$ can be non-stationary and thus depend on the covariate t .

$$H_u(y, t) = \mathbb{P}\{X - u(t) < y | X > u(t)\} = \begin{cases} 1 - \left(1 + \frac{\xi(t) \cdot y}{\sigma_u(t)} \right)^{-1/\xi(t)} & \text{if } \xi(t) \neq 0 \\ 1 - \exp \left(-\frac{y}{\sigma_u(t)} \right) & \text{if } \xi(t) = 0 \end{cases} \quad (3.18)$$

$$\text{for } y \geq 0 \text{ if } \xi(t) \geq 0 \text{ and } 0 \leq y \leq -\frac{\sigma_u(t)}{\xi(t)} \text{ if } \xi(t) < 0, \text{ where } y = x - u(t)$$

Non-stationarity of a design variable also affects the return period for a design (Salas and Obeysekera, 2014). For a stationary variable, the probability of occurrence of a certain value z_q does not change over time, therefore $p_0 = p_t$. However, for a non-stationary this probability does change, thus $p_0 \neq p_t$. Figure 3.12 shows the differences between a stationary and non-stationary return level. The non-stationary case shows that the probability p_t that value z_{q0} occurs becomes larger over time. The initial probability p_0 that z_{q0} occurred is pictured by the green-shaded area within p_t , demonstrating that p_t became larger over time by the yellow-shaded area. This results that the return period for a non-stationary variable is changing over time, as it is defined as the expected waiting time of the design flood z_{q0} to be exceeded for the first time. The return period for non-stationary cases is therefore referred to as the *effective return period*. The expression for the effective return level is defined in Equation 3.19 (Salas and Obeysekera, 2014).

$$T = \mathbb{E}(X) = 1 + \sum_{x=1}^{x_{max}} \prod_{t=1}^x (1 - p_t) \quad (3.19)$$

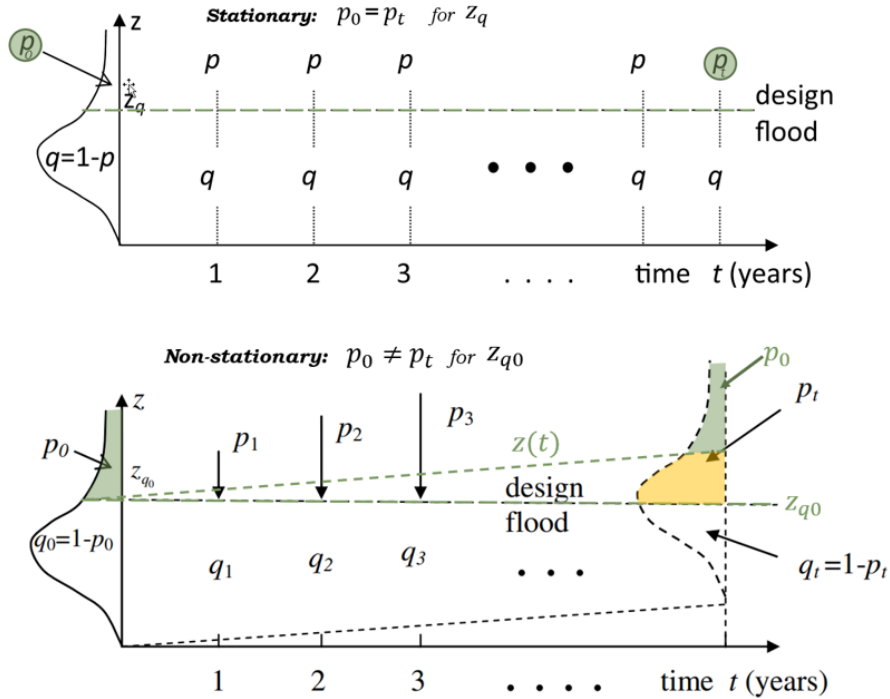


Figure 3.12: Return period for a stationary versus non-stationary random variable. Image retrieved and modified from Salas and Obeysekera (2014), pp. 554–568.

3.4.2 Application of multiple Non-stationary models

Section 3.2 provides the selected extremes using a POT method with the water level as the dominant variable. A linear regression on the results in Figure B.2 in Appendix B shows a first impression of whether a trend in the selected extremes is present. A NEVA is performed to provide a better insight into this trend. In performing the NEVA a linear trend of the model parameters in time is considered. In addition, a NEVA is performed to check the influence of a non-stationary analysis for water level as the dominant variable with the concomitant variable wave height as the covariate. This analysis is also performed using a linear trend in the model parameters. Figure B.5 in Appendix B shows the selected extreme water levels against the wave height values. The figure shows a clear (positive) dependence between the two variables.

The stationary analysis showed that the selected extreme water levels are best represented by a GPD. Therefore, the NEVA focuses on GPD models. A NEVA is applied for multiple GPD models with non-stationary scale $GPD_{t,\sigma}$ and shape $GPD_{t,\xi}$ parameters with the covariate time t . Also, a GPD model with a non-stationary threshold $GPD_{t,u}$ is investigated. A non-stationary threshold $u(t)$ resulted in a negative scale σ parameter and is therefore not viable. Furthermore, a combination of a non-stationary scale $\sigma(t)$ and shape $\xi(t)$ is applied as the $GPD_{t,\sigma,\xi}$ model. The non-stationary parameters, as defined in Equations 3.16 and 3.17, exist out of a constant part (σ_0 and ξ_0) and a coefficient part (σ_1 and ξ_1) that is multiplied by the covariate. The results of the parameter estimates (σ_i and ξ_i) and the standard errors ($\epsilon(\sigma_i, \xi_i)$) are found in Table 3.2. The table shows that there is no statistical significance of the time-dependent model parameters σ_1 and ξ_1 . The values of these parameters are negligible compared to the stationary part of the model parameters σ_0 and ξ_0 . The standard error in the estimation of the parameters is of the same order of magnitude as the estimated values. In addition, the goodness-of-fit criteria are found in Table 3.3. Where the fit of the models is better for low $-\mathcal{L}$, AIC and BIC scores and high R^2 scores. As found, the criteria do not improve over the stationary GPD. Therefore, a time-dependent GPD model is not optimal.

Table 3.2: Non-stationary GPD model parameters and standard errors for covariates (CV) t and H_s .

Model	Parameter & Standard error								CV
	σ_0	$\epsilon(\sigma_0)$	σ_1	$\epsilon(\sigma_1)$	ξ_0	$\epsilon(\xi_0)$	ξ_1	$\epsilon(\xi_1)$	
$\text{GPD}_{t,u}$	<0	NA	-	-	NA	NA	-	-	t
$\text{GPD}_{t,\sigma}$	0.5413	0.0581	$-6 \cdot 10^{-11}$	$2 \cdot 10^{-8}$	0.0313	0.0914	-	-	t
$\text{GPD}_{t,\xi}$	0.4767	0.0590	-	-	-0.1016	0.0923	$1 \cdot 10^{-10}$	$2 \cdot 10^{-8}$	t
$\text{GPD}_{t,\sigma,\xi}$	0.7266	0.0572	$-2 \cdot 10^{-10}$	$2 \cdot 10^{-5}$	-0.4130	0.0877	$4 \cdot 10^{-10}$	$2 \cdot 10^{-5}$	t
$\text{GPD}_{H_s,\sigma}$	-0.5455	0.0999	0.3458	0.0432	-0.2569	0.0524	-	-	H_s
$\text{GPD}_{H_s,\xi}$	0.4637	0.0611	-	-	-1.327	0.2544	0.3731	0.0993	H_s
$\text{GPD}_{H_s,\sigma,\xi}$	-0.5855	0.1238	0.3630	0.0546	-0.1771	0.1583	-0.0306	0.0557	H_s

Table 3.3: Goodness-of-fit criteria of the non-stationary GPD models for covariates t and H_s .

Criterion	t - models				H_s - models		
	$\text{GPD}_{t,u}$	$\text{GPD}_{t,\sigma}$	$\text{GPD}_{t,\xi}$	$\text{GPD}_{t,\sigma,\xi}$	$\text{GPD}_{H_s,\sigma}$	$\text{GPD}_{H_s,\xi}$	$\text{GPD}_{H_s,\sigma,\xi}$
$-\mathcal{L}$	NA	40.20	40.21	39.53	12.73	28.53	12.60
AIC	NA	86.40	86.42	87.05	31.46	63.06	33.21
BIC	NA	95.33	95.35	98.96	40.39	71.99	45.12
R^2	NA	0.94	0.94	0.94	0.78	-1.14	0.82

Besides time t , the wave height H_s is also investigated as a covariate. The same procedure is applied and a GPD model with a non-stationary scale $\text{GPD}_{H_s,\sigma}$, shape $\text{GPD}_{H_s,\xi}$ parameter or both $\text{GPD}_{H_s,\sigma,\xi}$ is considered. The results in Tables 3.2 and 3.3 suggest that this approach provides a better approximation of the extreme water levels, compared to a stationary model. The non-stationary scale σ_1 value is of significance compared to the stationary scale σ_0 value for the $\text{GPD}_{H_s,\sigma}$ model. The standard error of the estimates is an order of magnitude lower than the estimated values and thus the trend is not negligible. The $\text{GPD}_{H_s,\sigma}$ shows a relatively greater goodness-of-fit compared to the $\text{GPD}_{H_s,\xi}$ model, suggesting that the data is better approximated using a non-stationary scale parameter than a non-stationary shape parameter. The effective return levels of the non-stationary models are shown in Figure 3.13. The figure also shows that the introduction of a non-stationary shape parameter results in a significant influence on the tail of the $\text{GPD}_{H_s,\xi}$ model. The $\text{GPD}_{H_s,\sigma,\xi}$ model shows a slightly better goodness-of-fit compared to the $\text{GPD}_{H_s,\sigma}$ model. However, the standard error of the non-stationary shape $\epsilon(\xi_1)$ is of the same order of magnitude as ξ_1 . Therefore, this trend is not of statistical significance. The error of the estimate of ξ_1 could be of larger influence than the ξ_1 value itself. Thus, the $\text{GPD}_{H_s,\sigma}$ model is considered the best fit of the non-stationary models.

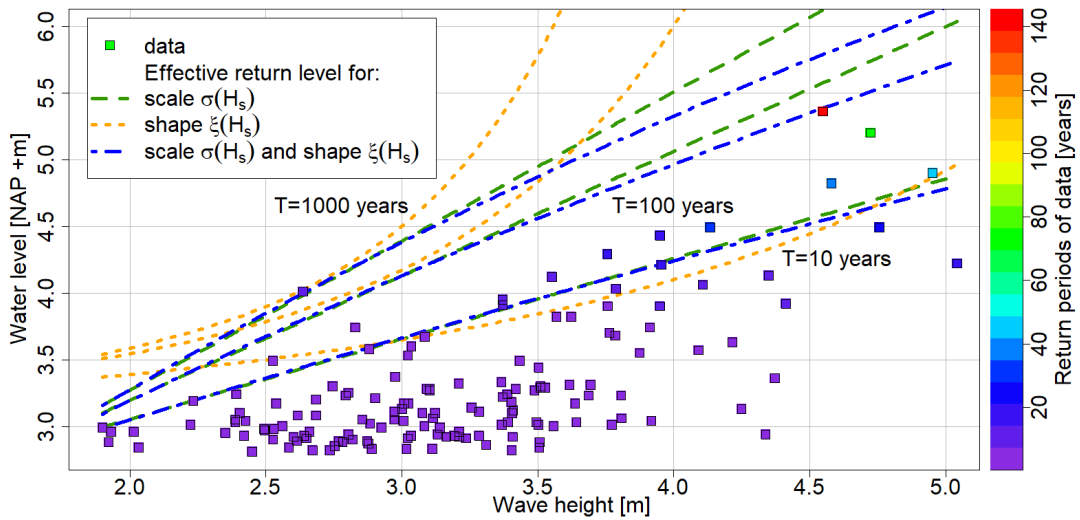


Figure 3.13: The 10-, 100- and 1000-year effective return levels for the non-stationary GPD_{H_s} models.

3.5 Conclusion of the Extreme Value Analysis

The aim of the EVA is to define a model that best approximates the extreme observations of the random variable for which the dike will be designed. In this project, the water level is considered the dominant variable. A POT method with a threshold of $u = \text{NAP} + 2.8$ meters and a declustering time of $\delta = 45$ hours resulted in 145 selected extreme water levels. The extreme values of the variables wave height, wave period, wind speed and wind direction, are the ones that coincide with the times of the extreme water levels.

The application and assessment of several stationary models showed that the tail of the extremes is best modelled by the GPD. The application of non-stationary models, with a linear trend in the model parameters, is investigated to approximate the extreme water level. The analysis showed that the extreme water levels do not show a statistically significant trend in time. Introducing a non-stationary GPD, with the covariate wave height H_s , resulted in an enhanced fit compared to the stationary model. The estimated model parameters are shown in Table 3.4.

Table 3.4: Comparison between the selected stationary and non-stationary GPD models.

Model	Parameter		Criterion			
	Scale σ	Shape ξ	$-\mathcal{L}$	AIC	BIC	R^2
Stationary GPD	0.473	0.026	40.31	84.63	90.58	0.95
Non-stationary GPD$_{H_s, \sigma}$	$0.346 \cdot H_s - 0.546$	-0.257	12.73	31.46	40.39	0.78

The behaviour of the extreme water level is well described by both a stationary GPD and a non-stationary GPD with the covariate wave height. However, when comparing the goodness-of-fit criteria results that the non-stationary model is preferred. Therefore, the application of a non-stationary marginal distribution in copula modelling is investigated in Section 4.4.

4 | Copula & Vine modelling

In this chapter, multivariate modelling is performed by bivariate copulas and vine modelling. Section 4.1 provides the theoretical framework for multivariate modelling on which the application is based. Sections 4.2 and 4.3 provide the selected models of the concomitant variables and a bivariate copula analysis. Section 4.4 answers to RQ1 and aims to combine a variable with a non-stationary marginal distribution with copula modelling. The bivariate copulas are combined using vines in Section 4.5. The chapter is concluded in Section 4.6.

4.1 Theory on multivariate modelling

Hydraulic structures are designed to withstand extreme natural events. Natural events can be characterized by the joint behaviour of several random variables, that usually share dependence. In hydraulic structure design, it is of interest to model the joint probability of the extreme values of the design variables. The maxima of all variables of interest mostly do not occur at the same time, hence modelling the dependence allows us to determine realistic loads and helps optimise the design. For instance, wind speeds above a certain threshold result in the capping of significant wave height. The joint probability could provide insights about significant wave heights to expect during storm surges with certain peak wind velocities. A possible way, and the one applied in this thesis, is to model multivariate data by separately studying the dependence function and the marginals. The dependence structure of random variables, independently of their marginal laws, can be described by copulas (Salvadori et al., 2007). Copulas can be applied to a d -dimensional framework, however often bivariate ($d = 2$) copulas are preferred. This is due to the larger extent of different copula models to be used and the larger flexibility to model the dependence structures between pairs of variables. Vine copula modelling opens the way to combine bivariate copulas to model multivariate (for $d > 2$) dependence structures, based on conditional probabilities. The following sections provide information about methods to describe the correlation between variables, copulae theory and copula families, vine modelling and multivariate return periods.

4.1.1 Measures of Association

There are several ways to measure the dependence between random variables. This thesis only considers the correlation coefficients between two random variables. The *measure of association* quantifies the degree of relationship between variables (Salvadori et al., 2007). Coefficients of association usually vary between -1 and +1. The strength of the relationship increases as their values increase, where a value of +1 (or -1) corresponds to a perfect positive (or negative) association. Two coefficients of association, Pearson's ρ_P and Spearman's r_S are discussed here, each measuring a different type of association.

The covariance indicates the amount of linear dependence. It is the expected value of the product of the deviations of the variables from their respective means, stated by Equation 4.1.

$$\text{cov}(X, Y) = \mathbb{E}\left[(X - \mathbb{E}[X]) \cdot (Y - \mathbb{E}[Y])\right] \quad (4.1)$$

Pearson's product-moment correlation coefficient ρ_P relates to the covariance. Pearson's ρ_P is the covariance of two random variables divided by the product of their standard deviations, provided by Equation 4.2.

$$\rho_P = \frac{\text{cov}(X, Y)}{\sigma_X \cdot \sigma_Y} \quad (4.2)$$

$$\text{with } \sigma_X = \sqrt{\mathbb{E}[(X - \mathbb{E}[X])^2]}$$

Pearson's ρ_P ranges between $-1 \leq \rho_P \leq +1$ for perfect negative to positive (linear) dependence between random variables X and Y . However, in the case of $\rho_P = 0$ it does not result that X and Y are independent. As Pearson's ρ_P is purely a measure of linear dependence, therefore non-linear dependencies between X and Y are not accounted for. In addition, Pearson's ρ_P strongly depends on the marginal laws of the two random variables. Therefore, if one would consider dependence measures that only depend upon the copula, Pearson's ρ_P cannot be used.

Spearman's rank correlation coefficient r_S is based on the ranks of two random variables X and Y . In statistics, ranking is the transformation of the n values of the variables X and Y , by ordering the values in ascending order. The smallest value is labelled as rank 1 and the largest value is ranked n . Spearman's r_S is stated in Equation 4.3. The variables X and Y can be mapped into unity space by dividing their respective ranks by $n + 1$.

$$r_S = \frac{\text{cov}(R_X, R_Y)}{\sigma_{R_X} \cdot \sigma_{R_Y}} \quad (4.3)$$

with $R_X = \text{Rank}(X)$

Spearman's r_S is a so-called *scale-invariant* measure, as stated by Salvadori et al. (2007). A scale-invariant measure means that it remains unchanged under strictly increasing (monotonic) transformations of the variables of interest. A monotonic transformation makes sure that the ranks of the variable are not changed. Spearman's r_S is a measure of *concordance*. Two random variables X and Y are concordant if small (or large) values of one are likely to be associated with small (or large) values of the other (Salvadori et al., 2007). Discordance is when a small value of one is likely to be associated with a large value of the other and vice versa.

When transforming two random variables into unity space, Spearman's r_S can be used to measure the correlation in the entire $[0, 1]^2$. Figure 4.1 shows an example of positive and negative correlation for two random variables X and Y .

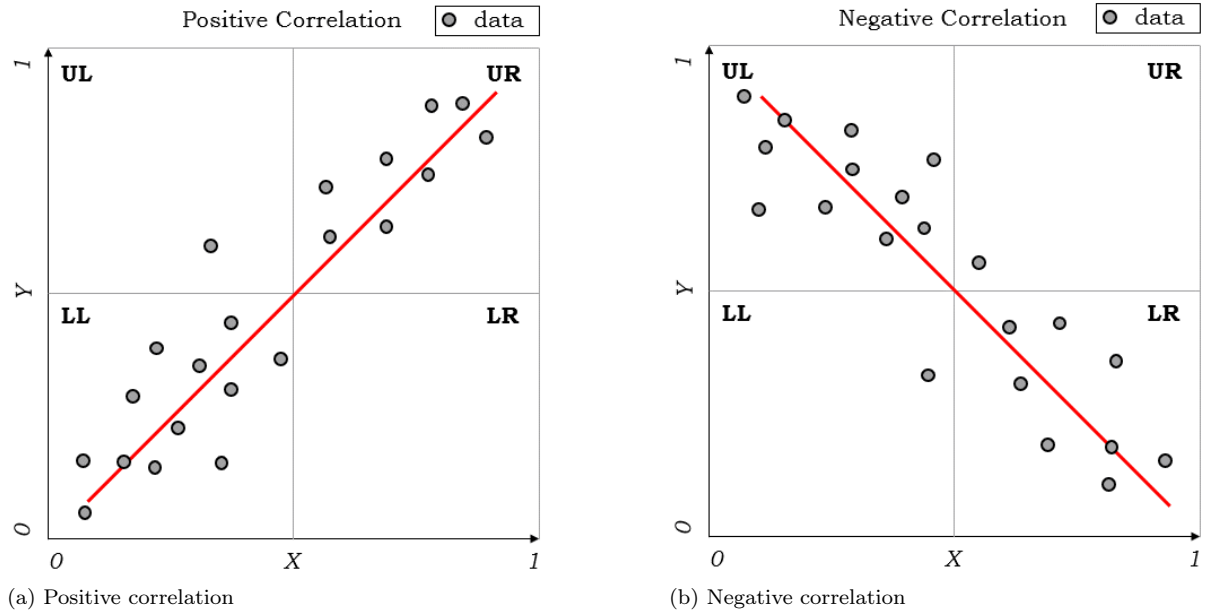


Figure 4.1: Examples of positive and negative correlation of two random variables X and Y in $[0, 1]^2$.

This thesis applies both Pearson's and Spearman's correlation coefficients for different cases. The correlation between two variables is determined using Spearman's r_S , unless stated otherwise. There are multiple other measures of association. Another widely known and applied scale-invariant measure is Kendall's tau, τ_K , which is also a measure of concordance. If one is interested in τ_K , Salvadori et al. (2007) provides the theoretical framework and various applications.

4.1.2 Bivariate Copulae

Copulae are functions for modelling joint probability distributions. A joint probability distribution of $d = 2$ random variables is referred to as a bivariate distribution. A multivariate distribution is for $d > 2$ random variables. This thesis only focuses on bivariate cases. Equation 4.4 shows that by integrating the joint density function $f(x, y)$, one can determine the probability that (X, Y) is within $[a_1, b_1] \times [a_2, b_2]$.

$$\mathbb{P}\{a_1 \leq X \leq b_1, a_2 \leq Y \leq b_2\} = \int_{a_1}^{b_1} \int_{a_2}^{b_2} f(x, y) dx dy \quad (4.4)$$

with

$$f(x, y) \geq 0 \quad \forall \quad x, y$$

$$\int_{-\infty}^{+\infty} \int_{-\infty}^{+\infty} f(x, y) dx dy = 1$$

and

$$f(x, y) = f(x)f(y) \text{ for } X \perp Y \text{ (independent)}$$

A bivariate copula expresses the joint distribution of two random variables in unity space $\mathbb{I}^2 = [0, 1]^2$. The definition of a bivariate copula is provided in Definition 4.1.

Definition 4.1. (2-Copula).

Let $\mathbb{I} = [0, 1]$. A 2-copula is a bivariate function $\mathbf{C}: \mathbb{I} \times \mathbb{I} \rightarrow \mathbb{I}$ such that (Salvadori et al., 2007):

1. (uniform marginals) for all $u, v \in \mathbb{I}$,
 $\mathbf{C}(u, 0) = 0$, $\mathbf{C}(u, 1) = u$, $\mathbf{C}(0, v) = 0$, $\mathbf{C}(1, v) = v$;
2. (2-increasing) for all $u_1, u_2, v_1, v_2 \in \mathbb{I}$ such that $u_1 \leq u_2$ and $v_1 \leq v_2$,
 $\mathbf{C}(u_2, v_2) - \mathbf{C}(u_2, v_1) - \mathbf{C}(u_1, v_2) + \mathbf{C}(u_1, v_1) \geq 0$.

Sklar's theorem provided by Theorem 4.1, by Sklar (1959), is the foundation of copulae. It defines the relationship between multivariate (or bivariate) distributions and the marginals by copulas. Copulas let one express the joint probability as a function of the marginal distributions.

Theorem 4.1. (Sklar's theorem (2-dimensional case)).

Let F_{XY} be a joint distribution function with marginals F_X and F_Y . Then there exists a 2-copula \mathbf{C} such that (Sklar, 1959; Salvadori et al., 2007):

$$F_{XY}(x, y) = \mathbf{C}(F_X(x), F_Y(y)) \quad (4.5)$$

for all reals x, y . If F_X, F_Y are continuous then \mathbf{C} is unique; otherwise \mathbf{C} is uniquely defined on $\text{Ran}(F_X) \times \text{Ran}(F_Y)$. Conversely, if \mathbf{C} is a 2-copula and F_X, F_Y are distribution functions, then the function F_{XY} given by equation 4.5 is a joint distribution with marginals F_X and F_Y .

In fitting copulas to experimental data, the empirical copulas play an important role. As stated by Salvadori et al. (2007), the empirical copula counts the number of pairs that satisfy given constraints, defined by Definition 4.2, in order to approximate the copula linking the pair (X, Y) . Goodness-of-fit procedures that are based on the empirical copula can provide insight into which copula models can best be used to approximate the data.

Definition 4.2. (Empirical Copula).

Let $\{R_k, S_k\}$ be the ranks associated with random sample $\{X_k, Y_k\}$, $k = 1, \dots, n$. The corresponding empirical copula \mathbf{C}_n is defined as (Salvadori et al., 2007):

$$\mathbf{C}_n(u, v) = \frac{1}{n} \sum_{k=1}^n \mathbf{1}\left(\frac{R_k}{n+1} \leq u, \frac{S_k}{n+1} \leq v\right), \quad (4.6)$$

where $u, v \in \mathbb{I}$ and $\mathbf{1}$ is an indicator function.

Copula modelling provides a wide range of different models to fit the multivariate behaviour of the variables of interest. There are numerous copula families, each with different characteristics. The Elliptical and Archimedean copulae are two widely used copula subclasses. The Gaussian and Student-t families are part of the Elliptical class. Their name results from their elliptical shape, leading to symmetrical tails. The Archimedean types are widely used for their versatility in terms of both the nature and

strength of the association they produce between the variables. Two examples of Archimedean types are the Clayton and Gumbel copulas. The measure of tail dependence is a useful indicator to determine which copula to use. The definition will follow below.

Tail dependence is a measure of dependence focusing on the upper-right (UR) or lower-left (LL) quadrant tail, for positive correlation. For negative correlation, the upper-left (UL) and lower-right (LR) quadrant tails are of interest. Tail dependence can be measured by the tail dependence coefficients λ_U and λ_L , defined in Definition 4.3.

Definition 4.3. (Tail dependence (2-dimensional case)).

Let $Z = (X, Y)$. The random vector Z is upper tail dependent if (Salvadori et al., 2007):

$$\lambda_U = \lim_{t \rightarrow 1^-} \mathbb{P}\left\{X > F_X^{[-1]}(t) | Y > F_Y^{[-1]}(t)\right\} > 0, \quad (4.7)$$

provided that the limit exists. If $\lambda_U = 0$ then Z is upper tail independent. λ_U is called the upper tail dependence coefficient. Similarly, Z is lower tail dependent if:

$$\lambda_L = \lim_{t \rightarrow 1^+} \mathbb{P}\left\{X \leq F_X^{[-1]}(t) | Y \leq F_Y^{[-1]}(t)\right\} > 0, \quad (4.8)$$

provided that the limit exists. If $\lambda_L = 0$ then Z is lower tail independent.

Tail dependence is an essential quantity for estimating risk in EVA. Extremes of different variables usually are more correlated than the average values, when they are generated by the same driver (storm). Different copula families have different tail dependence characteristics. Tail dependence is considered scale-invariant for relating dependencies and extremes, as the copula separates the dependence structure of the bivariate distribution from its underlying marginals (Salvadori et al., 2007). In the selection of a suitable copula family, tail dependence can provide useful indications for which copula to use. The Clayton and Gumbel copulas are examples of copulas that allow for specific levels of lower and upper tail dependence. Copulas can also be rotated to fit the tail dependence for a certain quadrant. A copula \mathbf{C} that is rotated 180 degrees is referred to as a Survival Copula $\overline{\mathbf{C}}$. In the case of negative correlation, as shown in Figure 4.1b, a copula can be rotated 90 (or 270) degrees.

4.1.3 Vine Copulae

A vine is a set of nested trees $\mathcal{V} = \{T_j, \dots, T_{n-1}\}$ that are used to represent high dimensional probability distributions (Cooke and Bedford, 2001; Morales-Nápoles et al., 2010). The vine structure defines how joint distributions and conditional probabilities are modelled. A regular vine is a case in which all constraints are two-dimensional or conditional two-dimensional. Combining regular vines with bivariate copulae enables the extension from two-dimensional to arbitrary dimensions; such regular vines are called vine copulae. Vine copulae have proven to be a flexible tool that can model a wide range of complex dependencies, such as multivariate modelling of flood characteristics (e.g. Zhang et al., 2020; Tosunoglu et al., 2020). This thesis considers vine copulae as means for multivariate modelling of the design variables of the WGD project. Next to vine copulae, also partial correlation vines are well studied. Detailed specifications of such vines can be found in Cooke and Bedford (2001) and Kurowicka and Cooke (2006).

Regular vines consist of n nodes where the edges of the tree T_j are the nodes of the tree T_{j+1} for $j = 1, \dots, n-2$. The nodes represent the variables, while the edges represent the conditional probabilities. A labelled tree is an undirected acyclic graph with a set of nodes $N = \{1, \dots, n\}$ and edges E consisting of a subset of pairs of N . A regular vine holds that two edges in tree T_j are only joined by an edge in tree T_{j+1} if they share a common node. The definition of a regular vine is provided in Definition 4.4 by Joe and Kurowicka (2011) based on Kurowicka and Cooke (2006).

Definition 4.4. (Regular Vine).

\mathcal{V} is a regular vine on n elements with $E(\mathcal{V}) = E_1 \cup \dots \cup E_{n-1}$ denoting the set of edges of \mathcal{V} if (Kurowicka and Cooke, 2006; Joe and Kurowicka, 2011):

1. $\mathcal{V} = \{T_1, \dots, T_{n-1}\}$

2. T_1 is a connected tree with nodes $N_1 = \{1, \dots, n\}$, and edges E_1 ; for $i = 2, \dots, n - 1$, T_i is a tree with nodes $N_i = E_{i-1}$,
3. (**proximity**) for $i = 2, \dots, n - 1$, $\{a, b\} \in E_i$, $\#(a \Delta b) = 2$ where Δ denotes the symmetric difference operator and $\#$ denotes the cardinality of a set.

In a regular vine, the nodes that are reachable from a given edge are referred to as the *constraint set* of that edge. The constraint set is found in tree T_1 for a given edge. The intersection of two edges that are joined by an edge in tree T_i for $i = 2, \dots, n - 1$, forms the *conditioning set* of that constraint set. The symmetric difference of the constraint sets is called the *conditioned set*. Figure 4.2 shows an example of a regular and a non-regular vine for $n = 4$ variables. The conditioned and conditioning set are separated by a vertical line '|'. The conditioning variables are shown to the right of the vertical line and the conditioned variables are to the left. As the proximity condition from Definition 4.4 states, a regular vine holds that the cardinality of all conditioned sets equals two. The figure shows that the vine on the right has a conditioned set smaller than two, namely one. Therefore, it is a non-regular vine.

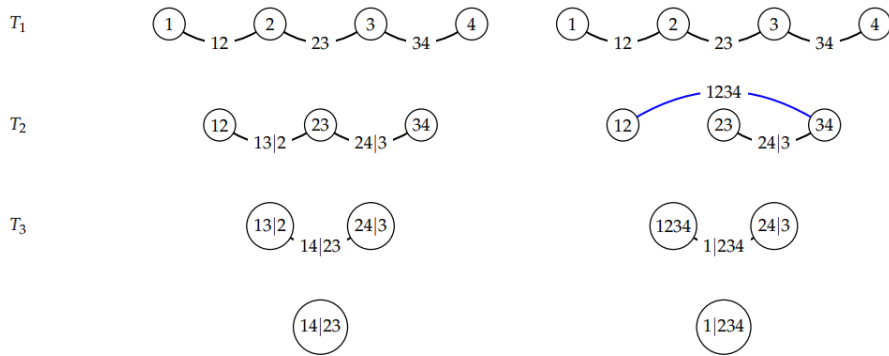


Figure 4.2: A regular vine (left) and non-regular vine (right) on $n = 4$ variables. The blue edge in the non-regular vine shows a connection between two nodes which do not share a common node. Every edge on the left vine represents a (conditional) bivariate copula. Retrieved from Timmermans (2021).

Figure 4.3 shows an example of a (drawable) D-vine and a (canonical) C-vine. Both class as a regular vine, as can be observed that the number of conditioned variables equals 2 for every edge. For a D-vine, all nodes are set in a straight line and connected without any side branches. The number of edges connected to a node defines the degree of a node. In a D-vine, the degree of a node can be a maximum of 2. Figure 4.3 shows that the nodes at the ends have a degree of 1, while the other nodes have a degree of 2. A C-vine has one node in each tree with a maximum degree of $n - 1$. In other words, all nodes are connected by a central node that has a maximum degree. All other nodes have a degree of 1.

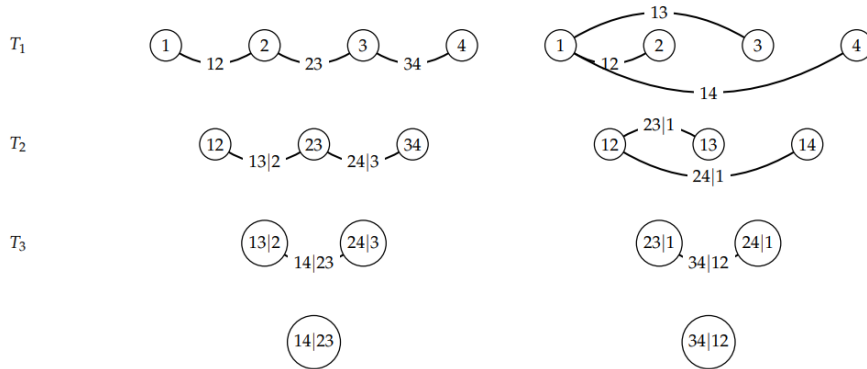


Figure 4.3: A D-vine (left) and a C-vine (right) on $n = 4$ variables. Retrieved from Timmermans (2021).

The number of possible trees and vines for n variables quickly grows to large numbers. The number of labelled trees and regular vines on n nodes are provided by Equations 4.9 and 4.10, as proved by Morales-Nápoles et al. (2010). In Table 4.1, the number of possible labelled regular vines is shown up to $n = 8$ variables. Note, that there is exactly one object for 1 and 2 nodes.

$$N_{trees} = n^{n-2} \quad (4.9)$$

$$N_{vines} = \binom{n}{2} \times (n-2)! \times 2^{\binom{n-2}{2}} \quad (4.10)$$

Table 4.1: Number of possible labelled trees and regular vines on 3, 4, 5, 6, 7, and 8 nodes. This table is retrieved and adapted from Morales-Nápoles et al. (2010).

Nodes	Trees ^a	Regular vines ^b
3	3	3
4	16	24
5	125	480
6	1,249	23,040
7	16,807	2,580,480
8	262,144	660,602,880

^a Number of labelled trees

^b Number of labelled regular vines

As the number of vines grows to large numbers, the classification of vines becomes important when comparing the different vines. Tree equivalence is used to define subclasses of vines. The classification of tree-equivalent vines is based on Definitions 4.5 and 4.6. According to Definition 4.6, one could permute the numbers in T_1 of the D-vine in Figure(s) 4.2 (and 4.3) to get different labelled regular vines, but the same tree-equivalent vine. The classification of vines can be useful in determining the number of vines that still can be created after the construction of the first tree T_1 , for example. Also, when adding an additional node to an existing vine, one could result in vines in different subclasses.

Definition 4.5. (Graph Isomorphism).

Two labelled graphs $G_i = (E_i, N_i)$ and $G_j = (E_j, N_j)$ are isomorphic if there is a bijection $\phi : N_i \rightarrow N_j$ such that for all pairs $(a, b) \in E_i \iff (\phi(a), \phi(b)) \in E_j$. If two graphs are isomorphic they are the same unlabeled graph.

Definition 4.6. (Tree-equivalent Vine).

If a bijection as in Definition 4.5 may be found for each $T_i \in \mathcal{V}_k(n)$ and $T_j \in \mathcal{V}_j(n)$ then we speak of the same tree-equivalent vine and accordingly the same tree-equivalent regular vine when the proximity condition holds.

Vine copula (or a pair-copula construction) are bivariate copula vine specifications (Kurowicka and Cooke, 2006). A vine copula is created by allocating a bivariate copula C_e to each edge e in the union $E(\mathcal{V}) = E_1 \cup \dots \cup E_{n-1}$ of the vine. Resulting that n -dimensional vine copulae are based on $\binom{n}{2}$ copulae, which can be selected independently of each other. The set of $\binom{n}{2}$ copulae is denoted by B . The joint density of a regular vine copula $\mathcal{V} = \{T_1, \dots, T_{n-1}\}$ with margins F_1, \dots, F_n is given by Theorem 4.2. Note, that C_e is a marginal bivariate copula in tree T_1 and a conditional bivariate copula in trees T_2, \dots, T_{n-1} . This leads to $n - 1$ marginal bivariate copulae and $(n - 1)(n - 2)/2$ conditional bivariate copulae.

Theorem 4.2. (Vine Copula Density).

Let $\mathcal{V} = \{T_1, \dots, T_{n-1}\}$ be a regular vine on n elements. For an edge $e \in E(\mathcal{V})$ with conditioned elements e_1, e_2 and conditioned set D_e , let the conditional copula and copula density be $C_{e_1, e_2 | D_e}$ and $c_{e_1, e_2 | D_e}$, respectively. Let the marginal distributions F_i with densities f_i , $i = 1, \dots, n$ be given. Then the vine-dependent distribution is uniquely determined and has a density given by: (Kurowicka and Cooke, 2006):

$$f_{1 \dots n} = f_1 \cdots f_n \prod_{e \in E(\mathcal{V})} c_{e_1, e_2 | D_e} \left(F_{e_1 | D_e}, F_{e_2 | D_e} \right) \quad (4.11)$$

From Theorem 4.2 the joint distribution can be determined using the selected marginal distributions F_1, \dots, F_n and marginal and conditional bivariate copulae in B . The joint distribution, satisfying the vine copulae specification, will preserve maximum entropy properties of the conditional bivariate copulae (Cooke, 1997; Cooke and Bedford, 2001). For the application of the vine copulae, one could sample the joint distribution to result in the joint probabilities to evaluate risks. There are two strategies for sampling vine copulae, i.e. the *cumulative* and *density* approaches.

For the cumulative approach, first n independent uniform $(0, 1)$ variables U_1, \dots, U_n are sampled. Then the uniform variable X_j can be expressed in terms U_i and U_j , using the conditional cumulative distribution function. The realizations x_i for the variables of interest X_1, \dots, X_n are obtained by applying successive inverse cumulative distribution functions (also called quantile functions). A general algorithm for sampling regular vines is provided by Kurowicka and Cooke (2007). The sampling procedure can be graphically visualized using so-called staircase graphs, as can be found in Kurowicka and Cooke (2007).

The density approach can be used when a vine copula density is fully specified as in Equation 4.11. The equation can be rewritten as Expression 4.12, whereby uniformity, the density $f_i(x_i) = 1$ (Joe and Kurowicka, 2011). The Expression 4.12 can be used to sample the vine copula.

$$\prod_{e \in E} c_{ij|D_e} \left(F_{i|D_e}(x_i), F_{j|D_e}(x_j) \right) \quad (4.12)$$

4.2 Selection of the Marginals of the Concomitant variables

In Section 3.2, a POT is applied to sample the extreme water level observations. This resulted in 145 extreme events. The concomitant variables wave height H_s , wave period T_p , wind speed w_s and wind direction w_d are selected at the same instances of the sampled extreme water levels, as visualized in Figure 4.4. From these sampled extremes, 142 extremes remain due to the lack of wind data for three events. A model is selected to approximate the 142 extreme values for each concomitant. Similar to the EVA of the water level, this selection is based on the AIC, BIC and the coefficient of determination R^2 , defined by Equations 3.11, 3.12 and 3.13 in Subsection 3.3.2. In addition, the exceedance probability and CDF plots for the concomitants are used to check the fit of the investigated models. The various models are fitted and assessed using the ‘*fitdistrplus*’ package by Delignette-Muller and Dutang (2020) and ‘*extraDistr*’ package by Wolodzko (2020) in *R*.

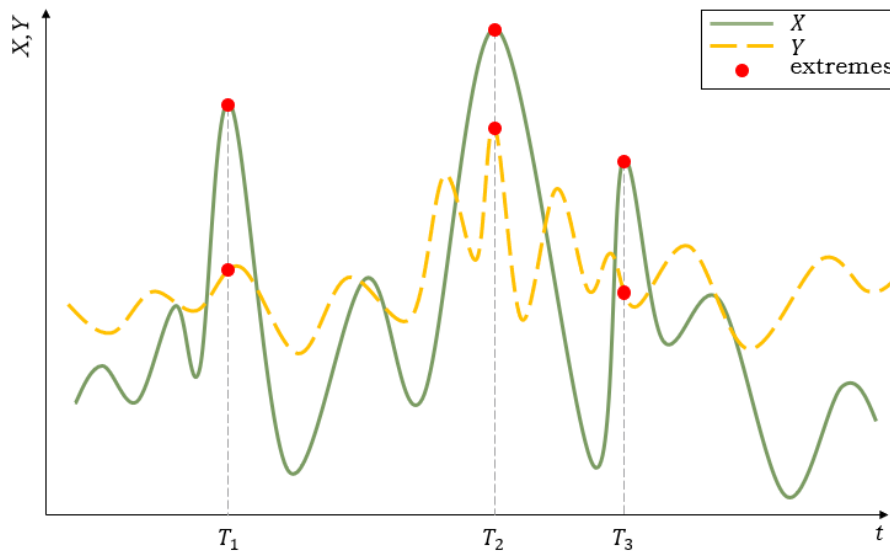


Figure 4.4: Selection of the concomitant variable Y at the coinciding times of the dominant variable X .

Several models are investigated to approximate the concomitants. These are the: Normal, Log-normal, Gamma, Weibull, GEV, Gumbel, GPD, Exponential and Rayleigh distributions. The AIC, BIC and R^2 values of the different models for the wave height and period are found in Table C.1 and for the wind speed and direction in Table C.2, in Appendix C. From these models, the six best-performing models in terms of R^2 are considered for further analysis. Their exceedance probabilities and CDF are plotted to investigate the tail behaviour and visualize the overall fit. For the concomitant variables wave height, wave period and wind speed, the most extreme values are of interest. Figure 4.5 shows the exceedance probabilities in logarithmic scale for the wave height H_s . A model is selected based on its performance of the goodness-of-fit criteria and exceedance probability and CDF plots. For the wave height, the Gamma model performs best for both the goodness-of-fit criteria, found in Table C.1, and in approximating the tail of the extremes. The GEV model provides similar results as the Gamma model. However, the Gamma model performs slightly better and thus is selected as the best model for the wave height. A similar procedure is performed for the wave period and wind speed. These results are found in Appendix C. The CDF plots of the applied models and the histogram of the selected models for the concomitants are also found in the appendix.

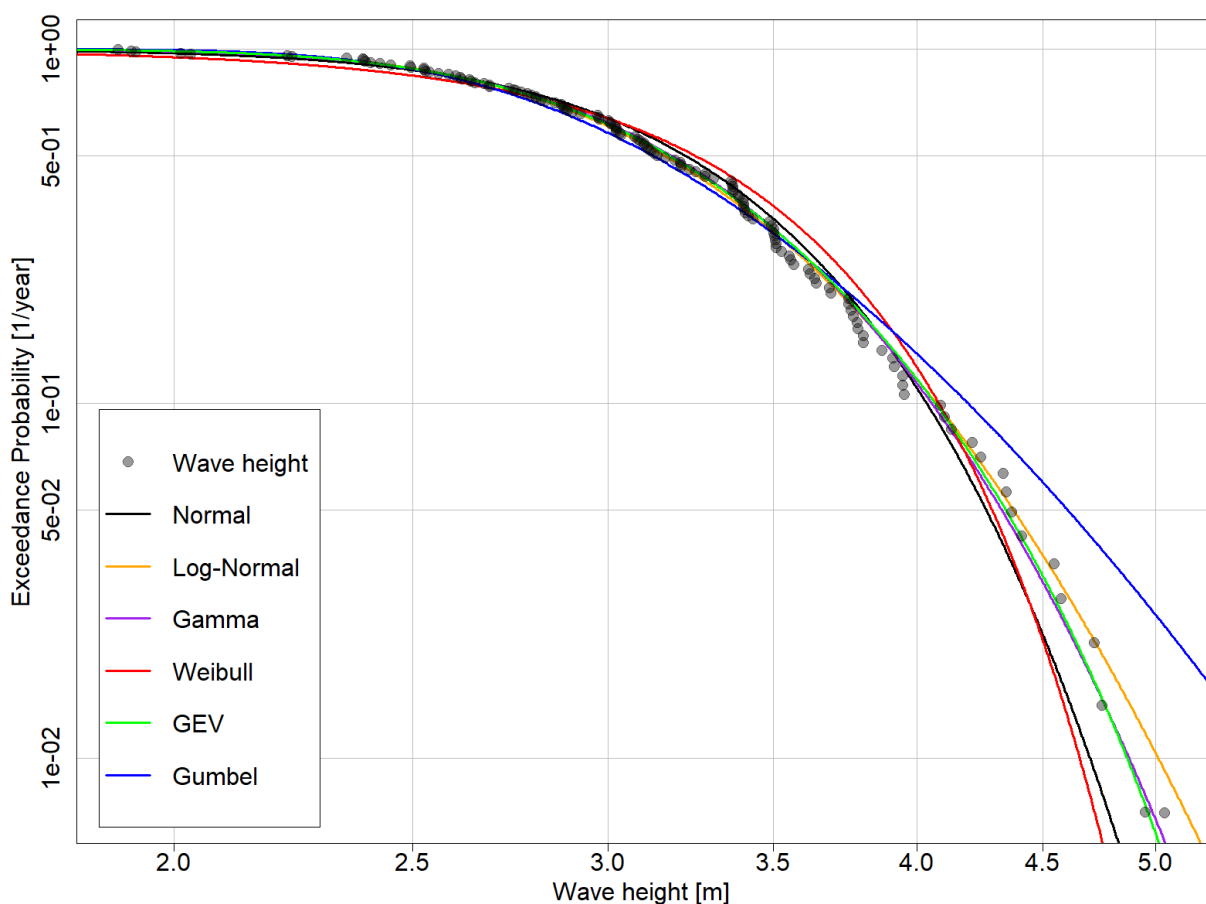


Figure 4.5: Exceedance probability $\mathbb{P}(H_s > x)$ of different models for wave height H_s .

For the wind direction w_d , the best model is selected based on the one that best approximates its entire range of values. The wind rose in Figure 4.6 shows the wind directions' respectable occurrence percentage and wind speeds in the 142 selected extreme events. To model the wind direction, the values are transformed to $[0,180]$ degrees. The coordinate system is rotated by 200 degrees clockwise. This way, all wind directions lie within $[0,180]$ degrees in the rotated system. Thus, the two most outer wind directions of 16° and 203° North are transformed to rotated wind directions of 176° and 3° , respectively. The wind direction is modelled using truncated models in the rotated domain for $[0,180]$ using the 'truncdist' package by Novomestky (2016). Truncated models are models in which the samples of the

modelled variable are truncated within certain ranges. In Figures C.3, C.4d and C.5d, the exceedance probabilities, CDF and histogram for the wind direction and the applied models are found. The plots and goodness-of-fit criteria show that the truncated Gumbel model best approximates the wind direction.

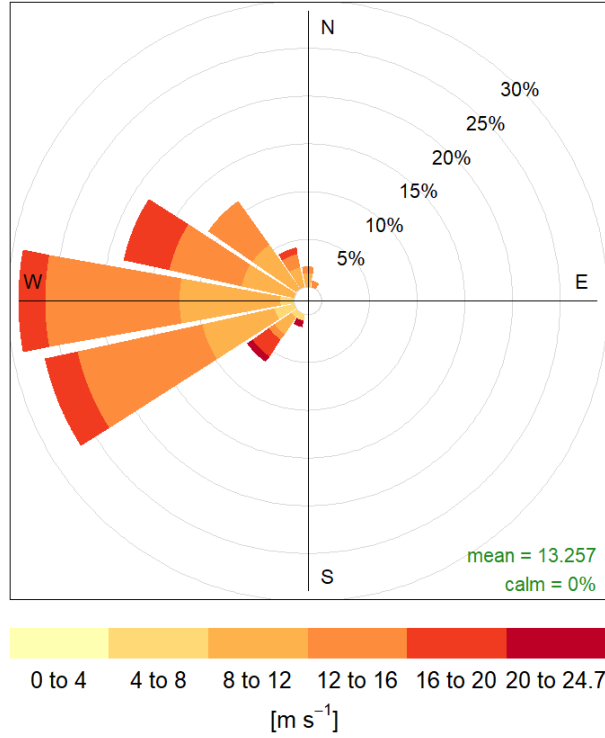


Figure 4.6: Wind rose of the selected extreme events.

In Table 4.2, the selected models and the model parameters are found for each concomitant variable. The wave height, wave period and wind speed will be modelled using a Gamma distribution and the wind direction using a truncated Gumbel distribution in the (rotated) domain of $[0,180]$ degrees.

Table 4.2: Estimated parameters of the selected concomitant models using MLE.

Concomitant	Model	Parameters [–]			
		Shape k	Rate θ	Location μ	Scale σ
Wave height H_s	Gamma	25.925	8.040	–	–
Wave period T_p	Gamma	62.276	7.682	–	–
Wind speed w_s	Gamma	18.855	1.422	–	–
Wind direction w_d	Truncated Gumbel	–	–	60.212	26.922

4.3 Application of Bivariate Copulae Modelling

In this section, it is investigated if the dependence structure of the variable pairs can be well-modelled by bivariate copulas. The modelling is performed using the ‘*copula*’ package by Maechler (2023) and ‘*VineCopula*’ package by Nagler (2023) in *R*. In order to fit the copula models to the variable pairs, first the global (Spearman’s) correlation between the variables is determined. Table 4.3 shows the correlation for all pairs. Pairs with a positive correlation can be modelled by the copula models or the survival models (rotated by 180 degrees). Pairs with a negative correlation can be modelled by rotating the copula models by 90 or 270 degrees.

Table 4.3: Spearman's r_S correlation for every variable pair.

r_S [-]	Water level h	Wave height H_s	Wave period T_p	Wind speed w_s	Wind direction w_d
h	1.000	0.559	0.540	0.318	0.179
H_s		1.000	0.762	0.309	0.459
T_p			1.000	0.025	0.370
w_s				1.000	-0.016
w_d					1.000

The data of the selected extreme events is transformed from variable space to unit space by the *pobs* function of the *copula* package. This function determines the so-called pseudo-observations based on the ranks of the variables (Maechler, 2023). Given n realizations $\mathbf{x}_i = (x_{i1}, \dots, x_{id})^T$ with $i \in \{1, \dots, n\}$ of a random variable X , the pseudo-observations u_{ij} are defined by Equation 4.13. Where, r_{ij} denotes the rank of x_{ij} among all x_{kj} with $k \in \{1, \dots, n\}$.

$$u_{ij} = \frac{r_{ij}}{n+1}, \text{ for } i \in \{1, \dots, n\} \text{ and } j \in \{1, \dots, d\} \quad (4.13)$$

Given the pseudo-observations of the 142 extreme events, multiple copulas are investigated to model the variable pairs. These are compared based on three criteria: the AIC, Cramér-Von Mises tests and the semi-correlations. The AIC estimates the relative goodness-of-fit criteria based on a trade-off between the goodness-of-fit for a certain model and its simplicity, as mentioned in Subsection 3.3.2. Equation 4.14 defines the AIC of a bivariate copula \mathbf{C} family with parameter(s) $\boldsymbol{\theta}$, in which u and v are the pseudo-observations of X and Y and k is the number of copula parameters (Akaike, 1974; Brechmann, 2010). A lower AIC corresponds to a greater fit.

$$AIC = -2 \sum_{i=1}^N \ln [\mathbf{C}(u_i, v_i | \boldsymbol{\theta})] + 2k \quad (4.14)$$

The Cramér-Von Mises (CM) tests indicate the deviation between the empirical copula and the fitted copula model. Equation 4.15 and 4.16 show the CM score, where R_i and S_i are the ranks associated with random samples X_i and Y_i (Salvadori et al., 2007). A low CM score indicates a small deviation between the empirical copula and the copula model. To validate the CM scores, the p -values of the CM tests are determined. A p -value is a statistical measurement to indicate the probability that the observed results can be produced by a model, assuming the null hypothesis is correct. The null hypothesis states that no statistical significance exists in a set of observations. Therefore, the lower the p -value, the greater the statistical significance of the CM scores. A p -value of 0.05 or lower is generally considered statistically significant. Using the *VineCopula* package, the CM scores are based on Kendall's process proposed by Wang and Wells (2000). The p -values are computed using the parametric bootstrap described by Genest et al. (2006). The CM score can be calculated for a limited number of copula models using the *VineCopula* package. Therefore, the following copula families are considered in this bivariate analysis: Gaussian, Clayton, Gumbel, Frank and Joe (including all rotations of the copula families).

$$CM_n = n \sum_{i=1}^n \left\{ C_n\left(\frac{R_i}{n+1}, \frac{S_i}{n+1}\right) - C_{\theta_n}\left(\frac{R_i}{n+1}, \frac{S_i}{n+1}\right) \right\}^2 \quad (4.15)$$

with

$$C_n(u, v) = \frac{1}{n} \sum_{i=1}^n 1\left(\frac{R_i}{n+1} \leq u, \frac{S_i}{n+1} \leq v\right) \quad (4.16)$$

The semi-correlations are the Pearson's ρ_P correlations in each quadrant (UL, UR, LL, LR). The semi-correlations of the empirical data are determined by transforming the pseudo-observations of the variables into standard normal (a Normal distribution with a mean of $\mu = 0$ and a standard deviation of $\sigma = 1$). Using Pearson's ρ_P , the correlation in each quadrant can be determined. To determine the semi-correlations of the copula models, 6000 samples are taken from each model. Using the *rcorr* function from the '*Hmisc*' package by Harrell Jr. (2023), the p -values of the semi-correlations are calculated. In

Table 4.4, the results of the AIC, CM scores and semi-correlations are shown for the variable pair water level h and wave height H_s . The quadrants that are of most importance are the quadrants with the largest correlation and low p -values, showing the tail dependence of the pairs. For this application, low p -values are considered p -values in the order of $p < 0.05$. The important quadrants are shown in bold green. The semi-correlations of the model that performs best for those quadrants are also shown in bold green, as are the best performances for the CM and AIC values. In Appendix D, the tables are found for the other variable pairs.

Table 4.4: AIC, CM scores and semi-correlations for the pair water level h and wave height H_s .

Criteria [–]	Empirical h & H_s	Gaussian	Survival Clayton	Gumbel	Frank	Joe
r_{UL}	0.249	0.181	0.077	0.025	0.077	0.082
r_{UR}	0.685	0.336	0.660	0.592	0.201	0.714
r_{LL}	0.012	0.399	0.111	0.247	0.224	0.097
r_{LR}	0.068	0.142	0.102	0.062	0.054	0.013
p_{UL}	0.251	0	0.024	0.455	0.020	0.013
p_{UR}	0	0	0	0	0	0
p_{LL}	0.935	0	0	0	0	0
p_{LR}	0.758	0	0.003	0.059	0.110	0.692
CM	–	0.207	0.030	0.079	0.146	2.749
PCM	–	0.010	0.990	0.400	0.040	0.360
AIC	–	–55.56	–74.76	–68.89	–50.02	–74.44

The table shows that the UR quadrant is of the largest significance for the water level and wave height, suggesting upper tail dependence. This upper tail dependence is best approximated by the Survival Clayton model. It also shows that the semi-correlations, the CM and AIC values do not necessarily result in the same best copula model. Furthermore, the lowest CM score does not have to correspond to the lowest p -value. In this case, the best CM scores are for the Survival Clayton copula. However, the p -values show that the CM score is of low statistical importance. Therefore, the Gaussian model performs better solely by looking at CM scores. In the selection of the best bivariate copula models, a comparison between the three criteria is taken into consideration, respecting the p -values of the semi-correlations and CM values. For the variable pair h & H_s , the Survival Clayton is selected as the best copula model. The semi-correlations of the selected Survival Clayton model and the empirical data are shown in Figure 4.7.

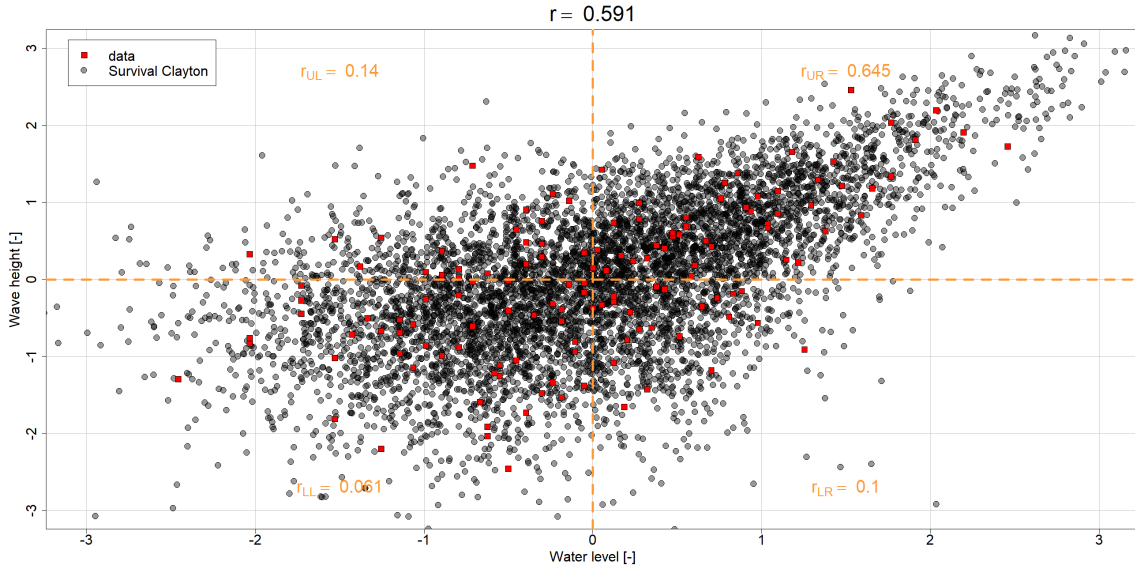


Figure 4.7: Semi-correlation of the Survival Clayton model for water level h and wave height H_s .

In Figure 4.8, the CDF of the selected Survival Clayton and the empirical copula are shown for the water level and wave height. The plot shows the cumulative probability of the Survival Clayton by a colour scale ranging from red to yellow (from 0 to 1). The plot shows that the model and the empirical copula have a decent fit, as the model approximates the black lines adequately.

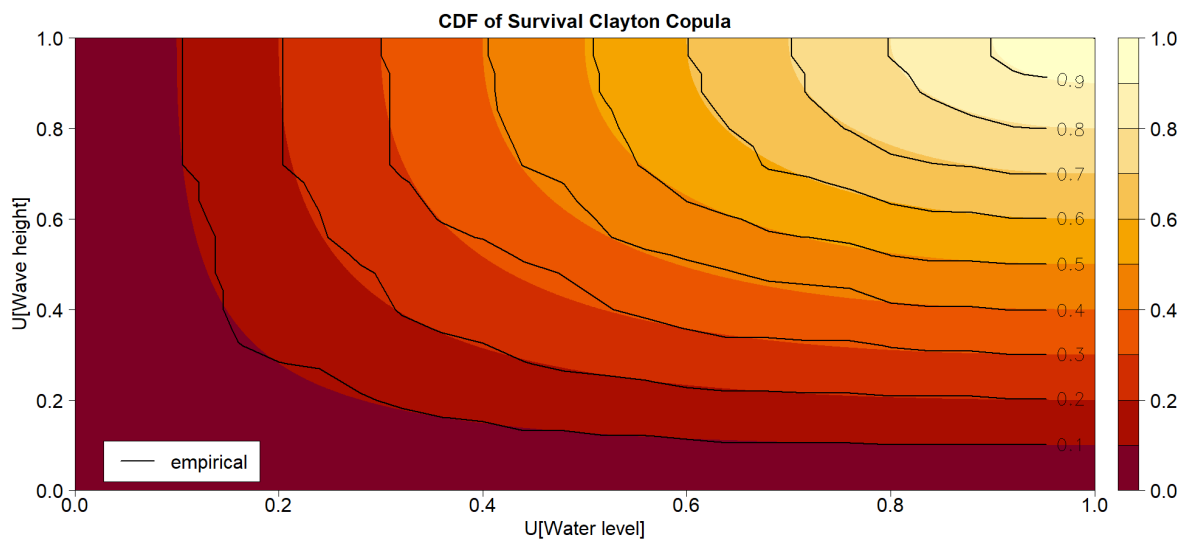


Figure 4.8: CDF of the Survival Clayton and empirical copula for water level h and wave height H_s .

The samples from the Survival Clayton in unity space are depicted in Figure 4.9. The samples show the underlying dependence structure of the variable pair. The figure shows that a large part of the samples are found in the upper tail, indicating the upper tail dependency between the water level and wave height.

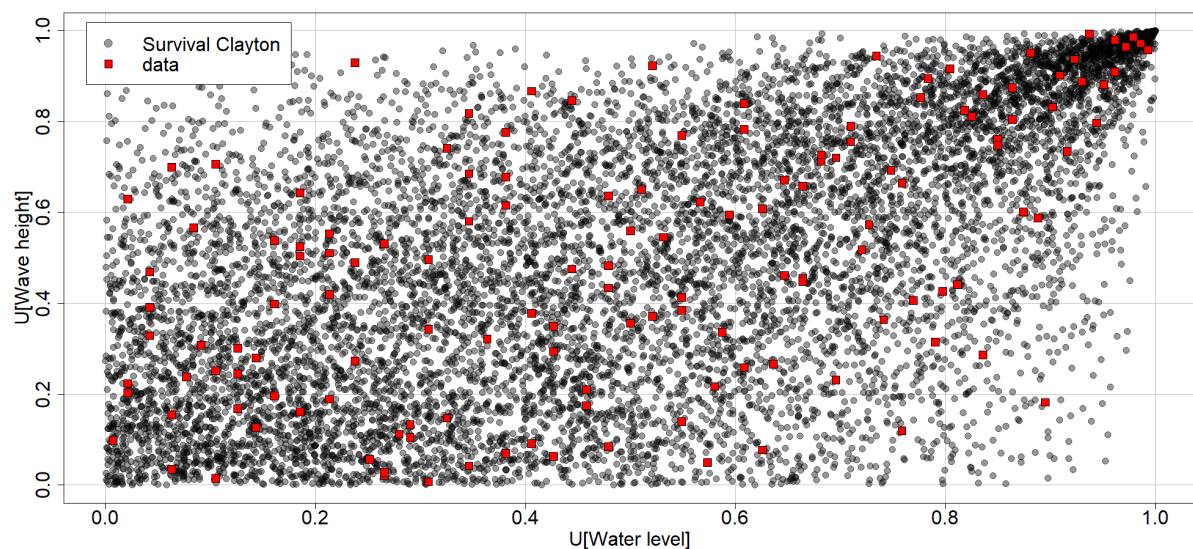


Figure 4.9: Samples of Survival Clayton in $[0, 1]^2$ for water level h and wave height H_s .

The samples from Figure 4.9 can be transformed into variable space to result in Figure 4.10. This is done by substituting the samples into the quantile (inverse of the marginal) distribution of the variables. In the figure, the samples of the water levels are substituted into the stationary GPD and the wave heights into the Gamma distribution.

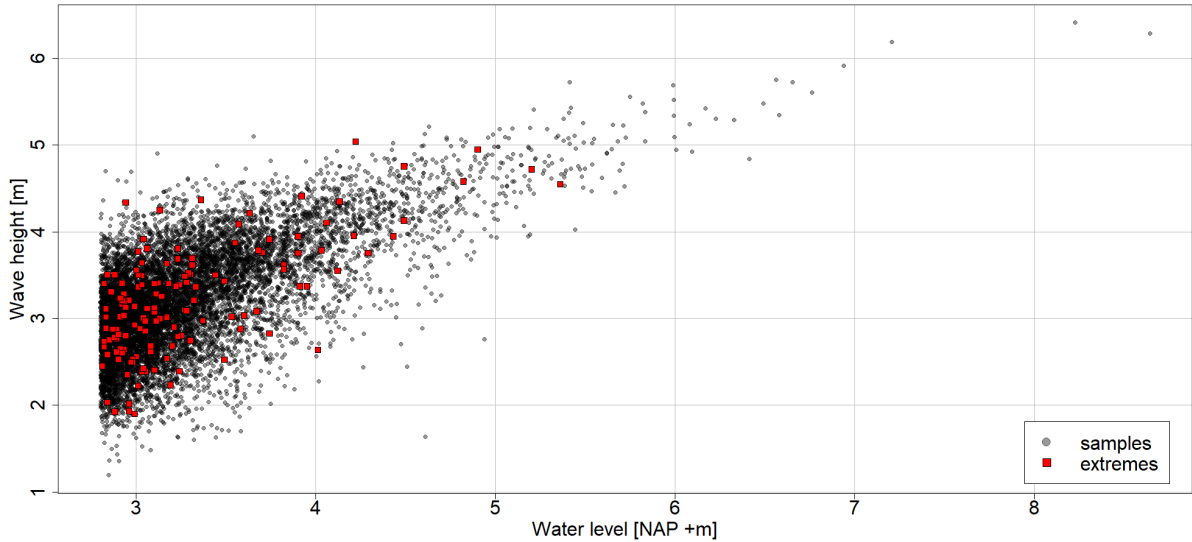


Figure 4.10: Samples of Survival Clayton in variable space for water level h and wave height H_s .

Appendix D includes the results for a similar bivariate analysis for the other variable pairs. In Table 4.5, the results of the analysis are shown. The selected models and the copula parameters θ are shown in the table for each variable pair. This analysis included a selection of the copula families: Gaussian, Clayton, Gumbel, Frank and Joe (and the rotated families). From the analysis can be concluded that the joint probability of the variable pairs can be well-modelled by bivariate copulas. Therefore, the multivariate dependence structure can be modelled by a vine copula structure, as performed in Section 4.5. The insights from the analysis can be used to validate the modelled vine copulae. In addition, the copula families that best represent the variable pairs are not only Gaussian. If this would be the case, other approaches could be of interest for modelling the joint distribution, such as Bayesian Networks (Couasnon et al., 2018).

Table 4.5: The selected bivariate copulas and copula parameter θ for every variable pair.

Copula	Water level h	Wave height H_s	Wave period T_p	Wind speed w_s	Wind direction w_d
h	–	Survival Clayton $\theta = 1.370$	Gumbel $\theta = 1.620$	Frank $\theta = 1.983$	Independent
H_s		–	Survival Gumbel $\theta = 2.471$	Gaussian $\theta = 0.325$	Survival Gumbel $\theta = 1.425$
T_p			–	Independent	Gaussian $\theta = 0.374$
w_s				–	Joe rotated 90° $\theta = -1.163$
w_d					–

4.4 Application of Non-stationary marginals in Copula modelling

In this section, the first research question is concluded. This section aims to apply the non-stationary marginal distribution of the water level into copula modelling. Subsection 4.4.1 introduces the proposed algorithm that is used. Subsection 4.4.2 goes over the findings of the applied approach and Subsection 4.4.3 provides the conclusion and remarks.

4.4.1 Proposed Algorithm

Chapter 3 showed that the non-stationary GPD, with the wave height as the covariate of the scale parameter, was deemed the best model to approximate the extreme water levels. This model is presented in Equation 4.17. The equation shows the relation between the model parameter $\sigma(H_s)$ and the design values of the wave height H_s .

$$H_{u,\sigma_{H_s}}(y, H_s) = 1 - \left(1 + \frac{\xi \cdot y}{\sigma(H_s)}\right)^{-1/\xi} \quad (4.17)$$

with $0 \leq y \leq -\frac{\sigma(H_s)}{\xi}$ for $\xi = -0.257$, where $y = x - u = x - 2.8[m]$

and $\sigma(H_s) = \sigma_1 \cdot H_s + \sigma_0 = 0.346H_s - 0.546$, for $\sigma(H_s) > 0$

The aim is to combine this model with the bivariate copula of the water level and wave height, to result in design values for the water level. The bivariate copula, of the water level and wave height, expresses the joint probability of the two variables in unity space. In Section 4.3, this bivariate copula is fitted based on the selected extremes resulting from the POT method. The Survival Clayton copula, with a parameter of $\theta = 1.370$, resulted in the best fit for the joint density function of the water level and wave height. Using this copula, the joint probabilities can be sampled and transformed into design values using the inverse of the marginal distributions (quantile functions) of the water level and wave height.

For the stationary marginal (Gamma distribution) of the wave height, the sampled joint probabilities can directly be transformed into variable space using the quantile function. However, for the non-stationary marginal of the water level first, the transformed values of the wave height must be known before the scale parameter can be determined. The following steps describe the applied method.

Algorithm 4.1: Transforming copula samples into variable space using non-stationary marginals

Step 1: Take n samples from the Survival Clayton copula to obtain the joint probabilities of the water level and wave height.

Step 2: Transform the n joint probabilities of the (Gamma distributed) wave height into variable space $H_s = \{H_{s,1}, H_{s,2}, \dots, H_{s,n}\}$ using its quantile function.

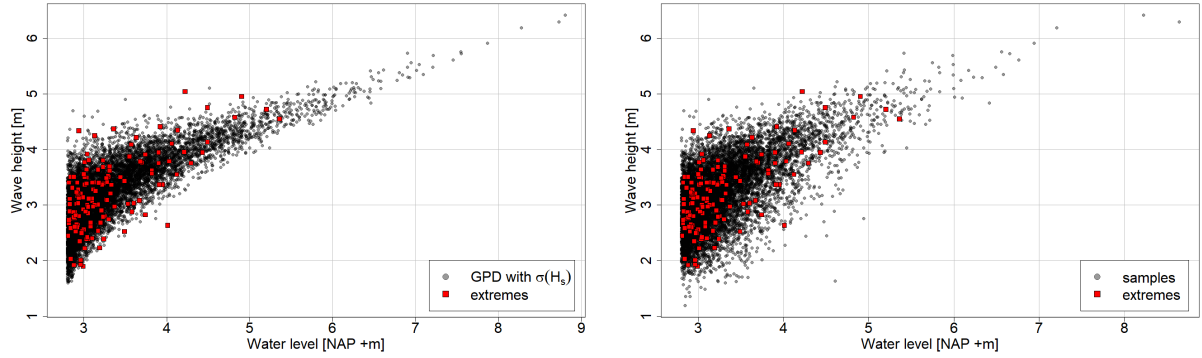
Step 3: Use the transformed wave height values H_s to determine n scale parameters $\sigma = \{\sigma_1, \sigma_2, \dots, \sigma_n\}$, resulting in a scale parameter value σ_i for every sample $H_{s,i}$ taken.

Step 4: From σ , each scale parameter value σ_i is used to derive a (stationary) GPD. This results in a list of GPD models corresponding to each sample $H_{u,\sigma_i}(y, H_{s,i})$ from Equation 4.17.

Step 5: Each sampled joint probability of the water level from Step 1, can be transformed into variable space using the quantile function of the corresponding $H_{u,\sigma_i}(y, H_{s,i})$ from Step 4.

4.4.2 Findings from the application

Using the proposed method, 10,000 samples are taken from the bivariate Survival Clayton copula and are transformed into the variable space for the water level. In Figure 4.11 the results are found for both the transformation using a non-stationary and stationary marginal distribution for the water level. In red, the original extremes are plotted. Comparing the two plots suggests that the application of the non-stationary marginal results in a more correlated combination of water levels and wave heights. For the stationary marginal the samples seem to be more spread out.



(a) Non-stationary GPD with $\sigma(H_s)$ for the water level (b) Stationary GPD for the water level

Figure 4.11: The results of transforming the copula samples of the water level and wave height into variable space using a non-stationary (left) and stationary (right) marginal for the water level.

The original extremes have a $r_S = 0.57$. This correlation is reproduced by the Survival Clayton copula, ensuring its dependence structure. The correlation is not affected by the transformation of the copula samples to variable space when using the stationary GPD for the water level. However, the transformation of copula samples into variable space using the non-stationary GPD does affect the correlation between the samples. The correlation of the transformed samples changed significantly to $r_S = 0.75$. Therefore, the dependence structure of the marginals is not preserved.

This phenomenon is further investigated here. Figure 4.12 shows the original extreme values and the Survival Clayton copula samples in unity space. From the original extremes, point 1 is selected. Regarding point 1, two areas are identified, these are shown by the orange marked planes. In the unity space, a larger value in $[0,1]$ corresponds to a larger value in the variable space and vice versa. Therefore, the upper left plane contains data and samples that correspond to larger wave heights and smaller water levels compared to point 1. The lower right plane contains data and extremes with lower wave heights but larger water levels compared to point 1. Since the model parameter $\sigma(H_s)$ is related to the wave height value (see Equation 4.17), a change in wave height results in a changed scale parameter and thus affects the transformed water level. A hypothesis is formed:

The change in correlation is caused by a change in the ranks of the samples, due to the low (or large) wave heights forcing low (or large) water levels.

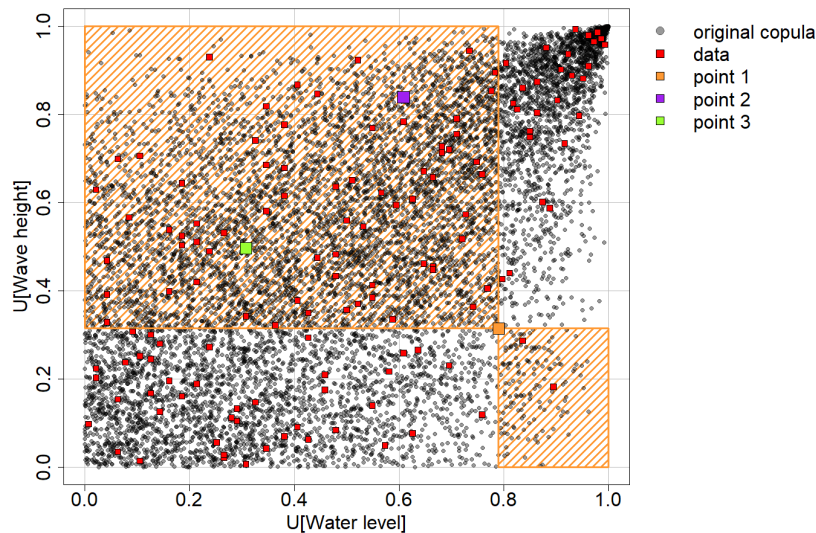


Figure 4.12: Original extreme values and Survival Copula samples in unity space. Three extremes are selected resulting in points 1, 2 and 3. The orange planes show the trouble areas for point 1.

The hypothesis states that the wave height could cause an increase in the water level rank of a point in the upper left area, such that it exceeds point 1. Likewise, the water level rank of a point in the lower right area could decrease to one below point 1. The lower left and upper right areas are not of interest when looking at point 1, as a lower (or larger) wave height than point 1 cannot result in a larger (or lower) water level compared to point 1.

To investigate the hypothesis with regard to point 1, points 2 and 3 are selected from the original extreme events. The points are chosen such that the ranks of the water levels of the original extremes are sorted by: $R_3 < R_2 < R_1$, where R_i is the water level rank of extreme i . Both points 2 and 3 lie in the upper left area. For point 2, the wave height is significantly larger than that of point 1 and the water level is slightly lower. For point 3, the water level is significantly lower than that of point 1 and the wave height is around 10% larger. The three points are transformed according to the algorithm proposed in Subsection 4.4.1. As stated in the algorithm, since each point has a different wave height, the scale parameters are also different. Therefore, each point has its own GPD.

In Figure 4.13, the exceedance probabilities are shown for the resulting GPD models for points 1, 2 and 3 and the original extremes of the points. It shows that the larger modelled scale parameter of point 2 results in a significantly larger transformed water level compared to its original point. For point 1, the smaller scale parameter results in a significant reduction of the original water level, resulting in a lower transformed water level than point 2. Thus, the ranks are not preserved ($R_3 < R_1 < R_2$). For point 3 the water level happens to stay approximately similar. The relation between wave height and water level shows that an event with a relatively low wave height will be modelled using a lower scale parameter compared to an event with a larger wave height. As Figure 4.13 shows, a GPD with a lower scale parameter will result in a lower water level for a constant exceedance probability. Hence, introducing a non-stationary marginal distribution, with the wave height as the covariate, in copula modelling can result in changing the ranks of the original copula samples, as with points 1 and 2.

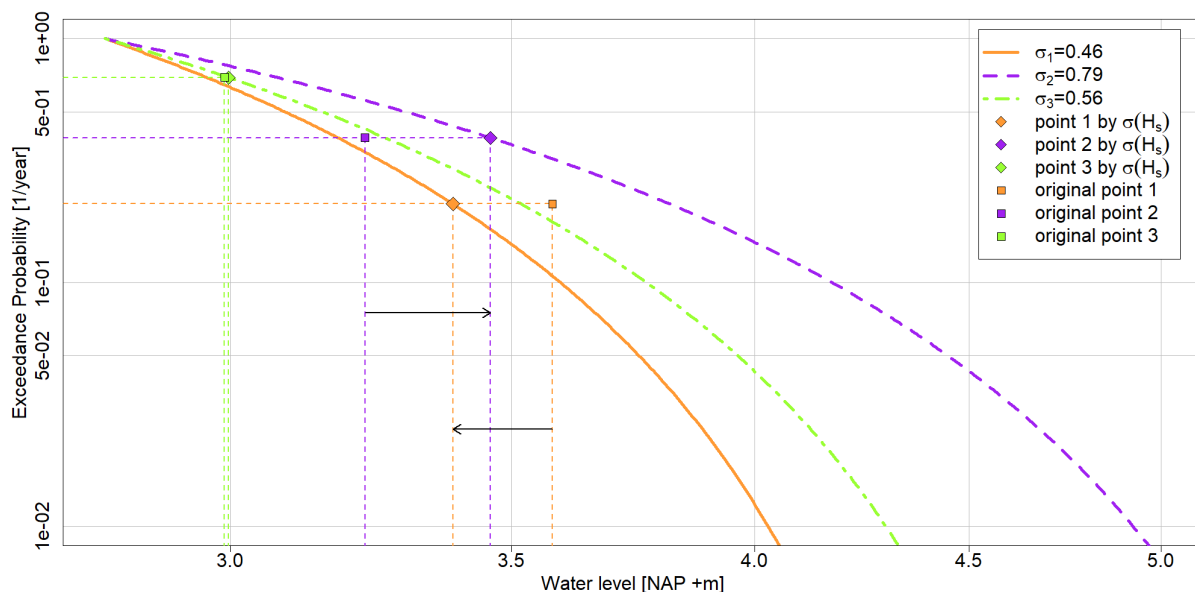


Figure 4.13: Exceedance probabilities of the original and transformed points 1, 2 and 3.

The transformed water level and wave height from variable space back into unity space are shown in Figure 4.14. From the figure, it is clear that the non-stationary model with the wave height as the covariate affects the correlation and thus does not preserve the dependence structure of the copula. Wave height as the covariate of the non-stationary model and as a variable in the bivariate copula, results in large wave heights forcing larger water levels and low wave heights forcing lower water levels, increasing the correlation.

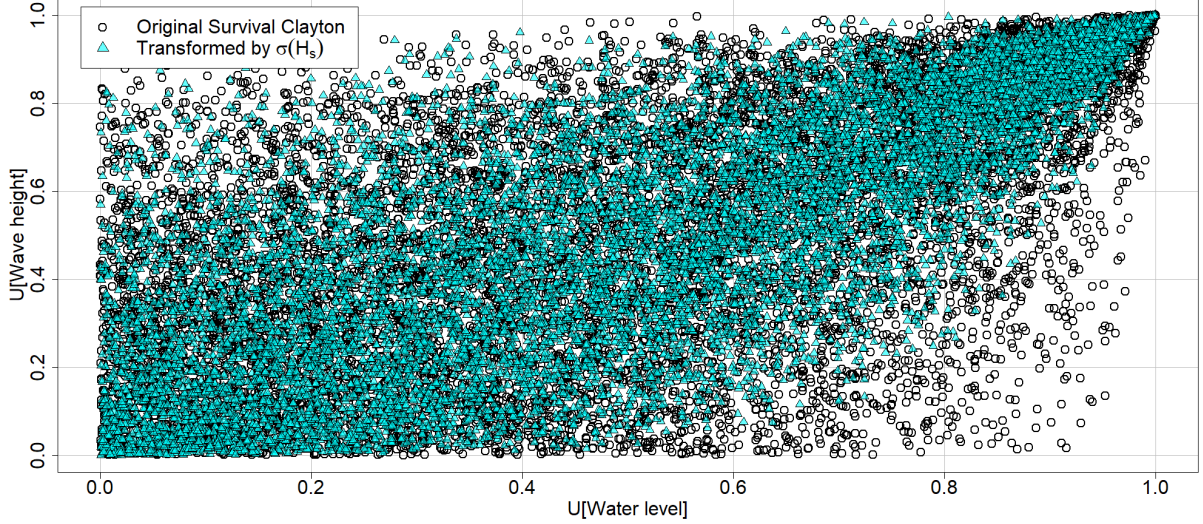


Figure 4.14: Transformation of variable space back into copula space. Showing the original samples for the Survival Clayton copula and the transformation by the non-stationary model.

In Table 4.6, the values of the original and transformed points 1, 2 and 3 are found. It shows the change in ranks of the transformed water level to $R_3 < R_1 < R_2$. In Appendix E, additional results of the analysis are found, e.g. the change in the copula family.

Table 4.6: The original and transformed wave height H_s and water level h values for points 1, 2 and 3.

Points	Original				Transformed by $\sigma(H_s)$				Scale $\sigma(H_s)$ [-]
	U[H_s] [-]	H_s [m]	U[h] [NAP +m]	h [-]	U[H_s] [-]	H_s [m]	U[h] [NAP +m]	h [-]	
Point 1	0.315	2.88	0.790	3.58	0.315	2.89	0.664	3.39	0.460
Point 2	0.839	3.81	0.608	3.23	0.839	3.85	0.727	3.46	0.794
Point 3	0.497	3.14	0.308	2.99	0.497	3.18	0.357	3.00	0.561

4.4.3 Conclusion and Remarks

Based on the findings of the applied method, the non-stationary marginal distribution of the water level with the wave height as covariate cannot be combined with copula modelling. In order to preserve the dependence structure built by the copula, the transformation from copula space to variable space must be increasingly monotonic. A monotonic transformation preserves the ranks of the variables and therefore the copula. The use of the non-stationary model results that the transformation of the samples depends on the covariate. Therefore, a different transformation is applied to each sample, changing the ranks of the variable modelled by the non-stationary marginal. This finding resulted in creating Lemma 4.1.

Lemma 4.1. (Copula modelling with a Non-stationary marginal and a node as covariate).
Consider $F_{X,y}$ with covariate y , in which y is a node of the copula, as the non-stationary marginal distribution and F_Y as the (stationary) marginal distribution of the random variables X and Y , respectively. Let $C(u,v)$ be the copula describing the joint distribution function F_{XY} of the two random variables X and Y , in which $F_{X,y}(x) = u$ and $F_Y(y) = v$. Then, the transformations of X or Y are not increasingly monotonic, implying that the dependence structure is not preserved, as stated in Equation 4.18.

$$F_{XY}\left(F_{X,y}^{[-1]}(u), F_Y^{[-1]}(v)\right) \neq C(u, v), \quad (4.18)$$

for any $(u, v) \in \mathbb{I}^2$. Where, $F_{X,y}^{[-1]}$ and $F_Y^{[-1]}$ denote, respectively, the quasi-inverses of $F_{X,y}$ and F_Y .

The conclusion that the non-stationary marginal in which the wave height is the covariate cannot be combined with copula modelling, results in the use of a stationary GPD to approximate the water level.

This has several consequences for the analysis. First of all, Section 3.4 showed that the non-stationary model performed better in modelling the water level compared to the stationary model. Figure E.3 shows that the non-stationary model provides larger water levels for the larger ranks between ranks 7,000-10,000. Therefore, the use of a stationary GPD might underestimate the water level for the largest extremes up to around 0.2 meters compared to the non-stationary model. Nevertheless, the stationary GPD from Subsection 3.3.2 will be used in the vine copula modelling.

Coles et al. (2001) showed that a non-stationary model with time as the covariate could be used in copula modelling. In such a case, the copula is built on observations based on the non-stationary transformation to unity space. This differs from the proposed method in Subsection 4.4.1, where the copula is built on the observations based on the empirical CDF of water level and wave height. Such a non-stationary transformation to unity space would be possible for the covariate time. The transformation standardizes the data conditioned on the fitted parameters of an estimation model, such as the GPD. As shown by Coles et al. (2001), in the case of a GPD, $u(t)$ is a set of thresholds that are possibly time-varying, leading to the threshold excesses y_{t_1}, \dots, y_{t_k} . The estimated model is in the general form of,

$$Y_t \sim GPD(\hat{\sigma}(t), \hat{\xi}(t)).$$

As the exponential distribution is a special case of the GPD family with $\xi \rightarrow 0$, a transformation is applied to a standard exponential distribution, resulting in the standardized variable \tilde{Y}_t :

$$\tilde{Y}_t = \frac{1}{\hat{\xi}(t)} \log \left\{ 1 + \hat{\xi}(t) \left(\frac{Y_{t_k} - u_t}{\hat{\sigma}(t)} \right) \right\}.$$

The ordered values of the observed \tilde{Y}_{t_j} by $y_{\tilde{(1)}}, \dots, y_{\tilde{(k)}}$, it follows that the probability plot is formed by the pairs:

$$\{(i/(k+1), 1 - \exp(-y_{\tilde{(i)}})); i = 1, \dots, k\}$$

In this thesis, the non-stationarity of the water level with time as the covariate is not accounted for by non-stationary copulae. As Section 3.4 showed, the non-stationary model with time as covariate did not show any statistically significant trend of the extreme water level in time. Furthermore, the historical trend of SLR may not represent the future SLR trend. As shown in Figure 2.9, the future SLR trend is largely dependent on different emission scenarios. The assumed future SLR scenario in a hydraulic structure design should be based on future projections. Therefore, this thesis relies on samples based on stationary copula modelling and adds SLR to the sampled extreme water levels afterwards.

4.5 Vine Copula modelling

The results in Section 4.3 showed that the variable pairs can be well-modelled through bivariate copulae. The set of selected copulas that resulted in the best fit contained multiple families. This section involves modelling the multivariate distribution of the five variables using vine copulae. In Subsection 4.5.1, a Brute Force procedure is applied to find the best fitting vine copula. Subsection 4.5.2 compares the results from the Brute Force method with the Maximum Spanning Tree algorithm by Dissmann et al. (2013). The results of Subsection 4.5.1 are validated in Subsection 4.5.3. The vine copulae will be modelled using the ‘*VineCopula*’ package by Nagler (2023) in *R*.

4.5.1 Selecting Vine Copulae by a Brute Force procedure

As this thesis considers five variables, there are a total of 480 possible unique regular vines that can be fitted, as shown in Table 4.1. A Brute Force approach is a method that relies on sheer computational power by calculating every possibility to solve the problem. As the computational time is manageable for 480 unique regular vines, a Brute Force approach is preferred. The Brute Force method does not make any sacrifices to improve efficiency as it goes over all possibilities. Therefore, this method results in the vine structure that best approximates (based on the selected goodness-of-fit criteria) the variables, as it is included in the computations. The vine structures can be written as matrices, as shown in Morales-Nápoles et al. (2010). A catalogue of the 480 unique matrices from Morales-Nápoles et al. (2023) is fitted for three procedures. Each procedure accounts for different copula families that can be allocated

as the bivariate copulae C_e to the edges e in the union $E(\mathcal{V})$ of the vine. Procedure 1 accounts for the copula families that were selected as the best copula models in Section 4.3, excluding independence. In Procedure 2, also independence is considered. For Procedure 3, all possible copulae families, including rotations and independence, in the *VineCopula* package are considered. The copula families for the procedures are listed below.

Procedure 1: Gaussian, Clayton, Survival Clayton, Gumbel, Survival Gumbel, Frank and Joe rotated by 90°

Procedure 2: Independence, Gaussian, Clayton, Survival Clayton, Gumbel, Survival Gumbel, Frank and Joe rotated by 90°

Procedure 3: Independence, Gaussian, Student-T, Gaussian, Clayton, Gumbel, Frank, Joe, BB1, BB6, BB7, BB8, Tawn Type I, Tawn Type II and all rotations of the listed copula families

The vine copula selection is based here on the AIC. The AIC is commonly used as a goodness-of-fit measure and is therefore selected as the one to select the best regular vines. The drawback of the AIC is that it does not allow for statistical significance, such as p -values corresponding to statistical goodness-of-fit tests. Goodness-of-fit criteria for multivariate cases are not yet widely accepted. There is a lack of suitable goodness-of-fit criteria for regular vine copulae. Several goodness-of-fit tests based on the information matrix equality of White (1982), first proposed by Huang and Prokhorov (2014) for copulae, have been worked out by Schepsmeier (2019) for regular vine copulae. These tests are also included in the *VineCopula* package. However, the proposed tests showed poor performance for small sample sizes (smaller than 10,000 for 5 nodes) (Schepsmeier, 2019). Therefore, the AIC is preferred for the basis of the best-fit vine copula.

In Table 4.7, the minimum and maximum AIC values are shown of the vine copulas for the three procedures. A lower AIC provides a greater fit, therefore the vine copula with the lowest AIC is selected as the best vine copula. The table shows that the best vine copula in Procedures 1 and 2 perform similarly. Procedure 3, which includes all possible copula families and rotations, performs best and has a significantly lower AIC score.

Table 4.7: The minimum and maximum AIC values for the three procedures of the Brute Force method and the p_i percentile and AIC of the Maximum Spanning Tree algorithm.

Procedure	Brute Force		MST Algorithm	
	min(AIC) [-]	max(AIC) [-]	AIC [-]	p_i [%]
Procedure 1	-319.05	-261.82	-292.66	62.50
Procedure 2	-319.77	-259.04	-275.69	94.17
Procedure 3	-355.77	-286.26	-323.10	49.58

The vine copulas with the best AIC scores from the three procedures are found in Appendix F. Each procedure resulted in a different vine structure. The analysis in Section 4.3 is conducted by a limited selection of copula families. There could be other families that perform better in approximating the dependence structure of the variable pairs, which are included in Procedure 3. This could be the reason for the different vine structures. In Appendix F, the (conditional) copulas for each vine copula are found. The vine copula from Procedure 3 is selected as the best vine copula to approximate the variables. This vine copula is a C-vine with the water level as the central node.

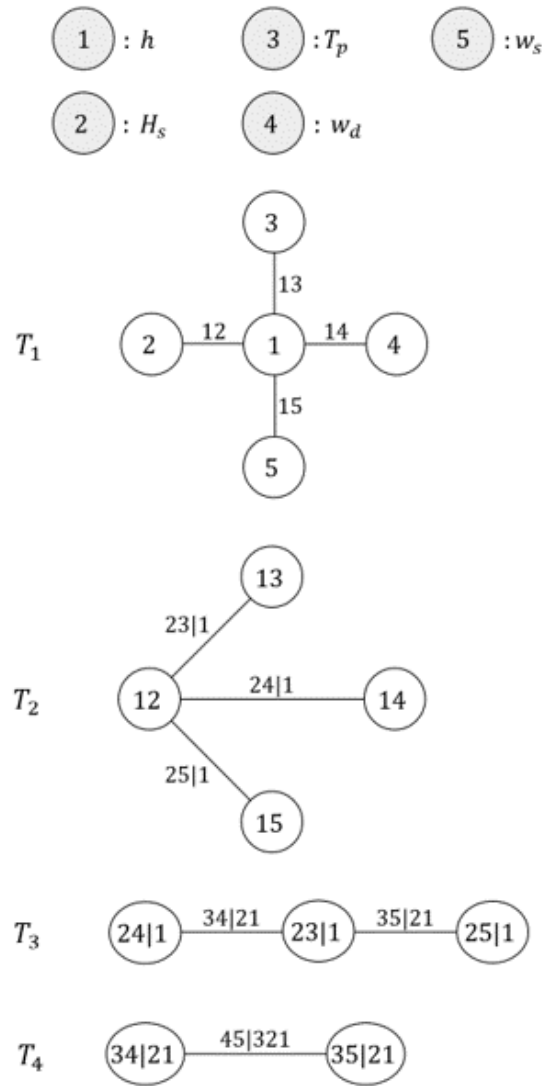


Figure 4.15: The best-performing vine copula based on AIC from Procedure 3. The vine is a C-vine with the water level as the central node.

4.5.2 Performance of the Maximum Spanning Tree Algorithm

The *VineCopula* package contains the function *RVineStructureSelect* that uses a Maximum Spanning Tree (MST) algorithm to significantly reduce computational time by optimising the edges of each tree. The MST algorithm based on Kendall's τ_K is introduced by Dissmann et al. (2013). The performance of the algorithm is investigated in order to check whether it could be a respected tool to use in the selection of a vine copula in a significantly reduced computational time.

The algorithm is used for the three procedures described in Subsection 4.5.1. The performance of the algorithm is based on its AIC value. Table 4.7 shows the percentile p_i and AIC values of the algorithm for all procedures. It shows that the algorithm performs poorly. The best performance of the algorithm is the 49.6% percentile for Procedure 3. This result shows that 49.6% (or 238/480) of the possible vines provide a better AIC value. The performance is visualized in Figure 4.16 using the CDF plot. Note, a lower AIC provides a greater fit. For Procedure 2 the algorithm performs very poorly as 94.2% of the possible vines perform better than the vine selected by the algorithm.

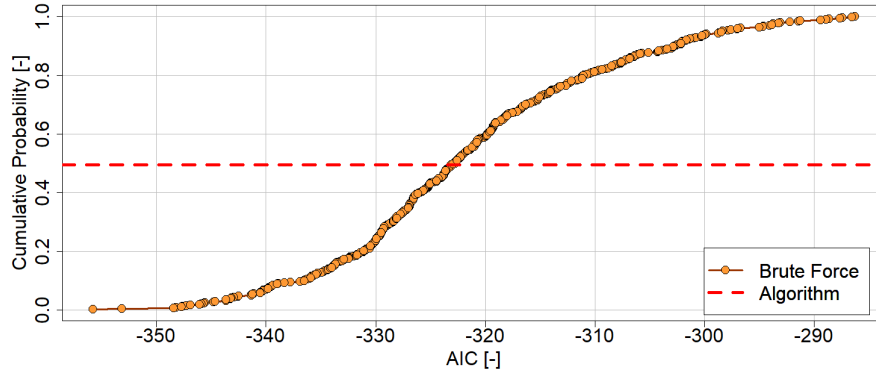


Figure 4.16: CDF of the performance of the MST algorithm versus Brute Force fitting for Procedure 3.

In Appendix F, the vine copulas selected by the algorithm can be found. It shows that the algorithm provides different vine structures compared to the best-performing vines from Procedures 1, 2 and 3. The vines selected by the algorithm are all C-vines with the wave period as the central node and are not tree-equivalent. This concludes that the use of the MST algorithm should be taken with care as the performance of the algorithm should be questioned.

4.5.3 Vine Copula Validation

From Procedure 3, there is one vine copula that provides a similar AIC (-353.16) to the best-performing vine copula (-355.77). This vine copula is found in Appendix F and is also further investigated here. To validate the output of the vines, the predicted versus the empirical exceedance probabilities for the 142 observed extremes are plotted in Figure 4.17. The closer the predicted and empirical exceedance probabilities for the observed extremes are, the closer the points follow the one-one line. The figure shows that the goodness-of-fit of the best-performing vine (vine copula 3) is greater than that of the second best-fitting vine (vine copula 3.2). The area of largest interest is that of the lower exceedance probabilities, as these correspond to the greatest storms. Figure 4.17 shows that the predicted exceedance probabilities by vine copula 3 are closer to the one-one line, especially for the lower exceedance probabilities. Therefore, the best-performing vine, vine copula 3 from Figure 4.15, is selected to model the design variables.

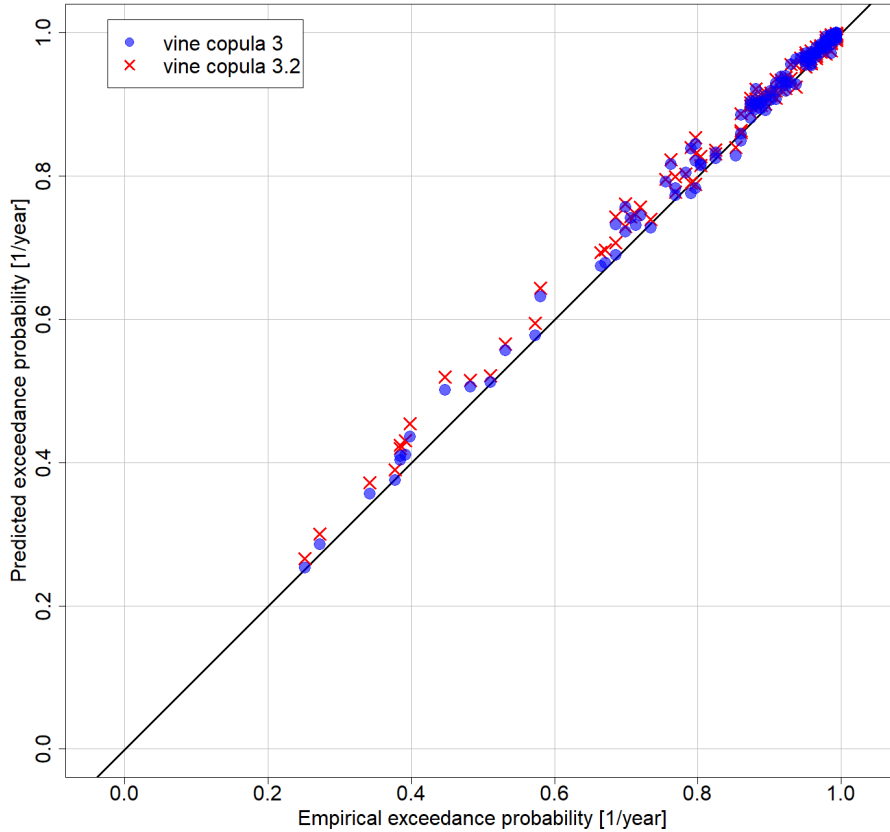


Figure 4.17: The predicted against empirical exceedance probabilities of the observations $\mathbb{P}(h > x \cap H_s > x \cap T_p > x \cap w_s > x \cap w_d > x)$ for the two best-fitting vine copulas from Procedure 3.

4.6 Conclusions of the Multivariate Modelling

The five design variables are modelled by vine copulas. Vine copulas capture the multivariate dependence structure by combining regular vines with bivariate copulae. In Section 4.3, the bivariate analysis showed that the variable pairs could be well-modelled by bivariate copulae. The analysis resulted in the copula families that best fit the variable pairs and provided insights for the vine copula modelling. The vine copula modelling was performed using a Brute Force procedure. A catalogue of the 480 unique matrices from Morales-Nápoles et al. (2023) was fitted for three procedures, each containing different copula families. The vine copulae resulting from the procedure were compared based on the AIC. It showed that the MST algorithm (Dissmann et al., 2013) performed poorly in selecting the best vine copula. The goodness-of-fit of the best-performing vine copulae was validated by the predicted against empirical exceedance probabilities of the observed extremes. The best-performing vine copula is a C-vine with the water level as the central node, found in Figure 4.15. In addition, RQ1 as stated;

RQ1: *Can a Non-stationary Extreme Value Analysis be applied in a multivariate design approach using Vine-Copulae?*

RQ1 resulted in the following findings; when combining a non-stationary marginal distribution with copula modelling, the transformation from copula space to variable space is not increasingly monotonic. Therefore, the dependence structure built by the copula is not preserved, thus a non-stationary marginal cannot be combined with copula modelling. This resulted in Lemma 4.1. The marginal distribution of the dominant variable, the water level, is modelled in Chapter 3. After concluding that copula modelling cannot be combined with non-stationary marginals, the stationary GP is selected. The marginals of the concomitant variables wave height, wave period and wind speed are Gamma distributed. A truncated Gumbel distribution models the wind direction. The design values for the WGD are obtained by sampling the selected vine copula and transforming the samples to variable space using the inverse of the selected marginals.

5 | Base Design of the Wide Green Dike

This chapter considers the base design of the WGD using the multivariate model resulting from Chapters 3 and 4. In Section 5.1, the offshore wave characteristics are transformed to nearshore. The clay-erosion failure mechanism of the WGD is assessed and a vine-based design is created in Section 5.2. The base design is compared to a deterministic design in Section 5.3. The comparison results in answering RQ2 to show the differences between a multivariate probabilistic and deterministic design for the WGD.

5.1 Offshore-Nearshore Transformation

In the propagation of wind waves in deep water to the coast, the waves are transformed due to their interaction with the bathymetry. The interaction induces variations in the significant wave height and the mean wave directions. Important processes causing this transformation are refraction, shoaling, diffraction, bottom friction and wave breaking. By taking wave measurements offshore, the true wave characteristics can be studied before these transformations take place. Studying the offshore wave characteristics provides insight into i.e. the risk assessment of potential hazards. The nearshore wave characteristics are also of great importance for a design, as they determine the loads that the design should withstand. An offshore-nearshore transformation aims to model these interactions.

To transform the simulated offshore wave characteristics from the multivariate model to nearshore characteristics a hybrid downscaling methodology, proposed by Camus et al. (2011a), is applied. This hybrid approach is a combination of a dynamical approach and a statistical approach. A dynamical approach consists of numerical modelling of the wave transformation processes (e.g. refraction, shoaling, diffraction, bottom friction, breaking) in their propagation to shallow waters. This can be done by a phase-resolving model, such as SWAN, which is based on mass and momentum balance equations. A statistical approach uses the empirical relationship between a deepwater variable and a nearshore variable to obtain (local) information on the coastal environment, usually by an interpolation scheme (Camus et al., 2011a). Although the dynamical approach is the most accurate, it is also very computationally expensive. A hybrid approach combines the dynamical and statistical approaches to reduce computational effort.

The considered hybrid approach aims to create a surrogate model that approximates the numerical model, based on the input-output behaviour of the simulated offshore-nearshore transformation. The surrogate is developed by selecting a subset of wave conditions, to represent the whole set of wave conditions, and performing the offshore-nearshore transformation of the subset using the numerical model. The input-output behaviour is captured through an interpolation scheme. Using the surrogate model, the computational effort can be significantly reduced for the offshore-nearshore transformation. Subsection 5.1.1 selects the subset of wave conditions to train the surrogate. In Subsection 5.1.2, the subset is transformed using the numerical model SWAN (Booij et al., 1999). The surrogate is built in Subsection 5.1.3. Subsection 5.1.4 shows the assumed storm progression in the Wadden Sea area, needed to create the input for the surrogate model. In Subsection 5.1.5, the results of the offshore-nearshore transformation are found.

5.1.1 Selection of representative Storm Conditions

The goal of the selection process is to select a subset of wave conditions that represent the entire database of wave conditions. To select a subset, the considered approach uses a Maximum-Dissimilarity Algorithm (MDA). The MDA was first described by Kennard and Stone (1969) and identifies a subset of size M comprising the most dissimilar data in a dataset of size N . This selection technique results in a fairly evenly distributed subset of points across the entire data space, with some points on the outline of the data space. The implemented MDA methodology to transfer the wave climate from deep water to shallow water is proposed by Camus et al. (2011b). This is the MaxMin version of the algorithm. A subset size of $M = 25$ is selected. Camus et al. (2011a) showed that the quality of performance for such a small subset is satisfactory.

The multivariate input data is defined as $X^* = \{X_1^*, \dots, X_N^*\}$ with $X_i^* = \{h_i^*, H_{s,i}^*, T_{p,i}^*, \theta_i^*, w_{s,i}^*, w_{d,i}^*\}; i = 1, \dots, N$, where $N = 142$ observed extremes. The obtained subset is $D_j = \{h_j^D, H_{s,j}^D, T_{p,j}^D, \theta_j^D, w_{s,j}^D, w_{d,j}^D\}; j = 1, \dots, M$, where $M = 25$. The data consists of the (nearshore) water level h , offshore wave height H_s , wave period T_p and wave direction θ , and the (nearshore) wind speed w_s and wind direction w_d . Note, that it is assumed that $\theta = w_d$. Using the $*$ it is denoted that X^* consists of the variable values. Each data in X^* is defined by scalar and directional variables of different magnitudes. The data is normalized such that it is equally weighted in the similarity criterion. As the data contains directional variables, this criterion is defined by the Euclidean Circular (EC) distance. The EC is defined by Equation 5.1, where ‘ $\| \cdot \|$ ’ stands for the EC distance.

$$\|X_i - D_j\| = \sqrt{\left((h_i - h_j^D)^2 + (H_{s,i} - H_{s,j}^D)^2 + (T_{p,i} - T_{p,j}^D)^2 + \left(\min(|\theta_i - \theta_j^D|, 2 - |\theta_i - \theta_j^D|) \right)^2 \right) + \left((w_{s,i} - w_{s,j}^D)^2 + \left(\min(|w_{s,i} - w_{s,j}^D|, 2 - |w_{s,i} - w_{s,j}^D|) \right)^2 \right)} \quad (5.1)$$

The scalar variables are normalized by scaling the variable values between $[0, 1]$ using their minimum and maximum values, denoted by H_s^{\min} and H_s^{\max} for variable H_s . The directional variables (in radians) are normalized between $[0, 1]$ by dividing the values by π . Note, the directional variables lie between $[0, 180]$ degrees. Thus, the maximum difference between the two directions is π and the minimum is equal to 0. The transformations are shown in Equation 5.2. The dimensionless data is expressed as $X_i = \{h_i, H_{s,i}, T_{p,i}, \theta_i, w_{s,i}, w_{d,i}\}; i = 1, \dots, N$.

$$h = \frac{h - h^{\min}}{h^{\max} - h^{\min}}; \quad H_s = \frac{H_s - H_s^{\min}}{H_s^{\max} - H_s^{\min}}; \quad T_p = \frac{T_p - T_p^{\min}}{T_p^{\max} - T_p^{\min}}; \quad (5.2)$$

$$\theta = \frac{\theta}{\pi}; \quad w_s = \frac{w_s - w_s^{\min}}{w_s^{\max} - w_s^{\min}}; \quad w_d = \frac{w_d}{\pi}$$

The subset is initiated by transferring one of the vectors of X to the subset, resulting in D_1 . The other $M - 1$ elements in the subset are obtained by the MDA. This is an iterative process, that calculates the dissimilarity between the remaining data and the transferred elements in the subset, and then transfers the most dissimilar one to the subset. The MDA finishes after $M = 25$ elements are selected in the subset. The proposed MDA uses a more efficient algorithm to reduce the expected time complexity of $O(M^2N)$ to $O(MN)$, developed by Polinsky et al. (1996). The algorithm is described in detail in Camus et al. (2011b). In this work, the sea state with the largest water level h is selected as D_1 .

Finally, the last step of the MDA is the denormalization of the subset. This is done by applying the opposite transformation of Equation 5.2, as shown in Equation 5.3.

$$h^D = h^D \cdot (h^{\max} - h^{\min}) + h^{\min}; \quad H_s^D = H_s^D \cdot (H_s^{\max} - H_s^{\min}) + H_s^{\min};$$

$$T_p^D = T_p^D \cdot (T_p^{\max} - T_p^{\min}) + T_p^{\min}; \quad \theta^D = \theta^D \cdot \pi;$$

$$w_s^D = w_s^D \cdot (w_s^{\max} - w_s^{\min}) + w_s^{\min}; \quad w_d^D = w_d^D \cdot \pi \quad (5.3)$$

The selected subset is shown in Figure 5.1 for all variables. The black line represents the entire database of variables. The red dots are the selected cases in the subset for each variable. The dashed red line represents the times corresponding to the observed extremes in the subset.

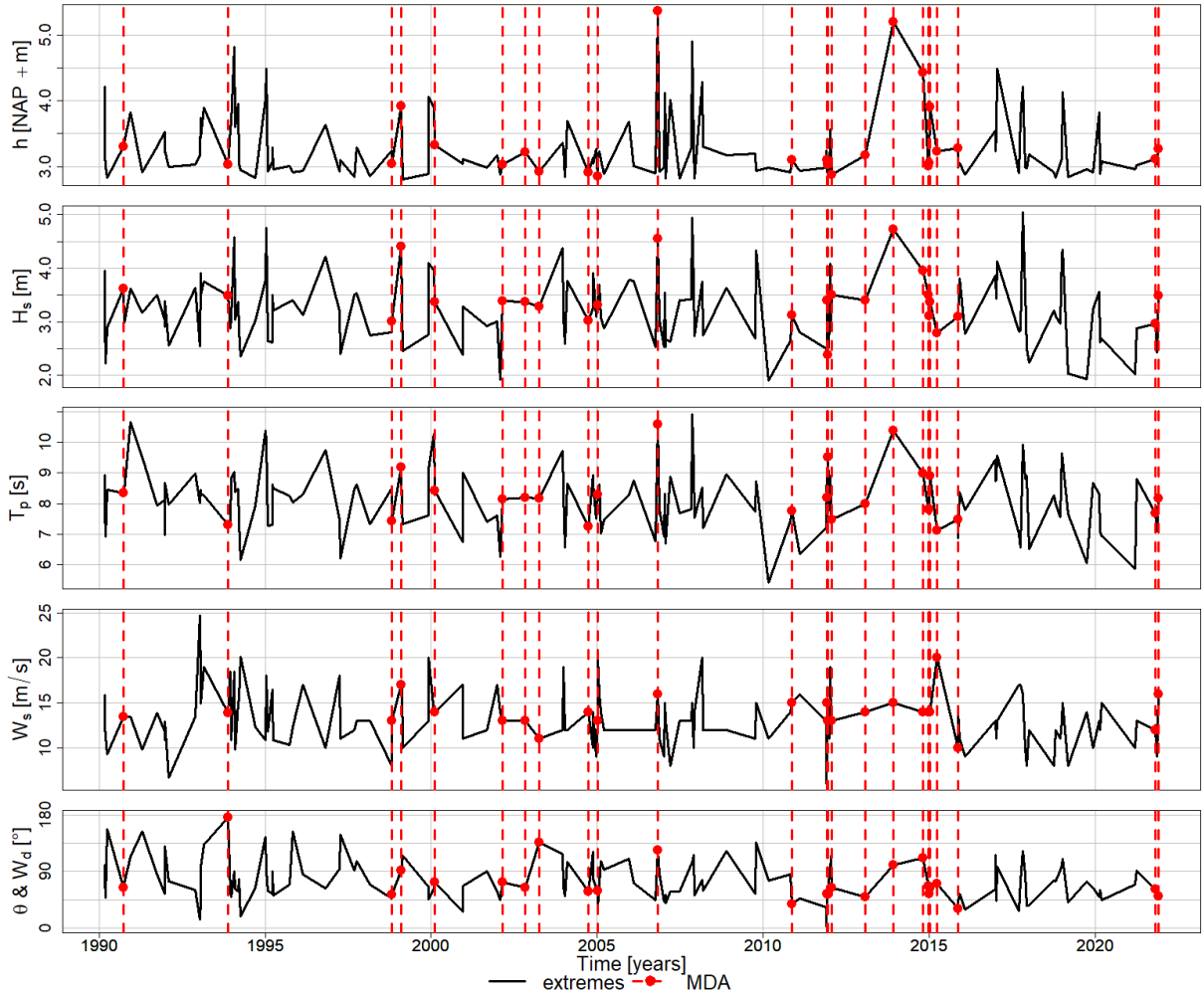


Figure 5.1: Selected cases for each variable using the MDA.

5.1.2 Transformation in SWAN

The subset of size $M = 25$ is propagated using the wave energy model SWAN, which stands for Simulating WAVES Nearshore (The SWAN Team, 2023). The bathymetry obtained from EMODnet (2016) is transformed into a rectangular grid with a spatial resolution of 50 meters. The computational grid with Cartesian coordinates overlaps the transformed bathymetry. The total domain has an area of 25×25 kilometres, resulting in 500×500 grid meshes. Each sea state defined by h , H_s , T_p , θ , w_s and w_d is propagated by a stationary 2-dimensional SWAN model. In the model, a constant wind field is defined by w_s and w_d . The boundary conditions are defined using a constant JONSWAP spectrum with a peak enhancement parameter of $\gamma = 3.3$ and a directional spreading interpreted as a directional standard deviation of $\sigma = 30^\circ$ (default). This boundary condition is applied at the inlet of the Ems-Dollard estuary, at the Northern boundary. One of the SWAN input files is found in Appendix G.

In Figure 5.2, one of the transformed 25 cases is shown. The filled contours show the significant wave height, the values are found in the colour bar. The arrows show the mean wave direction. The WGD location is indicated by the green line. From the 25 cases, three points of interest are indicated by P_1 , P_2 and P_3 . The dike orientation for each point is different. The consequence is that the angle of wave attack β for each point is different for a constant wave direction. Waves that strike the WGD at an angle have a reduced impact compared to waves that strike the dike perpendicular. Therefore, the loads on the WGD result from a combination of wave height and angle of wave attack. By comparing the 25 propagated cases, these three points resulted in the largest wave heights for the dike segments with the different dike orientations.

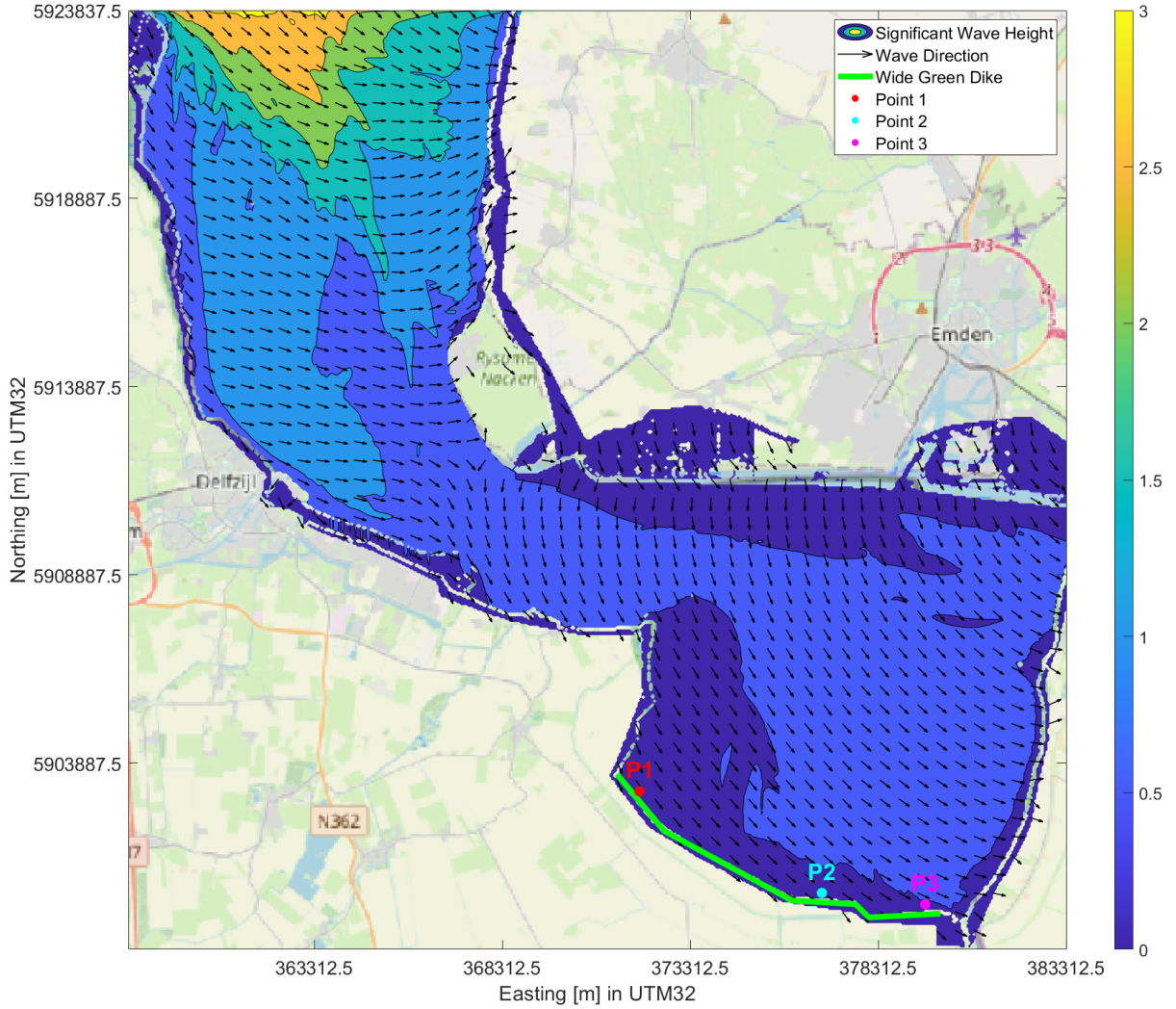


Figure 5.2: The significant wave height and directions for one of the selected cases transformed by SWAN.

5.1.3 Surrogate model using Radial Basis Functions

To reduce the computational effort, a surrogate model is built to approximate the SWAN model. The surrogate model is based on the input-output behaviour of the 25 propagated cases. The proposed method by Camus et al. (2011a) uses an interpolation technique based on Radial Basis Functions (RBF); a scheme which proved convenient for scattered and multivariate data (Hardy, 1990).

The selected subset of $M = 25$ data points is $D = \{D_1, \dots, D_M\}$ and has a dimension of $n = 6$, as there are six variables h , H_s , T_p , θ , w_s and w_d . Suppose that the transformation of the input data D to the real propagated data D_p by SWAN can be described by the associated real-valued functions $\{f_1, \dots, f_M\}$, where $f_j = f(D_j) = D_{p,j}$; $j = 1, \dots, M$. The RBF interpolation method aims to approximate these functions. By this approximation, a sea state $X_i = \{h_i, H_{s,i}, T_{p,i}, \theta_i, w_{s,i}, w_{d,i}\}$; $i = 1, \dots, N$, can be propagated using the RBF. The approximation function of the proposed method is in the form of Equation 5.4.

$$RBF(X_i) = p(X_i) + \sum_{j=1}^M a_j \cdot \Phi(\|X_i - D_j\|) \quad (5.4)$$

Here, $p(X_i) = b_0 + b_1 \cdot h_i + b_2 \cdot H_{s,i} + b_3 \cdot T_{p,i} + b_4 \cdot \theta_i + b_5 \cdot w_{s,i} + b_6 \cdot w_{d,i}$ is the monomial basis, with $b = \{b_0, \dots, b_6\}$ the coefficients of the monomials. The $a = \{a_1, \dots, a_M\}$ are the coefficients of the RBF.

The Φ is a Gaussian radial basis function described by Equation 5.5, where c is the shape parameter and ' $\| \cdot \|$ ' is the EC distance from the MDA.

$$\Phi\left(\|X_i - D_j\|\right) = \exp\left(-\frac{\|X_i - D_j\|^2}{2c^2}\right) \quad (5.5)$$

The optimal c is determined by the Leave-One-Out Cross Validation (LOOCV) algorithm proposed by Rippla (1999). The a and b coefficients are obtained by enforcing the interpolation conditions and the linear equations in Equations 5.6 and 5.7 (Micchelli, 1984). Prior to solving the system of linear equations, the scalar and directional variables in D_j are normalized in the same manner as in the MDA.

$$RBF(D_j) = f_j(D_j) = D_{p,j}; \quad j = 1, \dots, M \quad (5.6)$$

$$\sum_{j=1}^M a_j \cdot p(X_i) = 0; \quad i = 1, \dots, N \quad (5.7)$$

The real propagated data D_p contains the propagated significant wave height $H_{s-p,j}^D$, the propagated wave period $T_{p-p,j}^D$ and the x - and y -components of the propagated wave direction $\theta_{x-p,j}^D$ and $\theta_{y-p,j}^D$. Note that after the interpolation, the propagated wave direction $\theta_{p,j}$ is reconstructed. The sea state at deep water X_i is propagated to the point of interest through the RBF for each of the propagated parameters $H_{s-p,j}$, $T_{p-p,j}$, $\theta_{x-p,j}$ or $\theta_{y-p,j}$, found in Equation 5.8

$$\begin{aligned} H_{s-p,i} &= RBF_H\left(\left\{D_j, H_{s-p,j}^D(j = 1, \dots, M)\right\}, X_i\right); \quad i = 1, \dots, N \\ T_{p-p,i} &= RBF_T\left(\left\{D_j, T_{p-p,j}^D(j = 1, \dots, M)\right\}, X_i\right); \quad i = 1, \dots, N \\ \theta_{x-p,i} &= RBF_{\theta_x}\left(\left\{D_j, \theta_{x-p,j}^D(j = 1, \dots, M)\right\}, X_i\right); \quad i = 1, \dots, N \\ \theta_{y-p,i} &= RBF_{\theta_y}\left(\left\{D_j, \theta_{y-p,j}^D(j = 1, \dots, M)\right\}, X_i\right); \quad i = 1, \dots, N \end{aligned} \quad (5.8)$$

Here, the transfer of X_i to a point of interest at shallow water, results in the propagated wave condition $X_{p,i} = \{H_{s-p,i}, T_{p-p,i}, \theta_{p,i}\}$. Concluding from the real propagation in SWAN, there are three points of interest P_1 , P_2 and P_3 . Each point needs four interpolation functions, resulting in a total of twelve RBFs. Using the created RBFs, the sampled sea states from the multivariate model can be propagated to nearshore conditions at the three points. As an example, in this particular case, the interpolation function of the significant wave height at P_1 has a shape parameter of $c = 2.267$.

5.1.4 Storm Progression in the Wadden Sea area

Section 2.3 shows that the 18-hour average storm conditions are governing when assessing the clay-erosion failure mechanism. Accordingly, the extreme (maximum hourly) water levels that are sampled from the vine copula have to be transformed to an 18-hour storm average. To do so, a storm progression for the Wadden Sea area is assumed.

Deltares (2015) studied the storm progression for the Wadden Sea area. One of the studied locations, Delfzijl, is close to the WGD project as Figure 5.3 shows. Deltares (2015) selected 222 storms at Delfzijl using a POT procedure with a threshold of $\mu = \text{NAP} + 1.5$ meters and declustering time of $\delta = 24$ hours. The findings at Delfzijl resulted in a storm duration of 43 hours and a peak duration of 2 hours. The findings were combined with the other studied locations, resulting in a recommended approximation of the storm surge in the Wadden Sea area. The recommended shape is a buckled trapezium with a base duration of 45 hours and a peak duration of 2 hours. This shape is prescribed by the WBI-2017. To result in the water level progression during a storm, the astronomical tide must be accounted for. The study of Deltares (2015) resulted in a tidal amplitude of 1.5 meters and a phase difference between the tide and the storm surge of 5.5 hours for Delfzijl. These tidal characteristics are used in Sweco's design for the WGD. The same tidal amplitude and phase difference is found for the observed data. Therefore, a tidal amplitude of 1.5 meters and a phase difference of 5.5 hours is considered for all sampled extremes, resulting in the assumed water level progression during an extreme storm.

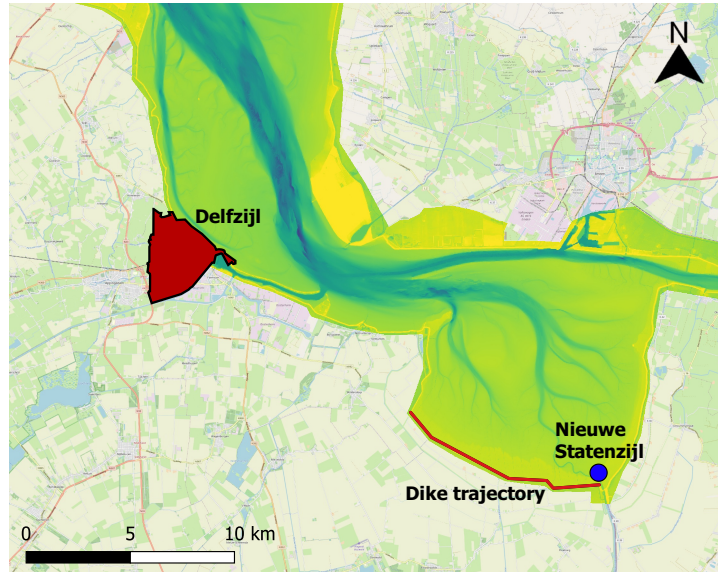


Figure 5.3: Locations of Delfzijl, the WGD trajectory and water level measurements at Nieuwe Statenzijl.

The assumed water level progression during an extreme storm is found in Figure 5.4. The figure shows the water level, storm surge and tide progression during the 45-hour storm duration for Sweco’s design. The 18-hour boundaries show the part of the storm that is considered when assessing the clay-erosion failure mechanism. The shape is assumed to be true for all sampled extremes. The maximum water level is transformed to an 18-hour average using a reduction factor r_{18} . The reduction factor is determined by dividing the 18-hour average water level by the maximum water level, resulting in $r_{18} = 0.93$.

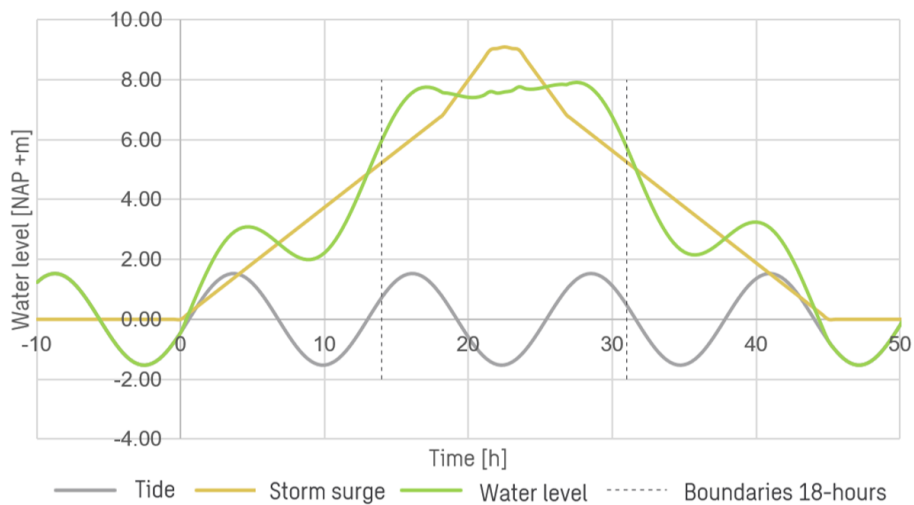


Figure 5.4: The assumed water level progression (green line) for a storm with a 45-hour duration. Image retrieved and modified from ‘Ontwerprapport Brede Groene Dijk’ by Sweco (2021b), p.21.

5.1.5 Simulating the Nearshore Wave conditions including Sea Level Rise

The created surrogate model in Subsection 5.1.3 is used to derive the nearshore wave conditions at the three locations; P_1 , P_2 and P_3 . To create the design values for the vine-based design, the vine copula is sampled to derive the multivariate input data $\{h, H_s, T_p, w_s, w_d\}$ in unity space. These samples are transformed into variable space using the obtained distributions of the design variables. The effect of climate change by SLR is not yet included in these samples. Including the SSP5-8.5 SLR scenario, can be done in multiple ways. First, the SLR can be introduced by changing the marginal distribution of the

water level. Secondly, the dependence structure between the water level and concomitant variables could be altered, for example by increasing the pair correlation between the water level and wave height. Note, that such an increase would also result in changing wave height samples. At last, both the marginal distribution of the water level and the water level pair correlations could be altered. In this work, SLR inclusion is achieved by changing the marginal distribution of the water level. The marginal distribution of the SLR scenario is found in Appendix J.

The procedure for the offshore-nearshore transformation is stated in Algorithm 5.1. As the required failure probability $P_{f,req} = 1/37,500$ per year is very low, a total of $n = 1,000,000$ samples are taken. The results from performing the procedure are found in Tables I.1 and I.2 in Appendix I.

Algorithm 5.1: Simulating the Nearshore Waves including Sea Level Rise

- Step 1:** Take n random samples from the vine copula obtained in Section 4.5.
- Step 2:** Transform the n samples into variable space using the quantile functions of the design variables from Sections 3.3 and 4.2.
- Step 3:** Create n random samples of SLR using the marginal distribution of the year 2150, found in Appendix J.
- Step 4:** Add the i^{th} SLR sample to the i^{th} water level sample, to create the extreme water levels for the year 2150; h_{SLR} .
- Step 5:** Reduce the extreme water level h_{SLR} to the 18-hour average water level according to Figure 5.4. This is done by multiplying h_{SLR} with r_{18} to create h_{18} .
- Step 6:** Perform the offshore-nearshore transformation using the surrogate model created in Subsection 5.1.3 for each location; P_1 , P_2 and P_3 . Use the multivariate input data $\{h_{18}, H_s, T_p, w_s, w_d\}$ to create the nearshore wave characteristics $\{H_{s-p}, T_{p-p}, \theta_p\}$ at each location.
-

5.2 Vine-based Design of the Wide Green Dike

Using the results of the offshore-nearshore transformation, the clay-erosion failure mechanism can be assessed. The clay erosion is evaluated for the three locations; P_1 , P_2 and P_3 . The nearshore waves are corrected for the angle of wave attack β by the influence factor f_β to determine the wave impacts (Deltares, 2022a). The influence factor is defined in Equation 5.9.

$$f_\beta = \max\left(0.35; (\cos \beta)^{0.67}\right) \quad \text{where } -90^\circ \leq \beta \leq 90^\circ \quad (5.9)$$

Where:

f_β	Influence factor for the angle of wave attack	[-]
β	Angle of wave attack relative to the dike normal	[°]

The reduced waves are found by multiplying the nearshore wave height H_{s-p} with f_β . The wave steepness s_{op} of the reduced waves is determined by Equation 5.10. Note, that the range of applications of the clay-erosion failure mechanism is for $0.01 \leq s_{op} \leq 0.05$, as stated in Section 2.3.

$$s_{op} = \frac{H_s}{g \cdot T_p^2 / 2\pi} \quad \text{where } 0.01 \leq s_{op} \leq 0.05 \quad (5.10)$$

Where:

s_{op}	Wave steepness	[-]
H_s	Significant wave height	[m]
T_p	Peak wave period	[s]
g	Gravitational constant (= 9.81)	[m/s ²]

As the locations P_1 , P_2 and P_3 have different dike orientations, the clay erosion is determined for all locations. The dike normal orientations for the locations are stated in Table 5.1.

Table 5.1: The WGD dike normal at P_1 , P_2 and P_3 .

Location	Dike normal
P_1	50 °N
P_2	3 °N
P_3	353 °N

The erosion volume V_e and erosion profile are determined using Equations 2.1, 2.2, 2.3 and 2.4 from Section 2.3. To model the erosion coefficient c_e , a truncated Normal distribution between [0.54, 1.00] is considered, see Appendix I. This results from the Delta Flume results and expert judgement (Sweco, 2021c; Deltares, 2022b). Note, that $V_e = 0$ if $H_s \leq 0.4$ meters (for the reduced waves) and if $h_{18} < \text{NAP} + 2$ meters as the salt marshes have a height of $\text{NAP} + 2$ meters, thus no erosion of the WGD takes place. The erosion volume and profile are determined according to Algorithm 5.2.

Algorithm 5.2: Determine the Erosion Volume and Profile for Clay-Erosion

Step 1: Acquire the multivariate data $\{h_{18}, H_{s-p}, T_{p-p}, \theta_p\}$ of size $4 \times n$, by performing Algorithm 5.1. The data contains the 18-hour average nearshore water level $h_{18,i}$ and the corresponding nearshore wave characteristics $H_{s-p,i}, T_{p-p,i}$ and $\theta_{p,i}$; $i = 1, \dots, n$.

Step 2: Correct the nearshore waves for the angle of wave attack β using the influence factor f_β found in Equation 5.9. This results in $\{H_{s,i}, T_{p,i}, \theta_i\}$.

Step 3: Determine the wave steepness of the reduced waves $s_{op,i}$ using Equation 5.10.

Step 4: Take n samples of a truncated Normal distribution with a mean $\mu = 0.54$ and a standard deviation $\sigma = 0.14$ in the domain [0.54, 1.00] to get the erosion coefficients $c_{e,i}$.

Step 5: Determine the erosion volume $V_{e,i}$ for the data $\{c_{e,i}, h_{18,i}, H_{s,i}, T_{p,i}, \theta_i\}$ using Equation 2.1.

Step 6: Determine the erosion profile using $d_{e,i}$, $L_{e,i}$ and $d_{t,i}$ for $V_{e,i}$ using Equations 2.2, 2.3 and 2.4.

Step 7: Using the erosion profile parameters from Step 5, determine the minimum needed crest height using Equation 5.11, where $\alpha = 1 : 7$ is the outer slope of the WGD. This results in a dataset $\{V_e, d_e, L_e, d_t, h_{cr,min}\}$ of size $5 \times n$.

$$h_{cr,min,i} = \sin \alpha \cdot L_{e,i} + h_{18,i} - d_{t,i} \quad (5.11)$$

By performing Algorithm 5.2, the erosion profile and minimum needed crest height are found for all samples. The WGD design results from an iterative process in which the design crest height $h_{cr,d}$ and design clay layer thickness $d_{e,d}$ are assessed for the calculated erosion profiles. The selected WGD design is based on the design on a failure probability of $P_f \leq P_{f,req}$ with a minimal cross-sectional area. As the probabilistic assessment determines the erosion profile for a range of water levels and wave characteristics, the locations of the erosion profiles and their size differ. To assess a dike design for the calculated erosion profiles, the design dike's geometry is used. The design parameters $h_{cr,d}$ and $d_{e,d}$ are used to determine the WGD design geometry. The WGD starts from the landward side of the current, beginning from the inner berm next to the road, and constructing seawards. The design has the following constraints:

- The road is located at $\text{NAP} + 3.05$ meters.
- There is a minimum crest width of $b_{cr,min} = 1$ meter.
- An outer berm is constructed for maintenance activities. The outer berm is located at $\text{NAP} + 3.55$ meters and has a width of 3 meters with a slope of 1 : 20.

- The inner slope is $\alpha_{in} = 1 : 3$.
- The outer slope is $\alpha = 1 : 7$.

From $h_{cr,d}$ and $d_{e,d}$ a ‘design erosion profile’ can be determined. This is done to determine the design crest width $b_{cr,d}$. The design erosion profile is determined by solving Equation 2.1 for d_e to get $V_{e,d}$. Using $V_{e,d}$, the design erosion profile location and shape are determined. This provides $b_{cr,d}$, as the WGD is constructed from the current dike seawards and a clay layer thickness of $d_{e,d}$ is applied at the design erosion profile location. The cross-sectional area A_d is the difference between the design area and the current dike’s area, as shown in Figure 5.5.

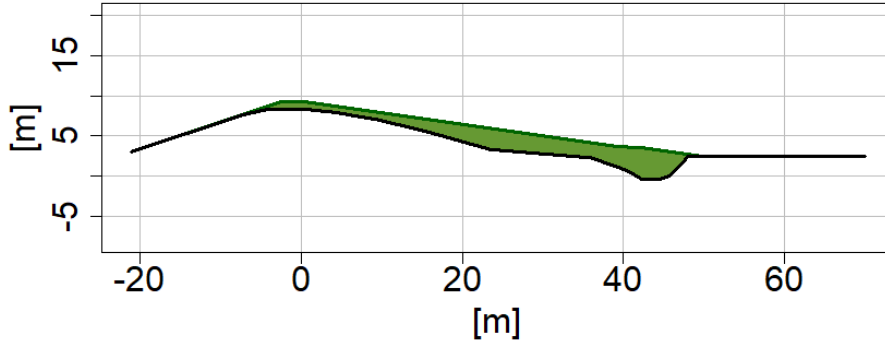


Figure 5.5: Sketch of the plot from Algorithm 5.3. The green area shows the calculated cross-sectional area A_d . The black line shows the current dike geometry.

Failure occurs when the calculated erosion profile hits the current dike’s clay layer or the design crest, as stated in Section 2.3. The failure probability of a design P_f is determined by dividing the total sum of failures over the number of samples $n = 1,000,000$. A design is valid if $P_f \leq P_{f,req}$, with $P_{f,req} = 1/37,500$ per year. To select the final WGD vine-based design, the full procedure from the calculated erosion profiles to the WGD design is automated in Algorithm 5.3.

Algorithm 5.3: Determine the WGD design with the minimal Cross-Sectional Area

- Step 1:** Perform Algorithm 5.2 to obtain the set of erosion profiles $\{V_{e,k}, d_{e,k}, L_{e,k}, d_{t,k}, h_{cr,min,k}\}$ corresponding to the data $\{c_{e,k}, h_{18,k}, H_{s,k}, T_{p,k}, \theta_k\}$; $k = 1, \dots, n$. Both sets are used as input.
- Step 2:** Create two arrays for the design parameters $h_{cr,d}$ and $d_{e,d}$. The arrays contain the range of values that are assessed for a possible WGD design. The design crest height has a minimum value of the current dike’s crest height.
- Step 3:** Create a data frame containing the x - and y -values of the current dike’s geometry $dike_x$, $dike_y$. A positive coordinate system is assumed to have a positive x -axis to the right and a positive y -axis upwards. The origin is set for $x = 0$ at the end of the crest of the current dike, $y = 0$ at NAP +0 meter.
- Step 4:** Determine the P_f for all $h_{cr,d,i}$ and $d_{e,d,j}$ combinations using a Monte Carlo simulation:

```

for(i in 1:length(h_cr,d)){
  for(j in 1:length(d_e,d)){
    ▷ Determine the design erosion profile parameters  $\{V_{e,d}, L_{e,d}, d_{t,d}\}$  using  $d_{e,d,j}$ .
    ▷ Determine the geometry of the design crest. The end of the crest  $x_{cr}$  is found by finding the  $x$ -value of the end of the design erosion profile. As the WGD is constructed seawards, a large  $h_{cr,d}$  combined with a small  $d_{e,d}$  could result in a  $b_{cr,d} < b_{cr,min}$ . Respect the minimum crest width of 1 meter.
  }
}

```

```

    ▷ Create a data frame containing the  $x$ - and  $y$ -values of the design WGD geometry. Respect the following set parameters:  $\alpha = 1 : 7$ ,  $\alpha_{in} = 1 : 3$ , the inner berm is located at NAP +3.05 meters, the outer berm is located at NAP +3.55 meters and has a width of 3 meters and slope of 1:20.
    for( $k$  in  $1 : n$ ){
      ▷ Using the calculated erosion profiles from Step 1 and the WGD geometry, for each sample  $k$  determine the  $x$ - and  $y$ -coordinates of the ‘kink’ in the erosion profile at which the terrace ends and the cliff starts;  $x_{kink}$ ,  $y_{kink}$ , see Figure 2.3.
      if( $x_{kink,k} < dike\_x[dike\_y == y_{kink}] \vee h_{cr,d} < h_{cr,min,k}$ ){
        ▷  $failure = failure + 1$ 
      }
    }
     $P_f = failure/1,000,000$ 
    if( $P_f \leq P_{f,req}$ ){
      ▷ Save the WGD design data frame as possible WGD design geometries
      ▷ Save the  $P_f$  of the possible WGD geometries
      ▷ Calculate the cross-sectional area  $A_d$  of the possible WGD geometry
    }
  }
}
▷ Return the WGD geometry,  $P_f$  and  $A_d$  corresponding to the geometry for which  $\min(A_d)$  is valid

```

Step 5: Plot the selected WGD geometry.

Algorithm 5.3 is run for all three locations P_1 , P_2 and P_3 . The input of the design parameters is two arrays with a step size of 1 centimetre. The design crest height is assessed for $NAP + 8.38m \leq h_{cr,d}$, where the lower boundary is defined by the current crest height. The design clay layer thickness is assessed for $0.50m < d_{e,d}$, as $d_0 = 0.50m$. The results show that location P_2 is governing for the vine-based design, with $h_{cr,d} = NAP + 9.25$ meters and $d_{e,d} = 0.90$ meters. The optimal design has a design cross-sectional area of $A_d = 98.0 m^2$, thus $98.0 m^3/m$ of clay is needed for the design.

Algorithms 5.2 and 5.3 are also run for an erosion coefficient of $c_e = 0.8$ for all samples at only the governing location P_2 . This is done to check the influence of considering c_e as stochastic and to check the assumption of $c_e = 0.8$ for the deterministic design. The results show a slight increase in design clay layer thickness of +5 centimetres, compared to the vine-based design with c_e as stochastic. This would result in a small additional cross-sectional area of $2.6 m^2$.

The selected vine-based design is shown in Figure I.4 in Appendix I. The figure shows the WGD design with the new to-be-constructed clay layer. The current dike geometry is shown by the bold black line, with a current clay layer thickness of 0.8 meters. Also, the old dike core, on which the current dike is constructed is shown. A road is located on the inner berm, hence the asphalt layer.

The 18-hour average water levels and wave heights for which the vine-based design failed, are found in Appendix I. The failures show that the North wind direction is dominant when creating the governing water levels and waves. This corresponds to the local knowledge by Sweco (2021a). The return period of the water level for which the design failed can be analysed to check whether the assumption of the storm progression in Subsection 5.1.4 was valid. This is done by determining the return period for the minimum water level for which the design failed, this is NAP +8.85 meters. To determine the return period, the 18-hour average is transformed back into an hourly maximum water level. From this water level, different SLR scenarios are subtracted to result in a ‘present’ water level, without any SLR. The return period for this water level is determined using the marginal distribution of the extreme water level. The results are shown in Table 5.2. The table shows that without any SLR, the return period is

260,150 years. The return period for 2.5 meters of SLR is 3,410 years, which is still a significant storm. Therefore, the assumption in Subsection 5.1.4 is deemed acceptable.

Table 5.2: The return period T in years for the 18-hour average water level h_{18} for different SLR scenarios for the year 2150.

SLR [m]	0	0.5	0.75	1.0	1.25	1.5	1.75	2.0	2.25	2.5
T [y]	260,150	112,075	73,230	47,700	30,975	20,050	12,935	8,320	5,330	3,410

5.3 Comparison with a Deterministic Design

In Appendix H, a deterministic design for the WGD is created. The design values result from the same marginal distributions as the vine-based design. The design values are the values corresponding to a return period of 37,500 years. To include SLR, the 95% value of the SSP5-8.5 scenario is considered, resulting in 2.3 meters of SLR in 2150. The design values are transformed using SWAN to create the nearshore wave conditions. The clay-erosion failure mechanism is assessed by performing Algorithms 5.2 and 5.3 in a deterministic manner. Therefore, the erosion profile is only assessed at one level on the outer slope, determined by the design water level. This results in the design crest height and clay layer thickness for the deterministic design. The full procedure and design are found in Appendix H.

In Table 5.3, the design crest height $h_{cr,d}$, clay layer thickness $d_{e,d}$, cross-sectional area A_d and the required total volume of clay V_{tot} are shown. The WGD trajectory is 12.5 kilometres long. By multiplying A_d with 12,500, V_{tot} is found.

Table 5.3: Comparison of the deterministic and vine-based design.

Design	$h_{cr,d}$ [NAP +m]	$d_{e,d}$ [m]	A_d [m^3/m]	V_{tot} [m^3]
Deterministic	11.24	1.45	241.2	3,015,000
Vine-based	9.25	0.93	98.0	1,225,000

The designs and their differences in dimensions are visualized in Figure 5.6. The current dike is shown in black, the vine-based design in blue and the deterministic design in red.

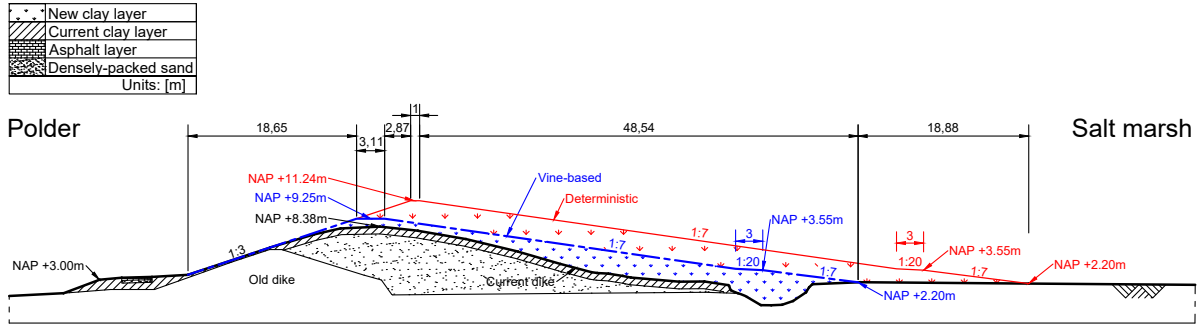


Figure 5.6: The vine-based and deterministic designs of the WGD for the year 2150.

Table 5.3 and Figure 5.6 show significant differences between the deterministic and vine-based designs. For the vine-based design, $h_{cr,d}$ is increased by almost 2 meters and $d_{e,d}$ by 0.52 meters. These are significant increases, of 21.5% of NAP +9.25 meters and 56% of 0.93 meters. The large increase in design parameters results in the deterministic design having a significantly larger footprint of +146% and an additional intrusion of 18.7 meters into the Natura 2000 area. For the total amount of clay needed for construction, this results in an additional 1,790,000 m^3 of clay.

By comparing the combinations of water levels and (reduced nearshore) wave heights for which both designs fail, it is clear that the deterministic design is designed for more extreme conditions. The design

value of the water level for the deterministic design is $h_{d,18} = \text{NAP} + 9.95$ meters and the wave height is $H_{d,s} = 1.96$ meters. The failures for the vine-based design have water level values between NAP +8.8 meters and NAP +10.6 meters. The wave heights are between 0.8 and 0.9 meters. The statistical summaries of the water level and wave height are found in Appendix I. The design water level of the deterministic design is 0.2 meters larger than the 3rd quartile of the failures from the vine-based design, which is significant. The difference in design wave height is relatively even more significant. The accounted wave height is more than double that of the wave heights in the vine-based design. However, from the vine-based design, it was found that the water level is the dominant variable for failure. The results show that failure occurs due to very extreme water levels. Therefore, the corresponding wave height can be significantly reduced as a much smaller wave height already results in an erosion profile for which failure occurs.

It is concluded that accounting for such significant values, determined in a deterministic approach, results in the large over-dimension of the WGD design. From these findings, RQ2 can be answered. RQ2 states;

RQ2: *What are the design differences between a multivariate probabilistic design and a deterministic design for the Wide Green Dike project?*

To answer RQ2, significant reductions in the WGD footprint are found when designing the WGD using a multivariate probabilistic approach. The multivariate approach resulted in design values that account for measured correlation between the design variables and, thus, in lower design values than one would consider using a deterministic approach. By doing so, close to 19 meters of intrusion into the Natura 2000 area could be saved. In addition, the probabilistic approach verified that the water level is the dominant variable for the clay-erosion failure mechanism.

6 | Adaptive Design Strategies

This chapter aims to answer RQ3; How can incorporating an adaptive design strategy to the Wide Green Dike concept promote its feasibility given the uncertainty of sea level rise? Section 6.1 introduces the adaptive design concept. In Section 6.2, the different adaptive strategies are created. The strategies are assessed and a preferred strategy is selected in Section 6.3.

6.1 Introduction to Adaptive Design Strategies

The design of hydraulic structures is bound to meet current and future social, economic and environmental needs (Ercicum et al., 2020). However, one cannot eliminate the uncertainties that lie in the future, therefore a wide range of future needs should be considered. A sustainable plan is one that not only performs for the current needs but should be robust, meaning that it also performs satisfactorily for a wide range of futures, and needs to be adaptive, meaning that it can be adapted to changing future conditions (Walker et al., 2013). In hydraulic engineering, such a sustainable plan, that is robust and adaptive, provides a solid base to cope with these future uncertainties. By incorporating the possibility of future adaptations, these uncertainties can be taken into in the design process. Ignoring these uncertainties can result in limiting future corrective actions. Consequently, resulting in negative situations that could have been prevented, thus leading to unsustainable plans. According to Walker et al. (2013) there are four ways for dealing with future uncertainty in sustainable plans:

- Resistance: planning for the worst possible future scenario
- Resilience: a system that can quickly recover from unforeseen future conditions
- Static robustness: a system that performs satisfactorily for a wide range of futures
- Dynamic robustness: a plan to change the system over time, in case future conditions change

In hydraulic structure design, static and dynamic robustness are the preferred two strategies for a sustainable design plan. Resistance would result in an over-investment. Resilience focuses on recovery, which is not preferred for hydraulic structures. Resilience would suggest that the structure is likely to fail. Static robustness is the traditional design strategy in a hydraulic structure design. The structure is designed to perform satisfactorily up to the end of its lifespan. However, climate change is accompanied by the uncertainty of future boundary conditions, such as SLR. The rate at which climate change will proceed depends on a large number of social, economic and political developments. Therefore, estimating future conditions cannot be done without uncertainty. Adaptive design strategies can provide a way to mitigate over-designing hydraulic structures to cope with the unknown SLR. The focus of adaptive design strategies differs from maintenance planning. Adaptive design strategies involve dynamic adjustments in the hydraulic structure design or operational plans based on evolving data and insights in order to optimize aspects of its performance, e.g. costs, safety, and efficiency. Maintenance planning focuses on preventive actions to ensure the functionality, reliable operation and longevity of the hydraulic structure over time.

Dynamic robustness aims to create a design that is suited to change over time and hence can be adapted as new information becomes available. In the design of hydraulic structures, such an adaptive plan can be used to protect against SLR. In the case of a static robust design, the design must be designed to withstand the SLR up to the end of its lifespan. However, since the amount of SLR at the end of its lifespan is paired with uncertainty, a choice must be made of the climate scenario taken into account. Depending on if this climate scenario becomes a reality or not, the design can be over- or under-designed. Adaptive design can be used to mitigate the risk of over-designing. The initial design can be developed for a less severe SLR case and once more information becomes available, adaptations can be made to reinforce the structure to withstand more severe SLR scenarios. There are two underlying approaches to creating an adaptive plan, Adaption Pathways and Adaptive Policymaking (Haasnoot et al. 2011; Kwakkel et al. 2010). Both approaches aim at handling the uncertainty in long-term decisions and emphasize the need for an adaptive design strategy to manage uncertainty (Haasnoot et al., 2013).

Adaption Pathways introduces an adaption map that includes multiple adaption trees. These consist of a sequence of possible actions after a tipping point is reached, similar to a road map. The Adaption Pathways map shows multiple possible strategies to achieve the same point in the future. These strategies or pathways are based on model results or expert judgement. All different pathways satisfy a minimum level of performance, but each comes with its own cost and benefits. Therefore, a specific pathway could be preferred. A comparison between the pathways can be made by a scoreboard where the different costs and benefits are displayed. Using the Adaption Pathways approach, decision-making in a changing environment can be supported by identifying opportunities, no-regret actions, lock-ins and the timing of action (Haasnoot et al., 2013).

Adaptive Policymaking is a generic structured approach to designing dynamic robust plans and originates from Assumption-Based Planning (Dewar et al., 1993). This method consists of several stages. First, the current requirements and conditions for a system are studied and the objectives for future conditions are specified. Then, a basic plan is assembled which is developed on how these objectives are to be achieved. Stage three emphasizes making the basic plan more robust. This is done using four types of actions: mitigating actions (actions that reduce likely adverse effects of a plan), hedging actions (actions that reduce uncertain effects of a plan), seizing actions (actions that seize likely available opportunities in a plan) and shaping actions (actions that reduce failure or enhance success). The next stage is called contingency planning. This is the monitoring of the plan’s performance and taking action if needed. The information that needs to be monitored is specified in signpost variables. Also, when critical values of the signpost variables are triggered, the signpost specifies which actions need to be taken. Stage five considers the different types of actions that can be triggered by a signpost. These consist of defensive actions (actions that clarify, preserve and meet unforeseen challenges of the basic plan in response to triggers that leave the basic plan unchanged), corrective actions (actions that adjust the basic plan), capitalizing actions (actions that take advantage of opportunities to improve the basic plan) and reassessment (once the core assumptions in the plan have lost validity). The design of the completed plan consists of the initial actions from stages one up to three and the monitoring system from stage four. During its design life, the signpost information is gathered and the corresponding actions are taken once a trigger occurs.

6.2 Creating the Adaptive Design Strategies

The key aspect of the WGD concept is constructing the embankment with locally ripened clay originating from the Ems-Dollard. The WGD project aims to tackle two main goals; restoring flood risk safety and increasing the local ecology by helping to solve the silt problem in the Ems-Dollard estuary. Constructing the WGD with a design life of up to 2150 in one go could result in a lack of upscaling capacity of the local clay refineries. The lack of locally repined clay must then be compensated by acquiring clay elsewhere, which is contrary to the aims of the WGD concept. Moreover, the uncertainty of SLR may lead to an over-design of the WGD. As the WGD is constructed seawards, over-designing results in a loss of the Natura 2000 area in the Ems-Dollard. The loss of area can even amplify the silt problem, as it results in less space for the silt to settle (Dijk, 2022). In addition, the loss of the Natura 2000 area must be compensated for, resulting in additional costs. In this work, the incorporation of adaptive design strategies is explored for the WGD project.

There are two main parameters that determine the dike profile; the design clay layer thickness $d_{e,d}$ and the design crest height $h_{cr,d}$. Figure 6.1 shows how the dike profile of a WGD design can change by adjusting one of these parameters. An increase in $d_{e,d}$ results in a more seaward outer slope. By increasing the crest width, the increase in $d_{e,d}$ can be accomplished without increasing $h_{cr,d}$ (shown in blue). The figure also shows that an increase in $h_{cr,d}$ also results in an increase in $d_{e,d}$ (shown in red).

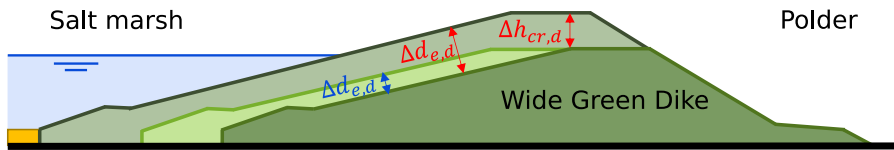


Figure 6.1: Sketch of the change in dike profile due to an adaption by increasing $d_{e,d}$ or $h_{cr,d}$.

To create the adaptive design strategies, multiple probabilistic designs are created for the years 2050 up to 2150 for every 10 years. Each probabilistic design corresponds to a different SLR distribution, according to the course and bandwidth of the SSP5-8.5 scenario from Figure 2.9 in Section 2.5. The SLR uncertainty over time is modelled by a range of Log-Normal distributions with an interval of 10 years. This is done by fitting the 5th, 17th, 50th, 83rd and 95th percentiles provided by KNMI (2021) of the SSP5-8.5 scenario from IPCC (2022). The resulting Probability Density Functions (PDFs) of the distributions are shown in Figure 6.2. The figure shows that over time the mean of the distributions shifts to larger SLR values and the standard deviation of the distributions increase. The Log-Normal distribution parameters and a 2-dimensional figure of the PDFs are found in Appendix J.

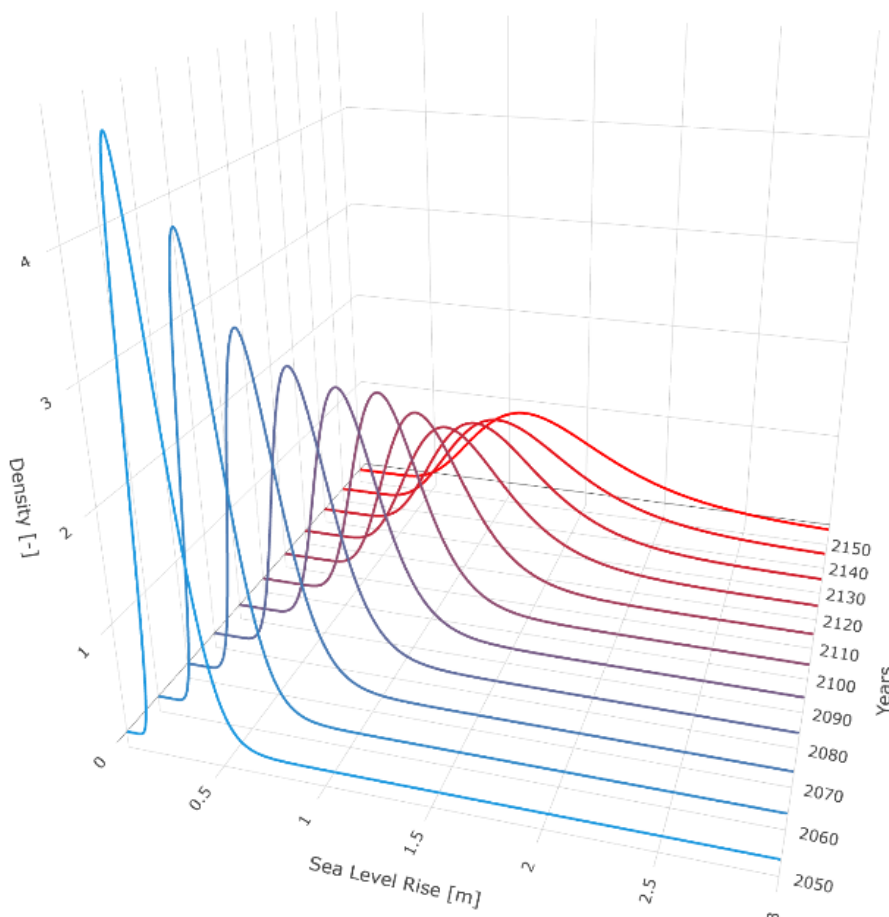


Figure 6.2: The considered Probability Density Functions over time for the SSP5-8.5 scenario.

The SLR distributions are used to create the 11 (multivariate) probabilistic designs, according to the same design methodology as in Chapter 5. The designs are created by performing Algorithm 6.1.

Algorithm 6.1: Create the Designs for the Adaptive Strategies

Step 1: Consider the SLR distributions from Figure 6.2, with the parameters stated in Appendix J. This results in 11 SLR distributions, referred to as S_s ; $s = 1, \dots, 11$, in which $s = 1$ corresponds to the year 2050, $s = 2$ to 2060, up to $s = 11$ corresponding to 2150.

Step 2: For every S_s perform Algorithm 5.1 at location P_2 . This provides the multivariate data $\{h_{18}, H_{s-p}, T_{p-p}, \theta_p\}$ for every SLR distribution S_s .

Step 3: Determine the erosion volume V_e and profile for clay erosion by performing Algorithm 5.2 for every S_s .

Step 4: Create the optimal probabilistic design with the minimal cross-sectional area by performing Algorithm 5.3 for every S_s .

Performing Algorithm 6.1 results in the overview of the required designs. This results in Table 6.1, showing the required $h_{cr,d}$, $d_{e,d}$ and A_d for every 10 years, governing the dike profile. The table shows six designs with a design life up to 2090, 2110, 2120, 2130, 2140 and 2150. The first design shows that the design with a design life of 2050 still complies up to 2090. The second design shows that the design with a design life of 2100 also complies with a design life up to 2110.

Table 6.1: The required design parameters: crest height $h_{cr,d}$, clay layer thickness $d_{e,d}$ and cross-sectional area A_d , over time for the WGD.

Design Parameters	Unit	Design Sight-year(s)					
		2050 – 2090	2100 – 2110	2120	2130	2140	2150
$h_{cr,d}$	[NAP +m]	8.38	8.38	8.44	9.00	9.25	9.25
$d_{e,d}^a$	[m]	0.50	0.60	0.70	0.74	0.83	0.93
A_d	[m^3/m]	79.3	82.7	87.0	90.8	94.2	98.0

^a Note, $d_{e,d}$ is the to-be-applied clay layer thickness on top of the current dike. The total clay layer thickness includes 0.8 meters of the current dike.

Using this insight, four different adaptive design strategies are created. The adaptive strategies are shown in Table 6.2. The table shows the first construction phase and possible adaptation phases. The construction phase (1st phase) is the first design that is constructed on the current dike. The strategies differ in the selected design for the different phases and in the number of possible adaptations. Each strategy ends with the probabilistic base design for the year 2150, designed in Chapter 5. The baseline constructs the final design in the 1st phase. The start of each adaptation phase differs for each strategy, depending on the selected design. Strategy 1 is the most adaptive strategy. It performs a total of five adaptations after the 1st phase. In the 1st phase, it constructs the design with a design life up to 2090. In the 2nd phase, it constructs its successor with a life of up to 2110, and so on. Adaptation phases are performed until the final design with a design life of up to 2150 is reached. Strategies 2, 3 and 4 lie between Strategies 1 and the baseline.

Table 6.2: Overview of the design combinations for each adaptive strategy.

Strategies	Construction 1 st Phase	Adaptation				
		2 nd Phase	3 rd Phase	4 th Phase	5 th Phase	6 th Phase
Strategy 1	2050 – 2090	2100 – 2110	2120	2130	2140	2150
Strategy 2	2050 – 2090	2120	2150	–	–	–
Strategy 3	2120	2150	–	–	–	–
Strategy 4	2050 – 2090	2150	–	–	–	–
Baseline	2150	–	–	–	–	–

6.3 Assessment of the Adaptive Strategies

The four adaptive design strategies are assessed on several considerations. First, the required amount of clay during the construction and adaptation phases is determined for each strategy. This is compared to the up-scaling forecast of the clay refinery of the ED2050 program. The required clay per adaptation is associated with material costs. The difference in clay per adaptation results in different material costs per phase for the different strategies. The clay requirements and associated costs are found in Subsection 6.3.1. The introduction of the adaptation phases results in savings in material and construction costs compared to the baseline for the adaptive strategies. These savings can compound over time, resulting in benefits. The value of such benefits is subject to the uncertainty of different SLR scenarios. In Subsection 6.3.2, these benefits are investigated. Based on the required amount of clay, up-scaling capacity, associated costs, possible benefits and other considerations for the Ems-Dollard estuary, a preferred strategy is selected in Subsection 6.3.3.

6.3.1 The Required Clay and associated Costs per Adaptive Strategy

The amount of required clay in time depends on which design, from Table 6.1, is constructed at which period. In addition, the construction time of the phases should be considered. The required amount of clay divided by the construction time results in the required clay capacity for the clay refinery. An adaptive strategy with a lower required clay capacity could be favoured compared to one with a larger required capacity. A larger required capacity involves a larger up-scaling of the clay refinery, which could be paired with feasibility issues. To assess the required clay during the lifetime of the WGD, the construction phases are studied.

The goal of the ED2050 ambition program is to extract one million tons of (dry) silt each year starting in 2026. The up-scaling of the refinery should account for 30 – 40% of this goal, resulting in roughly 400,000 m^3 of densely packed clay. However, the WGD project does not aim to use this full capacity, due to accounting for risks in construction capabilities, uncertainty in weather conditions and limitations due to the Natura 2000 area. For the WGD project, 2×125 hectare of clay refineries are to be constructed. The Waterboard Hunze and Aa's (personal communication, June 13 and 23, 2023) stated that such a refinery would approximately produce 260,000 m^3 of densely packed clay each year. Using this capacity, the aim is to construct around 2 kilometres of WGD per year. Such a construction rate is estimated to be feasible. Construction in a Natura 2000 area requires electric equipment and vehicles. As the energy transition is taking place, the availability of such equipment is still scarce. To minimize uncertainties paired with weather conditions, the refinery is split up into compartments. The maturing process for the compartments starts at different times, creating a variety of filling and harvesting periods.

This results that the construction time mandated for constructing the full WGD trajectory in 2050 is assumed to be 7 years. The construction time of the adaptations is estimated at 3 years. The construction time for the construction and adaptation phases for all strategies is assumed to be equal. The different footprints of the designs are not accounted for in the construction times. Figure 6.3 shows the required clay during the lifetime of the WGD design when accounting for these construction times. Note, that this figure considers the construction of the 1st phase in 2043 and of the other phases 3 years prior to the end of the lifetime of the to-be-constructed design.

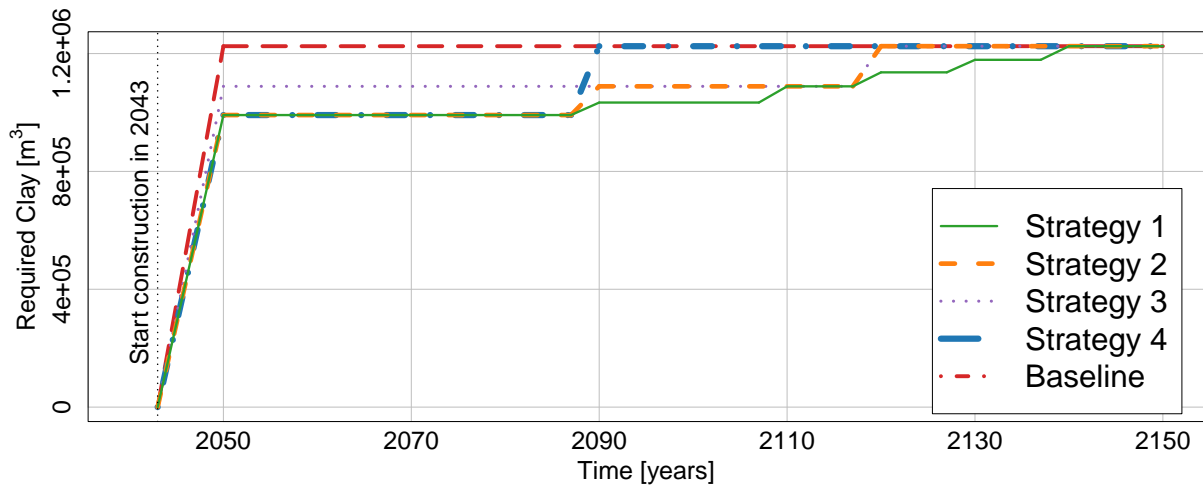


Figure 6.3: The required m^3 of clay over time for four different strategies and baseline.

Figure 6.3 shows that the most adaptive strategy, Strategy 1, involves the lowest clay capacity for the different phases. This is found by looking at the slopes during the construction and adaptation phases. A lower slope corresponds to a smaller demand for required clay. Strategies 1, 2 and 4 all start with the construction of the 2050 – 2090 design. This results in the lowest demand for clay in the 1st phase. The 1st phase demands the largest rate of clay for every strategy. Therefore, the 1st phase governs the up-scaling capacity for the clay refinery in the Ems-Dollard. Table 6.3 shows the total required clay during the 7-year-long construction phase and 3-year-long adaptation phases for each strategy. Dividing

the total amounts by the length of the phases, it is found that the minimum required capacity is 141,600 m^3 for Strategies 1, 2 and 4 in the 1st phase. The required capacity for the baseline is 175,000 m^3 .

Table 6.3: Required clay in m^3 for the construction and adaptation phases.

Strategies	Construction	Adaptation				
	1 st Phase	2 nd Phase	3 rd Phase	4 th Phase	5 th Phase	6 th Phase
Strategy 1	991,300 m^3	42,500 m^3	55,000 m^3	47,500 m^3	42,500 m^3	46,200 m^3
Strategy 2	991,300 m^3	97,500 m^3	136,200 m^3	–	–	–
Strategy 3	1,088,800 m^3	136,200 m^3	–	–	–	–
Strategy 4	991,300 m^3	233,700 m^3	–	–	–	–
Baseline	1,225,000 m^3	–	–	–	–	–

Preliminary studies presented in the webinar ‘Kleirijpen voor dijkversterking’ by Deltares (2023), estimated the costs to ripen clay in the Ems-Dollard estuary between $\text{€}25 - 35/m^3$ (based on the price level for the year 2021). These costs are based on a social cost-benefit analysis (SCBA, in Dutch: MKBA). SCBA costs also include non-financial effects, e.g. environmental effects, the economy and accessibility. Further details of these studies are discussed in Section 2.2. In this work, a cost of $\text{€}30/m^3$ of clay is considered to account for SCBA costs. Table 6.4 shows the clay costs in millions € for the construction phases. These costs are based on the 2021 price level and do not take into account inflation. The table shows that around 19% of the initial costs for clay can be saved if Strategies 1, 2 or 4 are selected instead of the baseline (since $(29.74 - 36.75)/36.75 \cdot 100\% = -19\%$). The savings in the 2nd phase for Strategy 1 are reduced to $((29.74 + 1.27) - 36.75)/36.75 \cdot 100\% = -15.6\%$.

Table 6.4: The total clay costs in million € for each phase for the strategies (based on the 2021 price level and not accounted for inflation).

Strategies	Construction	Adaptation				
	1 st Phase	2 nd Phase	3 rd Phase	4 th Phase	5 th Phase	6 th Phase
Strategy 1	$M\text{€} 29.74$	$M\text{€} 1.27$	$M\text{€} 1.65$	$M\text{€} 1.43$	$M\text{€} 1.27$	$M\text{€} 1.39$
Strategy 2	$M\text{€} 29.74$	$M\text{€} 2.92$	$M\text{€} 4.09$	–	–	–
Strategy 3	$M\text{€} 32.66$	$M\text{€} 4.09$	–	–	–	–
Strategy 4	$M\text{€} 29.74$	$M\text{€} 7.01$	–	–	–	–
Baseline	$M\text{€} 36.75$	–	–	–	–	–

6.3.2 Benefits per Strategy including the Uncertainty of Sea Level Rise

The introduction of adaptation phases reduces the starting amount of required clay and therefore material costs for the 1st phase. Over the lifetime of the WGD, the savings could yield over time resulting in benefits. Likewise, the construction and material costs of clay increase due to inflation. To determine the compounded interest, a fixed interest rate of 4% and a fixed inflation rate of 2% are considered (European Commission nd; Navarro et al. 2020). Although introducing these two concepts provides additional insights into the strategies, the results should be taken with care. The assumed fixed rates largely impact the compounded benefits and thus the outcome of the analysis. The real interest and inflation rates can have large fluctuations and depend on the future global economy, e.g. the large inflation hike in 2022 (Ferber, 2023). The assumed fixed rates are based on historical averages, which are not guaranteed to be similar for future scenarios. Using the assumed rates, the compounded benefits and costs can be calculated according to Equation 6.1.

$$R = I \cdot (100\% + i)^t \quad (6.1)$$

Where:

R	Compounded investment	$[\text{€}]$
I	Starting investment (principal)	$[\text{€}]$
i	Interest or inflation rate	$[\%]$
t	Accumulation period (time)	$[\text{years}]$

The moments in time at which adaptations take place depend on the uncertainty of SLR. To model the benefits over time, different SLR scenarios should be considered. An adaptation takes place based on the evolving data and insights, which determine whether the current design is still sufficient or not. If not, an adaptation can be applied. If it still is sufficient, the adaptation can be prolonged into the future. The possible benefits of the adaptive design strategies can be positive or negative. If the saved material costs compared to the baseline compound into larger values than the compounding costs needed for possible adaptations, then the benefits are positive. If the costs for the required adaptations become larger, then the benefits can become negative. The costs associated with the adaptations consist of material and construction costs. The material costs per adaptation for each strategy are found in Table 6.4. The construction costs are assumed to be 13% of the total costs per adaptation. This assumption is based on Lenk et al. (2017), which states that the construction costs are approximately 9% of the total costs for flood protection works such as dikes. This includes e.g. site preparation, core material preparation and site restoration. On top of this, an additional 2% is added to account for other one-time construction costs and another 2% is added to account for general construction costs, based on expert judgement by Anne Bonthuis from Sweco. Thus, the construction costs CC are calculated by $CC = M \cdot 13/87$ per adaptation, in which M represents the material costs. Using these assumptions, the benefits of the different adaptive strategies are modelled by Algorithm 6.2.

Algorithm 6.2: Modelling the Benefits for the Adaptive Strategies

Step 1: From Algorithm 6.1, consider the multivariate data $\{h_{18}, H_{s-p}, T_{p-p}, \theta_p\}$ of size $n \times 4$ for every SLR distribution S_s ; $s = 1, \dots, 11$, in which $s = 1$ corresponds to the year 2050, $s = 2$ to 2060, up to $s = 11$ corresponding to 2150.

Step 2: Reorder each multivariate dataset based on the ranks of h_{18} . Create n SLR scenarios by combining the data of the 11 multivariate datasets based on the ranks of h_{18} in each dataset. This results in n SLR scenarios with $\{h_{18,s}, H_{s-p,s}, T_{p-p,s}, \theta_{p,s}\}$; $s = 1, \dots, 11$. The i^{th} SLR scenario corresponds to the i^{th} rank of h_{18} ; $i = 1, \dots, n$. The $h_{18,s}$ values of the SLR scenarios are visualized in Figure 6.4 for $n = 10,000$.

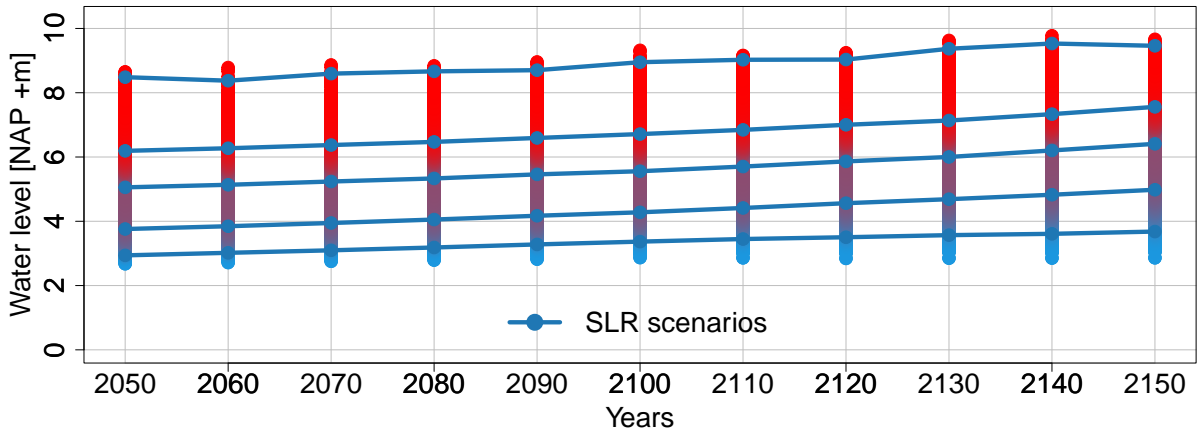


Figure 6.4: Samples of the SLR scenarios, connecting the SLR samples in each year based on their ranks.

Step 3: For each adaptive strategy, loop through all n SLR scenarios over time t and determine if a failure occurs for the design constructed in the 1st phase at t_1 . If so, add an adaptation at time $t_1 - 3$, as the construction time of an adaptation is 3 years. After an adaptation is applied, loop through the n SLR scenarios from time $t_1 - 3$ up to $t_{end} = 2150$ or the next failure, which implies an adaptation at time $t_2 - 3$. Using the derived times of required adaptations, the compounded benefits can be determined for every n SLR scenario.

```

for(i in 1 : n){
  ▷ Determine the erosion volume  $V_e$  and profile for clay erosion by performing Algorithm 5.2.
  ▷ For all adaptive strategies, determine if a failure occurs for the 1st phase using Algorithm 5.3. If failure occurs, take the following steps:
    ▷ Save the time of failure as  $t_1$ . Apply an adaptation at  $t_1 - 3$  as the construction time of an adaptation is 3 years.
    ▷ For the applied adaptation, determine if failure takes place starting from time  $t_1 - 3$  using Algorithm 5.3.
    ▷ If failure takes place at  $t_2$ , again apply an adaptation at  $t_2 - 3$ .
    ▷ Go through this procedure until time  $t_{end} = 2150$  is reached or until the final design in a strategy is reached. This results in an array for each strategy of the length of the number of phases, containing the times of adaptations  $t_{adapt}$  for every phase. The array contains a 0 if no failure takes place for that phase. Note, if a strategy has four phases and there is no failure in the 2nd phase, then  $t_{fail}$  has a 0 for phases 2, 3 and 4.
  ▷ Determine the compounded benefits over time  $benefits[t, i]$ . The initial savings  $benefits[t = 2043, i]$  result from Table 6.4. Note, the savings created by introducing the adaptive strategy compound by a fixed interest rate of 4%, while the material and construction costs compound by a fixed inflation rate of 2%. The construction costs are assumed at 13% of the total adaptation costs.

  for(t in 2043 : 2150){
    if( $t \in t_{adapt}$ ){
      ▷ The benefits compound until  $t = t_{adapt}$  is reached. At the times of adaptations, the compounded costs are subtracted from the benefits. Note,  $t_{adapt}$  has the length of the number of phases of the adaptive strategy. In addition, several phases could fail at the same moment in time. For example, for a certain SLR scenario, it could be that phases 2 and 3 of Strategy 1 must be applied at  $t = t_2 = t_3$ . In this case, the sum of the costs is accounted for.
      ▷  $benefits[t + 1, i] = benefits[t, i] \cdot 1.04 - costs \cdot 1.02^t$ 
    }
    else{
      ▷  $benefits[t + 1, i] = benefits[t, i] \cdot 1.04$ 
    }
  }
}

```

Step 4: Step 3 results in four data frames of size $108 \times n$ containing the compounded benefits for the years 2043 until 2150 for every n SLR scenario, one data frame per adaptive strategy. For each adaptive strategy, determine the 1st, 50th and 99th percentiles of the data frames for each year. Return these percentiles.

Step 5: Plot the 1st, 50th and 99th percentiles for each strategy.

The results of performing Algorithm 6.2 are found in Table 6.5 and Figure 6.5. The results show a wide range of possible benefit outcomes for each strategy. The benefits can compound into significant values. The 50th percentile of Strategy 1 is €436.2 million for 2150. To provide a perspective, the construction costs of the baseline strategy are €36.75 million in 2043. Adjusting the baseline costs from 2043 to a 2150 price level, accounting for 2% inflation, these would be €311.9 million. This would mean that incorporating Strategy 1 could be a very positive business case, as the potential benefits could compensate for the initial construction of the WGD and could result in net profits.

Table 6.5: The total benefits in 2150 in million € for the 1st, 50th and 99th percentiles for each strategy, based on a fixed 4% interest rate and 2% inflation rate per year.

Strategies	Unit	Total Benefits in 2150		
		p_1	p_{50}	p_{99}
Strategy 1	M€	153.0	436.2	465.9
Strategy 2	M€	75.0	423.6	465.9
Strategy 3	M€	87.4	256.8	271.8
Strategy 4	M€	-29.6	400.3	465.9

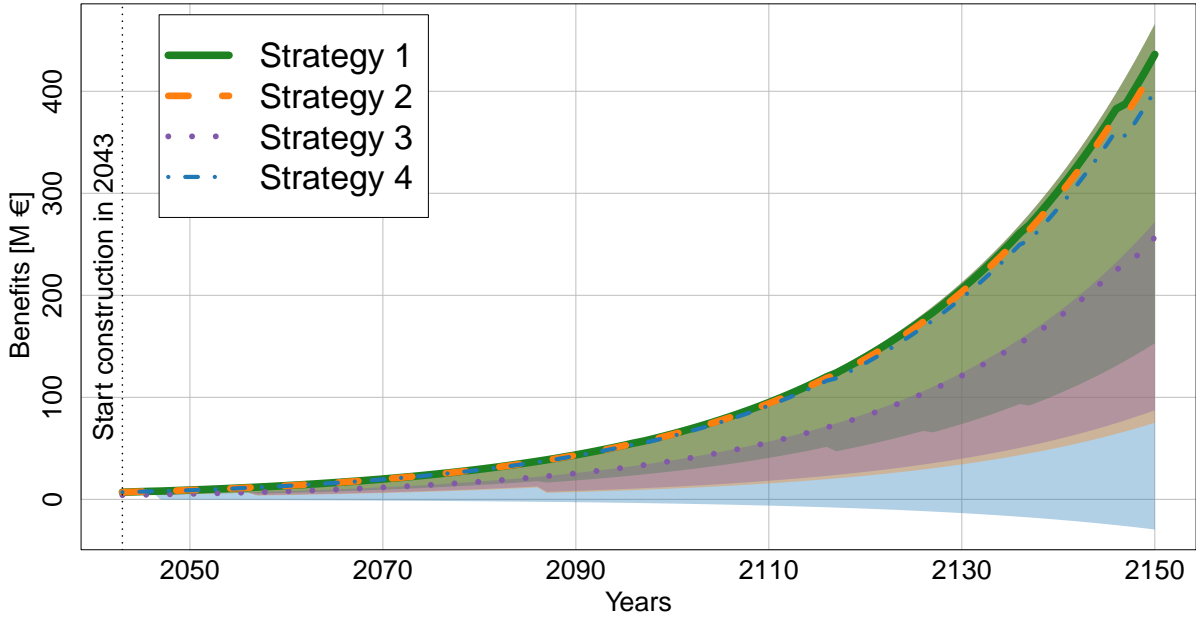


Figure 6.5: Benefits in million euros created by investing the benefits in clay costs against 4% interest per year. The costs of clay ($\text{€}30/\text{m}^3$) increase by 2% per year, accounting for inflation. The shaded areas enclose the 1st and 99th percentiles and the lines show the 50th percentile of the strategies.

The results show that the benefits can compound into significant values. This is due to the positive net interest rate and the large design life of the WGD of 100 years (for example $\text{€}1$ compounds into $\text{€}50$ for a fixed interest rate of 4% in 100 years, while in 50 years it ‘only’ compounds into $\text{€}7.1$). The lower bound corresponds to the most severe SLR scenarios. For these scenarios, the designs during the different phases are more likely to fail and the adaptations are applied at earlier moments in time compared to the less severe SLR scenarios. The upper bound corresponds to the mildest SLR scenarios, resulting in the largest benefits. The 50th percentile value is very close to the 99th percentile value. This is due to the small failure probability of the designs of $P_f = 1/37,500$ per year. Therefore, failure of a design only occurs for very severe SLR scenarios. For most scenarios, the design does not fail resulting in similar possible benefits. However, if the design in any phase does fail, the possible benefits are significantly reduced.

For the modelled WGD boundary conditions, introducing an adaptive design strategy thus seems to result in positive benefits for most adaptive strategies. The 1st percentile value of Strategy 4 is the only negative benefit. This strategy first constructs the design with a sight-year of 2090 and has one adaptation which is the final design. The investment for this adaptation is significant. A failure in an early stage of the design life can result that the benefits have not yet compounded into large enough values to compensate for this investment. This results in a negative benefit, which then will compound into larger negative values, as shown in Figure 6.5. Comparing Strategy 4 to Strategy 2 shows that introducing a second adaptation increases the possible benefits. An additional adaptation helps mitigate the possibility to result in negative benefits at an early stage of the design life, as the investment of

the next adaptation is smaller. This enables more time for the benefits to compound in time and thus larger than the required investment. Strategy 3 reduces this risk by constructing a design with a larger sight-year of 2120 in its 1st phase, thus reducing the failure probability at early stages. However, this results that the upper bound of the benefits is lower as the initial savings is less. Strategy 1 is the most adaptive strategy and corresponds to the largest possible benefits.

6.3.3 The Preferred Adaptive Strategy

Resulting of the amount of required clay, the up-scaling capacity, the associated costs, possible benefits and other considerations for the Ems-Dollard estuary, Strategy 2 is selected as the preferred strategy. The up-scaling expectation of 260,000 m^3 per year results in all strategies being feasible. Strategy 2 requires together with Strategies 1 and 4, the least amount of clay needed for the 1st construction phase. The required capacity of 141,610 m^3 per year could be preferable as the up-scaling capacity for the WGD is more easily met than for Strategies 3 and the baseline strategy. If the full capacity of 260,000 m^3 per year is met, then the excess clay can be exported to other projects and purposes. This can result in additional benefits for Strategies 1, 2 and 4.

Table 6.5 and Figure 6.5 show that Strategy 1 results in the largest benefits. However, the strategy does involve three additional construction periods compared to Strategy 2. The 50th percentile value of Strategy 2 is €13.4 million lower in 2150 compared to Strategy 1. This results in €1.6 million for a 2043 price level, accounting for a 2% inflation rate. Compared to the construction costs of the baseline strategy of €36.75 million, this is 4.3%. This is not a significant increase when considering the three additional adaptations from Strategy 1. Each adaptation disturbs the adjacent Natura 2000 area, thus it is preferable to limit the construction works in the area. This results in a dilemma where the number of adaptations should be limited. The disruption of the Natura 2000 area could also be introduced as additional costs during each adaptation. This would further close the difference in performance between the most adaptive versus the least adaptive strategies. However, if one would select the baseline, one could risk over-designing due to the uncertainty of SLR. Over-designing the WGD results in a permanent loss of the Natura 2000 area, which counteracts one of the WGD project's main goals. Therefore, Strategy 2 seems to combine both adaptability and limit the number of adaptations to around once per 30 years and is preferred.

The phases of Strategy 2 are shown in Figure K.1 in Appendix K. The first design in Strategy 2 saves 1.7 meters of intrusion into the Natura 2000 area compared to its final design. The second design saves 0.7 meters. This corresponds to 21,250 m^2 and 8,750 m^2 less intrusion along its entire trajectory, respectively. Due to the nature of adaptive design, this intrusion can be saved if in the future milder SLR scenarios become a reality and a slimmer design suffices.

To conclude RQ3, stated by;

RQ3: *How can incorporating an adaptive design strategy to the Wide Green Dike concept promote its feasibility given the uncertainty of sea level rise?*

Incorporating an adaptive design strategy into the WGD project can promote its business case and help mitigate the risk of over-designing in a Natura 2000 area. Adaptive strategies can help lower the initial clay capacity required for the construction of the WGD. Hence, the risk of not meeting the ambitious up-scaling capacity goals could be reduced. If the goals are met, the excess clay can be used for other purposes, resulting in an export product. Including adaptive strategies can also be beneficial for the business case of the WGD. The possible benefits can be reinvested elsewhere and compound over time. Moreover, the risk of over-designing can be mitigated by using adaptive strategies. The uncertainty in SLR could result in the risk of over-designing when a milder SLR scenario becomes a reality.

7 | Discussion

Over the course of this work, several assumptions were made and limitations and challenges were found. This chapter discusses these points for topics including, but not limited to, data availability, offshore-nearshore transformation and sea level rise.

7.1 Available Data in the Ems-Dollard estuary

The availability and quality of data used in this project are of significant influence on the models used to describe the multivariate extreme events. To describe a multivariate extreme event, sufficient data must be available for all variables of interest. In this work, the data is acquired from several sources. Water level data by Rijkswaterstaat (2022) from five locations in the Ems-Dollard estuary are compared; Dollard West, Groote Gat, Schankersdiep, Reide and Nieuwe Statenzijl. The data available at Nieuwe Statenzijl spans from December 1st 1990 up to November 11th 2022. Data for the other locations are more sparse and stray between 1994 and 2001. Discrepancies between the datasets are inventoried in Chapter 2. The found deviations in measured significant water levels for the locations were deemed as limited, after which the data at Nieuwe Statenzijl is selected to proceed. As the data for the other locations were limited, additional data would allow a better comparison of whether the data at Nieuwe Statenzijl reflects the water level along the dike's trajectory.

The wave data available from Rijkswaterstaat (2022) was limited to August 20th 2008 up to February 1st 2021. To perform the multivariate analysis, this was found insufficient. Therefore, model data by ERA5 was used (ECMWF, 2022). The ERA5 database combines historical data with model data to provide hourly data estimates of e.g. ocean-wave quantities. The selected extraction point for the wave data was selected in a deep part of the Ems River, with its exact location at 53°28'12.0"N 6°53'24.0"E. The waves at this location are partly propagated by the influence of the Wadden Sea and the Wadden Islands. Model biases from ERA5 could be introduced into the data. In this work, the possible introduced biases by ERA5 are not investigated nor corrected. Therefore, the wave characteristics in this project, such as wave height, could be under- or overestimated. According to (Kalverla et al., 2020), the extreme significant wave height in the North Sea area could be underestimated by ERA5.

For the wind data, a dataset by KNMI (2022) spanning from January 1st 1990 up to October 10th 2022 is used. This was the only available dataset near the dike's trajectory and was located approximately 4.5 kilometres from the WGD. To model the wind speeds during a storm, the maximum hourly mean wind speeds are considered. The wind characteristics are used for offshore-nearshore transformations of the wave characteristics. Considering the maximum hourly mean wind speed could result in an overestimation of the representative wind speeds that transform an offshore wave to nearshore conditions.

7.2 Multivariate Modelling of Extremes by Vine Copulae

The WGD is designed to withstand extreme loading conditions. In Chapter 3, a POT method is applied to the data of the considered design variables to determine what an 'extreme event' is. The POT method resulted in a multivariate dataset of 142 extreme events on which the vine copula is based. Two main points of discussion arise from this method. The vine copula is used to model representative extreme events respecting the correlations between the variables. These modelled events are used as the design values for the WGD design. The considered failure mechanism has a required failure probability of $P_{f,req} = 1/37,500$ per year. This results that $n = 1,000,000$ samples being taken from the vine copula to assess such a failure probability. The $P_{f,req}$ corresponds to approximately 27 failures for the n samples. Multiple assessment criteria are used to verify the used models. Nevertheless, it could be questioned whether the extrapolation of the 142 observed extremes to generate the n samples provides representative extreme conditions. Additional data on extreme events would provide great help in increasing the confidence in creating representative conditions by sampling such large numbers.

Secondly, the definition of an 'extreme event' becomes more ambiguous for multivariate cases. A method to define an extreme event, suggested by Zachary et al. (1998), is to select one dominant variable and

consider the values at the same moments in time for the other variables (concomitant variables). In the applied POT method, the water level is selected as the dominant variable. The definition of an extreme event is therefore based on the selected extreme water levels. The corresponding extremes of the other variables are thus the concomitants. Selecting the dominant variable could be not that straightforward. In this work, lab results from the Delta Flume and preliminary calculations from Sweco provided insight into the dominant variable for the assessed clay-erosion failure mechanism Sweco (2021b). However, including another failure mechanism, for which the water level is not dominant would require creating a second multivariate model based on a different dominant variable.

Another point of discussion is the number of variables considered in the multivariate model created in Chapter 4. This project considered five variables: water level, wave height, wave period, wind speed and wind direction. It assumed that the wave and wind direction are equal for extreme conditions to reduce computational effort. This assumption is based on Sweco (2021a) as wind waves are governing for the WGD and grounded by Bowers et al. (2000); Hildebrandt et al. (2019). Still, the assumption provides additional uncertainty in the model. Including additional variables, such as wave direction or storm duration could improve the ability of the model to create representative conditions. It should be noted that accounting for additional variables drastically increases the computational effort needed as the possible number of vines increases significantly, as proved by Morales-Nápoles et al. (2010).

At last, the goodness-of-fit of the models used to create extreme events should be discussed. In this work, the number of models considered was limited by the availability of the R packages used and the scope of the thesis. Although quite a wide range of models was available and a number of models were assessed based on multiple criteria, it could be that the ‘best’ model was not selected. Moreover, the definition of a ‘best model’ is ambiguous. A model could be the so-called best model based on certain criteria, while another model approximating the same observed extremes could be the best model based on different criteria. In this work, the models were assessed by multiple criteria and using engineering judgement a model was selected. This thesis focused on describing multivariate data using a vine-copula-based approach. Despite vine copulae being greatly flexible and useful for multivariate applications, as this thesis and multiple other works showed (e.g. Zhang et al., 2020; Tosunoglu et al., 2020), multiple other approaches could be considered to model multivariate data, such as Bayesian Networks (Couasnon et al., 2018).

7.3 The effect of Climate Change on Extremes

The consequences of climate change on hydraulic boundary conditions, such as water levels and wave heights, are very much uncertain. The reports by IPCC (2022) and KNMI (2021) aim to project possible outcomes for different emission scenarios. The large bandwidths in, for example, the projected SLR for each of those scenarios clearly show the uncertainty linked with climate change. In this work, the effect of climate change is considered by accounting for the projected SLR for the Dutch coast by KNMI (2021) according to the projected SSP5-8.5 scenario by IPCC (2022). A change in correlation between the design variables over time is not considered. Neither is a change in wave and wind climate or storm duration considered.

This thesis aimed to combine a non-stationary marginal of the extreme water level with vine copula modelling. In Section 4.4, it was proved that non-stationary marginals could not be combined with copula modelling if the covariate is one of the variables, e.g. water level. Therefore, the extreme water level was modelled by a stationary marginal distribution. To account for SLR, the distribution of the projected SSP5-8.5 scenario was added to the extreme water level for the sight year of interest, i.e. for a design with a design life of up to 2150, the projected SLR distribution in 2150 was added. This assumption is a simplification of reality. It is unknown if a certain amount of SLR of the mean sea level at the Dutch coast translates one-to-one to an increase in the extreme water level in the Ems-Dollard estuary. The translation of SLR from the coast to the estuary could be affected by numerous elements, e.g. temperature difference, salinity difference, and bathymetry. Additionally, the effect of a changing mean sea level on extreme water levels is to be well studied and much is still unknown.

7.4 Offshore-Nearshore Transformation by SWAN and a Surrogate model

The samples from the multivariate model are used to derive the nearshore wave characteristics. This offshore-nearshore transformation is performed by a hybrid approach, where a numerical model and a data-driven model are combined, see Section 5.1. The methodology, proposed by Camus et al. (2011a), significantly reduced the computational effort compared to a transformation performed using only numerical modelling. A group of 25 empirical cases are selected to represent 142 empirical extremes by selecting the most dissimilar data. These 25 cases are propagated by the numerical model SWAN to create the transformed cases. The input-output behaviour is approximated using an interpolation technique based on RBFs, the surrogate model. Both models have limitations, which should be discussed.

The surrogate model is based on the results of the 2-dimensional SWAN model. Therefore, the shortcomings in SWAN also create shortcomings in the surrogate. The limitations of SWAN are stated in The SWAN Team (2023). For this project, a 2-dimensional SWAN model was created with a grid with a spatial resolution of 50 meters. The model accounted for water level setup, quadruplet wave-wave interactions, white capping, breaking (limited) and diffraction (limited). A constant JONSWAP spectrum is applied at the inlet of the estuary, a constant wind field is defined and most parameters are held constant. The SWAN model could be further optimized for the area of interest. In addition, the effects due to the 1-kilometre-long salt marsh could be further investigated.

To reduce the number of SWAN runs and thus computational effort, a total of 25 cases are selected to represent the 142 empirical extremes. This number could be increased, to for example 100 cases, to decrease possible errors by the surrogate model (Camus et al., 2011a). Furthermore, a similar point of discussion to Section 7.2 can be addressed. The surrogate model is trained using limited empirical data to describe extreme events. In addition, significant levels of SLR are included in the offshore-nearshore transformation. The water levels for which the design fails are in the order of NAP +9.5 meters, while the surrogate is trained for water levels up to NAP +5.4 meters. The physical behaviours of the waves for these larger water levels could be different. The extrapolation of the surrogate model to these larger water levels could thus be questioned.

7.5 The Design and Clay-Erosion failure mechanism

In creating the designs several assumptions were made. These assumptions range from loading conditions to the scope of the design. The critical cross-section of the WGD was determined by studying three locations resulting from the offshore-nearshore transformations. The water level was assumed constant along the dike's trajectory. The location of the critical cross-section for the deterministic design was different than for the probabilistic design. In the adaptive designs, only the critical location resulting from the probabilistic design was considered. It could be that the actual critical cross-section of the WGD was not one located at one of these three locations.

The storm duration and progression were assumed constant for all extremes, with a storm duration and profile according to Deltares (2015). The extreme water levels were reduced to 18-hour average storm conditions based on the assumed storm profile. The water level extremes for which the design failed, corresponded to significant return periods. Nevertheless, storms with such return levels could have a different storm duration and profile. The assumption that the 18-hour storm average is governing resulted from Delta Flume tests and Sweco's calculations (Sweco, 2021c). For longer storm durations, the governing storm average could also change.

The assessed clay-erosion failure mechanism for the WGD is unique and case-specific. The outer slope of the embankment of 1:7 resulted in an adaptation of the model used to assess the mechanism. The adaptations resulted from multiple Delta Flume tests by Deltares (Sweco, 2021b). The formula results from minimizing the error of the fit for a range of tests in the Delta Flume. Hence, the formula has an intrinsic prediction error that should be accounted for (Deltares, 2020). In addition, such a case-specific failure mechanism results in a larger uncertainty in the range of applications compared to a widely used and better-studied mechanism. The inaccuracy of the clay-erosion formula increases as it is used for situations outside of which it is tested. For example, the application is restricted to a wave steepness

between [0.01, 0.05]. For waves outside this range, a wave steepness of $s_{op} = 0.05$ is applied. Such assumptions could skew the results and it could be advised to perform a greater number of Delta Flume tests or account for an additional margin of safety for the design.

To create the WGD design and geometry, several assumptions are included. First of all, the construction of the WGD starts at the end of the inner berm next to the road at NAP +3.05 meters and is constructed seawards. It follows the inner slope of $\alpha = 1 : 3$ until the design crest height is reached. The crest width results from the design clay thickness, with a minimum width of 1 meter. At the seaward side, an outer berm is located as NAP +3.55 meters to act as a maintenance road. These aspects resulted from the WGD demonstration project designed by Sweco. However, whether these principles are similar for the full project along the entire trajectory is not known. In addition, the design results from the assessed failure mechanism. The required additional height and thickness, due to e.g. soil subsidence and construction margins, are not taken into account.

Another important assumption is made for the foreshore. It is not considered that the salt marsh grows or shrinks over time, it is assumed to remain at the current height. This assumption is to simplify the design. Much is unknown about the potential accumulation of sediment at the foreshore of the WGD for different SLR scenarios. Marijnissen et al. (2020) showed that the accretion of the foreshore could even outpace SLR for milder SLR scenarios and thus could play an important role in flood risk safety.

7.6 Adaptive Design Strategies and the Clay Ripening process

To cope with the uncertainty in SLR, the incorporation of an adaptive design strategy for the WGD is explored. To select a preferable strategy, several assumptions are made. The emphasis lay on selecting a strategy that fits into the main WGD project's aims. Aspects such as minimizing the required clay during the construction phases, exploring the business case, the up-scaling of the clay refinery and the Natura 2000 area were considered. For each aspect, a point of discussion could be made.

While minimizing the required clay during the 1st construction phase was emphasized, each of the strategies could be constructed if the ED2050 program goals are met. A reduction of the required amount would thus result in an excess of clay. This clay could be used as an export product for other projects and thus beneficial. However, an excess could be unfavourable by introducing for example disposal costs. In addition, it is assumed that the ED2050 goal of capturing one million tons of (dry) silt each year remains constant along the design life of the WGD. Retrieving such large quantities of sediment each year could affect the growth of the salt marshes. Flood risk safety would benefit from the growth of the salt marshes, which could partly compensate for SLR. Hence, this goal could be altered in the future for flood risk safety.

Introducing adaptive design strategies results in benefits that compound in time. In this work, a fixed interest rate of 4% and a fixed inflation rate of 2% are accounted for. These assumptions are based on historical averages. Therefore, great care should be taken when examining the results. Due to the fixed rates and the large design life, the compounded interest benefits the most adaptive strategies. The disruption of the Natura 2000 area could also be included in the costs for each adaptation. The case of incorporating an adaptive strategy is contradictory. On one hand, constructing the WGD in one go could result in over-designing. Therefore, significant parts of the Natura 2000 area could be lost. A more adaptive strategy could mitigate this potential loss. On the other hand, the mild outer slope and the connection of the WGD with the Natura 2000 area could provide benefits for the ecology and the Natura 2000 area could extend up the outer slope. In addition, introducing adaptations could harm the recovery process of the Natura 2000 area. To conclude, there is a range of multidisciplinary arguments for and against introducing an adaptive design strategy. Several of which lie outside the scope of this thesis.

At last, the capacity of the clay refinery and construction times were assumed based on the latest studies and projections. These could change in the future. The capacity of the clay refinery is greatly dependent on the ED2050 program and weather conditions. Electric equipment needed to construct near a Natura 2000 area is still scarce and upcoming. As the construction starts in 2043, it is assumed that the availability of such equipment is sufficient.

8 | Conclusion & Recommendations

This chapter covers the key conclusions of this thesis and aims to answer the proposed research questions in Section 8.1. The recommendations resulting from these findings are found in Section 8.2.

8.1 Conclusion

The WGD project is a project that combines flood risk safety and sustainability. Hydraulic structures like the WGD are designed to withstand extreme natural events. Studying the joint behaviour of the variables of interest could provide additional insights to determine realistic loads and help optimize the design. Vine copulae are a technique for multivariate modelling and provide a tool to study the dependence structures between the variables. This thesis aimed to apply vine copulae to model the multivariate probabilities of the hydraulic loads for the WGD given the uncertainty of SLR. The knowledge gathered from the multivariate analysis was applied to assess its design and explore the possible adaptive design strategies for the project. The main objective of the thesis is stated by ‘*develop a multivariate probabilistic tool to provide insight into incorporating adaptive design strategies, and to gain extra information that contributes to assessing the feasibility of the Wide Green Dike concept given the uncertainty of sea level rise*’. This objective was achieved by answering three research questions.

RQ 1: *Can a Non-stationary Extreme Value Analysis be applied in a multivariate design approach using Vine-Copulae?*

Investigating the application of a non-stationary marginal of the extreme water level with the wave height as covariate into the dependence structure described by a copula, resulted in the conclusion that a NEVA cannot be applied in copula modelling if the covariate is one of the nodes in the copula. A copula builds the dependence structure of a variable pair based on the ranks of the variables. In order to preserve the dependence structure, the transformation from unity to variable space must be increasingly monotonic. A non-stationary applies a different transformation to each sample based on its covariate. Therefore, the transformations are not increasingly monotonic and thus the dependence structure is not preserved. These findings resulted in creating the lemma shown here. Note, accounting for non-stationarity is possible with time as covariate as shown by Coles et al. (2001). However, it could be questioned whether accounting for SLR based on its historical trend is representative of the future SLR trend.

Lemma. (Copula modelling with a Non-stationary marginal and a node as covariate).
Consider $F_{X,y}$ with covariate y , in which y is a node of the copula, as the non-stationary marginal distribution and F_Y as the (stationary) marginal distribution of the random variables X and Y , respectively. Let $\mathbf{C}(u,v)$ be the copula describing the joint distribution function F_{XY} of the two random variables X and Y , in which $F_{X,y}(x) = u$ and $F_Y(y) = v$. Then, the transformations of X or Y are not increasingly monotonic, implying that the dependence structure is not preserved, as stated in Equation 8.1.

$$F_{XY}\left(F_{X,y}^{[-1]}(u), F_Y^{[-1]}(v)\right) \neq \mathbf{C}(u,v), \quad (8.1)$$

for any $(u,v) \in \mathbb{I}^2$. Where, $F_{X,y}^{[-1]}$ and $F_Y^{[-1]}$ denote, respectively, the quasi-inverses of $F_{X,y}$ and F_Y .

This result led to the use of a stationary marginal distribution to describe the extreme water level. Accordingly, the defined ‘extreme event’ by the POT method remains constant in time. To account for SLR in vine copula modelling, changing the stationary distribution or changing the dependence structure for a particular moment in time could be introduced. This thesis showed the implementation of SLR using the marginal distribution of the water level. To create a design with a different design life, a different marginal distribution of the SLR is accounted for.

RQ 2: *What are the design differences between a multivariate probabilistic design and a deterministic design for the Wide Green Dike project?*

Significant differences are found when comparing the vine-based and deterministic designs. The design values from the deterministic design are significantly larger than the design values for which

the vine-based design failed. The design water level of the deterministic design is NAP +9.95 meters, compared to NAP +9.53 which is the median of the failures from the vine-based design. The wave height was more significant at 1.96 meters compared to (reduced nearshore) wave heights ranging from 0.8 to 0.9 meters for the vine-based design. Note, the vine-based design showed that the water level is the governing variable for failure. Therefore, a lower wave height paired with an extreme water level can already result in failure.

The large differences in design values and the full probabilistic approach to assess the clay erosion in the vine-based design resulted in significant differences in the dimensions of the WGD, as shown in Figure 8.1. Considering a deterministic approach would result in an additional 2 meters of crest height compared to the vine-based design with a crest height of NAP +9.25 meters. The design clay layer thickness would increase in the order of 56%, resulting in a thickness of 1.45 meters compared to 0.93 meters. The increase in crest height and clay layer thickness have significant consequences for the cross-sectional area of the WGD. This is due to the mild outer slope of 1:7, resulting that a small increase in crest height or layer thickness resulting in significant volume increases. The deterministic design has a cross-sectional area of $241 \text{ m}^3/\text{m}$ compared to $98 \text{ m}^3/\text{m}$ for the vine-based design.

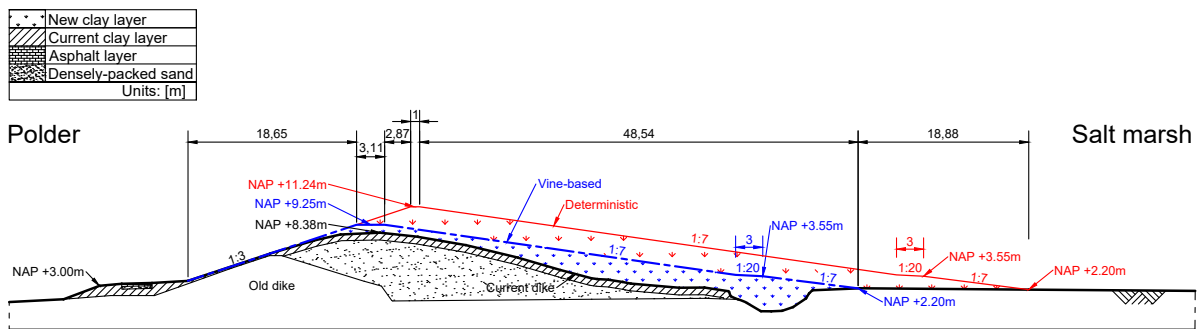


Figure 8.1: The vine-based and deterministic designs of the WGD for the year 2150.

From the results, it is concluded that accounting for the dependence structures of the design variables by a multivariate approach such as vine copulae, can be of added value for the WGD project. Where a deterministic approach simply combines the extreme loads, the multivariate approach considers the joint behaviour of the extremes. The gained knowledge of the joint behaviour of the local extreme conditions results in a better-optimized design. In addition, considering a full probabilistic assessment compared to a deterministic one can optimize the design further. This could result in a reduction of the WGD dimensions and thus a reduction of the intrusion into the Natura 2000 area.

RQ 3: *How can incorporating an adaptive design strategy to the Wide Green Dike concept promote its feasibility given the uncertainty of sea level rise?*

In this thesis, the incorporation of adaptive design strategies for the WGD is explored. Four adaptive strategies were created and assessed against a baseline strategy, which constructs the WGD for 2150 in one go. The strategies were formed by combining different designs with different designs lives in multiple construction phases. The strategies were assessed based on the following requirements: the required clay needed during the construction phases, the up-scaling of the clay refinery of the ED2050 program, potential benefits and the effects on the Natura 2000 area.

The exploration showed that incorporating an adaptive design strategy into the WGD project can promote its business case and help mitigate the risk of over-designing. The potential benefits from including an adaptive strategy could compound into significant values over time. It also helps lower the risk of over-designing, which would result in a loss of the Natura 2000 area. From the analysis, Strategy 2 was preferred. This strategy included two adaptation phases after the construction of the 2090 design in the 1st construction phase, as shown in Figure 8.2. Including a limited amount of reinforcements was found beneficial as the disruption in the Natura 2000 area would be limited.

However, due to the uncertainty of SLR, the most adaptive design strategies resulted in the largest benefits.

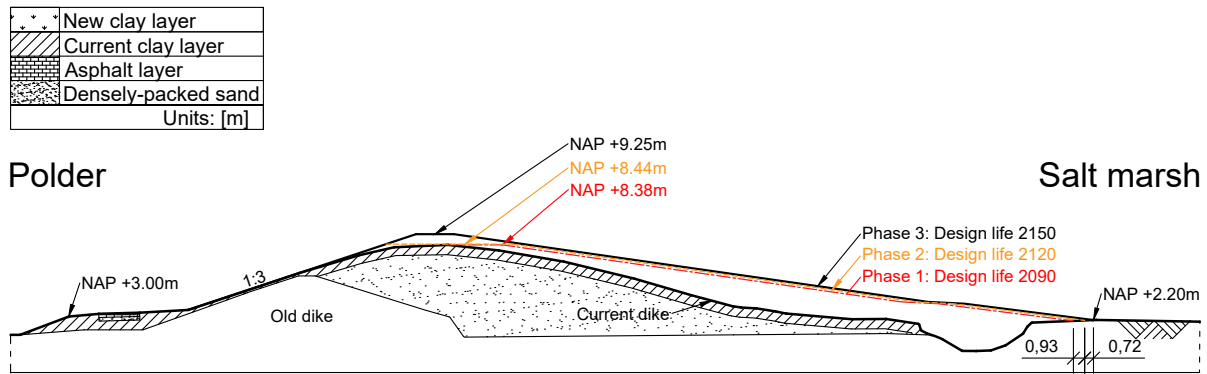


Figure 8.2: The cross-section and construction phases of the selected adaptive design strategy.

To summarize the overall conclusion of the thesis, the main research question is answered, as stated here:

How can a multivariate probabilistic tool provide insight into incorporating adaptive design strategies and how could it provide additional insights regarding the feasibility of the Wide Green Dike concept given the uncertainty of sea level rise?

In this thesis, it was found that a multivariate design approach could result in significant insights for the WGD in the Ems-Dollard area. The vine-based design showed that significant reductions in the loading conditions could be made when compared to a deterministic design. This resulted in a better-optimized design for the vine-based approach, with a significantly smaller cross-sectional area as shown in Figure 8.1. The vine-based design resulted in less intrusion into the Natura 2000 area, which is of great importance for the WGD project.

The vine-based design approach was used to create the designs that were applied in the adaptive design strategies. These designs helped to assess different strategies and their feasibility. It was concluded that an adaptive design strategy could be beneficial for the WGD project. However, the number of construction phases for a strategy should be limited. A large number of adaptations could negatively impact the Natura 2000 area. A strategy with two reinforcements was found optimal in this thesis. In the 1st construction phase, it was found that a design up to 2090 was most beneficial.

8.2 Recommendations for future work

The recommendations based on the conclusions, points of discussion and limitations are discussed below.

8.2.1 Case Study: The Wide Green Dike

Measurement Program Ems-Dollard:

To provide greater insight into the local hydraulic conditions in the Ems-Dollard a 12-year-long measurement program is initiated in 2019 by Waterboard Noorderzijlvest (2019). In the program, measurements of storms are taken at the dike. The findings and conclusions of this program could be of great value to gaining further insights into the hydraulic conditions in the Ems-Dollard estuary. The findings could also be a great opportunity to create a nearshore multivariate model. Nonetheless, it is recommended to extend the program. The program could be used to gain insight into the behaviour of extreme conditions. However, as the design is based on extremes with return periods in the order of 38,000 years, large extrapolations are still necessary. Such extrapolations are paired with large uncertainties in the estimation models. In addition, if an adaptive design strategy would be proposed in the WGD project,

having up-to-date data on the hydraulic boundary conditions, e.g. water level and wave height, available is crucial for the planning of possible adaptations. Thus, extending such measurement programs to larger time periods (50+ years) is highly recommended.

Incorporating an Adaptive Design Strategy:

It is recommended to do further research on possible adaptive design strategies for the WGD. This thesis explored the possibility of incorporating an adaptive design strategy. The exploration showed possible benefits in reducing the required clay during a construction phase and mitigating the risk of over-designing. It is advised to study the consequences of an adaptive strategy for the Natura 2000 area. The area is disrupted during the adaptation phases, and the consequences of such disruptions could have a significant impact on the adaptive strategy to be chosen. In addition, the logistics around adaptive design strategies, e.g. construction time and permit applications, should be investigated further. It could be favourable to decrease the construction time of an adaptation. However, this would increase the required clay capacity. Moreover, aspects such as license applications could limit the number of possible adaptations. Also, the effects on the clay layer should be investigated. The introduction of adaptations results in a final design which contains several layers of clay that are constructed at different time periods. The effect of interaction between those layers could negatively impact the resistance of the final design, such effects should be investigated.

Up-scaling of the Clay Refinery:

The pilot studies that were shared in the webinar ‘Kleirijpen voor dijkversterking’ by Deltares (2023) regarding the up-scaling of the clay refinery will be published in the near future. It is recommended to study these publications in assessing the design strategy for the WGD. These publications include the future projections of the capacity of the clay refinery in the Ems-Dollard estuary, expected clay characteristics, and the business case of the clay refinery. The clay capacity and business case provide information about the availability of clay and are of large importance in the assessment of adaptive design strategies. A positive business case of the clay refinery could benefit the adaptive design strategies.

Updated Climate Change Scenarios:

This thesis accounts for the SLR projections according to the ‘Klimaatsignaal 21’ by KNMI (2021). The updated version ‘Klimaatsignaal 23’ will be published in October 2023. This publication could provide new insights into SLR scenarios.

8.2.2 Results of the Multivariate Design

Goodness-of-fit of Vine Copulae:

In the selection of a vine copula, it is recommended to assess the predicted against the empirical exceedance probabilities for all vines considered. In this work, this assessment was performed graphically for a limited number of vines from a preselection using the AIC. A goodness-of-fit criteria such as the coefficient of determination could be introduced to review the goodness-of-fit on the empirical exceedance probabilities. This criterion could be used in combination with the AIC to select the best vine copula. Especially in extreme value modelling, the goodness-of-fit at the tail of the exceedance probabilities is of large importance. Including this criterion at the start of the selection could therefore be of value. In addition, great care should be taken in selecting a vine copula using the MST algorithm introduced by Dissmann et al. (2013). The results based on the AIC showed poor performance of the algorithm for this specific dataset.

Surrogate model for the Offshore-Nearshore Transformation:

It is recommended to study the limitations of a surrogate model in the offshore-nearshore transformation of waves. A surrogate model can be used to significantly reduce the computational effort in performing a large number of offshore-nearshore transformations. However, to design for extreme conditions and include SLR, the surrogate model is extrapolated to larger values than what it is trained on. Additional research on the performance of the surrogate model for extreme conditions would provide great insights into the applicability of the model.

8.2.3 Future Applications of a Multivariate Approach

Including Additional Nodes:

In this work, the vine-based design is created using five variables. Morales-Nápoles et al. (2023) showed the potential of performing multivariate analysis of up to eight variables and provided the atlas containing all unique (regular) vine combinations. It is recommended to increase the number of nodes in the multivariate model to assess some of the assumptions made in this work. An assumption that could be investigated is the offshore wave direction being equal to the wind direction during extreme conditions.

Nearshore Multivariate model:

Creating a multivariate model for purely nearshore conditions could be of great interest to study the dependence structure of the variables near the dike. Such a model could also be used as a surrogate model. The vines could be fitted to the output of a numerical model. This creates the possibility to describe the dependence structure of the numerical model and then sample from this copula for the hydraulic structure design. The performance of such a model could be compared to the performance of the surrogate model based on RBFs. It could be interesting to compare the two models in their performance of the extrapolation of the water level due to SLR.

Accounting for Sea Level Rise:

To account for SLR in copula modelling, it was concluded that the historical trend of SLR might not be representative of the future SLR trend. Therefore, combining NEVA with copula modelling with time as covariate was not performed. Nevertheless, it is interesting to determine the effect of a changing dependence structure between the water level and other design variables due to SLR.

References

- Akaike, H. (1974). A new look at the statistical model identification. *IEEE Transactions on Automatic Control*, 19(6):716–723.
- Anderson, C., Carter, D., and Cotton, P. (2001). Wave climate variability and impact on offshore design extremes. *Report commissioned from the University of Sheffield and Satellite Observing Systems for Shell International*.
- Bommier, E. (2014). Peaks-over-threshold modelling of environmental data. *Uppsala University*, MSc thesis.
- Booij, N., Ris, R. C., and Holthuijsen, L. H. (1999). A third-generation wave model for coastal regions: 1. model description and validation. *Journal of geophysical research: Oceans*, 104(C4):7649–7666.
- Bowers, J., Morton, I., and Mould, G. (2000). Directional statistics of the wind and waves. *Applied Ocean Research*, 22(1):13–30.
- Brechmann, E. (2010). Truncated and simplified regular vines and their applications. <https://mediatum.ub.tum.de/?id=1079285>.
- Camus, P., Mendez, F., and Medina, R. (2011a). A hybrid efficient method to downscale wave climate to coastal areas. *Coastal Engineering*, 58(9):851–862.
- Camus, P., Mendez, F. J., Medina, R., and Cofiño, A. S. (2011b). Analysis of clustering and selection algorithms for the study of multivariate wave climate. *Coastal Engineering*, 58(6):453–462.
- Coles, S., Bawa, J., Trenner, L., and Dorazio, P. (2001). *An introduction to statistical modeling of extreme values*, volume 208. Springer.
- Cooke, R. and Bedford, T. (2001). Probability Density Decomposition for Conditionally Dependent Random Variables Modeled by Vines. *Annals of Mathematics and Artificial Intelligence*, 32.
- Cooke, R. M. (1997). Markov and entropy properties of tree-and vine-dependent variables. In *Proceedings of the ASA section of Bayesian statistical science*, volume 27.
- Couason, A., Sebastian, A., and Morales-Nápoles, O. (2018). A copula-based bayesian network for modeling compound flood hazard from riverine and coastal interactions at the catchment scale: An application to the houston ship channel, texas. *Water*, 10(9):1190.
- Cunnane, C. (1979). A note on the poisson assumption in partial duration series models. *Water Resources Research*, 15(2):489–494.
- Davison, A. C. and Smith, R. L. (1990). Models for exceedances over high thresholds. *Journal of the Royal Statistical Society: Series B (Methodological)*, 52(3):393–425.
- Delignette-Muller, M. L. and Dutang, C. (2020). fitdistrplus. An R Package for Fitting Distributions. <https://cran.r-hub.io/web/packages/fitdistrplus/index.html>. Version 1.1-8.
- Deltares (2011). Extreme value analysis: Wave data. *Deltares*, 1200129-000-HYE-0003.
- Deltares (2012). Erosie van een dijk na bezwijken van de steenzetting door golven. *Technical Report*, 1204200-008-HYE0008.
- Deltares (2015). Waterstandsverlopen kust. wettelijk toetsinstrumentarium wti-2017. *Deltares*, 1220082-002-HYE-0003(2).
- Deltares (2020). Prediction of the erosion velocity of a slope of clay due to wave attack. *Technical Report*, 1209437-017-HYE-0003 v4.0.
- Deltares (2022a). Erosie van kleibekleding met gras op boventalud van Waddenzeedijken. *Technical Report*, 11204841-006-HYE-0011.

- Deltares (2022b). Onderzoek Geschiktheid Deltaklei in kader van demonstratieproject Brede Groene Dijk. *Technical Report*, 11207091-006-GEO-0003.
- Deltares (2023). K&I Café: Kleirijpen voor dijkversterking. <https://www.deltares.nl/evenementen/k-i-cafe-kleirijpen-voor-dijkversterking>. Webinar.
- Dewar, J. A., Builder, C. H., Hix, W. M., and Levin, M. H. (1993). Assumption-based planning; a planning tool for very uncertain times. Technical report, RAND CORP SANTA MONICA CA.
- Di Bucchianico, A. (2008). Coefficient of determination (r^2). *Encyclopedia of statistics in quality and reliability*.
- Dijk, S. (2022). ED2050 Program Brede Groene Dijk. <https://eemsdollar2050.nl/project/brede-groene-dijk/>.
- Dissmann, J., Brechmann, E. C., Czado, C., and Kurowicka, D. (2013). Selecting and estimating regular vine copulae and application to financial returns. *Computational Statistics & Data Analysis*, 59:52–69.
- Duits, M. (2020). Hydra-NL Gebruikershandleiding. *HKV lijn in water*, versie 2.8.
- ECMWF (2022). ERA5 hourly data on single levels from 1940 to present. Copernicus Climate Change Service (C3S). Climate Data Store (CDS). <https://cds.climate.copernicus.eu/cdsapp#!/dataset/reanalysis-era5-single-levels?tab=form>.
- EMODnet (2016). HRDTM 1/512 Ems approach - Version 2. European Marine Observation and Data Network (EMODnet). Federal Maritime and Hydrographic Agency. <http://www.emodnet-bathymetry.eu>.
- Epicum, S., Crookston, B., Bombardelli, F., Bung, D., Felder, S., Mulligan, S., Oertel, M., and Palermo, M. (2020). Hydraulic structures engineering: An evolving science in a changing world. *Wiley Interdisciplinary*, Volume 8, Issue 2.
- European Commission (n.d.). Eurocodes: building the future. *Technical report, European Commission*.
- Ferber, M. (2023). The rocky path to inflation reduction. *Intereconomics*, 58(3):148–150.
- Ferro, C. A. T. and Segers, J. (2003). Inference for clusters of extreme values. *Journal of the Royal Statistical Society: Series B (Statistical Methodology)*, 65(2):545–556.
- Genest, C., Quessy, J.-F., and Rémillard, B. (2006). Goodness-of-fit procedures for copula models based on the probability integral transformation. *Scandinavian Journal of Statistics*, 33(2):337–366.
- Gilleland, E. (2022). 'extRemes'. <https://cran.r-project.org/web/packages/extRemes/index.html>. Version 2.1-2.
- Gumbel, E. (1958). *Statistics of Extremes*. Columbia University Press.
- Haasnoot, M., Kwakkel, J. H., Walker, W. E., and ter Maat, J. (2013). Dynamic adaptive policy pathways: A method for crafting robust decisions for a deeply uncertain world. *Global Environmental Change*, 23(2):485–498.
- Haasnoot, M., Middelkoop, H., Van Beek, E., and Van Deursen, W. P. A. (2011). A method to develop sustainable water management strategies for an uncertain future. *Sustainable Development*, 19(6):369–381.
- Hardy, R. (1990). Theory and applications of the multiquadric-biharmonic method 20 years of discovery 1968–1988. *Computers & Mathematics with Applications*, 19(8):163–208.
- Harrell Jr., F. (2023). Hmisc. HarrellMiscellaneous. <https://cran.r-project.org/web/packages/Hmisc/index.html>. Version 5.0-1.
- Hildebrandt, A., Schmidt, B., and Marx, S. (2019). Wind-wave misalignment and a combination method for direction-dependent extreme incidents. *Ocean Engineering*, 180:10–22.

- Hosking, J. R. M. (1986). *The theory of probability weighted moments*. IBM Research Division, TJ Watson Research Center New York, USA.
- Huang, W. and Prokhorov, A. (2014). A goodness-of-fit test for copulas. *Econometric Reviews*, 33(7):751–771.
- IPCC (2022). *Climate Change 2022: Impacts, Adaptation and Vulnerability. Contribution of Working Group II to the Sixth Assessment Report of the Intergovernmental Panel on Climate Change*. Cambridge University Press.
- Joe, H. and Kurowicka, D. (2011). *Dependence modeling: vine copula handbook*. World Scientific.
- Kalverla, P. C., Holtslag, A. A. M., Ronda, R. J., and Steeneveld, G.-J. (2020). Quality of wind characteristics in recent wind atlases over the north sea. *Quarterly Journal of the Royal Meteorological Society*, 146(728):1498–1515.
- Kennard, R. W. and Stone, L. A. (1969). Computer aided design of experiments. *Technometrics*, 11(1):137–148.
- Kirchhoff, J. (1992). *Über den Strassen von Torum*. Risius.
- KNMI (2006). KNMI Climate Change scenarios 2006 for the Netherlands. *KNMI Scientific Report*, WR 2006-01.
- KNMI (2021). Klimaatsignaal’21: hoe het klimaat in Nederland snel verandert. *KNMI, De Bilt*, page 72.
- KNMI (2022). Daggegevens van het weer in Nederland. <https://www.knmi.nl/nederland-nu/klimatologie/daggegevens>.
- Kurowicka, D. and Cooke, R. M. (2006). *Uncertainty analysis with high dimensional dependence modeling*. John Wiley & Sons.
- Kurowicka, D. and Cooke, R. M. (2007). Sampling algorithms for generating joint uniform distributions using the vine-copula method. *Computational statistics & data analysis*, 51(6):2889–2906.
- Kwakkel, J. H., Walker, W. E., and Marchau, V. (2010). Adaptive airport strategic planning. *European Journal of Transport and Infrastructure Research*, 10(3).
- Lenk, S., Rybski, D., Heidrich, O., Dawson, R. J., and Kropp, J. P. (2017). Costs of sea dikes-regressions and uncertainty estimates. *Natural Hazards and Earth System Sciences*, 17(5):765–779.
- Maechler, M. (2023). copula. Multivariate Dependence with Copulas. <https://cran.r-project.org/web/packages/copula/index.html>. Version 1.1-2.
- Marijnissen, R., Esselink, P., Kok, M., Kroeze, C., and van Loon-Steensma, J. M. (2020). How natural processes contribute to flood protection-a sustainable adaptation scheme for a wide green dike. *Science of The Total Environment*, 739:139698.
- Micchelli, C. A. (1984). *Interpolation of scattered data: distance matrices and conditionally positive definite functions*. Springer.
- Morales-Nápoles, O., Rajabi-Bahaabadi, M., Torres-Alves, G. A., and ’t Hart, C. M. P. (2023). Chimera: An atlas of regular vines on up to 8 nodes. *Scientific Data*, 10(1):337.
- Morales-Nápoles, O., Cooke, R., and Kurowicka, D. (2010). About the number of Vines and Regular Vines on n Nodes. *Delft University of Technology*.
- Nagler, T. (2023). VineCopula. Statistical Inference of Vine Copulas. <https://cran.r-project.org/web/packages/VineCopula/index.html>. Version 2.4.5.
- Nationaal, D. (2022). Brede groene dijk wint het Zonnetje. Deltanieuws Nationaal Deltacongres 2022. <https://magazines.deltaprogramma.nl/deltanieuws/2022/04/zonnetje>.

- Navarro, I. J., Yepes, V., and Martí, J. V. (2020). Sustainability assessment of concrete bridge deck designs in coastal environments using neutrosophic criteria weights. *Structure and Infrastructure Engineering*, 16(7):949–967.
- Novomestky, F. (2016). `truncdist`. Truncated Random Variables. <https://cran.r-project.org/web/packages/truncdist/index.html>. Version 1.0-2.
- Official Journal of the European Union (2016). Paris Agreement. <https://eur-lex.europa.eu/content/paris-agreement/paris-agreement.html>.
- Picklands, J. (1975). Statistical inference using extreme order statistics. *the Annals of Statistics*, 3(1):119–131.
- Polinsky, A., Feinstein, R. D., Shi, S., and Kuki, A. (1996). Librain: Software for automated design of exploratory and targeted combinatorial libraries. *Molecular diversity and combinatorial chemistry: Libraries and drug discovery*, 219:232.
- Ribatet, M. A. (2011). A User Guide to the POT Package. <https://cran.r-project.org/web/packages/POT/index.html>. Version 1.1-10.
- Rijksoverheid (2022). Het Nationaal Water Programma 2022-2027. <https://www.helpdeskwater.nl/onderwerpen/wetgeving-beleid/nationaal/nationaal-water-programma-2022-2027/>.
- Rijkswaterstaat (2022). Waterinfo. In Waterinfo vindt u actuele, verwachte én historische meetgegevens over de rijkswateren. <https://waterinfo.rws.nl/#!/bulkdownload/kaart/>.
- Rippa, S. (1999). An algorithm for selecting a good value for the parameter c in radial basis function interpolation. *Advances in Computational Mathematics*, 11:193–210.
- Salas, J. and Obeysekera, J. (2014). Revisiting the concepts of return period and risk for nonstationary hydrologic extreme events. *Journal of Hydrologic Engineering*, 19:554–568.
- Salvadori, G., De Michele, C., Kottegoda, N., and Rosso, R. (2007). Extremes in nature. an approach using copulas. *Springer Dordrecht*.
- Schepsmeier, U. (2019). A goodness-of-fit test for regular vine copula models. *Econometric Reviews*, 38(1):25–46.
- Schwarz, G. (1978). Estimating the dimension of a model. *The annals of statistics*, pages 461–464.
- Shumway, R. and Stoffer, D. (2011). *Time Series Analysis and Its Application with R Examples*. Springer Texts in Statistics.
- Sklar, M. (1959). Fonctions de repartition an dimensions et leurs marges. *Publ. inst. statist. univ. Paris*, 8:229–231.
- Sweco (2021a). Motivatie keuze voor combineren faalmechanismen GEBU en GEKB. *Sweco Nederland*, NL21-648800269-3169.
- Sweco (2021b). Ontwerprapport Brede Groene Dijk. *Sweco Nederland*, NL21-648800269-2801.
- Sweco (2021c). Oplegnotitie Definitief Ontwerp Brede Groene Dijk. *Sweco Nederland*, NL21-648800269-6196.
- Sweco (2021d). Vergelijking erosieprofiel Deltagoot en berekend. *Sweco Nederland*, NL21-648800269-3185.
- The SWAN Team (2023). SWAN User Manual. https://swanmodel.sourceforge.io/online_doc/swanuse/swanuse.html. SWAN Cycle III version 41.45.
- Timmermans, M. (2021). A practical assessment of the impact of using multivariate statistical models in the design of coastal infrastructure. *Delft University of Technology*, MSc thesis.

- Tosunoglu, F., Gürbüz, F., and İspirli, M. N. (2020). Multivariate modeling of flood characteristics using vine copulas. *Environmental Earth Sciences*, 79:1–21.
- van Aalst, J. (2021). OpenStreetmap, BAG, TOP10NL. <https://www.imergis.nl/>.
- Walker, W. E., Haasnoot, M., and Kwakkel, J. H. (2013). Adapt or perish: A review of planning approaches for adaptation under deep uncertainty. *Sustainability*, 5(3):955–979.
- Wang, W. and Wells, M. T. (2000). Model selection and semiparametric inference for bivariate failure-time data. *Journal of the American Statistical Association*, 95(449):62–72.
- Waterboard Hunze and Aa’s (2022). Proefproject Brede Groene Dijk. <https://www.hunzeenaas.nl/projecten/brede-groene-dijk/brede-groene-dijk/>.
- Waterboard Noorderzijlvest (2019). Project Meerjarige Veldmetingen Eems-Dollard. <https://www.noorderzijlvest.nl/project-meerjarige-veldmetingen>.
- White, H. (1982). Maximum likelihood estimation of misspecified models. *Econometrica: Journal of the econometric society*, pages 1–25.
- Wolodzko, T. (2020). extraDistr. Additional Univariate and Multivariate Distributions. <https://cran.r-project.org/web/packages/extraDistr/index.html>. Version 1.9.1.
- Zachary, S., Feld, G., Ward, G., and Wolfram, J. (1998). Multivariate extrapolation in the offshore environment. *Applied Ocean Research*, 20(5):273–295.
- Zhang, Z., Stadnyk, T. A., and Burn, D. H. (2020). Identification of a preferred statistical distribution for at-site flood frequency analysis in canada. *Canadian Water Resources Journal/Revue canadienne des ressources hydriques*, 45(1):43–58.

A | Information on the Datasets used

This appendix contains information about the datasets and variables used in this thesis. Table A.1 shows the information on the datasets used and their sources, locations and the variables that each dataset contains. Table A.2 shows the information on the variables, such as start and end dates and times. The dates are provided in $[dd-mm-yyyy]$ and the times in $[hh:mm:ss]$. Note that the data amount provided in table A.2 includes NA -values. Figure A.1 shows the data points from datasets 2 and 3.

Table A.1: Information on the original datasets used in this project

Dataset	Source	Data Type	Location	Variable(s)	Symbol
1	Rijkswaterstaat (2022)	Buoy	Randzelgat	Wave height Wave period	$H_{m0,b}$ $T_{p,b}$
2	ECMWF (2022)	ERA5	53°28'12.0"N 6°53'24.0"E	Wave height Wave period	H_{m0} T_p
3	Rijkswaterstaat (2022)	Measurement	Nieuwe Statenzijl	Water level	h_{NS}
4	Rijkswaterstaat (2022)	Measurement	Dollard West	Water level	h_{DW}
5	Rijkswaterstaat (2022)	Measurement	Schansersdiep	Water level	h_{Sc}
6	Rijkswaterstaat (2022)	Measurement	Groote Gat	Water level	h_{GG}
7	Rijkswaterstaat (2022)	Measurement	Reide	Water level	h_{Re}
8	KNMI (2022)	Measurement	Nieuw Beerta Station 286	Wind speed Wind direction	w_s w_d
9	EMODnet (2016)	Bathymetry	Ems-Dollard	-	-

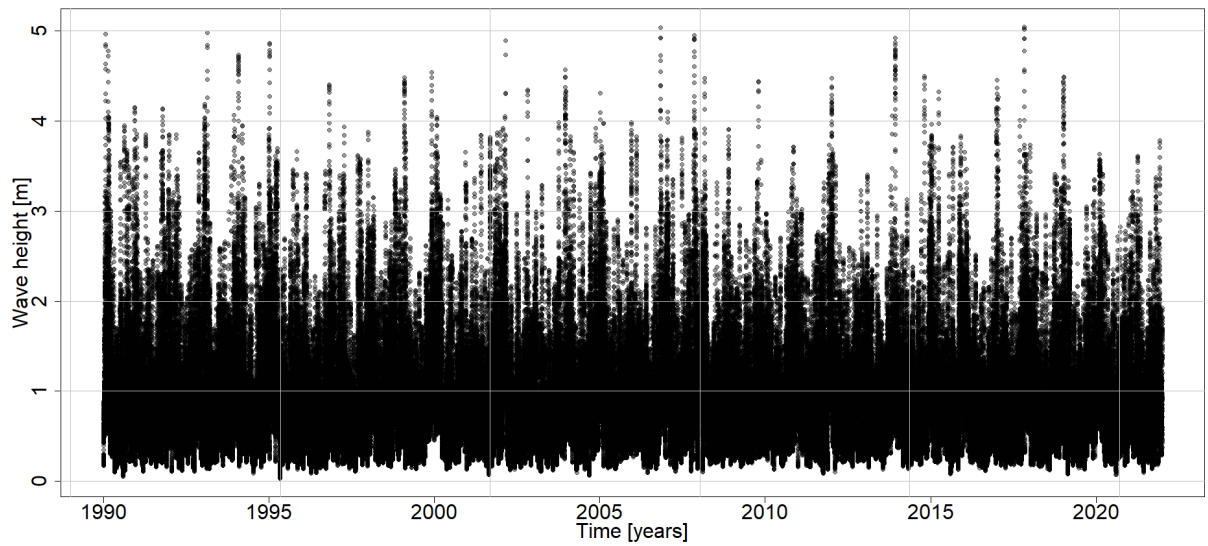
Table A.2: Information of the original wave, water level and wind variable data used in this project

Variable	Dataset	Start	End	Freq.	Data amount	Unit	Decimals
$H_{m0,b}$	1	20-08-2008 00:00:00	01-02-2021 21:30:00	10 min. ^a	654,770	[m]	2
$T_{p,b}$	1	20-08-2008 00:00:00	01-02-2021 21:30:00	10 min.	654,770	[s]	0
H_{m0}	2	01-01-1990 00:00:00	31-12-2021 23:00:00	hourly	280,512	[m]	7
T_p	2	01-01-1990 00:00:00	31-12-2021 23:00:00	hourly	280,512	[s]	7
h_{NS}	3	01-01-1990 00:00:00	31-12-2021 23:50:00	10 min.	1,726,423	[NAP+m]	2
h_{DW}	4	27-03-1996 00:00:00	04-11-1996 11:50:00	10 min.	32,040	[NAP+m]	2
h_{Sc}	5	05-04-1995 00:00:00	22-09-1997 23:50:00	10 min.	87,335	[NAP+m]	2
h_{GG}	6	21-03-1994 00:00:00	30-07-2000 23:50:00	10 min.	144,432	[NAP+m]	2
h_{Re}	7	27-03-1996 00:00:00	27-06-1996 23:50:00	10 min.	87,204	[NAP+m]	2
w_s	8	01-01-1990	09-10-2022	daily ^b	11,970	[m/s]	1
w_d	8	01-01-1990	09-10-2022	daily	11,970	[°] ^c	0

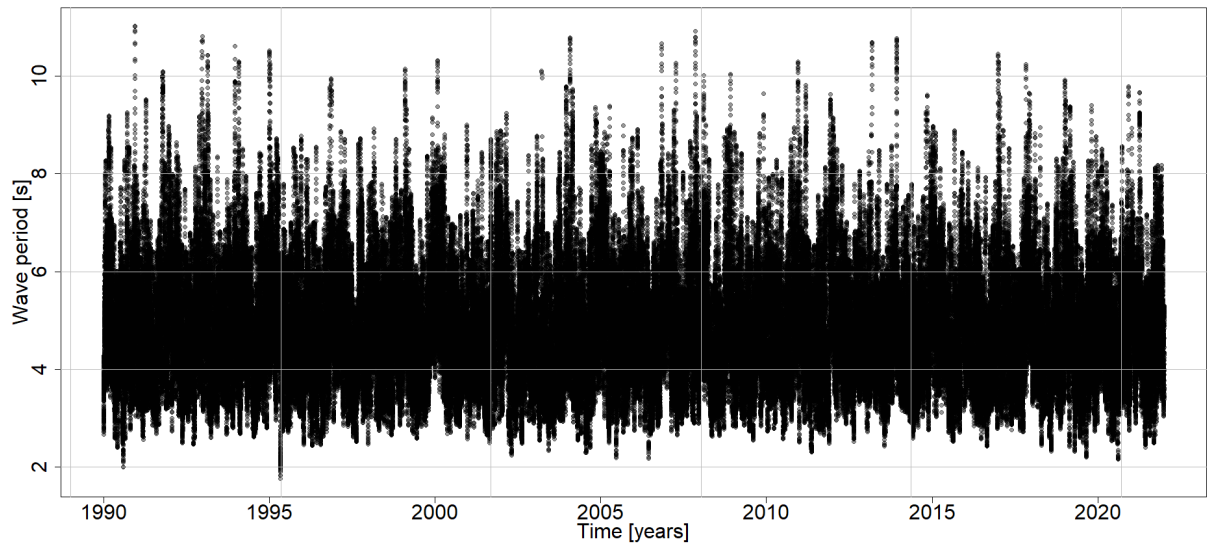
^a The measurement frequency in minutes is abbreviated to ‘min.’

^b In this dataset, the measurement frequency depends on the variable considered

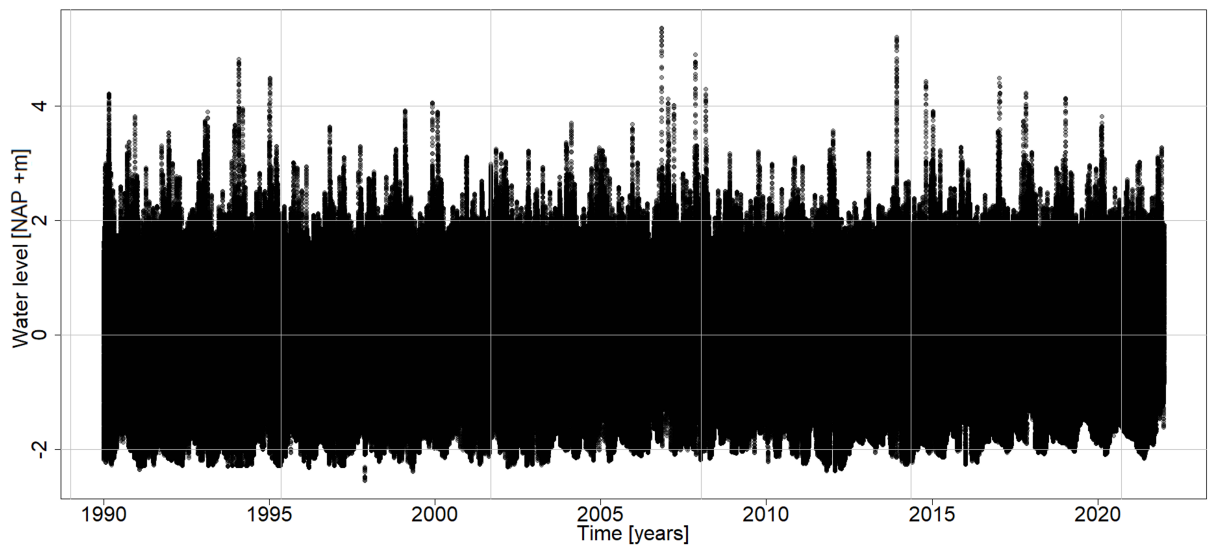
^c Degrees where: 360=North, 90=East, 180=South, 270=West, 0=windstill/varying



(a) Wave height (dataset 2)



(b) Wave period (dataset 2)



(c) Water level at Nieuwe Statenzijl (dataset 3)

Figure A.1: Data points of the water level, wave height and wave period.

B | Results Extreme Value Analysis

This appendix provides additional figures and results from the EVA. The results can be found in the following sections of the applied POT method, data overview, stationary analysis and non-stationary analysis.

Additional results of the Peaks-Over-Threshold method

Figure B.1 shows the selected extreme water levels and threshold on top of the time series of the complete water level dataset.

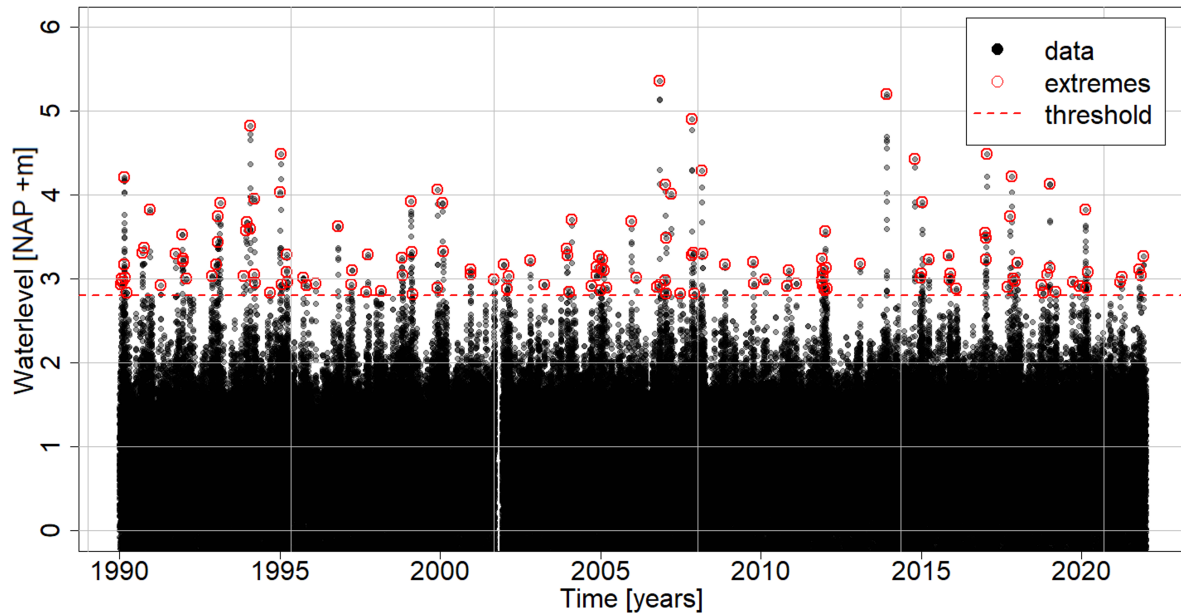
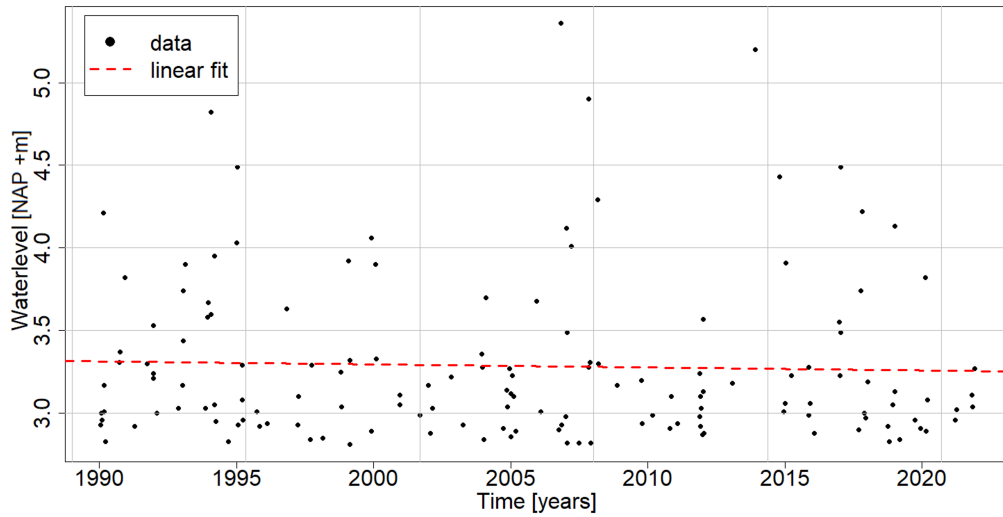


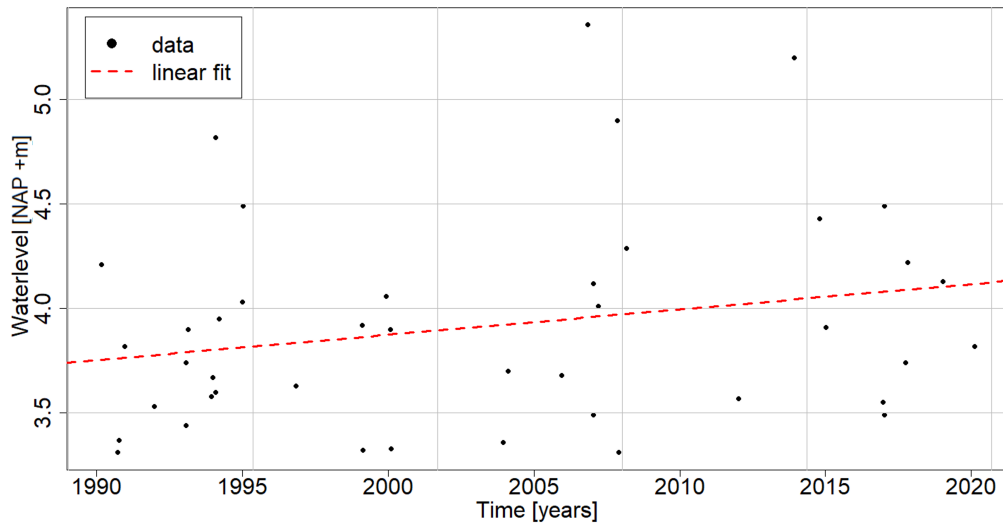
Figure B.1: Selected extreme water levels on top of the hourly water level data points.

Data overview

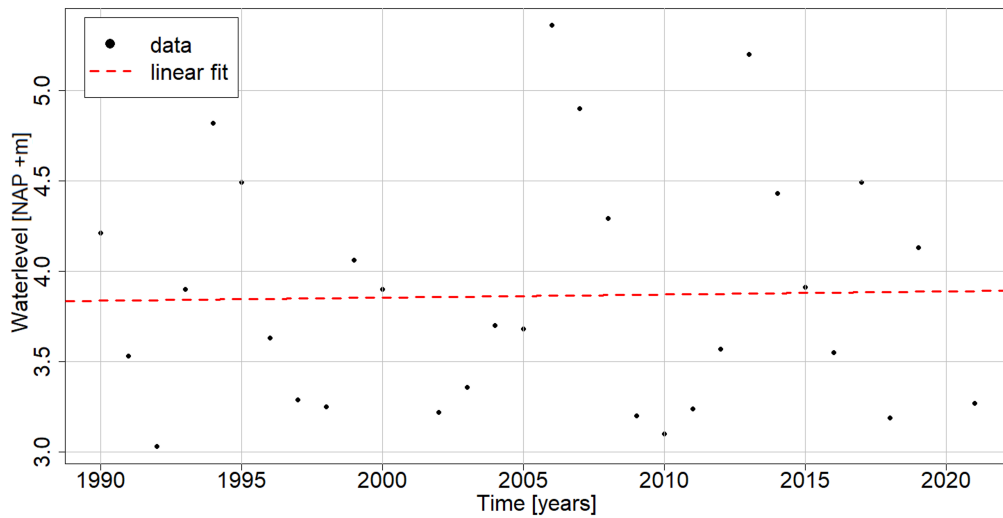
The result of the selected extreme water levels is found in Figure B.2a. It shows that when taking the water level as the dominant variable with a threshold ranging from [1.1, 3.2], the extremes do not have a clear trend over time (slightly negative). A threshold selection above 3.2 meters NAP does result in a clear positive trend over time, as shown in Figure B.2b. Similar results are found when comparing the concomitant variables (the coinciding wave height and wave period) for these thresholds. Figure B.3, in Appendix B, shows the concomitant wave height and period for a threshold of $u = 2.8$ meters NAP. The linear regression on the selected values shows a slightly decreasing trend over time. However, Figure B.4 shows that the concomitant variables for a threshold of $u = 3.3$ meters NAP result in a positive trend over time. This could be caused by a lack of data, implying that 30 years of data could be too little to observe a clear trend in the extremes over time (for this specific threshold range). It could also be because of the dependence of extremes on other events than climate change, meaning that extreme water levels rely on other meteorological events rather than on climate change. Figure B.2c shows a BM sampling method by selecting the yearly maxima of the water level. This selection approach shows a minor increase in the maximum water level by 1.7 millimetres per year. This would suggest that climate change only affects the extremest events, but not those you can see every year due to damping caused by the islands. The damping is not that felt in the largest events.



(a) Selected extreme water levels with $u = 2.8$ meters NAP and $\delta = 45$ hours



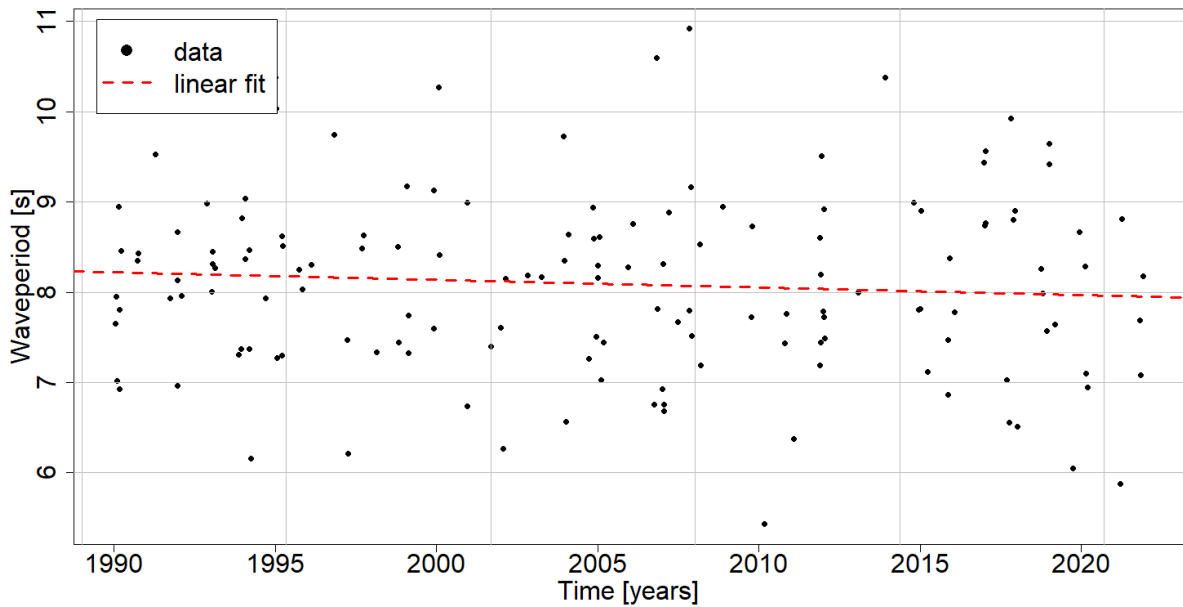
(b) Extreme water levels for $u = 3.3$ meters NAP and $\delta = 45$ hours



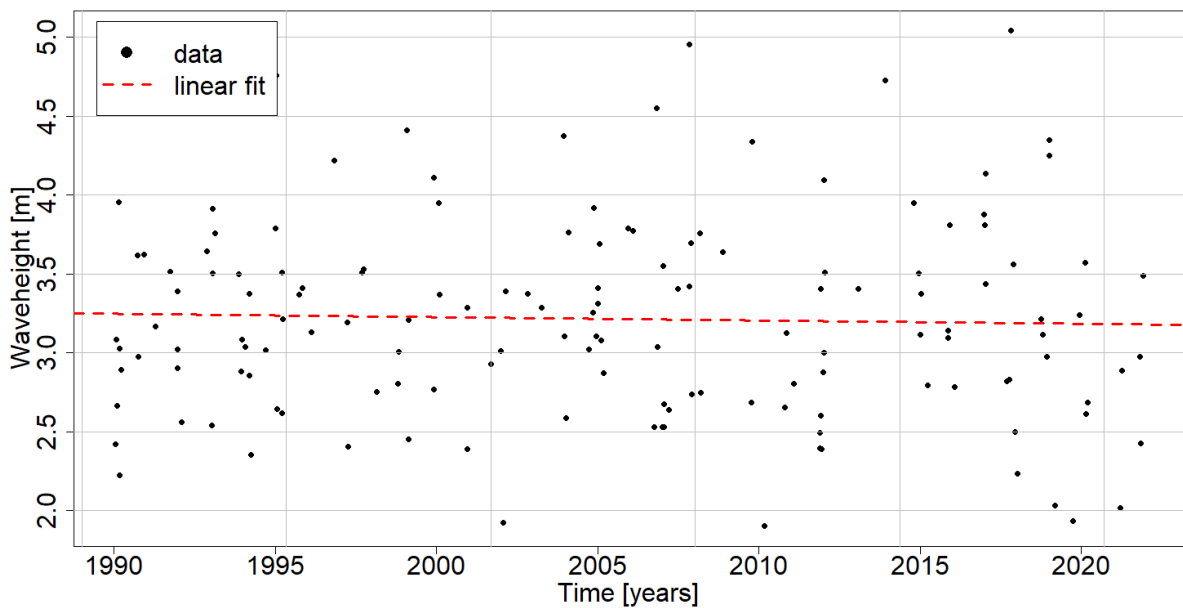
(c) Yearly maxima of the water level over time

Figure B.2: Extreme water levels for a threshold u of 2.8 and 3.3 meters NAP and the yearly maxima

In Figures B.3 and B.4, the concomitant wave height and period are shown for the selected extreme water levels. The concomitant variables are those corresponding to the same time of occurrence as the dominant variable, in this case, the water level. The linear regression in Figure B.3a shows that the concomitant wave period, for the dominant water level with a threshold of $u = 2.8$ meters NAP, follows a slight negative trend in time. In Figure B.3b, the linear regression on the concomitant wave height stays approximately constant in time.



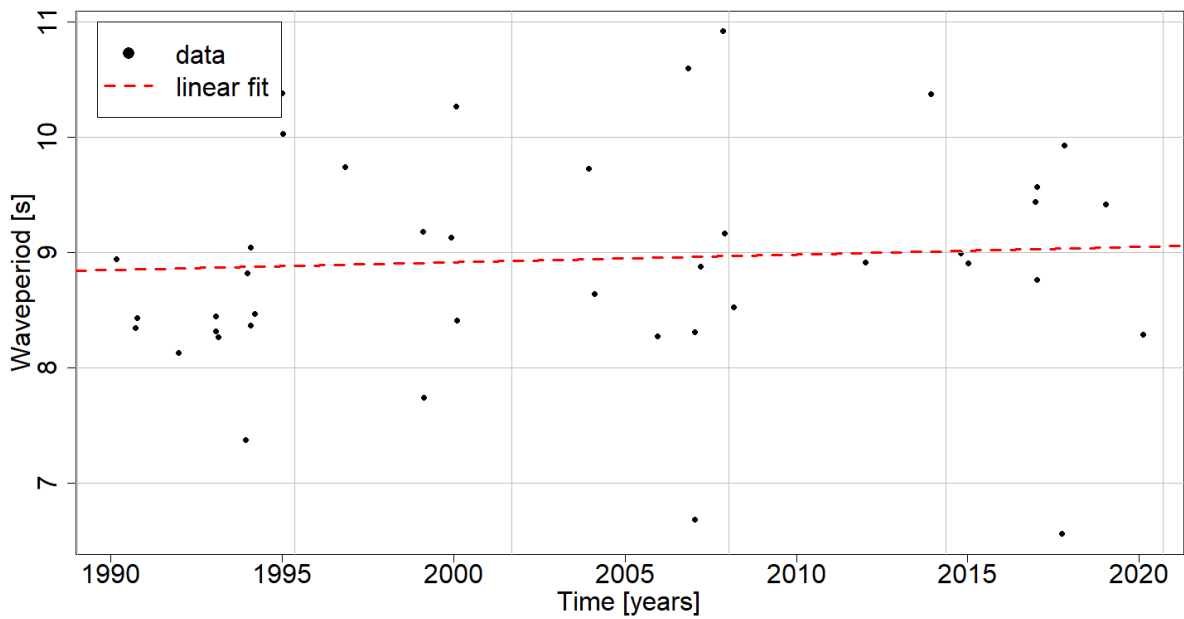
(a) Wave period as concomitant variable over time



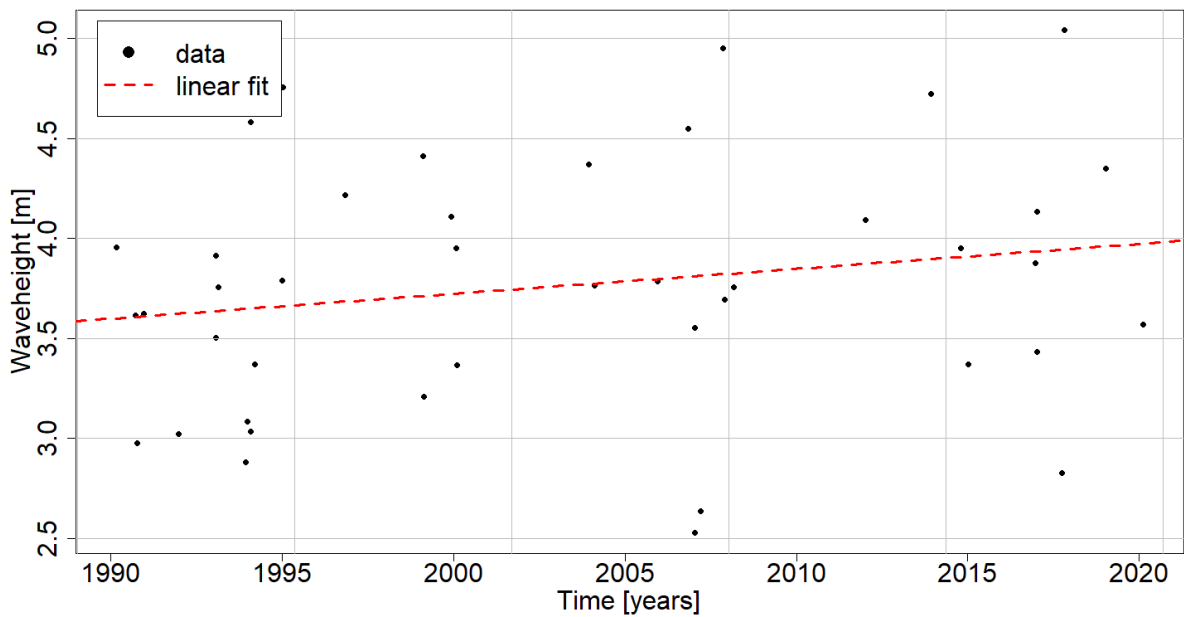
(b) Wave height as concomitant variable over time

Figure B.3: The concomitant variables with water level as the dominant variable. A threshold of $u = 2.8$ meters NAP, showing a slightly decreasing trend over time.

A positive trend of the variables is found when the threshold of the extreme water levels is set at > 3.2 meters NAP. This is also found in Figure B.4b, where both linear regressions of the concomitant wave height and period show a positive trend in time.



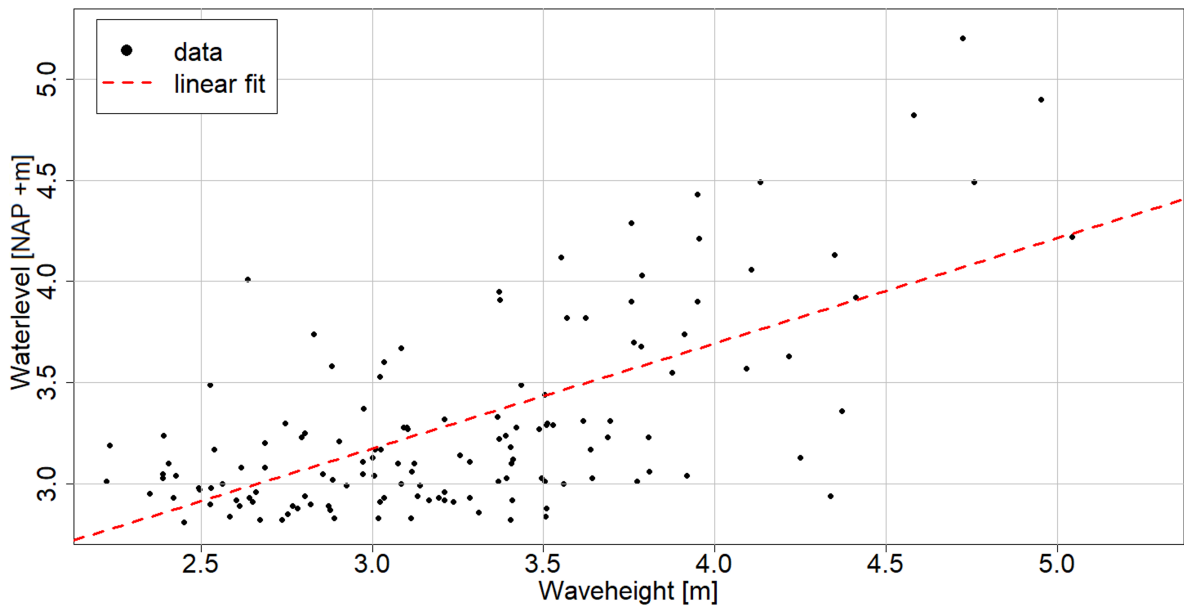
(a) Wave period as concomitant variable over time



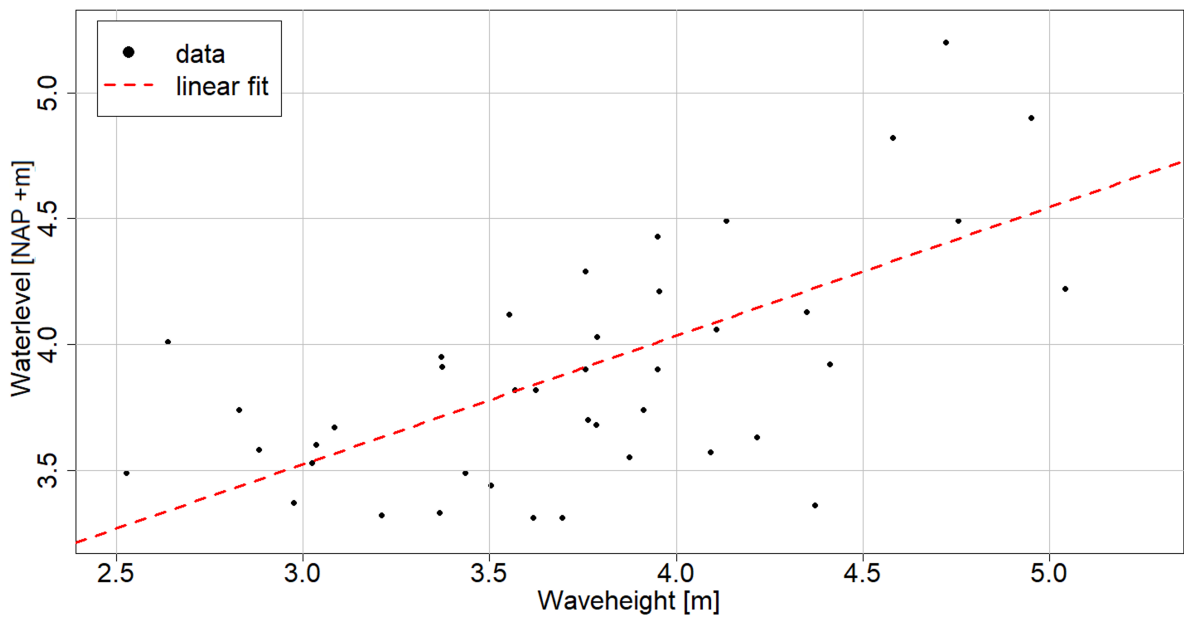
(b) Wave height as concomitant variable over time

Figure B.4: The concomitant variables with water level as the dominant variable. A threshold of $u = 3.3$ meters NAP, showing a clear positive trend over time.

Figure B.5 shows the selected extreme water levels against the concomitant wave height for the thresholds $u = 2.8$ and $u = 3.3$ meters NAP. Both figures show a strong correlation between the extreme water levels and the coinciding wave heights.



(a) Selected extreme water level with $u = 2.8$ meters NAP



(b) Selected extreme water level with $u = 3.3$ meters NAP

Figure B.5: Selected extreme water levels with u of 2.8 and 3.3 meters NAP against the concomitant wave height.

Additional results of the Stationary analysis

In this section, the return level plots and CDF plots are found for the different models that are applied. In addition, a table is found providing the return levels for different return periods, including the upper and lower bounds. Figure B.6 up to Figure B.10 show the return level plots for the fitted GPD using MLE, GPD using LM, GEV, Gumbel and Exponential distributions. The return level plots include a 95% confidence interval of the estimated models.

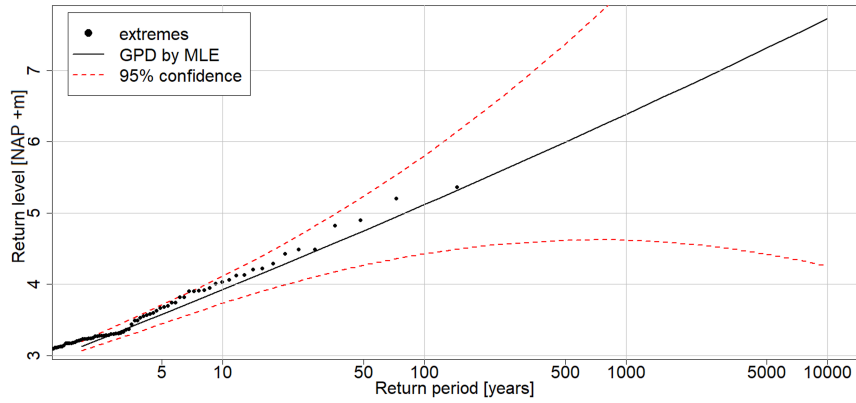


Figure B.6: Return level plot of the extreme water level for GPD using the MLE.

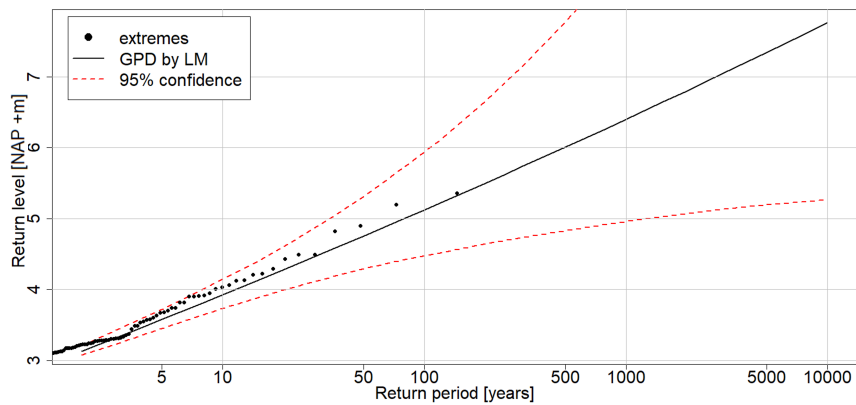


Figure B.7: Return Level plot of GPD with the LM method.

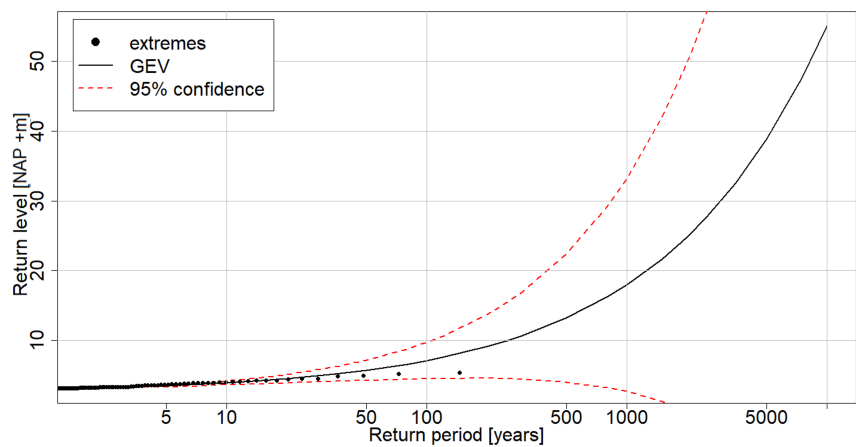


Figure B.8: Return Level plot of GEV with the MLE.

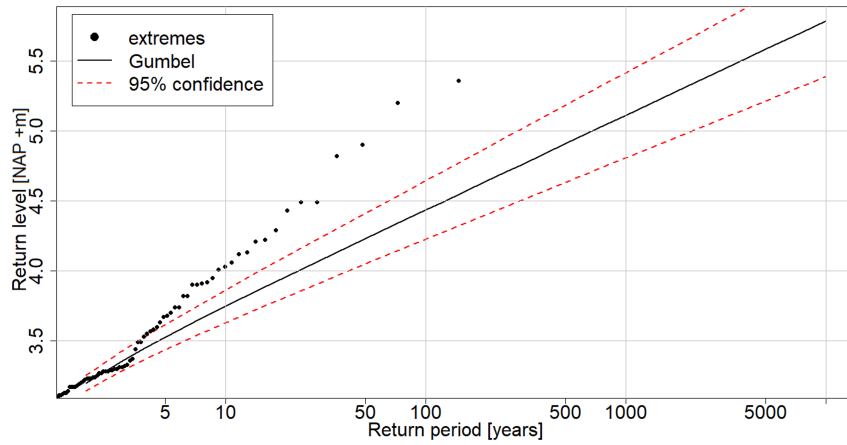


Figure B.9: Return Level plot of Gumbel with the MLE

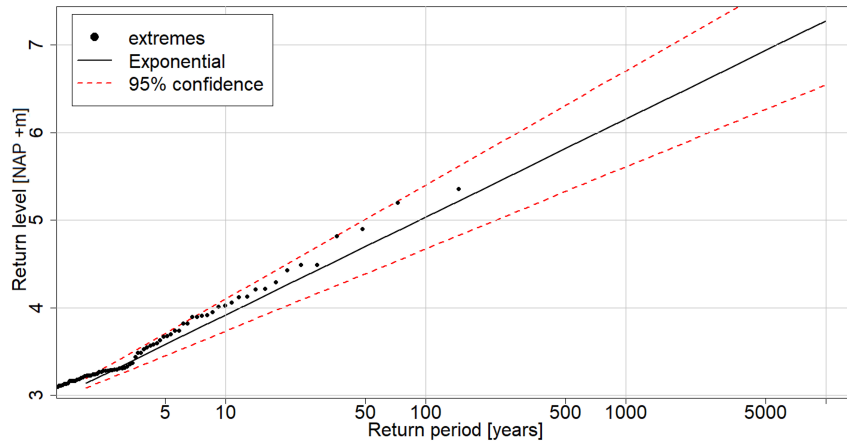


Figure B.10: Return Level plot of Exponential with the MLE

In Figure B.11 the histogram of the extreme water level and the GPD model is found.

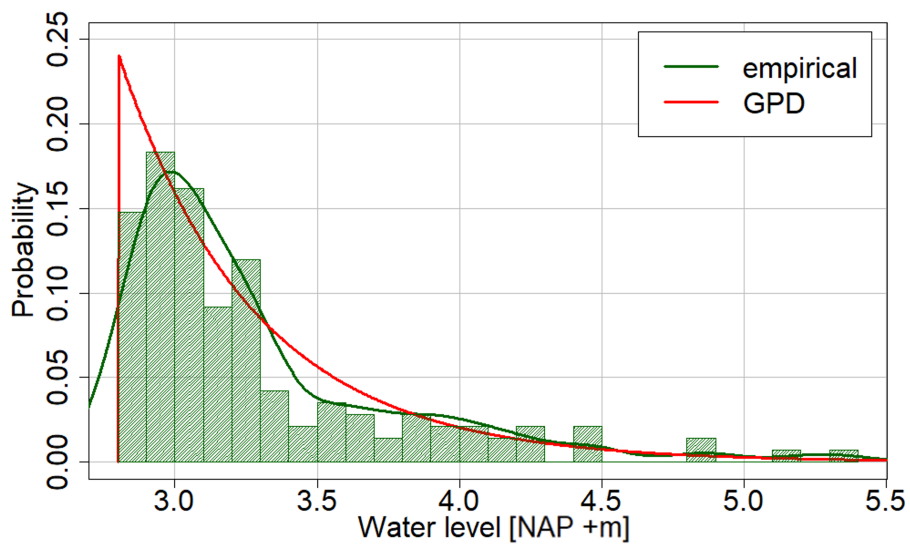


Figure B.11: Histogram of the extreme water level and the fitted GPD.

In Figure B.12 the CDF plot is shown for the fitted models, showing a similar fit for the Exponential and GPD models.

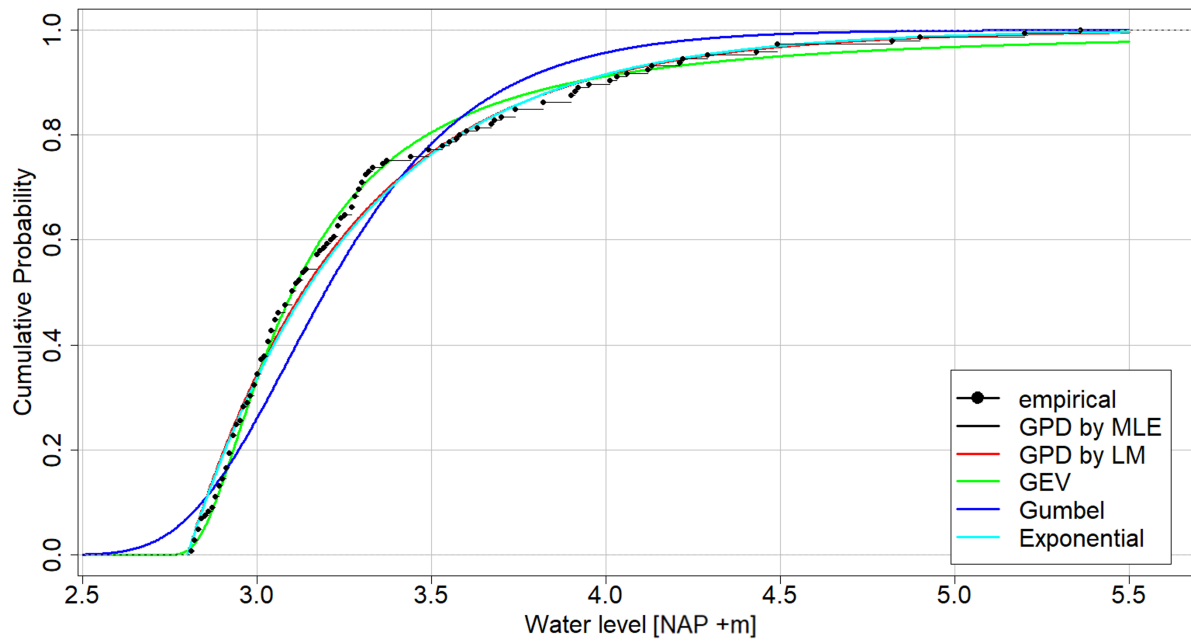


Figure B.12: CDF plot of all models for the extreme water levels.

In Figure B.13 the CDF plot is shown for the GPD using MLE.

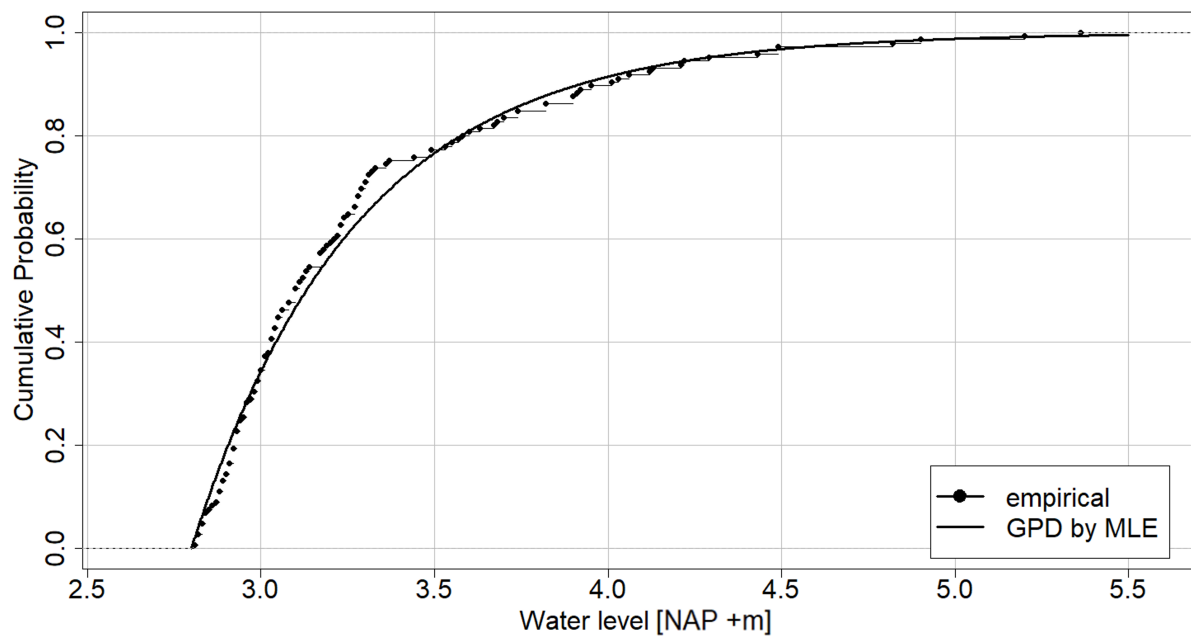


Figure B.13: CDF plot of GPD with the MLE for the extreme water level.

Table B.1 shows the return levels for a range of return periods for all fitted models. It also includes the lower bound (L.B.) and upper bound (U.B.) of the 95% confidence interval of the fitted models. The results show that the difference between the GPD by MLE and GPD by LM is minimal. In addition, it shows that the GEV distribution severely overestimates the tail of the extremes. The estimates of the return level for large return periods of the GEV are significant compared to the other models. The Gumbel distribution shows an underestimation of the tail compared to the GPD and Exponential distribution.

Table B.1: Return levels of extreme water level for different stationary models.

Return level of the fit [m]	Return period [year]									
	10	20	50	100	200	500	1,000	2,000	5,000	10,000
GPD _{MLE} L.B.	3.73	3.99	4.27	4.43	4.54	4.62	4.62	4.57	4.42	4.25
GPD _{MLE}	3.92	4.27	4.75	5.12	5.49	5.99	6.38	6.78	7.31	7.73
GPD _{MLE} U.B.	4.11	4.56	5.23	5.81	6.44	7.37	8.15	8.99	10.21	11.20
GPD _{LM} L.B.	3.72	3.99	4.29	4.48	4.64	4.86	4.97	5.08	5.20	5.28
GPD _{LM}	3.92	4.28	4.75	5.12	5.50	6.01	6.40	6.80	7.35	7.77
GPD _{LM} U.B.	4.12	4.58	5.33	5.95	6.70	7.86	8.89	10.06	11.89	13.61
GEV L.B.	3.61	3.90	4.28	4.50	4.55	4.02	2.69	-0.15	-8.16	-19.88
GEV	3.91	4.51	5.71	7.10	9.11	13.21	17.96	24.83	38.85	55.07
GEV U.B.	4.20	5.11	7.15	9.71	13.67	22.41	33.23	49.81	85.85	130.03
Gumbel L.B.	3.63	3.81	4.05	4.23	4.40	4.63	4.81	4.98	5.21	5.39
Gumbel	3.75	3.96	4.23	4.43	4.64	4.91	5.11	5.31	5.58	5.79
Gumbel U.B.	3.86	4.10	4.41	4.64	4.88	5.18	5.41	5.65	5.95	6.18
Exponential L.B.	3.74	4.02	4.39	4.67	4.96	5.33	5.61	5.89	6.27	6.55
Exponential	3.92	4.26	4.70	5.04	5.37	5.82	6.16	6.49	6.94	7.28
Exponential U.B.	4.10	4.49	5.01	5.40	5.79	6.31	6.70	7.09	7.61	8.00

Additional results of the Non-stationary analysis

In Figure B.14 the histogram of the extreme water level and the non-stationary GPD_{H_s,σ} model is found.

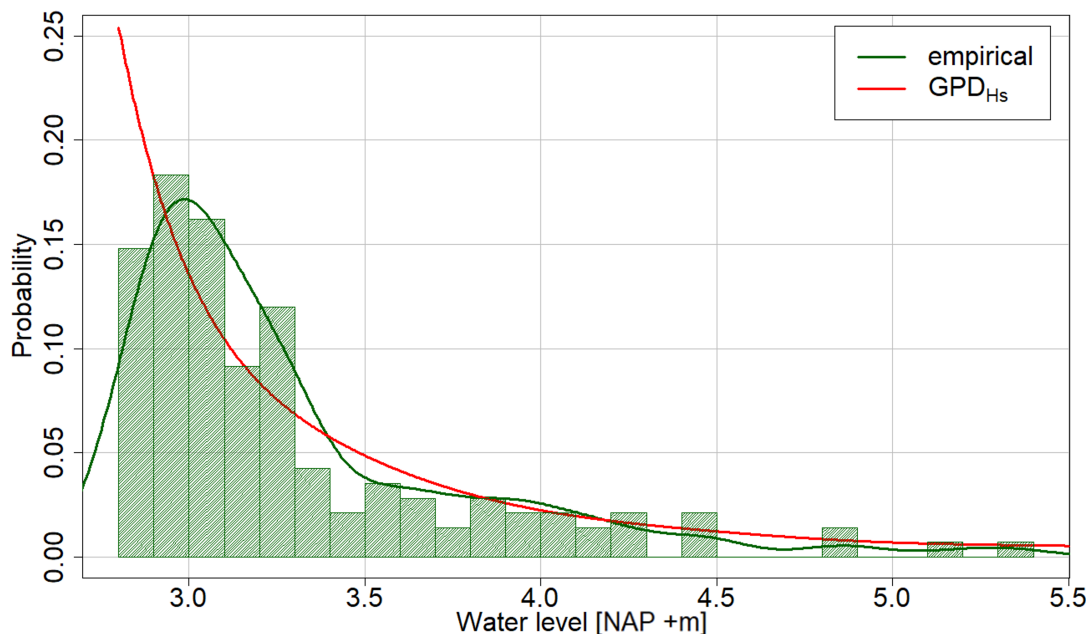


Figure B.14: Histogram of the extreme water level and the non-stationary GPD_{H_s,σ} model.

C | Modelling the Concomitants

This appendix shows the results of approximating the concomitant variables: wave height, wave period, wind speed and wind direction. In this appendix, the goodness-of-fit criteria, exceedance probability plots, CDF plots and histograms of the concomitants are found.

Goodness-of-fit Criteria of the applied models

Table C.1 shows the goodness-of-fit criteria for the wave variables. In Table C.2, the goodness-of-fit criteria for the wind variables are found. The goodness-of-fit is greater for lower values of the $-\mathcal{L}$, AIC and BIC and for values close to 1 for R^2 . The best scores are displayed in bold green. The tables also show some models with a negative R^2 value suggesting very poor fits, see Equation 3.13. The models with values between $0 < R^2 \leq 1$ are selected for the exceedance probability plots and CDF plots.

Table C.1: Goodness-of-fit criteria of wave height H_s and wave period T_p for several models. The best scores are displayed in bold green.

Model	Wave height H_s				Wave period T_p			
	$-\mathcal{L}$	AIC	BIC	R^2	$-\mathcal{L}$	AIC	BIC	R^2
Normal	137.06	278.11	284.03	0.988	204.99	413.98	419.89	0.993
Log-normal	134.96	273.93	279.84	0.995	204.96	413.92	419.84	0.992
Gamma	134.77	273.53	279.44	0.996	204.57	413.15	419.06	0.994
Weibull	142.63	289.25	295.17	0.958	212.34	428.69	434.60	0.952
GEV	134.60	275.19	284.06	0.996	204.66	415.32	424.19	0.992
Gumbel	138.07	280.14	286.05	0.960	212.14	428.27	434.18	0.901
GPD	158.64	321.28	327.19	-9.254	241.56	487.12	493.04	-31.35
Exponential	308.25	618.49	621.45	-14.68	439.17	880.35	883.30	-43.78
Rayleigh	217.98	437.97	440.92	-1.212	344.14	690.28	693.24	-7.016

Table C.2: Goodness-of-fit criteria of wind speed w_s and wind direction w_d for several models. The best scores are displayed in bold green.

Model	Wind speed w_s				Wind direction ^a w_d			
	$-\mathcal{L}$	AIC	BIC	R^2	$-\mathcal{L}$	AIC	BIC	R^2
Normal	360.57	725.15	731.57	0.961	-693.24	1390.48	1396.40	-8.72
Log-normal	358.04	720.08	725.99	0.961	-703.93	1411.86	1417.77	0.982
Gamma	357.45	718.89	724.81	0.969	-691.42	1386.83	1392.74	0.992
Weibull	365.84	735.68	741.59	0.936	-690.21	1384.41	1390.32	0.982
GEV	357.53	721.05	729.92	0.966	-687.05	1388.97	1380.10	0.991
Gumbel	360.68	725.36	731.27	0.895	-688.21	1380.40	1386.32	0.993
GPD	396.82	797.63	803.55	-3.690	-714.13	1432.27	1438.17	0.721
Exponential	509.00	1020.01	1022.96	-688.21	-755.30	1512.59	1515.55	0.456
Rayleigh	421.77	845.55	848.50	-714.13	-695.32	1392.64	1395.60	0.955

^a The models that model w_d are truncated models in $[0, 180]$ degrees

Exceedance Probability plots for Concomitants

Figures C.1, C.2 and C.3 show the exceedance probabilities of the concomitants wave period, wind speed and wind direction. The exceedance probability of the wave height is shown in Figure 4.5 in Subsection 4.2. The exceedance probability plots show the models resulting from the first selection by the goodness-of-fit criteria in Tables C.1 and C.2. In the application of extreme value modelling, the tail of the concomitants is of great interest. Therefore, the model that best represents the tail of the concomitants is selected as the best model for the wave height, wave period and wind speed. For the wind direction,

the tail is not necessarily of interest. For this variable, the best model is the one that best models the entire range of values.

Figure C.1 shows that the Gamma model, as indicated by the goodness-of-fit criteria, results in the best approximation of the wave period. The Gamma model is the best model to approximate the tail. In addition, it is also the model that best models the entire range of values. The GEV model performs similarly to the Gamma model, showing very close goodness-of-fit criteria and exceedance probabilities. This is surprising since, as stated in Subsection 3.3.1, the GEV model can be used for an EVA sampled by a BM method. However, the concomitants are selected from the coinciding times of the extreme water levels by POT. In addition, also the Normal and Log-normal models provide decent results. Especially the Log-normal model shows a decent fit of the exceedance probabilities. Nevertheless, the Gamma model performs slightly better and is therefore chosen as the best model for the wave period T_p .

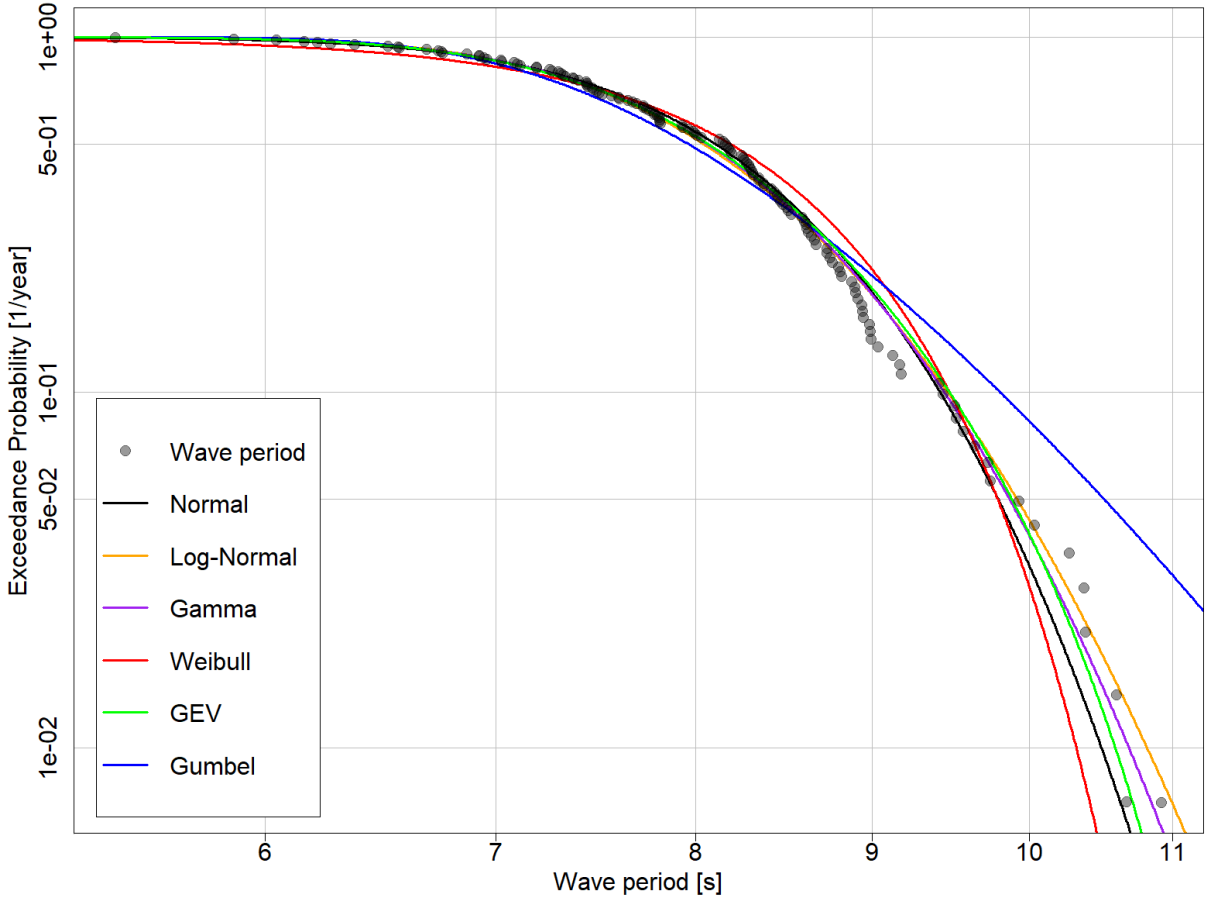


Figure C.1: Exceedance probability $\mathbb{P}(T_p > x)$ of different models for wave period T_p .

Figure C.2 shows the exceedance probabilities of the wind speed. For this variable, also the Gamma model performed best by the goodness-of-fit criteria in Table C.2. From Figure C.2 all shown models could be argued to have a decent fit of the exceedance probabilities. The Normal and Weibull models show a decent fit for the tail, however, underestimate the most extreme value of 24.7 meters per second. The Gumbel model is closest to the most extreme value, however, overestimates the wind speed for smaller exceedance probabilities. The behaviour of the Gamma, GEV and Log-Normal models is in between the previous models. The Gamma model is selected as the best model to approximate the wind speed w_s , following the goodness-of-fit criteria.

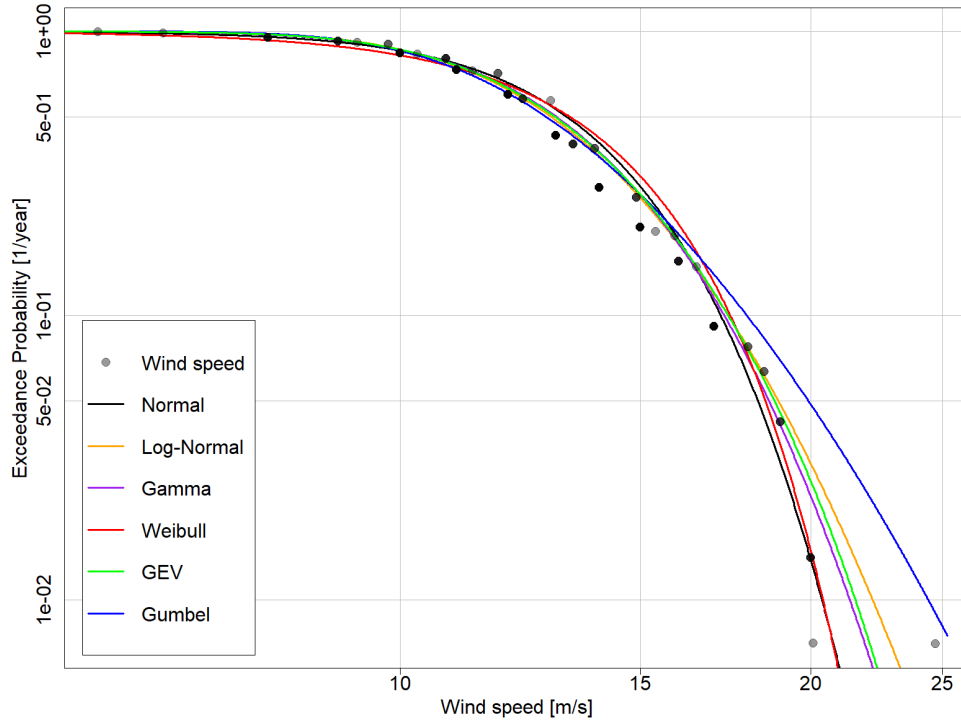


Figure C.2: Exceedance probability $\mathbb{P}(w_s > x)$ of different models for wind speed w_s .

Figure C.3 shows the exceedance probabilities of the wind direction. The Weibull model clearly shows the best fit of the wind direction over the entire range of values. Therefore, the Weibull model is selected to approximate the wind direction w_d .

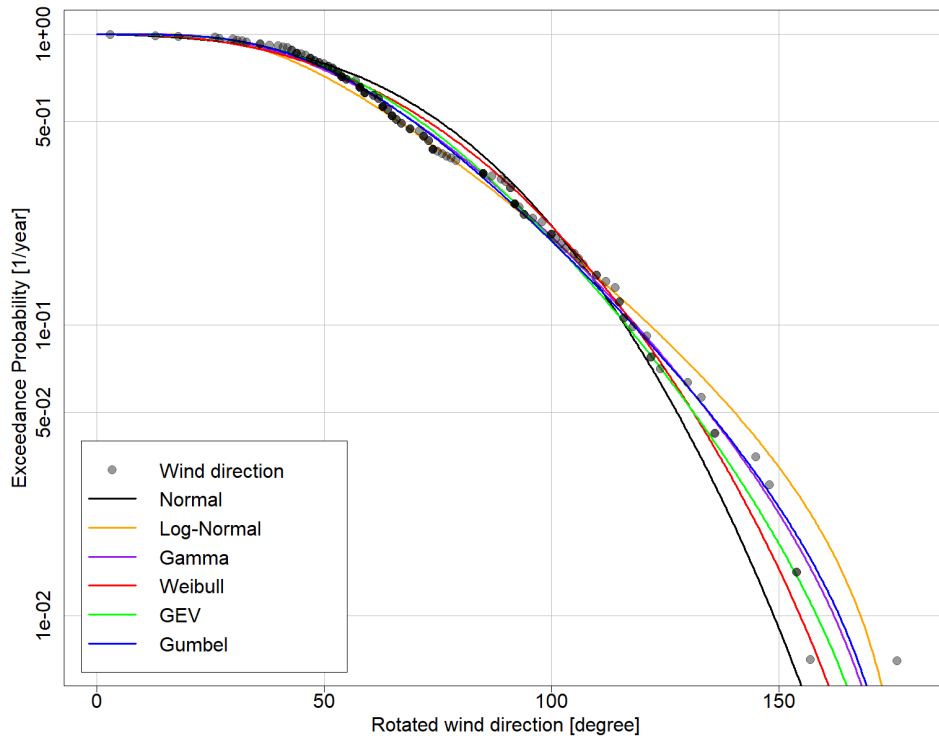


Figure C.3: Exceedance probability $\mathbb{P}(w_d > x)$ of different models for rotated wind direction w_d .

CDF plots for Concomitants

Figure C.4 shows the CDF plots of the concomitants and the several models that were fitted. Although the tail of the concomitants is of the largest significance, it is wise to validate the models over the entire range of values. The CDF plots provide another visualization to check that the selected models well approximate the values over the entire range of values. From the figure, it is clear that the selected models do provide a decent fit over the entire range. Some of the models perform very similarly for the lower exceedance probabilities, resulting in the overlap in the CDF plots.

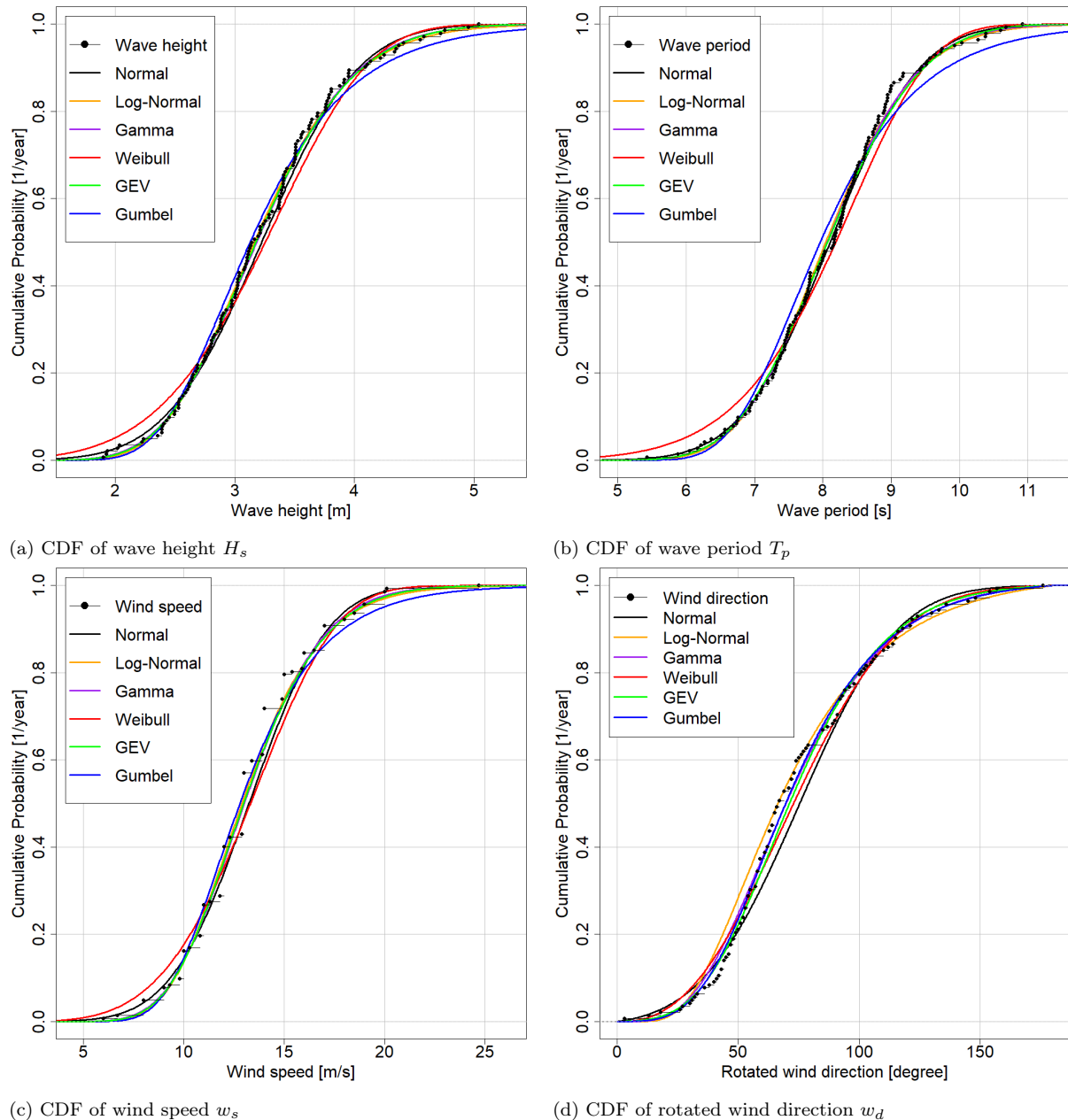
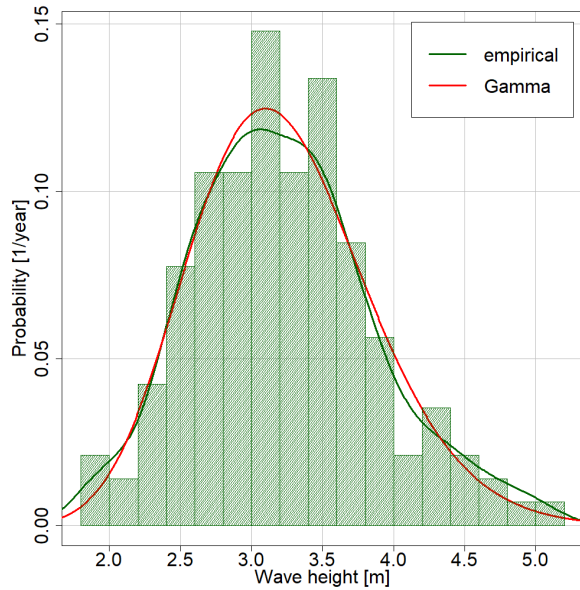


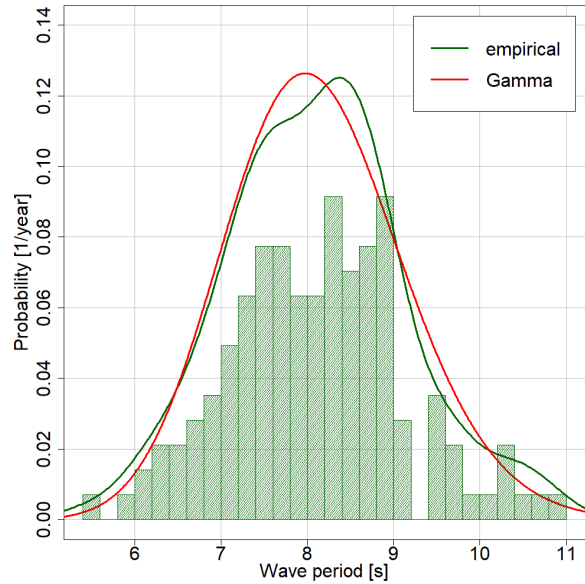
Figure C.4: CDF plots of the concomitant variables and the selected models.

Histograms for Concomitants

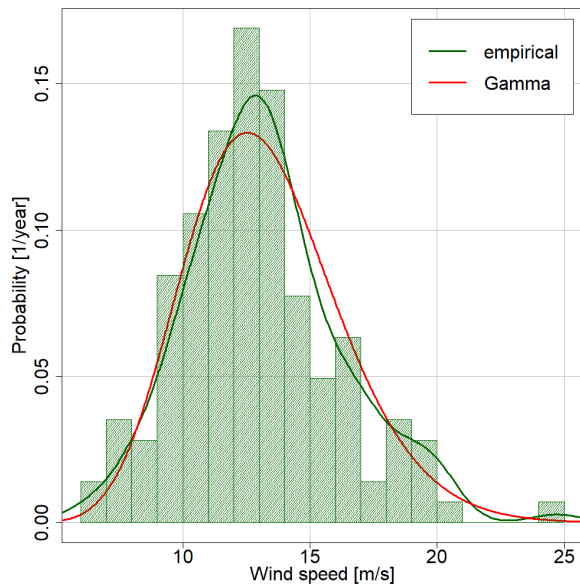
Figure C.5 shows the histograms of the concomitant variables and the selected models for each concomitant. In green, the empirical (yearly) probabilities are found for the variables. In red, the selected models are shown to approximate the concomitant variables.



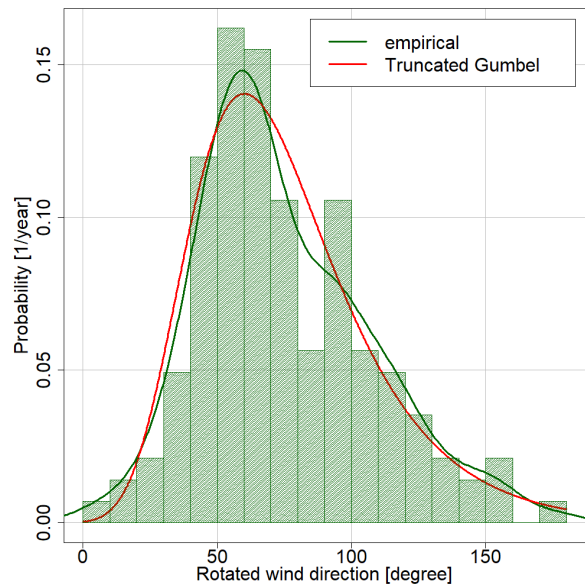
(a) Histogram of wave height H_s



(b) Histogram of wave period T_p



(c) Histogram of wind speed w_s



(d) Histogram of rotated wind direction w_d

Figure C.5: Histograms of the concomitant variables and the selected models.

D | Selection of Bivariate Copulae

This appendix shows the results of the bivariate copula modelling. The appendix contains the goodness-of-fit criteria, semi-correlations, CDF and copula samples in unity space and in variable space.

Tables of Goodness-of-fit Criteria and Semi-Correlations

In the tables below the semi-correlations, CM and AIC values for all variable pairs and a selection of copula models are found. The most important quadrants and the best model performances are shown in bold green. Important quadrants or the best models with p -values of less significance ($p > 0.1$) are shown in bold orange. Table D.1 shows that the UR and LR quadrants are of statistical significance. Therefore, a copula model is selected that best represents these two quadrants. This results in the Gumbel copula. The best CM score is found for the Frank copula, as the CM score of the Gumbel copula is of low statistical value ($p = 0.31$). The Survival Clayton provides the lowest AIC value. However, the Gumbel model also performs adequately for the AIC value. Therefore, the Gumbel copula is selected as the best model.

Table D.1: AIC, CM scores and semi-correlations for the pair water level h and wave period T_p .

Criteria [–]	Empirical h & T_p	Gaussian	Survival Clayton	Gumbel	Frank	Joe
r_{UL}	0.244	0.130	0.040	0.096	0.052	0.052
r_{UR}	0.497	0.332	0.620	0.543	0.232	0.666
r_{LL}	–0.139	0.342	0.613	0.244	0.169	0.694
r_{LR}	–0.378	0.094	0.101	0.068	0.156	0.068
p_{UL}	0.287	0	0.214	0.003	0.124	0.100
p_{UR}	0	0	0	0	0	0
p_{LL}	0.329	0	0.006	0	0	0.002
p_{LR}	0.091	0.004	0.002	0.042	0	0.038
CM	–	0.173	0.031	0.093	0.138	2.512
PCM	–	0.050	0.950	0.310	0.040	0.660
AIC	–	–48.550	–63.420	–58.000	–45.120	–61.130

From Table D.2 it is found that UL is the most important quadrant. However, this is not of large statistical importance as $p = 0.16$. The overall (Spearman’s) correlation, from Table 4.3, is positive. Therefore, this variable pair cannot be modelled by a copula rotated by 90 (or 270) degrees using the *VineCopula* package. For this variable pair, the Frank copula is selected as the best model. The Frank model provides the best CM scores and has an AIC value that matches the Gaussian copula. The Gaussian copula performs marginally better in approximating the semi-correlations.

Table D.2: AIC, CM scores and semi-correlations for the pair water level h and wind speed w_s .

Criteria [–]	Empirical h & w_s	Gaussian	Survival Clayton	Gumbel	Frank	Joe
r_{UL}	0.242	0.089	0.051	–0.014	0.063	–0.011
r_{UR}	0.063	0.159	0.347	0.365	0.074	0.444
r_{LL}	–0.096	0.125	0.034	0.0564	0.104	0.0387
r_{LR}	–0.027	0.138	0.058	0.080	0.062	0.025
p_{UL}	0.161	0.003	0.075	0.638	0.035	0.699
p_{UR}	0.679	0	0	0	0.001	0
p_{LL}	0.516	0	0.153	0.017	0	0.108
p_{LR}	0.878	0	0.044	0.004	0.038	0.368
CM	–	0.130	0.041	0.067	0.146	1.975
PCM	–	0.140	0.900	0.560	0.070	0.450
AIC	–	–12.620	–12.830	–11.730	–12.620	–10.310

In Table D.3, the semi-correlations of water level and wind direction are found. The semi-correlations show that the LR quadrant could be assumed as the most important quadrant. However, the semi-correlations do not seem to be adequately approximated by the selection of copula models. As the overall correlation of the empirical data is positive, found in Table 4.3, the data cannot be approximated by rotating the copula models 90 or 270 degrees. Therefore, these variables are considered independent.

Table D.3: AIC, CM scores and semi-correlations for the pair water level h and wind direction w_d .

Criteria [–]	Empirical h & w_d	Gaussian	Clayton	Survival Gumbel	Frank	Survival Joe
r_{UL}	–0.152	0.084	–0.033	–0.008	0.032	–0.007
r_{UR}	0.138	0.040	0.189	0.158	0.062	0.249
r_{LL}	0.009	0.109	–0.022	0.108	0.051	0.013
r_{LR}	0.214	0.069	0.003	0.036	0.087	0.036
p_{UL}	0.391	0.002	0.233	0.781	0.249	0.801
p_{UR}	0.405	0.103	0	0	0.012	0
p_{LL}	0.957	0	0.369	0	0.037	0.595
p_{LR}	0.224	0.014	0.919	0.182	0.001	0.185
CM	–	0.049	0.033	0.051	0.057	0.542
p_{CM}	–	0.820	0.950	0.770	0.630	0.550
AIC	–	–1.965	–1.908	–1.689	–2.572	–0.914

The wave height and wave period show three quadrants of statistical significance, namely UR , UL and LL , shown in Table D.4. From these three quadrants, the UR and LL quadrants are of the largest significance, as these define the tails (positive overall correlation). These quadrants are best approximated by the Survival Gumbel copula. This model also provides the best CM score and AIC value. Therefore, this variable pair is best approximated by the Survival Gumbel copula.

Table D.4: AIC, CM scores and semi-correlations for the pair wave height H_s and wave period T_p .

Criteria [–]	Empirical H_s & T_p	Gaussian	Clayton	Survival Gumbel	Frank	Survival Joe
r_{UL}	–0.680	0.235	0.072	0.115	–0.013	0.097
r_{UR}	0.645	0.591	0.133	0.485	0.436	0.178
r_{LL}	0.678	0.609	0.787	0.735	0.432	0.787
r_{LR}	0.061	0.175	0.025	0.058	0.126	0.048
p_{UL}	0.015	0	0.054	0.004	0.783	0.011
p_{UR}	0	0	0	0	0	0
p_{LL}	0	0	0	0	0	0
p_{LR}	0.850	0	0.510	0.163	0.003	0.205
CM	–	0.024	0.178	0.105	0.0781	1.248
p_{CM}	–	0.980	0.020	0.030	0.200	0.990
AIC	–	–134.500	–120.200	–143.500	–129.600	–119.400

Table D.5 shows that the UR quadrant is of significance for the wave height and wind speed pair. The LR quadrant shows some degree of importance as $p = 0.11$. The UR quadrant is best approximated by the Gaussian model. The Frank model has the best CM score, however, this is of low statistical significance as $p = 0.19$. The Frank also has the lowest AIC, however, the Gaussian’s AIC value is very similar. Therefore, the Gaussian is selected as the best model.

Table D.5: AIC, CM scores and semi-correlations for the pair wave height H_s and wind speed w_s .

Criteria [–]	Empirical H_s & w_s	Gaussian	Clayton	Survival Gumbel	Frank	Survival Joe
r_{UL}	–0.005	0.085	0.073	0.041	0.008	0.041
r_{UR}	0.278	0.148	0	0.109	0.005	0.014
r_{LL}	0.175	0.125	0.281	0.310	0.050	0.367
r_{LR}	0.276	0.080	0.028	0.051	0.037	0.010
p_{UL}	0.979	0.004	0.010	0.152	0.789	0.149
p_{UR}	0.053	0	0.992	0	0.030	0.563
p_{LL}	0.241	0	0	0	0.032	0
p_{LR}	0.114	0.005	0.319	0.069	0.212	0.729
CM	–	0.064	0.062	0.068	0.099	1.391
p_{CM}	–	0.660	0.720	0.540	0.190	0.590
AIC	–	–12.080	–11.010	–11.390	–12.580	–8.552

As Table D.6 shows for the wave height and wind direction, the LR quadrant is of some importance. The Gaussian model best approximates this quadrant and has the best AIC. However, the semi-correlations in LR are modelled rather low. The Frank model provides a slightly better CM value. Nevertheless, the Gaussian is considered the best model to approximate the wave height and wind direction.

Table D.6: AIC, CM scores and semi-correlations for the pair wave height H_s and wind direction w_d .

Criteria [–]	Empirical H_s & w_d	Gaussian	Clayton	Survival Gumbel	Frank	Survival Joe
r_{UL}	0.107	0.130	0.029	0.096	0.058	0.031
r_{UR}	0.061	0.261	0.036	0.110	0.170	0.011
r_{LL}	0.405	0.218	0.442	0.428	0.195	0.518
r_{LR}	–0.047	0.075	0.109	0.043	0.088	0.020
p_{UL}	0.610	0	0.340	0.001	0.079	0.296
p_{UR}	0.683	0	0.117	0	0	0.645
p_{LL}	0.005	0	0	0	0	0
p_{LR}	0.818	0.016	0	0.163	0.007	0.492
CM	–	0.068	0.083	0.067	0.078	1.558
p_{CM}	–	0.620	0.370	0.550	0.330	0.890
AIC	–	–29.943	–26.983	–29.774	–31.491	–24.702

Table D.7 shows that there is no quadrant of statistical significance for the wave period and wind speed. Therefore, this variable pair is considered independent.

Table D.7: AIC, CM scores and semi-correlations for the pair wave period T_p and wind speed w_s .

Criteria [–]	Empirical T_p & w_s	Gaussian	Clayton	Survival Gumbel	Frank	Survival Joe
r_{UL}	–0.069	0.0285	0.026	–0.006	0.026	–0.018
r_{UR}	–0.022	0	–0.021	0.017	0.010	0.006
r_{LL}	0.031	0.036	0.024	0.024	–0.044	0.072
r_{LR}	0.090	–0.017	–0.022	–0.009	0.008	0.0224
p_{UL}	0.678	0.273	0.312	0.806	0.339	0.496
p_{UR}	0.889	0.987	0.411	0.519	0.686	0.828
p_{LL}	0.841	0.156	0.359	0.369	0.088	0.006
p_{LR}	0.590	0.523	0.401	0.722	0.742	0.374
CM	–	0.117	0.097	0.044	0.126	0.044
p_{CM}	–	0.310	0.280	0.930	0.170	0.920
AIC	–	1.952	2.001	2.002	1.910	2.003

Table D.8 shows that there is no quadrant of statistical significance for the wave period and wind direction. Therefore, this variable pair is considered independent.

Table D.8: AIC, CM scores and semi-correlations for the pair wave period T_p and wind direction w_d .

Criteria [–]	Empirical T_p & w_d	Gaussian	Clayton	Survival Gumbel	Frank	Survival Joe
r_{UL}	0.068	0.168	0.070	0.058	0.039	0.078
r_{UR}	0.251	0.193	0.369	0.393	0.114	0.402
r_{LL}	0.274	0.159	0.037	0.128	0.123	0.028
r_{LR}	0.130	0.117	0.029	0.038	0.058	0.007
p_{UL}	0.728	0	0.017	0.043	0.204	0.005
p_{UR}	0.104	0	0	0	0	0
p_{LL}	0.076	0	0.118	0	0	0.252
p_{LR}	0.500	0	0.319	0.205	0.064	0.813
CM	–	0.047	0.060	0.074	0.070	1.322
p_{CM}	–	0.830	0.720	0.470	0.400	0.820
AIC	–	–17.356	–15.342	–	–17.471	–13.595

The LR quadrant is of some significance for the wind speed and wind direction as shown in Table D.9. This semi-correlation is best modelled by the rotated Clayton model by 90 degrees. The rotated Clayton also provides the best CM scores. The rotated Joe by 270 degrees performs slightly better for the AIC. However, the rotated Clayton is considered as the best model for the wind speed and wind direction.

Table D.9: AIC, CM scores and semi-correlations for the pair wind speed w_s and wind direction w_d .

Criteria [–]	Empirical w_s & w_d	Gaussian	Clayton rotated by 270°	Gumbel rotated by 90°	Frank	Joe rotated by 90°
r_{UL}	–0.534	–0.030	–0.169	–0.151	0.046	–0.244
r_{UR}	–0.077	–0.020	–0.005	0.002	0.006	0.014
r_{LL}	0.393	0.038	–0.213	–0.079	–0.020	0.007
r_{LR}	–0.020	0.023	0.021	0	–0.065	0.022
p_{UL}	0	0.243	0	0	0.073	0
p_{UR}	0.636	0.446	0.838	0.954	0.829	0.600
p_{LL}	0.010	0.144	0.425	0.004	0.433	0.793
p_{LR}	0.901	0.357	0.396	0.991	0.010	0.384
CM	–	0.161	0.356	0.316	0.164	1.937
p_{CM}	–	0.210	0	0	0	0.030
AIC	–	1.838	–1.226	–2.506	1.961	–4.482

Figures of the Semi-Correlations of the Copula models

Below the semi-correlations are found for the samples of the selected copula models. The semi-correlation plot of the copula pair: water level h and wave height H_s , is found in Section 4.3. The semi-correlations in each quadrant of the models result from the tables above. The empirical data points are shown in red squares. The samples of the models are shown as black dots. The title of each plot shows the overall (Pearson’s) correlation of the copula samples.

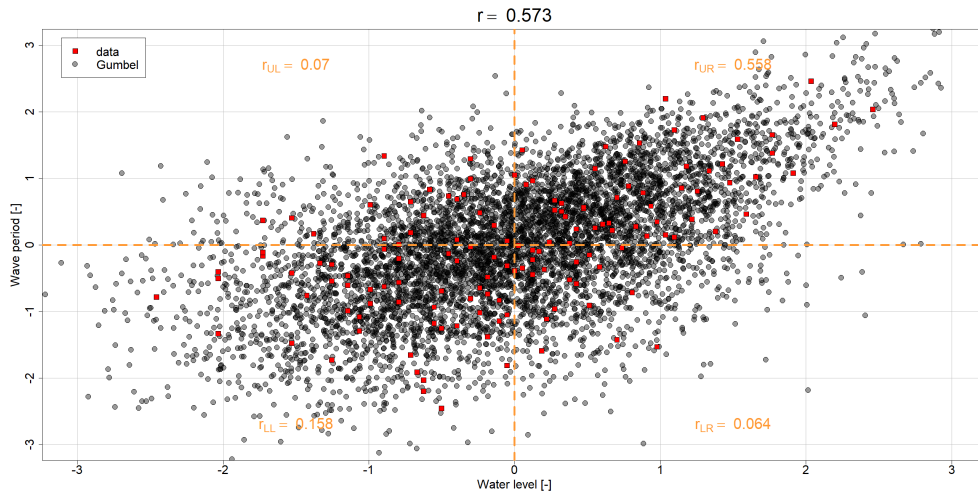


Figure D.1: Semi-correlation of the Gumbel model for water level h and wave period T_p .

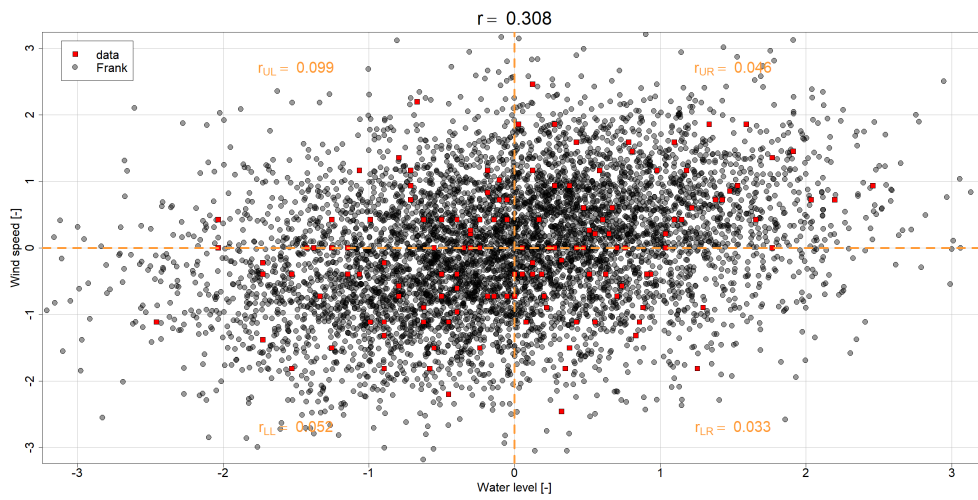


Figure D.2: Semi-correlation of the Frank model for water level h and wind speed w_s .

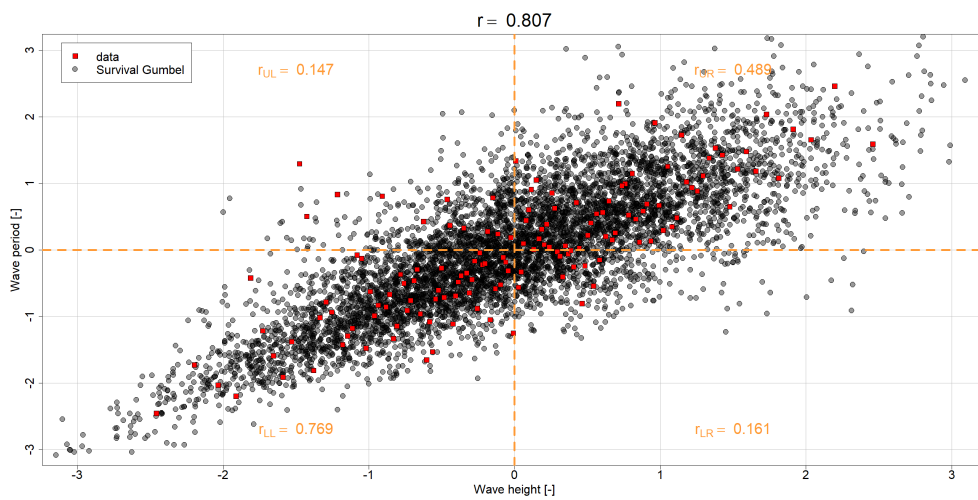


Figure D.3: Semi-correlation of the Survival Gumbel model for wave height H_s and wave period T_p .

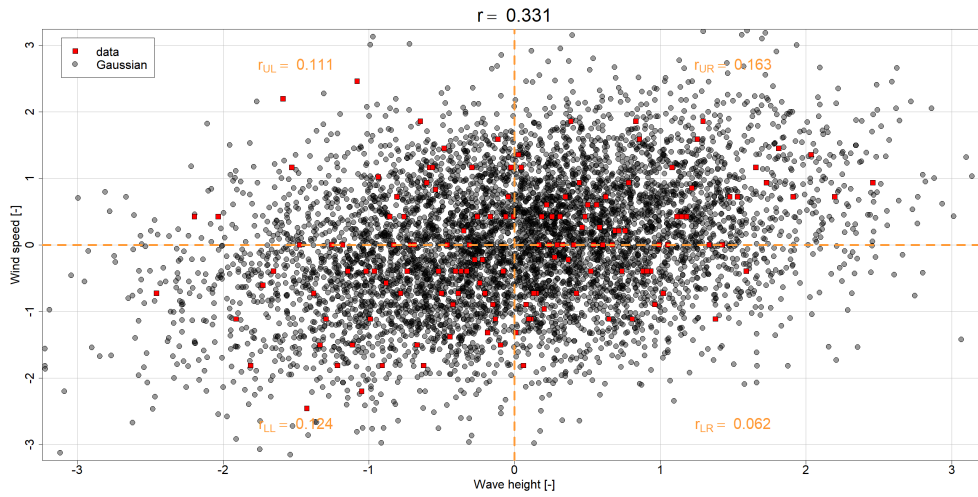


Figure D.4: Semi-correlation of the Gaussian model for wave height H_s and wind speed w_s .

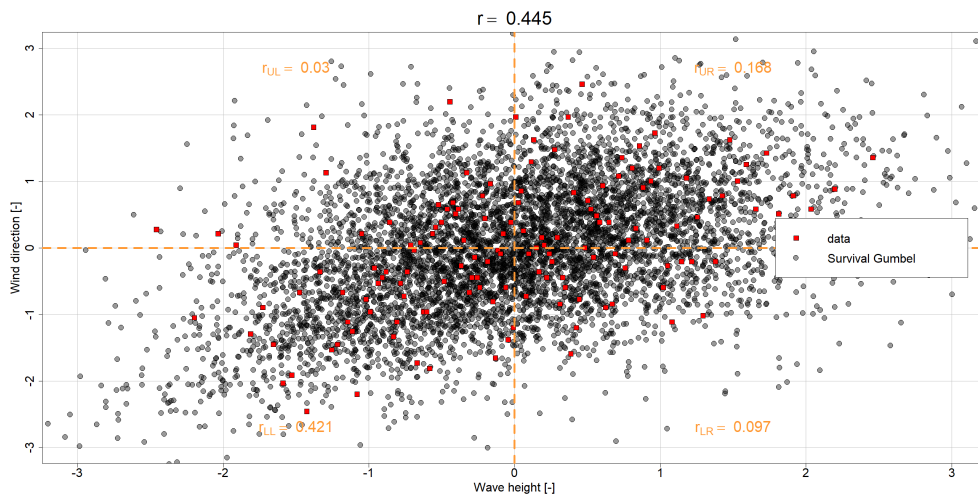


Figure D.5: Semi-correlation of the Survival Gumbel model for wave height H_s and wind direction w_d .

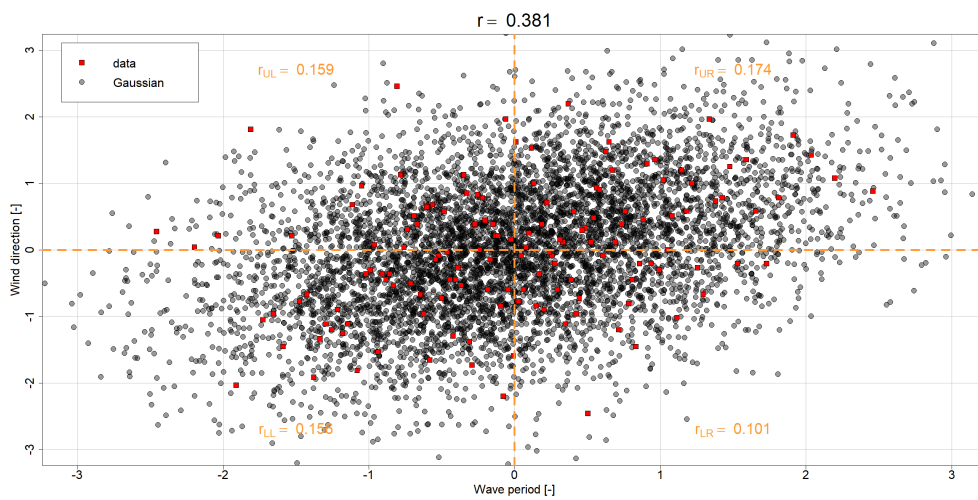


Figure D.6: Semi-correlation of the Gaussian model for wave period T_p and wind direction w_d .

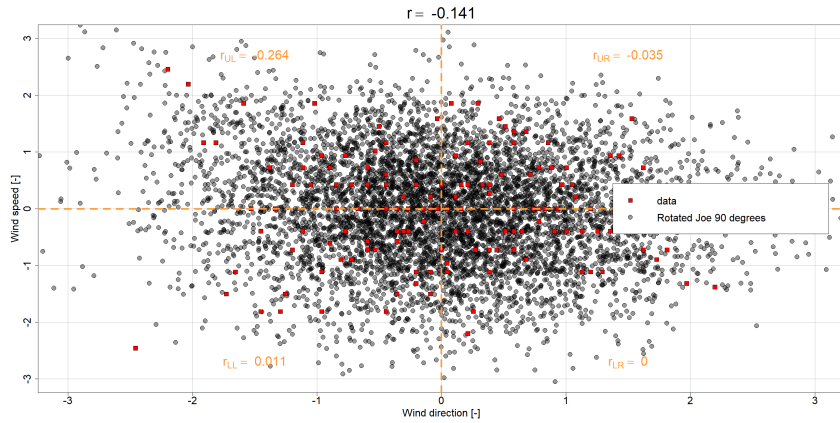


Figure D.7: Semi-correlation of the Joe rotated by 90° for wind direction w_d and wind speed w_s .

CDF of selected Copula models and Empirical Copulas

Below the CDF plots of the selected copula models are found, as well as the empirical copula of the variable pairs. The CDF of the copula pair: water level h and wave height H_s , is found in Section 4.3. The CDF plots show the cumulative probability of the copula models by a colour scale ranging from red to yellow. The variable pairs between water level, wave height and wave period show a decent fit of the model on the empirical copula. For the pairs including the wind speed and wind direction, the models still approximate the empirical copula, however, these fits are less decent.

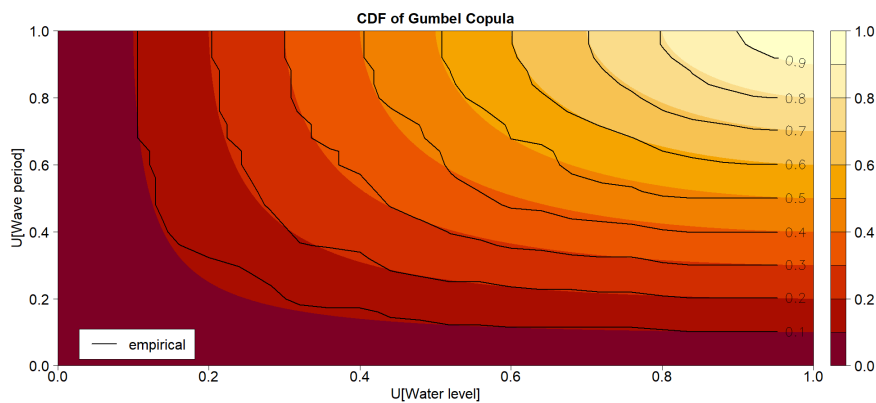


Figure D.8: CDF of the Gumbel and empirical copula for water level h and wave period T_p .

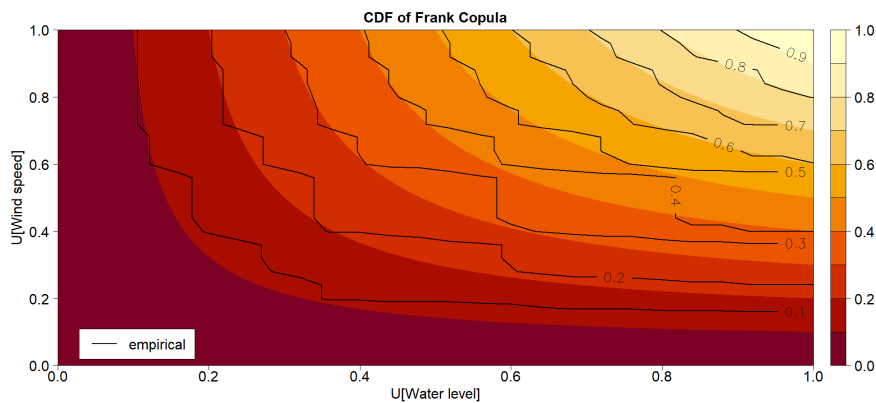


Figure D.9: CDF of the Frank and empirical copula for water level h and wind speed w_s .

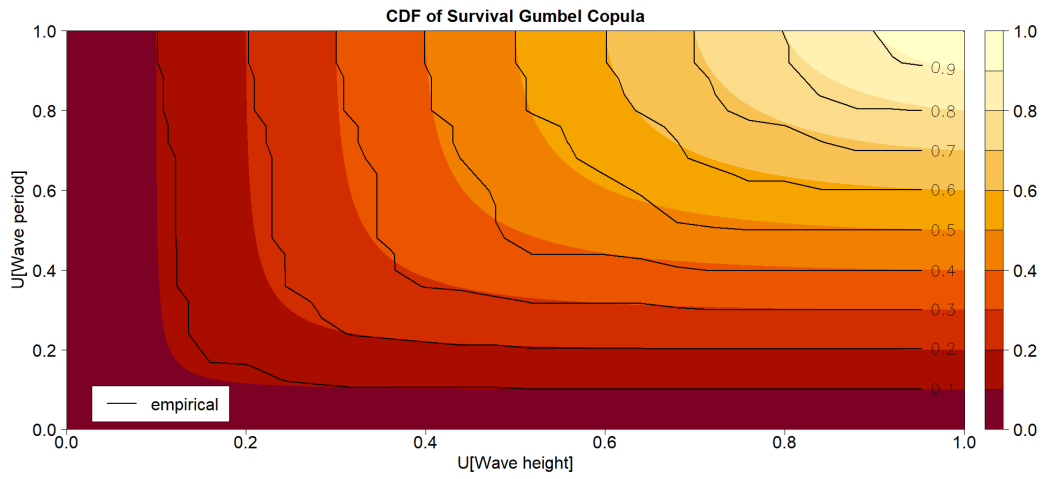


Figure D.10: CDF of the Survival Gumbel and empirical copula for wave height H_s and wave period T_p .

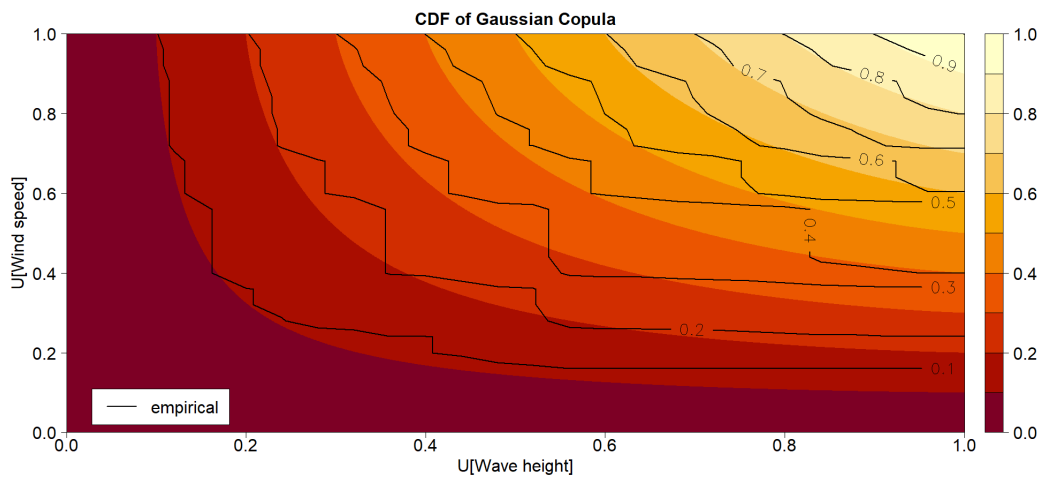


Figure D.11: CDF of the Gaussian and empirical copula for wave height H_s and wind speed w_s .

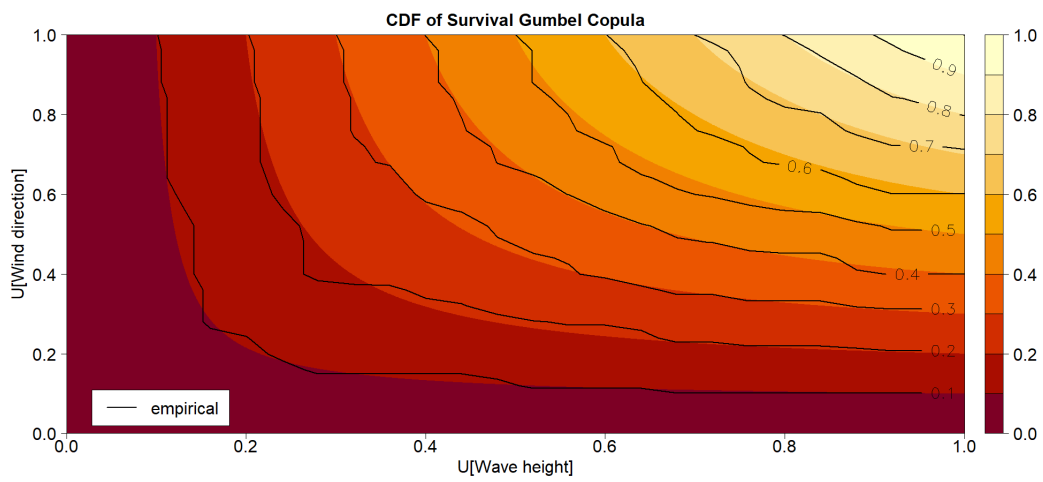


Figure D.12: CDF of Survival Gumbel and empirical copula for wave height H_s and wind direction w_d .

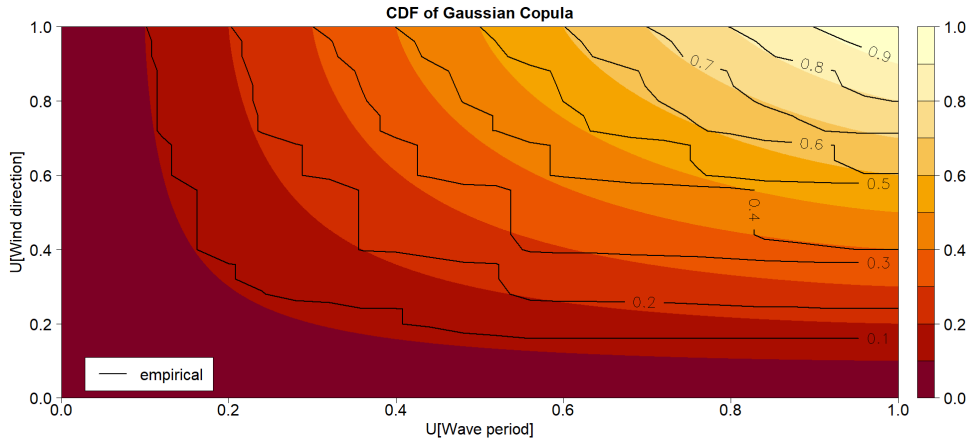


Figure D.13: CDF of the Gaussian and empirical copula for wave period T_p and wind direction w_d .

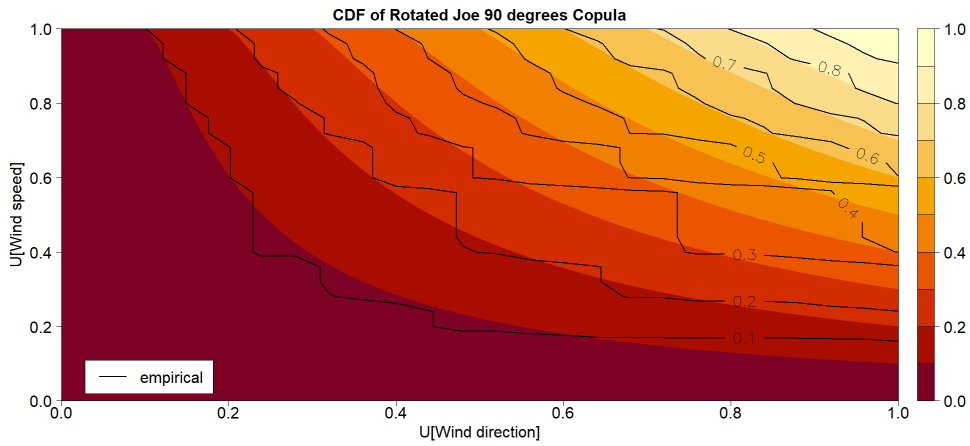


Figure D.14: CDF of Joe rotated by 90° and empirical copula for wind direction w_d and wind speed w_s .

Samples of the selected Copula models in $[0, 1]^2$

In the figures below, the samples in the unity space of the selected copula models are shown for all variable pairs (except water level and wave height, found in Figure 4.9).

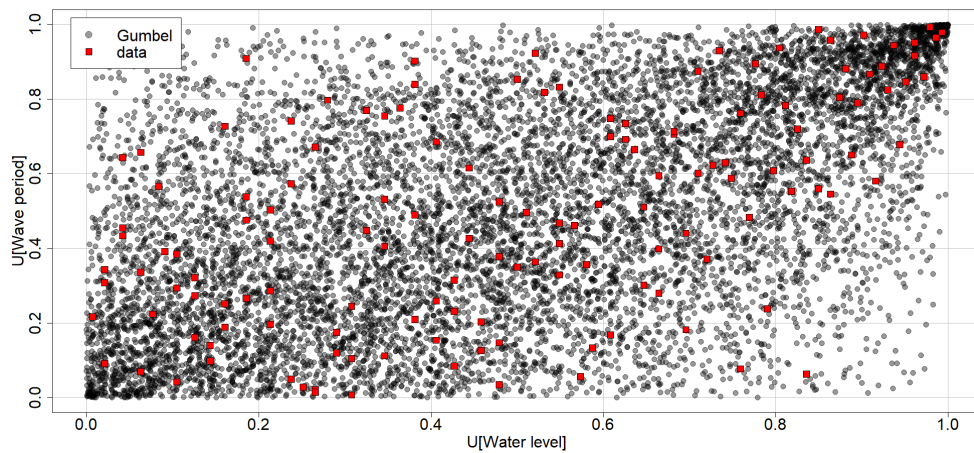


Figure D.15: Samples of Gumbel in $[0, 1]^2$ for water level h and wave period T_p .

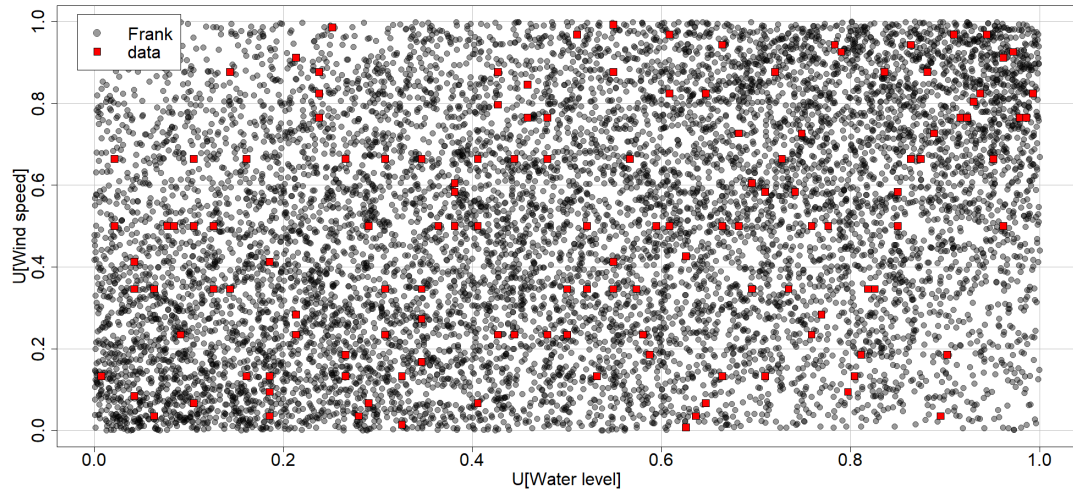


Figure D.16: Samples of Frank in $[0, 1]^2$ for water level h and wind speed w_s .

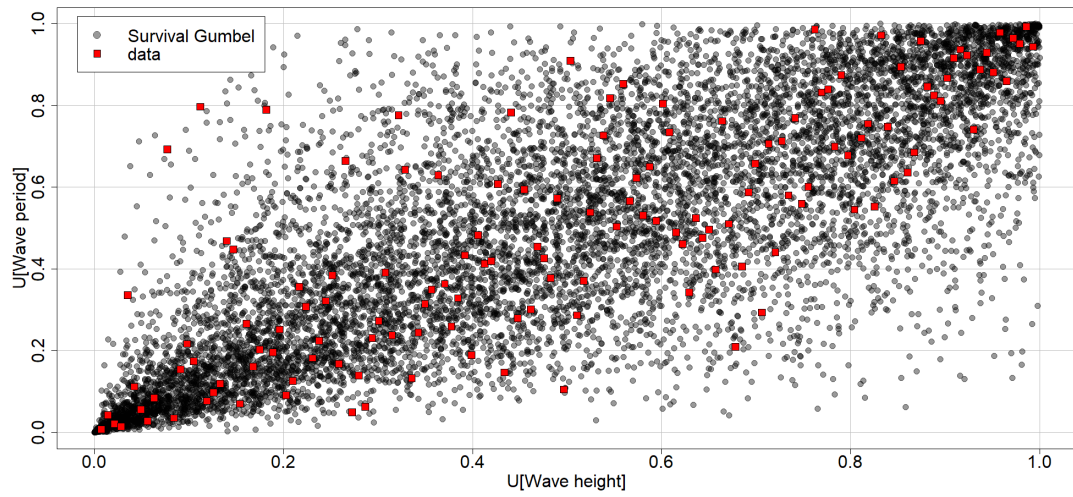


Figure D.17: Samples of Survival Gumbel in $[0, 1]^2$ for wave height H_s and wave period T_p .

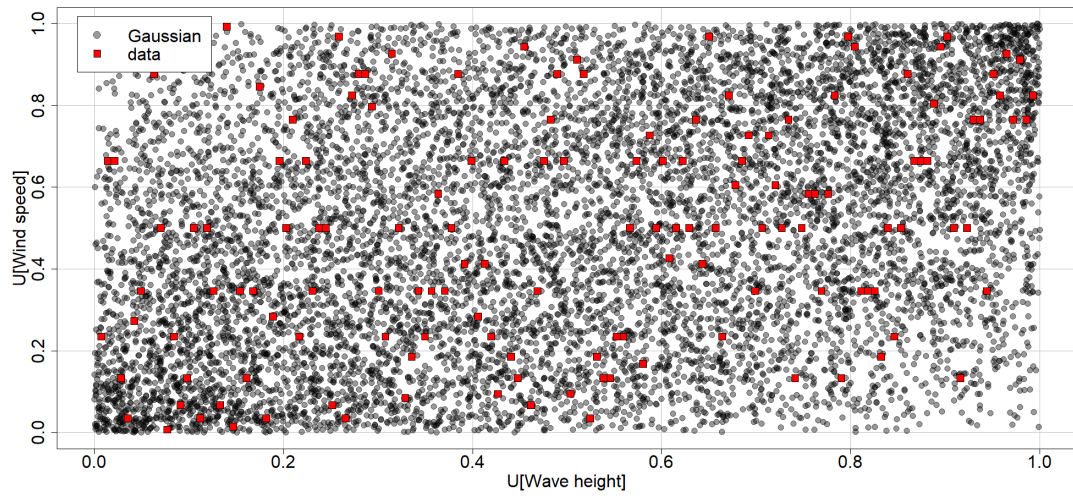


Figure D.18: Samples of Gaussian in $[0, 1]^2$ for wave height H_s and wind speed w_s .

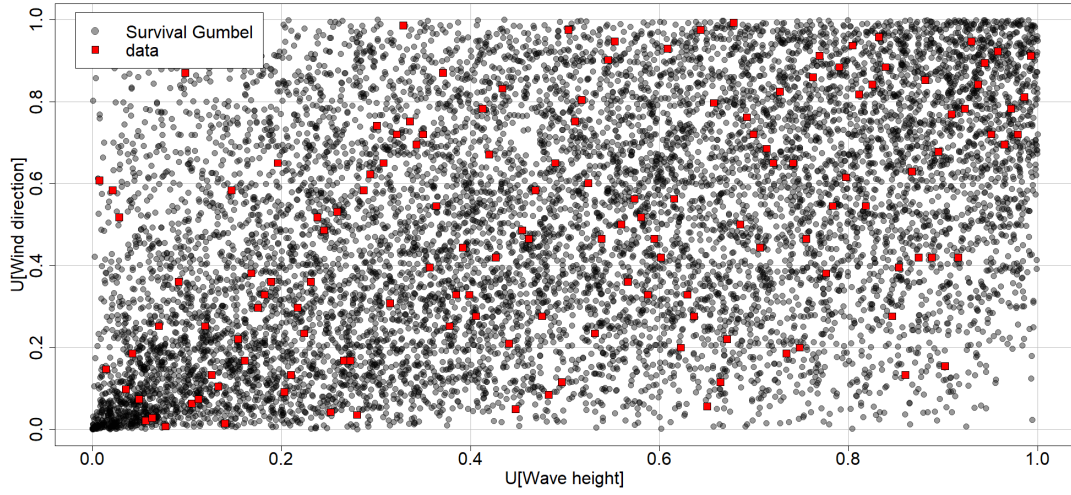


Figure D.19: Samples of Survival Gumbel in $[0, 1]^2$ for wave height H_s and wind direction w_d .

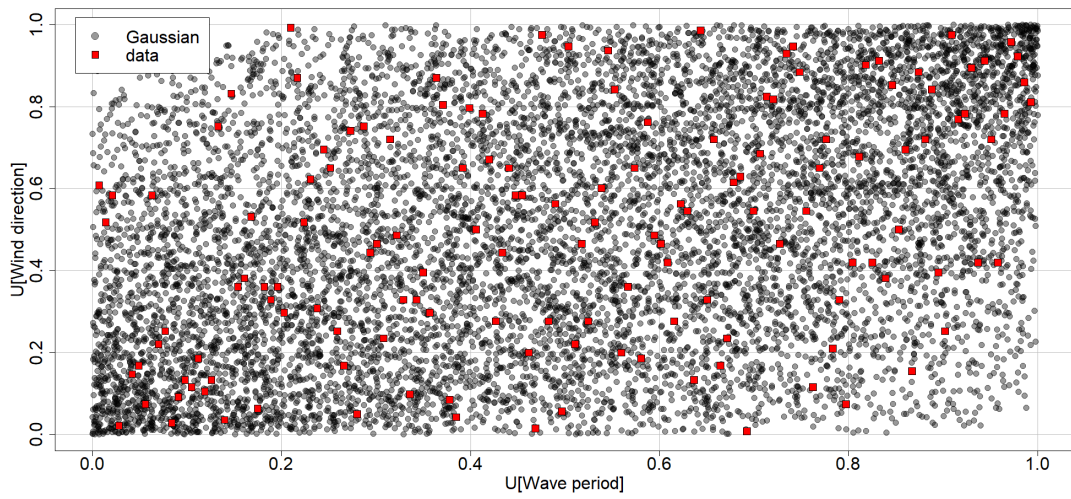


Figure D.20: Samples of Gaussian in $[0, 1]^2$ for wave period T_p and wind direction w_d .

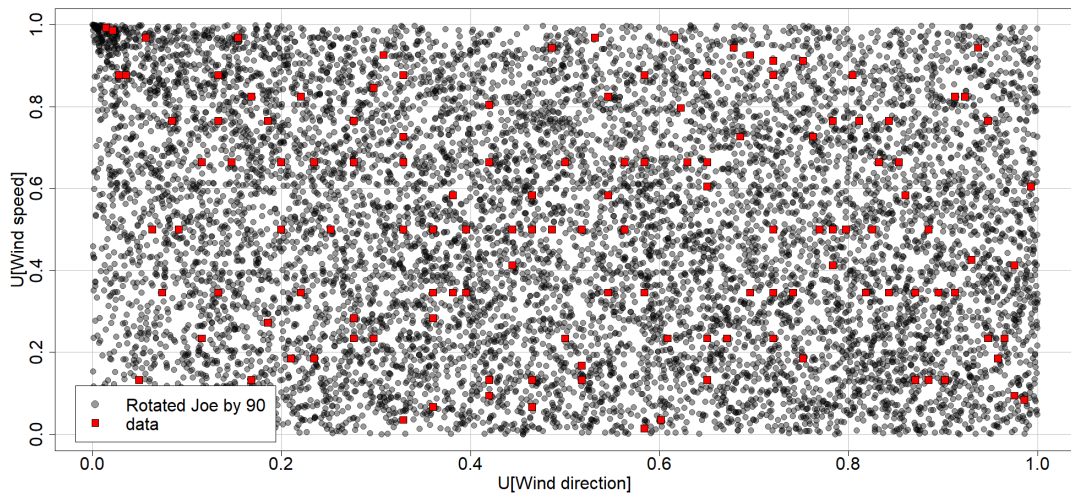


Figure D.21: Samples of Joe rotated by 90° in $[0, 1]^2$ for water level h and wave period T_p .

Copula samples transformed to variable space

In the figures below, the samples in variable space of the selected copula models are shown for all variable pairs (except water level and wave height, found in Figure 4.10).

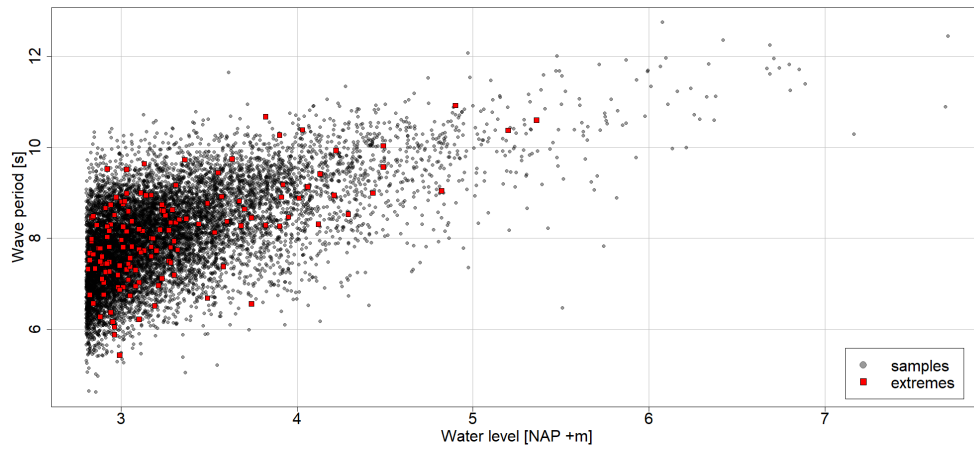


Figure D.22: Samples of Gumbel in variable space for water level h and wave period T_p .

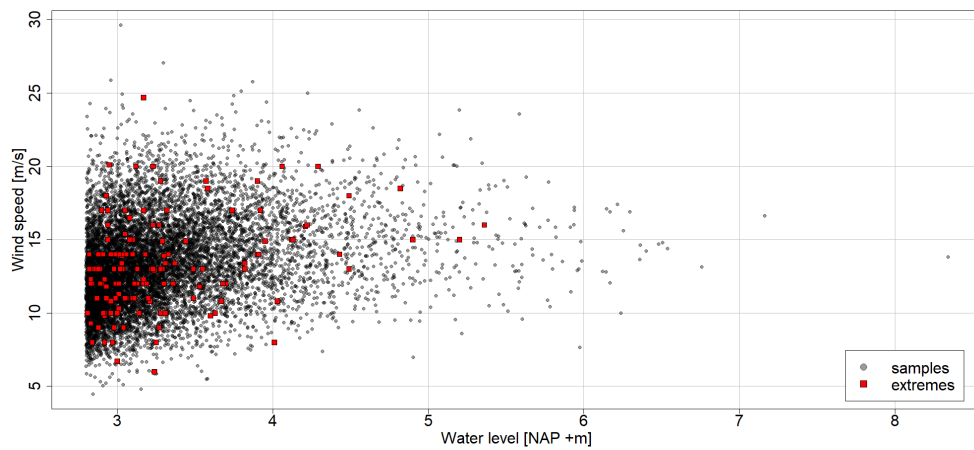


Figure D.23: Samples of Frank in variable space for water level h and wind speed w_s .

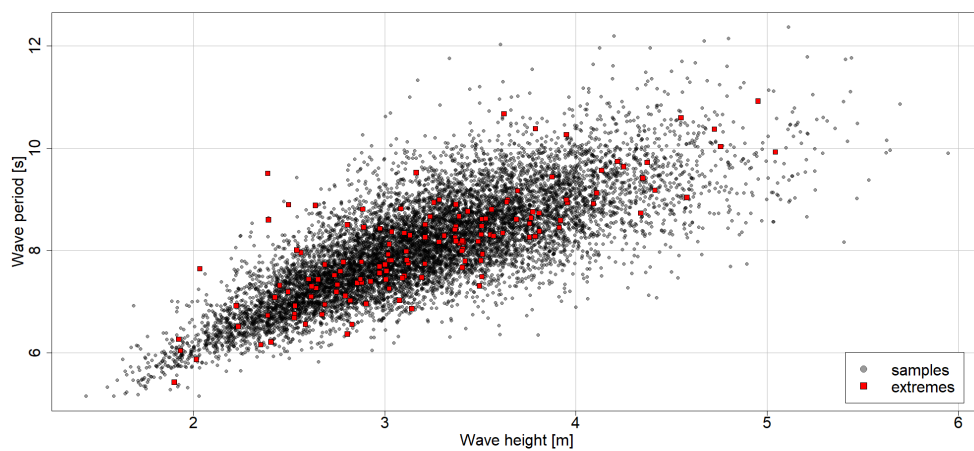


Figure D.24: Samples of Survival Gumbel in variable space for wave height H_s and wave period T_p .

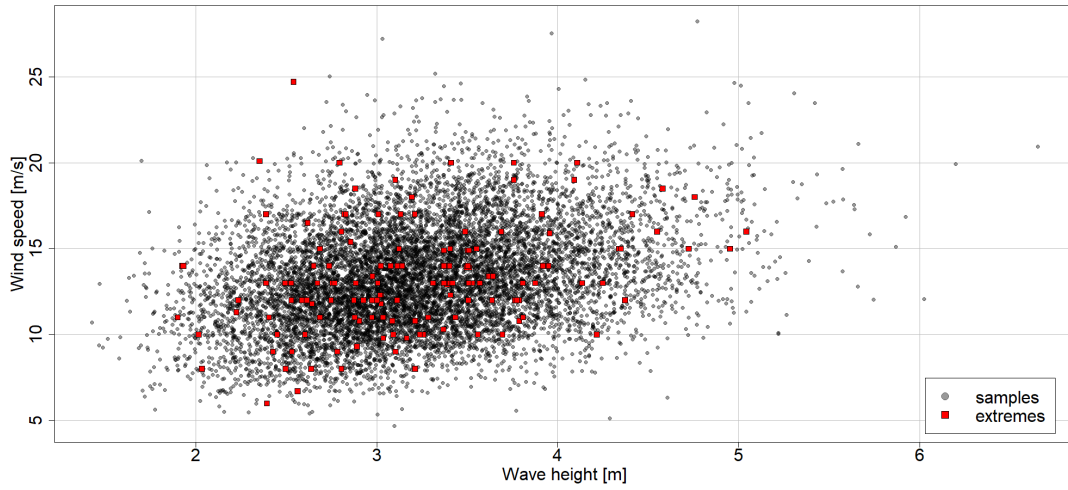


Figure D.25: Samples of Gaussian in variable space for wave height H_s and wind speed w_s .

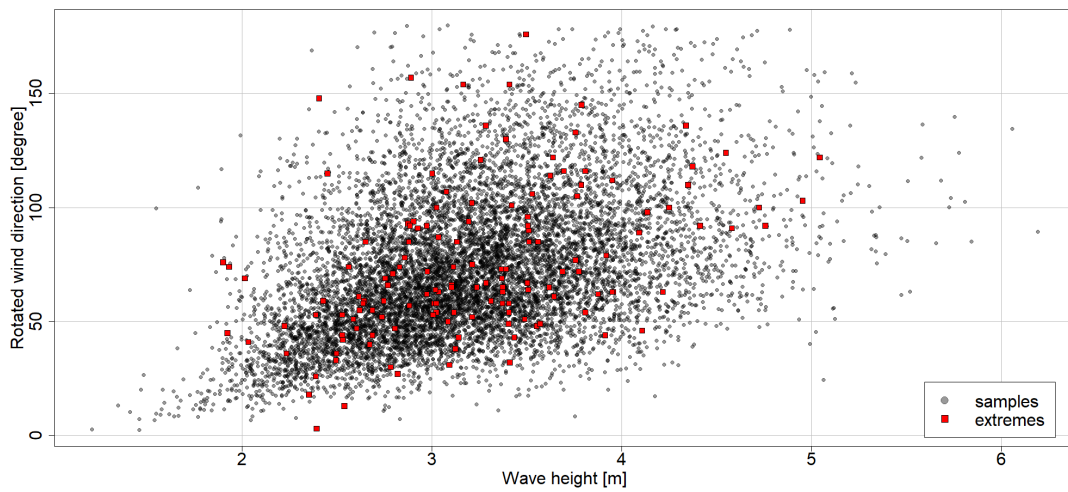


Figure D.26: Samples of Survival Gumbel in variable space for wave height H_s and wind direction w_d .

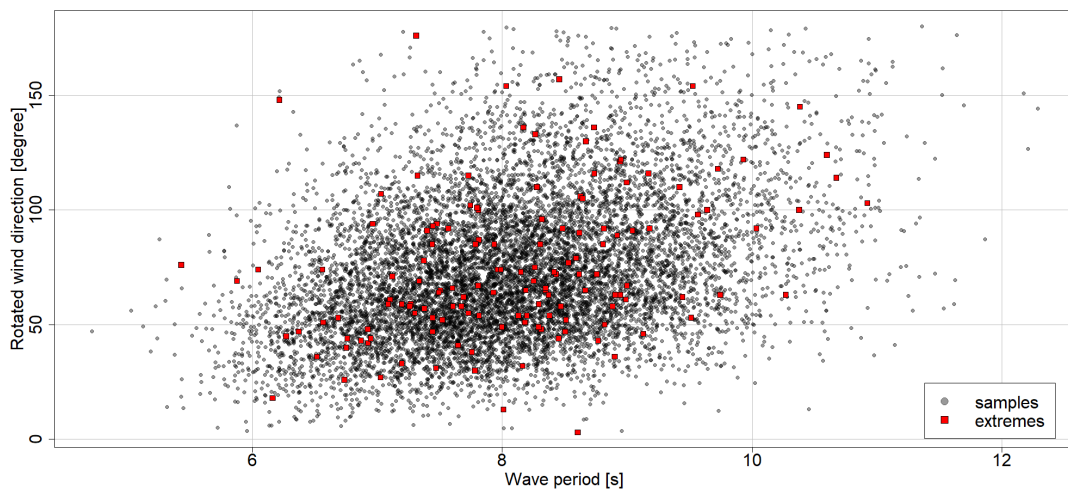


Figure D.27: Samples of Gaussian in variable space for wave period T_p and wind direction w_d .

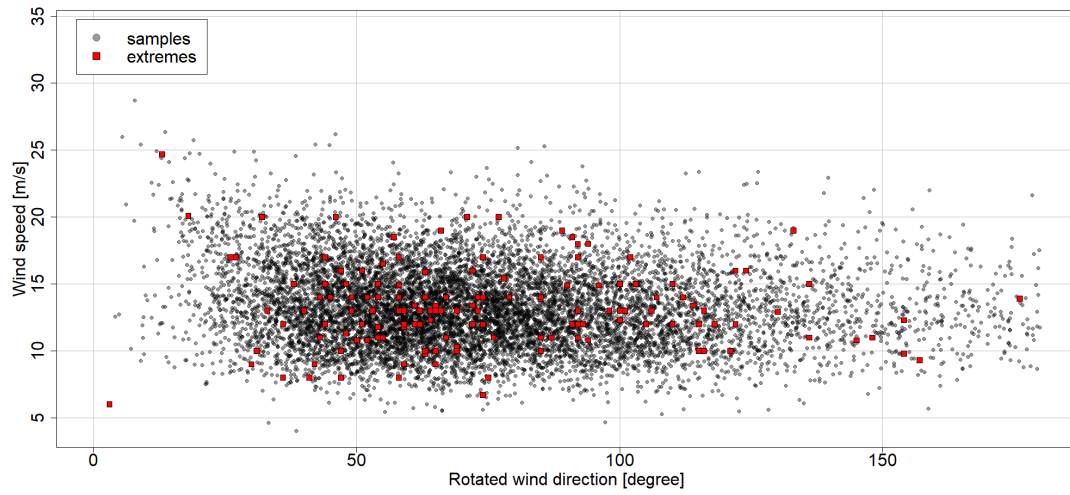


Figure D.28: Samples of Joe rotated by 90° in variable space for wind direction w_d and wind speed w_s .

E | Additional Results for Non-stationary marginals in Copula modelling

This appendix shows additional results of the analysis of a non-stationary marginal for the water level in copula modelling. The relation of the wave height and water level with the scale parameter can be found. As well as the changed ranks for all samples. In addition, the change in the copula family is found.

In Figure E.1, the (linear) relation between the wave height H_s and the scale parameter $\sigma(H_s)$ is shown. The sampled joint probabilities of points 1, 2 and 3 are transformed to wave heights using the quantile function of the (Gamma distributed) wave height.

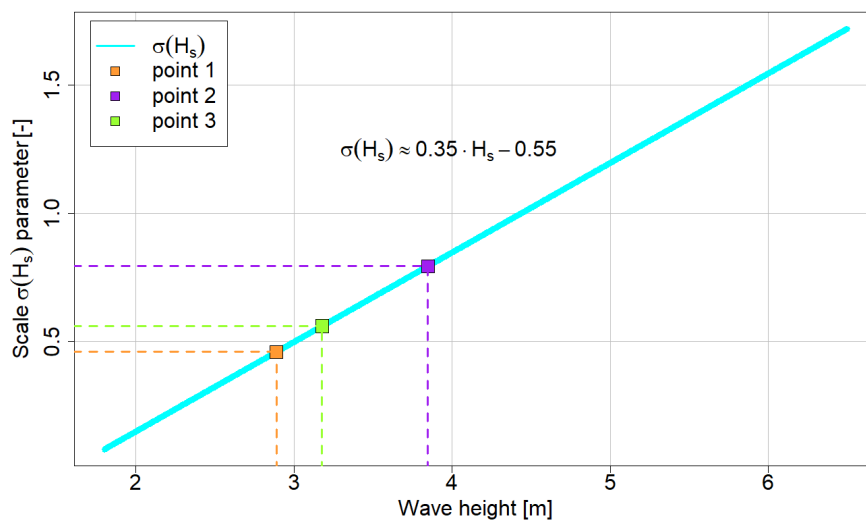


Figure E.1: The relation between the wave height and the scale parameter $\sigma(H_s)$.

Figure E.2 shows the transformed joint probabilities for the water levels using the non-stationary model. Each transformed sample i from Figure 4.12 has its own scale parameter $\sigma(H_{s,i})$ that depends on the wave height $H_{s,i}$, according to the relation shown in Figure E.1.

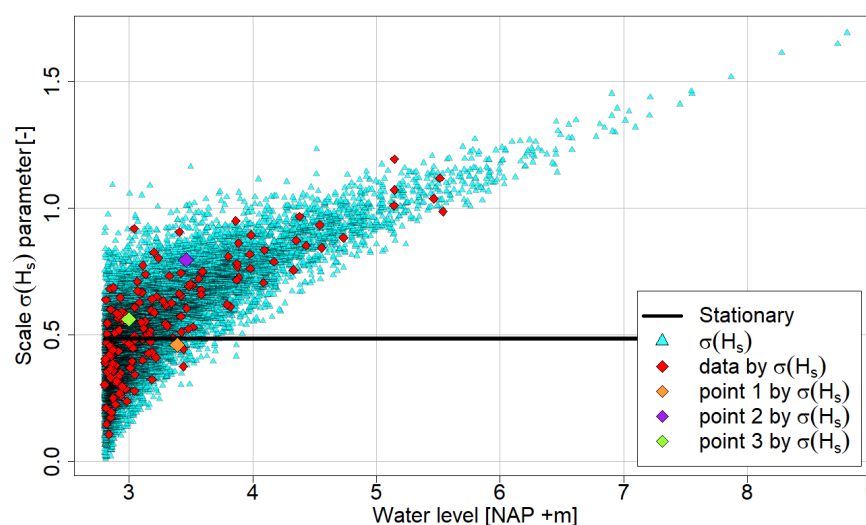


Figure E.2: The transformed samples to water levels against the scale parameter $\sigma(H_s)$.

The change in the ranks of the water level for all samples is shown in Figure E.3. The black solid line shows the transformed water levels by a stationary GPD model for the original ranks. The cyan solid line shows the transformed water levels by the non-stationary model plotted for the original ranks. The line shows an oscillating behaviour, concluding that the ranks of the water level change. The dashed blue line shows the sorted ranks for the transformed water levels by the non-stationary model.

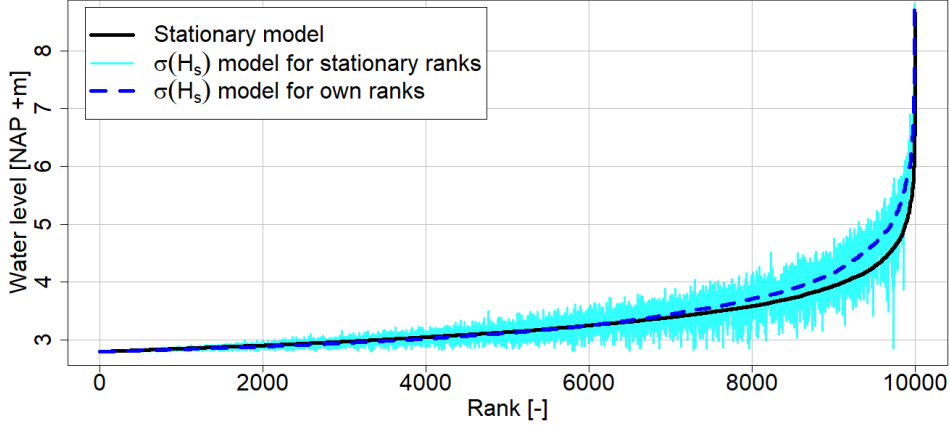


Figure E.3: The water level plotted against its ranks. The ranks of the original samples change due to the introduction of the non-stationary model.

In Table E.1, the change in semi-correlations for the upper right (*UR*) and lower left (*LL*) quadrants are shown when transforming the original Survival Clayton into variable space by the non-stationary model. The semi-correlations of the samples increase in both quadrants. In the *LL* quadrant, the correlation changes significantly from $r_{LL} = 0.003$ to $r_{LL} = 0.299$. To check whether the copula family remains unchanged, a bivariate copula is fitted for the transformed samples from Figure 4.14. The results in Table E.1 show that the copula family changes to a Survival BB1 copula. In addition, a Survival Clayton copula is forced to fit these values. The table shows that the semi-correlations in the quadrants are better approximated by the Survival BB1 copula. Also, the Survival BB1 copula provides a greater AIC.

Table E.1: Parameter, semi-correlations and AIC of the original copula and transformed variable space and copulas samples from the non-stationary model $H_{u,\sigma_{H_s}}$.

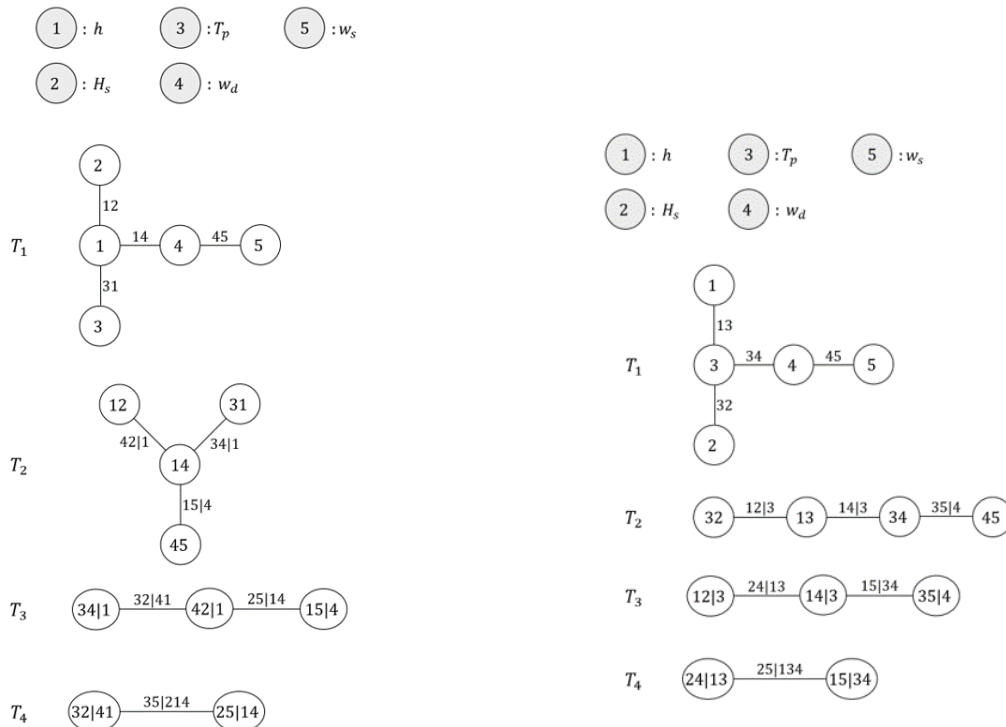
Transformed by $H_{u,\sigma_{H_s}}$	Original Survival Clayton	$H_{u,\sigma_{H_s}}$ model		
		Variable space	Survival BB1	Survival Clayton
Parameter:				
θ_1 [-]	1.370	–	2.110	2.444
θ_2 [-]	–	–	1.108	–
Criteria:				
r_{UR} [-]	0.734	0.800	0.816	0.806
r_{LL} [-]	0.003	0.299	0.309	0.092
AIC [-]	–	–	-10,671	-10,590

F | Vine Copulae Analysis

This appendix contains additional information on the Vine Copulae Analysis from Section 4.5.

Best Vine Copulas of Procedures 1 and 2

Figure F.1 shows the best-performing vine copulas from Procedures 1 and 2.



(a) Vine copula of Procedure 1

(b) Vine copula of Procedure 2

Figure F.1: Best vine copulas of Procedure 1 and 2.

Table F.1: The (conditional) copulas and parameters θ for the vines of Procedures 1, 2 and 3.

Tree	Procedure 1			Procedure 2			Procedure 3		
	Edge	Copula ^{a, b, c}	θ	Edge	Copula	θ	Edge	Copula	θ
T_1	12	SC	1.37	13	SC	1.18	12	SC	1.37
	14	F	1.09	34	F	2.49	14	Ta2	5.21
	31	SC	1.18	32	SGu	2.47	15	SC	0.46
	45	J 90°	-1.16	45	J 90°	-1.16	13	SC	1.18
T_2	15 4	SC	0.60	12 3	Ga	0.32	23 1	STa2	2.80
	42 1	Ga	0.42	14 3	J 90°	-1.09	24 1	Ga	0.42
	34 1	Gu	1.25	35 4	I	-	25 1	STa	1.85
T_3	25 14	F	1.39	15 34	SC	0.65	34 21	T	0.08
	32 41	SGu	1.85	24 13	C	0.39	35 21	BB8 270°	-2.87
T_4	35 214	F	-3.16	25 134	SGu	1.39	45 321	Ta2 90°	-20.00

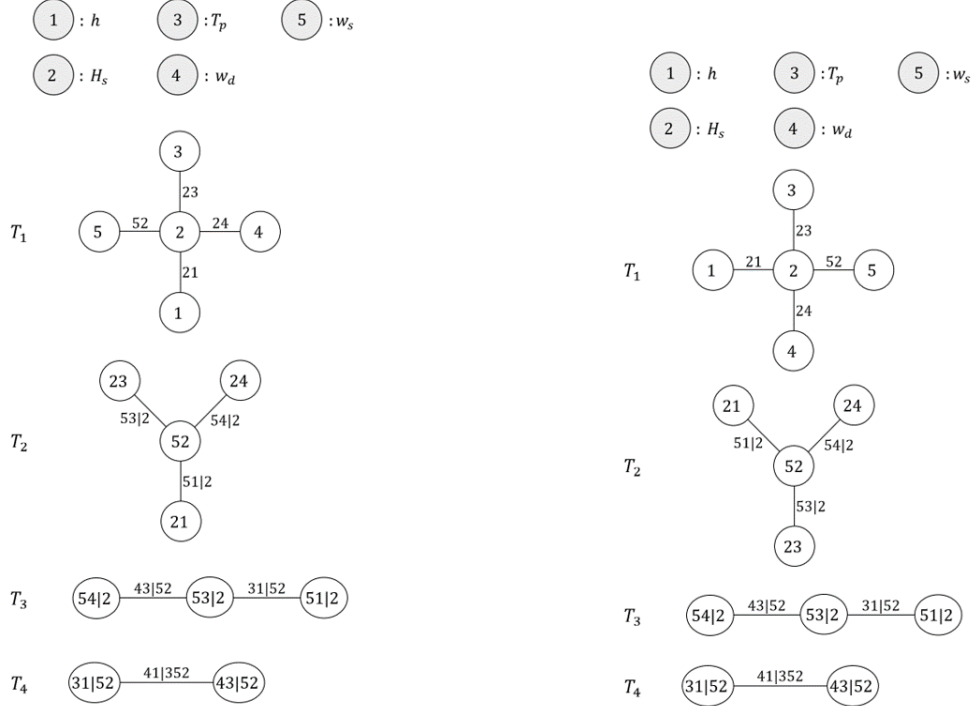
^a The following abbreviations are used for the copula families: I: Independent; Ga: Gaussian; T: Student-T; C: Clayton; Gu: Gumbel; F: Frank; J: Joe; Ta: Tawn; Ta2: Tawn 2.

^b If a copula is a Survival copula, an 'S' is set in front of the abbreviations, e.g. SC: Survival Clayton

^c If a copula is rotated by 90° or 270°, it is indicated behind the abbreviation

Selected Vine Copulas by the MST algorithm

Figures F.2 show the selected vine copulas using the MST algorithm for Procedures 1, 2 and 3. It shows that the selected vine copulas for Procedures 1 and 2 are tree-equivalent. The vine copula for Procedure 3 is not tree-equivalent but is very similar. Both vine structures are C-vines with the wave period T_p as the central node. In Figure F.3, the CDF plots of the performance of the MST algorithm are found for Procedures 1 and 2.



(a) Vine copula by MST algorithm of Procedure 1 and 2 (b) Vine copula by MST algorithm of Procedure 2

Figure F.2: Vine copulas of Procedure 1, 2 and 3 selected by the MST algorithm. Note, the vine copulas selected for Procedures 1 and 2 are tree-equivalent.

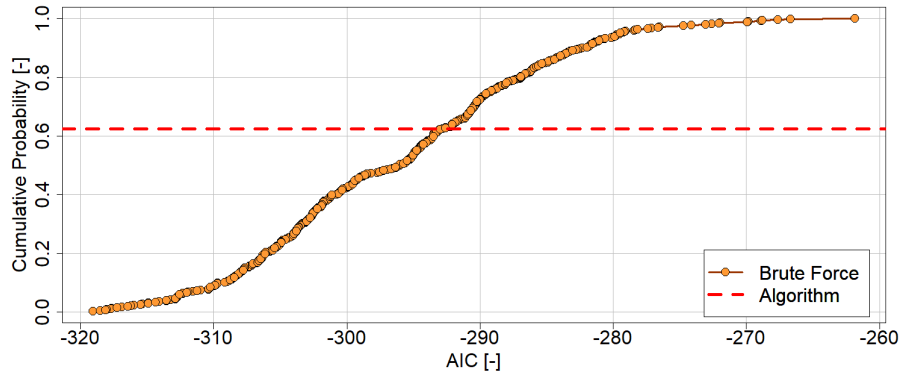
Table F.2: The (conditional) copulas of the selected vines using MST for Procedures 1, 2 and 3.

Tree	Procedure 1			Procedure 2			Procedure 3		
	Edge	Copula ^{a, b, c}	θ	Edge	Copula	θ	Edge	Copula	θ
T_1	21	SC	1.37	21	SC	1.37	21	SC	1.37
	23	SGu	2.47	23	SGu	2.47	23	STa	3.26
	24	SG	1.43	24	SG	1.43	24	SBB8	3.49
	52	F	2.03	52	F	2.03	52	STa2	2.12
T_2	51 2	SC	0.19	51 2	SC	0.19	51 2	T2	1.55
	53 2	I	—	53 2	F	-2.53	53 2	BB8 90°	-2.10
	54 2	J 270°	-1.24	54 2	J 270°	-1.24	54 2	J 270°	-1.28
T_3	31 52	SC	0.23	31 52	SC	0.25	31 52	SC	0.27
	43 52	I	—	43 52	SG	1.03	43 52	Ta	15.92
T_4	41 352	I	—	41 352	J 270°	-1.07	41 352	I	—

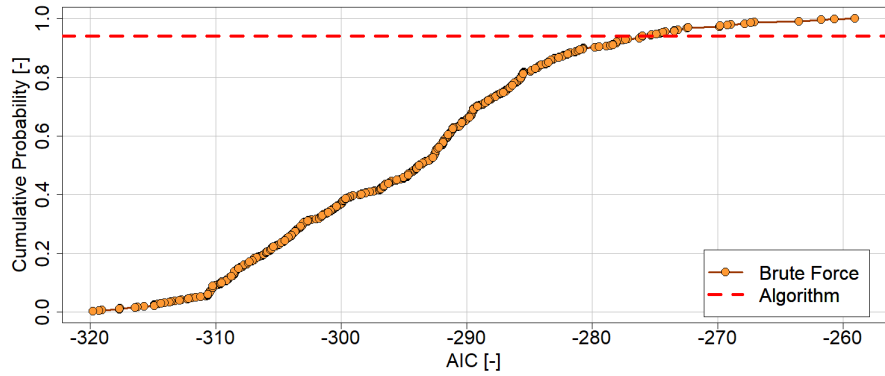
^a The following abbreviations are used for the copula families: I: Independent; Ga: Gaussian; T: Student-T; C: Clayton; Gu: Gumbel; F: Frank; J: Joe; Ta: Tawn; Ta2: Tawn 2.

^b If a copula is a Survival copula, an 'S' is set in front of the abbreviations, e.g. SC: Survival Clayton

^c If a copula is rotated by 90° or 270°, it is indicated behind the abbreviation



(a) Performance of the MST algorithm for Procedure 1



(b) Performance of the MST algorithm for Procedure 2

Figure F.3: CDF of the performance of the MST algorithm versus Brute Force fitting for Procedures 1 and 2.

The 2nd best-fitting vine copula of Procedure 3

The performance of the AIC for all matrices is visualized in Figure F.4. It shows that the best-performing vine copula with an AIC of -355.77 is matrix 424. The 2nd best-performing vine copula with an AIC of -353.16 is matrix 243.

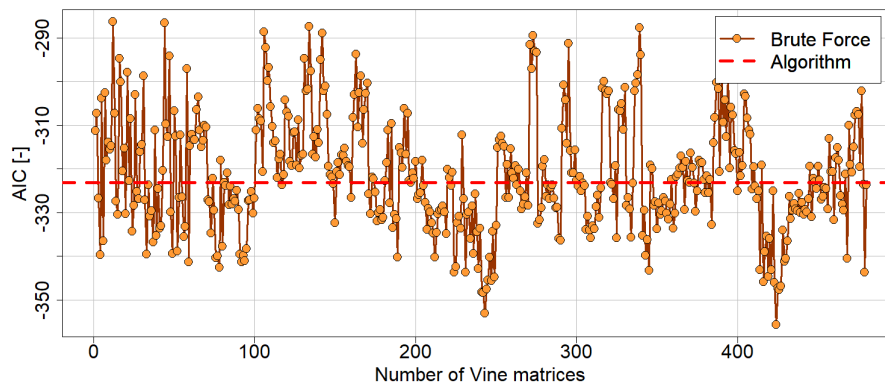


Figure F.4: Plot of the performance of the MST algorithm and all possible matrices for Procedure 3.

In Figure F.5, the 2nd best-performing vine copula from Procedure 3 is shown. The vine copula has a similar vine structure as the best vine copula of Procedure 1. The (conditional) copulas are found in Table F.3.

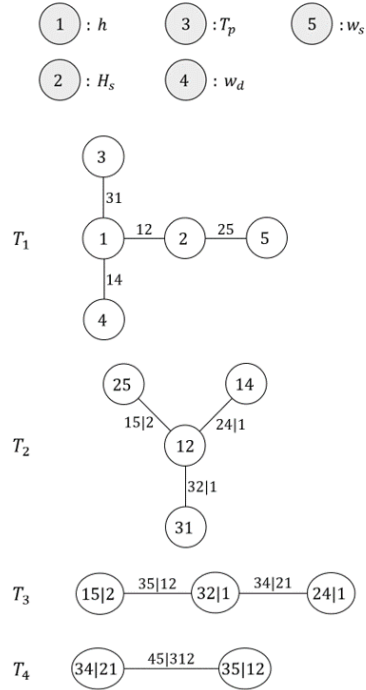


Figure F.5: 2nd best-fitting vine copula from Procedure 3.

Table F.3: The (conditional) copulas of the 2nd best-fitting vine copula of Procedure 3.

Tree	Edge	Copula ^{a, b, c}	θ
T_1	31	SC	1.18
	12	SC	1.37
	14	Ta2	5.21
	25	STa	2.12
T_2	15 2	Ta	1.55
	24 1	Ga	0.42
	32 1	STa2	2.80
T_3	35 12	BB8 270°	-3.50
	34 12	T	0.08
T_4	45 312	Ta2 90°	-5.77

^a The following abbreviations are used for the copula families: I: Independent; Ga: Gaussian; T: Student-T; C: Clayton; Gu: Gumbel; F: Frank; J: Joe; Ta: Tawn; Ta2: Tawn 2.

^b If a copula is a Survival copula, an 'S' is set in front of the abbreviations, e.g. SC: Survival Clayton

^c If a copula is rotated by 90° or 270°, it is indicated behind the abbreviation

G | SWAN Input File

This appendix contains one of the input files of the 25 propagated cases.

SWAN Input file case 1/25

```
PROJ 'EEMSDOLLARD' '01'  
SET LEVEL 5.36  
MODE STAT  
COORD CART  
CGRID REG 0 25000 0 25000 25000 500 500 CIRCLE 360 0.03 1  
INPGRID BOT REG 0 25000 0 500 500 50 50 EXC -9999  
READINP BOT 1 'z_mesh.bot' 1 0 FREE  
WIND 16.0 216  
BOUN SHAP JONSWAP 3.3 PEAK DSPR DEGR  
BOUND SIDE N CCW CON PAR 4.548729 10.598121 216 30  
SETUP  
QUAD  
WCAP  
BREA  
DIFFR  
NUM ACCUR STAT MXITST=50  
POINTS 'loc' FILE 'mypoints.loc'  
TABLE 'loc' HEAD 'table1' XP YP HS TM01 TPS DIR DEP WATLEV WIND  
BLOCK 'COMPGRID' NOHEADER 'chris1.mat' LAY 3 XP YP DEP HSIGN TM01 TPS DIR WIND  
COMPUTE  
STOP
```

H | The Deterministic Design of the Wide Green Dike

In this appendix, a deterministic design is created to act as a benchmark for the probabilistic design. The design is created by performing Algorithm H.1. This algorithm is stated and performed below.

Algorithm H.1: Deterministic Design

- Step 1:** Acquire the design values $\{h_d, H_{s,d}, T_{p,s}, w_{s,d}\}$ for the required failure probability of $P_{f,req} = 1/37,500$ [1/year]. The design values result from evaluating the quantile functions of the water level (GPD-distributed) and the concomitant variables, wave height, wave period and wind speed (each is Gamma-distributed), at the $P_{f,req}$ probability.
- Step 2:** Determine the governing wind direction $w_{d,d}$ for offshore-nearshore transformation. According to Sweco (2021b), the North-West direction governs the water level set-up during storm conditions.
- Step 3:** The 95% value of the SSP5-8.5 SLR scenario for the year 2150, is added to the h_d design water level. This results in an extreme water level design value that includes SLR; $h_{d,SLR}$.
- Step 4:** Transform $h_{d,SLR}$ to an 18-hour average water level $h_{d,18}$ according to the assumed storm progression from Figure 5.4. This is done by multiplying $h_{d,SLR}$ by the reduction factor r_{18} .
- Step 5:** Perform the offshore-nearshore transformation in SWAN using the input data $\{h_{d,18}, H_{s,d}, T_{p,d}, w_{s,d}, w_{d,d}\}$ to create the nearshore wave characteristics $\{H_{s-p}, T_{p-p}, \theta_p\}$.
- Step 6:** Determine the angle of wave attack β of the nearshore waves at the three locations P_1, P_2 and P_3 . Determine the reduced wave height and reduced wave period by multiplying $H_{s,p}$ and $T_{p,d}$ with the influence factor f_β . The WGD orientation for the three locations is found in Table 5.1.
- Step 7:** Determine the wave steepness s_{op} for the reduced waves from Step 6. Note, the wave steepness must lie in the domain $[0.01, 0.05]$ in order to be in the range of application of the failure mechanism.
- Step 8:** Determine the erosion volume V_e , erosion length L_e , erosion depth d_e and the start of the erosion pit relative to the 18-hour average water level d_t at P_1, P_2 and P_3 . Use a safe erosion coefficient of $c_e = 0.8$ [-], resulting from expert judgement (Sweco, 2021c).
- Step 9:** Using the derived erosion profile at the governing location, determine the design crest height $h_{cr,d}$ and dike profile.
-

In the deterministic design, the design values result from the required exceedance probabilities for the design. The required failure probability is $P_{f,req} = 1/37,500$ per year. The design values result from evaluating the quantile functions of each variable for an exceedance probability of $\mathbb{P}(X > x) = P_{f,req}$. The design wind direction is North-West (Sweco, 2021b). In addition, the 95 percentile value of the SSP5-8.5 SLR scenario is added to h_d , resulting in $h_{d,SLR}$. The water level $h_{d,SLR}$ is then reduced by r_{18} to result in an 18-hour average water level during a storm event. The resulting design values are shown in Table H.1.

Table H.1: Design values of the deterministic design.

h_d [NAP +m]	$H_{s,d}$ [m]	$T_{p,d}$ [s]	$w_{s,d}$ [m/s]	$w_{d,d}$ [°N]	$h_{d,SLR}$ [NAP +m]	$h_{d,18}$ [NAP +m]
8.38	6.44	12.94	29.32	315	10.70	9.95

The values from Table H.1 are propagated by SWAN to result in the nearshore wave characteristics. The propagated values for the locations of interest are found in Table H.2.

Table H.2: Propagated wave characteristics at points P_1 , P_2 and P_3 of the deterministic design.

Location	$H_{s,p}$ [m]	$T_{p,p}$ [s]	θ_p [$^\circ N$]	f_β [-]
P_1	2.61	4.23	132	–
P_2	2.45	4.04	146	0.80
P_3	2.31	3.90	158	0.88

The angle of wave attack β at each of the locations determines the reduction factor for the design wave loads. The wave characteristics from Table H.2 are reduced by f_β . Using the reduced wave height, wave period and wave steepness (limited between [0.01, 0.05]), the erosion profile at each location is determined. The governing location for the deterministic design is P_3 , as found in Table H.3. Note, the $|\beta| > 90$ for P_1 .

Table H.3: Erosion profile at point P_3 of the deterministic design.

Location	V_e [m^3/m]	d_e [m]	L_e [m]	d_t [m]
P_3	22.60	1.45	23.45	2.03

The erosion profile at P_3 results in a design crest height of $h_{cr} = \text{NAP} + 11.24$ meters and a design clay layer thickness of $d_e = 1.45$ meters. Using the design crest height, the dike profile is constructed. The new dike profile starts at the road at the inside of the current dike and is constructed outwards. The following items are accounted for:

- The road is located at NAP +3.05 meter.
- There is a minimum crest width of 1 meter.
- The outer berm is located at NAP +3.55 meters and has a width of 3 meters with a slope of 1 : 20.
- The inner slope is $\alpha_{in} = 1 : 3$.
- The outer slope is $\alpha = 1 : 7$.

The final design is shown in Figure H.1. The deterministic design resulted in a clay volume of 241.2 m^3/m . This results in a total of 3,015,000 m^3 of clay for the entire dike trajectory of 12.5 kilometres.

	New clay layer
	Current clay layer
	Asphalt layer
	Densely-packed sand
Units: [m]	

Polder

Salt marsh

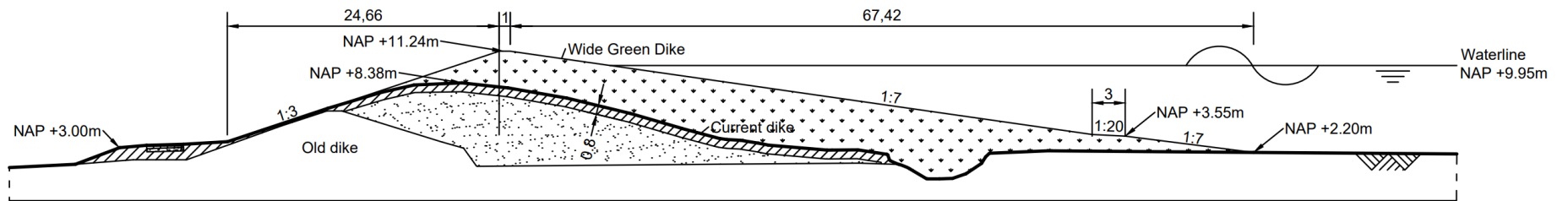


Figure H.1: The deterministic design of the WGD.

I | Additional results of the Vine-Based Design

This appendix provides additional results and information on the vine-based probabilistic design. Tables I.1 and I.2 show the input and output of the offshore-nearshore transformation.

Table I.1: Statistical summary of the input for the offshore-nearshore transformation.

Input	Unit	Min. value	1 st Quartile	Median	Mean	3 rd Quartile	Max. value	Standard deviation
h	[NAP + m]	2.87	3.86	4.22	4.33	4.68	10.58	0.66
H_s	[m]	1.05	2.78	3.18	3.22	3.63	6.96	0.63
T_p	[s]	4.13	7.39	8.06	8.11	8.77	13.42	1.03
w_s	[m/s]	2.91	11.09	13.02	13.26	15.17	34.94	3.05
w_d	[$^{\circ}N$]	200 ^a	251.2	269.6	274.0	292.7	360.0	30.8

^a Note, w_d shows where the wind direction comes from and is truncated between [200, 360] $^{\circ}N$ (clockwise)

Table I.2: Statistical summary of the input for the offshore-nearshore transformation.

Location & Output	Unit	Min. value	1 st Quartile	Median	Mean	3 rd Quartile	Max. value	Standard deviation
Point 1								
H_{s-p}	[m]	0.43	0.72	0.76	0.77	0.82	1.56	0.08
T_{p-p}	[s]	3.86	5.18	5.47	5.46	5.75	7.55	0.40
θ_p	[$^{\circ}N$]	76.4 ^a	106.1	116.4	118.2	128.6	173.7	16.3
Point 2								
H_{s-p}	[m]	0.50	0.59	0.62	0.62	0.65	0.96	0.05
T_{p-p}	[s]	4.11	4.75	4.89	4.91	5.05	6.67	0.22
θ_p	[$^{\circ}N$]	45.1 ^a	77.6	90.4	93.8	106.7	173.4	22.0
Point 3								
H_{s-p}	[m]	0.49	0.63	0.67	0.67	0.70	1.05	0.05
T_{p-p}	[s]	3.80	4.83	4.98	4.96	5.11	6.15	0.24
θ_p	[$^{\circ}N$]	54.6 ^a	79.2	88.2	91.0	100.0	163.3	16.2

^a Note, θ_p shows where the waves move towards in $^{\circ}N$ (clockwise)

In Figure I.1, the modelled erosion coefficient c_e is found. The orange bars show c_e modelled by a truncated Normal distribution with a mean of $\mu = 0.54$ and standard deviation of $\sigma = 0.14$ for the boundaries [0.54, 1.00]. This distribution results from the Delta Flume results and expert judgement in Sweco (2021c) and Deltares (2022b). The experts stated that for a deterministic design, an erosion coefficient of $c_e = 0.8$ is advised to be used. Moreover, the expert stated that it is unwise to design a WGD for a c_e outside the boundary of [0.54, 1.00]. A lower c_e results in a stronger clay layer. A $c_e < 0.54$ corresponds to a very strong clay layer, which is also very well applied during construction. A $c_e > 1.00$ corresponds to an erosion-prone clay layer which is applied poorly during construction. The experts stated that an c_e between [0.54, 1.00] should be feasible for the locally ripened clay and a decent construction plan. Comparing the results with a design that only accounts for $c_e = 0.8$ shows that the clay layer thickness increases with 5 centimetres.

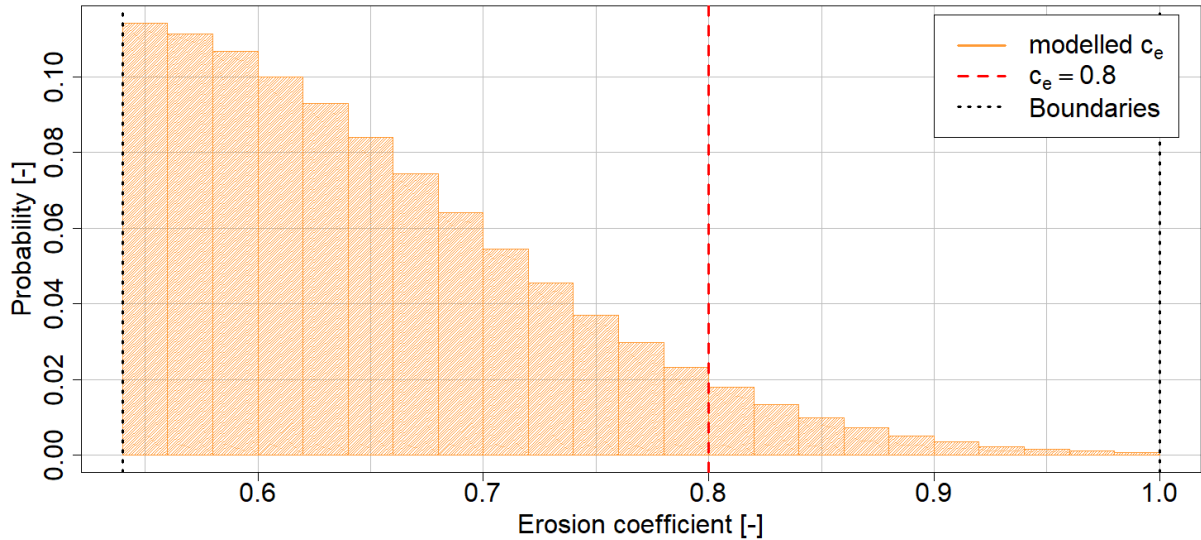
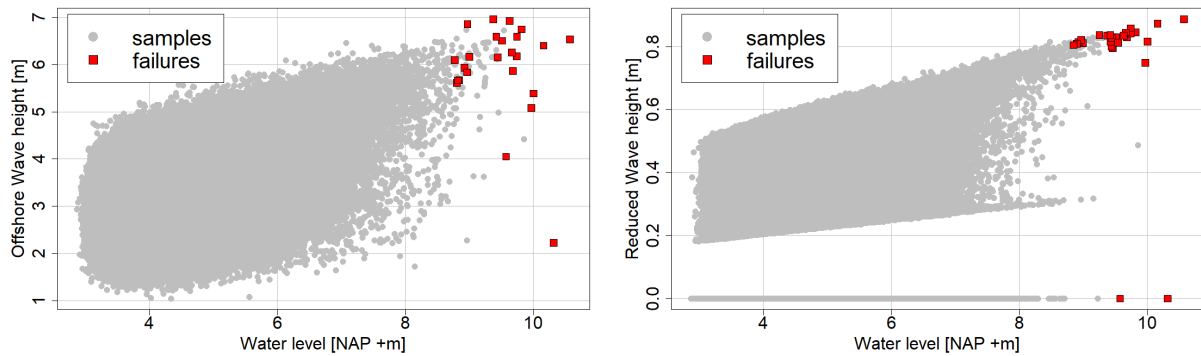


Figure I.1: The modelled erosion coefficient c_e for $n = 1,000,000$ samples.

The 18-hour water level and offshore wave height combinations for which the probabilistic design failed are shown in Figure I.2a. Figure I.2b shows the 18-hour water level and reduced nearshore waves from the offshore-nearshore transformation and the influence factor f_β . Notice that there are two failures that solely depend on h_{18} since $H_s = 0$.



(a) The sampled offshore wave height H_s versus 18-hour average water level h_{18} . The red squares indicate the combinations, for which the probabilistic design failed

(b) The reduced nearshore wave height H_s versus 18-hour average water level h_{18} . The red squares indicate the combinations, for which the probabilistic design failed

Figure I.2: The 18-hour average water level and wave height combinations for which the probabilistic design failed.

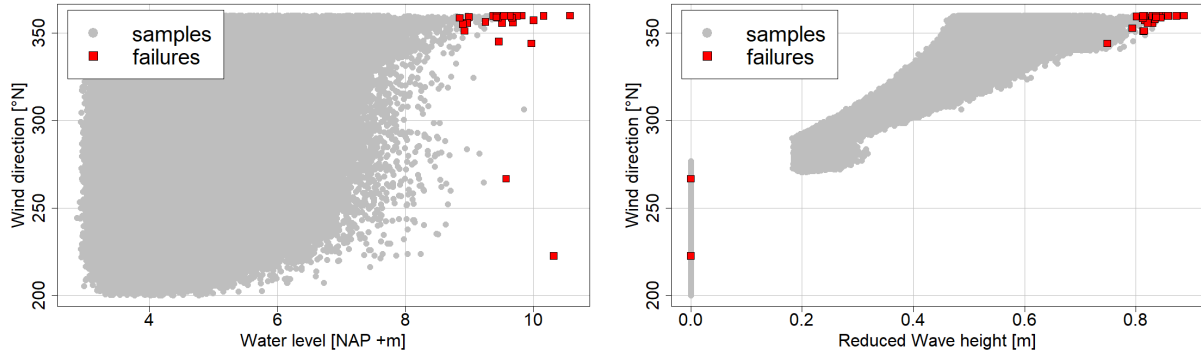
Tables I.3 and I.4 show the statistical summaries of the vine copula samples and reduced nearshore waves, for which the probabilistic design failed. Comparing the tables and Figure I.2b shows that h_{18} is the dominant cause for failure. The large h_{18} causes the erosion profile to reach the design crest. Furthermore, Table I.3 clearly shows that the dominant wind direction for the failures is North. This corresponds to the local knowledge in Sweco (2021a). The dominant wind direction for the most significant waves is North. For the water level set-up, this is slightly more from the North-West. In the vine copula samples, the North wind direction is most predominant for both the most significant water levels and wave heights, as found in Figure I.3. The figure shows that most failures are for wind direction between 350 and $360^\circ N$ (clockwise).

Table I.3: Statistical summary of the 18-hour average water level h_{18} , offshore wave height $H_{s,o}$ and period $T_{p,o}$ and wind speed w_s and direction w_d for which the probabilistic design failed.

Variable	Unit	Min. value	1 st Quartile	Median	Mean	3 rd Quartile	Max. value	Standard deviation
h_{18}	NAP +m	8.85	9.39	9.53	9.55	9.75	10.58	0.43
$H_{s,o}$	m	2.23	5.83	6.16	5.94	6.58	6.96	1.00
$T_{p,o}$	s	8.57	11.73	12.49	12.15	12.76	13.40	1.13
w_s	m/s	6.48	20.94	25.97	23.89	27.99	31.06	5.85
w_d	$^{\circ}N$	222.5	355.7	358.7	348.3	359.7	359.9	31.5

Table I.4: Statistical summary of the reduced nearshore wave height H_s and period T_p for which the probabilistic design failed.

Variable	Unit	Min. value	1 st Quartile	Median	Mean	3 rd Quartile	Max. value	Standard deviation
H_s	m	0	0.81	0.82	0.76	0.84	0.89	0.23
T_p	s	4.82	5.23	5.28	5.26	5.32	5.51	0.27



(a) The sampled w_d versus the sampled h_{18}

(b) The sampled w_d versus the reduced wave heights H_s

Figure I.3: The combinations of wind direction w_d and 18-hour average water level h_{18} and reduced wave height H_s that led to the failure of the probabilistic design.

	New clay layer
	Current clay layer
	Asphalt layer
	Densely-packed sand
Units: [m]	

Polder

Salt marsh

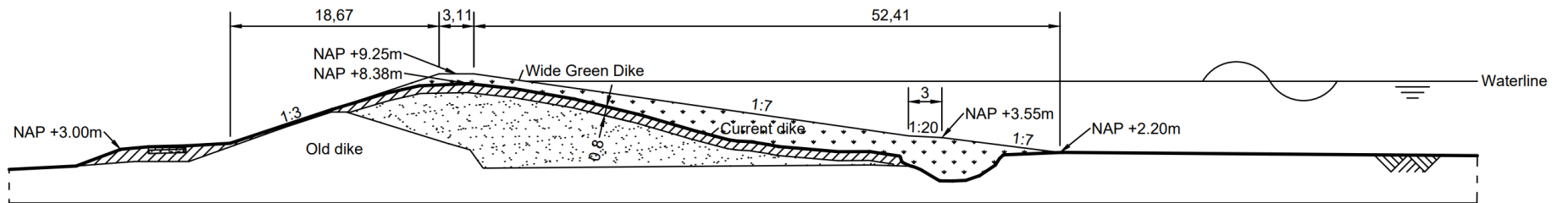


Figure I.4: The probabilistic design of the WGD for the year 2150. A water line is drawn to emphasize the seaward side of the dike.

J | SSP5-8.5 Sea Level Rise scenario

This appendix shows the accounted SLR distributions for the SSP5-8.5 scenario. The SLR distributions are selected by fitting the percentiles provided by KNMI (2021) for the SSP5-8.5 scenario of the IPCC (2022). For the years 2050 to 2100, five percentiles are provided. The 5th, 17th, 50th, 83rd and 95th percentiles. Three percentiles are provided for the years 2110 up to 2150, namely the 17th, 50th and 83rd percentiles. Figure 2.9 show that the mean of the distribution is not in the middle of the confidence interval. Therefore, these percentiles are fitted by Log-Normal distributions. The fits from the Log-Normal distributions also provided better approximations than other distributions; Normal, Weibull and Gamma.

The resulting parameters are found in Table J.1. Note, that for a Log-Normal distribution μ and σ are not the mean and standard deviation, but the parameters of the distribution.

Table J.1: Log-Normal distribution parameters of the SLR for different years.

Log-Normal	Sight-year for SLR					
Year	2050	2060	2070	2080	2090	2100
μ	-1.24	-0.97	-0.75	-0.55	-0.37	-0.23
σ	0.30	0.27	0.28	0.27	0.26	0.25
Year	2110	2120	2130	2140	2150	
μ	-0.10	0.00	0.09	0.16	0.25	
σ	0.27	0.31	0.32	0.35	0.36	

In Figure J.1, the PDFs of the distributions are shown. In the figure, it is clearly shown that the confidence interval of the distributions becomes larger over time. It also shows the shift of the mean of the distribution over time towards a larger SLR.

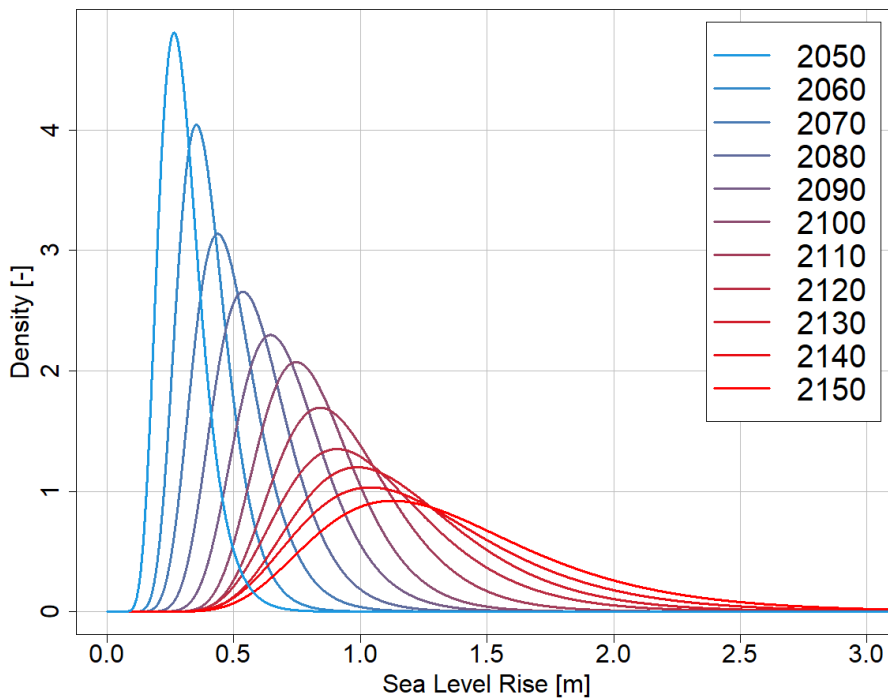


Figure J.1: The considered Probability Density Functions for different years for the SSP5-8.5 scenario.

K | Selected Adaptive Design Strategy

The design and construction phases of the selected adaptive design strategy, Strategy 2, are shown in Figure K.1. The 1st phase is shown in the red dashed-dotted line, the 2nd phase by the orange dashed line and the 3rd phase by the solid black line. The solid bold black line represents the current dike. This phase has a $h_{cr,d} = \text{NAP} + 8.38$ meters. The 2nd phase has a $h_{cr,d} = \text{NAP} + 8.44$ meters. The final design has a $h_{cr,d} = \text{NAP} + 9.25$ meters. The figure shows that the additional intrusion into the Natura 2000 area is 0.93 meters from the 1st to 2nd phase and 0.72 meters from the 2nd to 3rd phase.

	New clay layer
	Current clay layer
	Asphalt layer
	Densely-packed sand
Units: [m]	

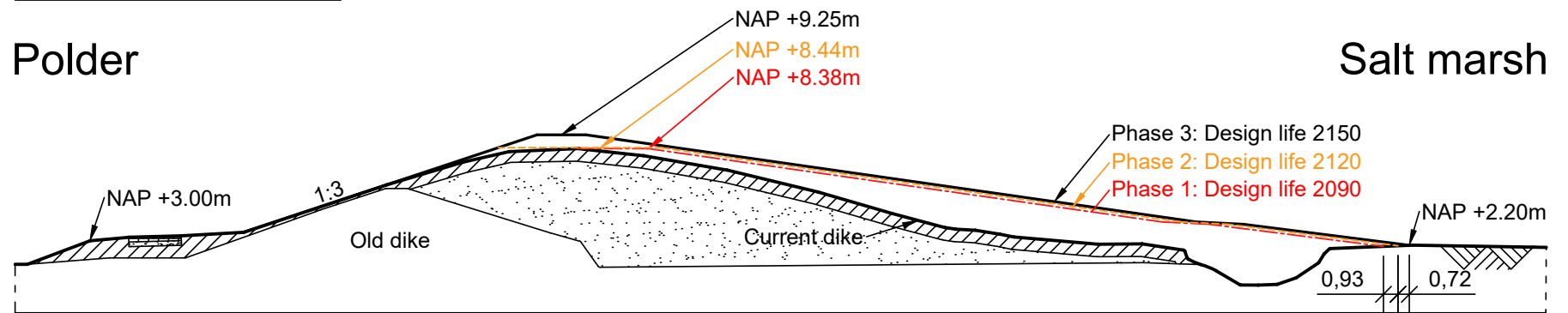


Figure K.1: The cross-section and construction phases of the selected strategy, Strategy 2.